UNIVERSITA' degli STUDI di MILANO-BICOCCA

Dottorato di Ricerca XXVI ciclo

in

Scienze della Terra

Heavy minerals: a key to unravel orogenic processes

Sediment generation and recycling at convergent plate boundaries (Indo-Burman-Andaman-Nicobar and Barbados Ridges)

Tutor: Eduardo Garzanti
Co-tutor: Sergio Andò

Laboratory for Provenance Studies
Department of Earth and Enviromental Sciences
University Milano-Bicocca, Italy

Mara Limonta
matr. 076180

Abstract

Sediments can be considered geological archives as they record and preserve the signatures of ancient geological events affecting source areas. This primitive provenance signal is modified by physical and chemical processes during transport and deposition.

The present thesis is devoted to highlight the importance of heavy minerals analysis on modern sediments to refine classical provenance models, unraveling sediment sources, transport conditions, diagenetic processes and recycling phenomena.

In the first part of the thesis a classification of surface textures observed on detrital heavy mineral grains in sands and sandstones is proposed in order to enhance data reproducibility among operators and to implement the use of high-resolution heavy-mineral data in studies on sediment-generation, provenance and diagenesis. Different stages of progressive weathering are collected in numerous color tables for visual comparison. They are specifically devised to systematically collect valuable information for paleoclimatic or diagenetic interpretation during routine grain-counting operations under the microscope. This catalog (Andò et al., 2012) represents a useful subsidiary tool to reveal the different degrees of weathering for diverse minerals in modern sands of equatorial Africa, and to identify post-depositional modifications of detrital assemblages in buried orogenic sediments of the Bengal Basin. These data, integrated with the concentration of heavy minerals in each sample, provide the fundamental clue to quantify the degree of heavy-mineral depletion caused by either pre-depositional or post-depositional processes (useful to understand the development of secondary porosity and to assess the potential of water and hydrocarbon reservoirs).

The second part of the thesis focuses on two regional studies on compositional variability, provenance and long-distance trasport of terrigenous sediments from Barbados Island (Limonta et al., in prep.) and Indo-Burma-Andaman-Nicobar Ridge (Garzanti et al., 2013a).

Subduction complexes large enough to be exposed subaerially and to become significant sources of terrigenous detritus are formed by tectonic accretion above trenches choked with thick sections of remnant-ocean turbidites. They thus need to be connected along strike to a large Alpine-type or Andean-type orogen, where huge volumes of orogenic detritus are produced and conveyed via a major fluvio-deltaic system to the deep sea (Ingersoll et al., 2003).

We investigated sediment generation and recycling in the Indo-Burman-Andaman-Nicobar subduction complex, representing the archetype of such settings in the eastern prolongation of the Himalayan collisional system. “Subduction Complex Provenance” is composite, and chiefly consists of detritus recycled from largely turbiditic parent rocks (Recycled Clastic Provenance), with local supply from ultramafic and mafic rocks of forearc lithosphere (Ophiolite Provenance) or recycled paleovolcanic to neovolcanic sources (Volcanic Arc Provenance; Garzanti et al., 2007). In order to specifically investigate the effect of recycling, we characterized the diverse detrital signatures of Cenozoic sandstones deposited during subsequent stages of “soft” and “hard” Himalayan collision and exposed from Bangladesh to the Andaman Islands, and discuss the reasons for compositional discrepancies between parent sandstones and their recycled daughter sands.

A companion study was carried out with the same methodologies, rationale and goals on Barbados Island. Also modern Barbados sands are largely multicyclic, reflecting mixing in various proportions of detritus from the basal Scotland Formation (sandstones and mudrocks), their stratigraphic and tectonic cover, the Oceanic Formation (quartzose turbidites and deep-water biogenic oozes including radiolarites), and from the Pleistocene calcarenite and reef caps, as well as from volcanic layers ultimately derived from the Lesser Antilles. Mixing of detritus recycled from orogen-derived turbidites transported long distance with detritus from oceanic mèlange, pelagic sediments and younger calcareous cap rocks and in addition volcaniclastic products thus redefines the diagnostic mark of Subduction Complex Provenance as quite distinct from the original definition by Dickinson and Suczek (1979).

Index

1. Introduction

Sediments can be considered as geological archives; they record and preserve the signatures of ancient geological events affecting source areas. This provenance signal is modified by physical and chemical processes during transport and deposition.

Sediment particles cover a spectrum of more than 5 orders of magnitude in diameter ($-1<\varphi<4$), deriving from the physical and chemical weathering of parent rocks exposed at the Earth surface. The size and composition of detrital grains largely depends on their genetic processes (mainly linked to climate and relief) and can dramatically change in time and space during transport due to mechanical crushing, chemical alteration, and formation of oxide coatings during burial diagenesis.

Among sediment particles, sand is the best suited for analysis as it is quite common in many tectonic and climatic settings (unlike coarser sediments, which require extreme high-energy conditions to be produced and transported) and its analysis can be performed under a polarizing microscope.

Finer sediments, silt and clay, which are hard to recognize under a standard polarizing microscope, represent the largest amount of sediment on Earth and are considered the future evolution of provenance analyses, thanks to the development and refinement of new techniques (e.g. X-Ray diffraction, Raman spectroscopy: Heberer et al., 2010; Morton and Chenery, 2009; Andò et al., 2009). The development of major, minor and trace element geochemistry and single-crystal geochronometers (e.g. Bernet et al., 2004) has given a further impulse over sediment analysis, allowing a better discrimination of sediment provenance.

The idea that sand particles can be considered a microscopic representation of the geological setting of the source area is very old. All arenites classification and heavy mineral analysis had been proposed so far (De Filippi, 1839; Dick, 1887; Artini, 1891; Salmojraghi, 1892; Fleet, 1926; Krynine, 1948; Pettijohn, 1972, 1954; Gilbert, 1954). Unravelling the provenance of a sedimentary basin fill has always been interpreted as a fundamental tool to reconstruct and eventually interpret the evolution of sediments, from their initial erosion to their final lithification, through transport, reworking and deposition.

As tectonics and climate are the main controlling factors on source rocks composition and sediments modifications through time and space (Dickinson, 1970), the correct identification

of sediment sources can provide insights both on paleogeography (paleocurrents orientation, paleodrainage patterns, localization of uplifting and subsiding area) and paleoclimatology (mainly due to chemical weathering features).
Sedimentary rocks are thus the complex product of the interactions of source rocks composition, erosion, transport, deposition, weathering and lithification. For this reason, progressively greater importance has been attributed to the study of modern sediments, allowing reconstructing the effects tectonics or climate on modern sediments from settings of well-constrained climate or geological setting, respectively.
If the present can be the key to understand the past, this actualistic approach allows to create refined models for sediment provenance, individually investigating the effects of climate and/or tectonics, which can eventually be combined to unravel clastic rock provenance, shedding new light on long-term evolution of the Earth surface.

1.1. Aims and outline of the thesis

The present thesis is devoted to the analysis of heavy minerals on modern sand-sized sediments to refine classical provenance model, unravelling sediment sources, transport conditions, diagenetic processes and recycling phenomena.
In the first part of the thesis a classification of surface textures observed on detrital heavy mineral grains in sands and sandstones is proposed in order to enhance data reproducibility among operators and to implement the use of high-resolution heavy-mineral data in studies on sediment-generation, provenance, and diagenesis. Different stages of progressive weathering are collected in numerous color tables for visual comparison. They are specifically devised to systematically collect valuable information for paleoclimatic or diagenetic interpretation during routine grain-counting under the microscope. This catalog (Andò et al., 2012; Chapter 5) represents a useful subsidiary tool to reveal the different degrees of weathering for diverse minerals in modern sands of equatorial Africa, and to identify post-depositional modifications of detrital assemblages in buried orogenic sediments of the Bengal Basin. These data, integrating with the concentration of heavy minerals in each sample, provide the fundamental clue to quantify the degree of heavy-mineral depletion caused by either pre-depositional or post-depositional processes (useful to understand the development of secondary porosity and to assess the potential of water and hydrocarbon reservoirs).

The second part of the thesis focuses on two regional studies on compositional variability, provenance and long-distance trasport of terrigenous sediments from Barbados Island (Limonta et al., in prep.) and Indo-Burma-Andaman-Nicobar Ridge (Garzanti et al., 2013a). These two places, where a large accretionary prism is subaerially exposed, are the best suited natural laboratory in which investigate sediment formation and recycling at convergent plate margins. These studies also allow us to redefine the diagnostic mark of Subduction Complex Provenance as quite distinct from the original definition by Dickinson and Suczek (1979).

Chapter 1 gives an outline of the Thesis.

Chapter 2 briefly traces back the evolution of petrographic and heavy mineral analyses on sand and sandstones.

Chapter 3 illustrates the importance of heavy mineral analysis in the determination of sediment provenance. Their concentration and their assemblages in modern sediment sample depend on the characteristics of the source rocks, transport conditions and depositional processes.

Chapter 4 describes the methods used to observe heavy mineral concentration and assemblages in modern sediment and sandstone samples analyzed in this Thesis.

Chapter 5 presents a catalog of corrosion features of heavy minerals formed by weathering, on modern sands of equatorial Africa, and by diagenesis, on samples from a core of the Bengal delta.

Chapter 6 presents the characteristics of different subduction zones in the world and shows why those areas are very interesting for provenance studies.

Chapter 7 shows a regional provenance study on compositional variability and long-distance multicyclic transport of terrigenous sediments of the Indo-Burma–Andaman-Nicobar Ridge. Sediment formation and recycling are analyzed by studying the petrography and mineralogy of modern fluvial to beach sands derived from the Indo-Burman–Andaman–Nicobar accretionary prism, integrated with analyses of sandstone clasts and of Cenozoic parent sandstones exposed from Bangladesh to the Andaman Islands.

Chapter 8 shows an other regional provenance study on compositional variability and long-distance multicyclic transport of terrigenous sediments along the convergent plate boundaries of Central America, from the northern termination of the Andes to the Lesser Antilles arc-trench system. We specifically focus on petrographic composition and heavy-mineral assemblages characterizing modern fluvial and beach sediments of Barbados Island, one of the few places in the world where an active accretionary prism is subaerially exposed.

2. History of provenance studies

It is now more than 100 years since the study of heavy minerals was established.
The notion that the origin of sand can be deduced from the mineralogical properties of its constituents dates back to end of the nineteenth century.
During this pioneering phase of sedimentary petrology, attention was paid both to framework (Sorby, 1880) and heavy mineral assemblages (De Filippi, 1839; Levy, 1878; Dick, 1887; Van Hise, 1885; Artini, 1891; Salmojraghi, 1892). The aim of these works was to define qualitatively and entirely descriptively the parent rocks of single minerals or mineral varieties (Illing, 1916; Boswell, 1933) and the recognition of characteristic "distribution provinces" (Brammall, 1928; Groves, 1931).
The quantitative study of heavy-mineral assemblages began with the works of Fleet (1926) and Edelmann (1931, 1933), who introduced the method of counting grains in order to make the determination of the relative frequency of mineral occurrences more objective.
In the 1930's and 1940's it was recognized that factors other than provenance exert fundamental controls on the composition of the heavy-mineral assemblages. Hydrodynamic (Rubey, 1933) and diagenetic processes (selective transport, weathering and intrastratal dissolution) transform the original provenance composition of heavy-mineral assemblages (Pettijohn, 1941). In the same years, interest for the bulk mineralogy of sandstones increased after Krynine and Pettijohn proposed the first version of the sandstones classification scheme which are still being used (Klein, 1963; Okada, 1971).
The early recognition of a link between framework composition, source rocks and climate setting (Barrell, 1908; Krynine, 1935, 1936, 1941; Blatt, 1967; Suttner, 1976; Crook, 1974; Schwab, 1975), received a great impulse by the advent of plate tectonics and the contribution of W. R. Dickinson (Dickinson 1974; Dickinson and Suczek 1979) who demostrated that the modal composition of sand-sized sediments is largely determined by plate-tectonic setting. Since sandstones are the combined product of tectonic setting – i.e. source rocks – relief, climate, and transport, it soon became clear that each of these factors should be individually investigated in modern settings to highlight their effects and produce an integrated and holistic approach over sediment provenance interpretation (Wetten and Kelley, 1969; Dickinson and Valloni, 1980; Suttner et al., 1981; Basu, 1985; Grantham and Velbel, 1988).

Another important development for provenance determination was the use of stable isotope data, bulk chemical compositions and trace elements (Suttner, 1989; Haughton et al. 1991).

In the last years, framework composition studies have still been applied to ancient sandstones successions (DeCelles et al., 2004; Fuentes et al., 2009; Di Giulio et al., 1999, 2001), and combination of framework, heavy mineral and geochemical studies on modern sediments allows to revise and refine classical provenance models, integrating the effects of source rocks, climate, hydraulic sorting, weathering and lithification (Garzanti et al., 2000, 2002a, 2002b, 2004a, 2004b, 2005, 2006a, 2006b, 2007a, 2007b).

3. Heavy minerals in the study of sediments

Sediments are unrivalled geological archives. They record and preserve the signatures of ancient geological events in source areas, along transport pathways and in the depositional basins. Sediments mineralogy and chemical composition depend chiefly on the characteristics of source area, but also on hydraulic regime during transport and on burial conditions. Source-rock composition, climate, relief, slope, vegetation, and dynamics of the fluvial environment are the more important features of source area. Moreover weathering and erosion play important roles in controlling the composition of sediments (Johnsson et al., 1991).

Heavy mineral analysis is one of most sensitive and widely-used techniques in the determination of sediment provenance. Heavy minerals are high density accessory minerals of siliciclastic sediments. In their parent rocks, they are present either as essential rock forming minerals (e.g. amphiboles, pyroxenes) or as accessory components, such as zircon, apatite, tourmaline, occurring in a wide variety of rock types. Heavy mineral grains are seldom encountered in appreciable quantities in thin sections; their total quantity rarely makes up more than one per cent of the rocks. In order to study heavy minerals we need to concentrate them, and this is normally done by mineral separation, using liquid with high density (e.g. sodium polytungstate, δ = 2.90 g/cm^3). Heavy mineral fractions in sediment contain diverse mineral species and each grain conveys its own history. Usually heavy mineral assemblages can be used for:

(a) determining provenance: reconstructing the nature and characteristics of source area;
(b) tracing sediment transport paths: these are particularly useful for complementing paleocurrent analyses;
(c) mapping sediment dispersal patterns;
(d) delineating sedimentary “petrological provinces”;
(e) outlining and correlating various sand bodies;
(f) indicating the action of particular hydraulic regimes and concentrating processes;
(g) locating potential economic deposits;
(h) elucidating diagenetic processes.

Heavy mineral studies are also useful in studies of sedimentation related to tectonic uplift, as the evolution and unroofing episodes of orogenic belts are faithfully reflected in their foreland sediments. Analyses of heavy minerals are also important in pedology, as they provide clues to soil formation.

The composition of heavy mineral assemblages is chiefly controlled by the mineralogical composition of the source region, but this original provenance signal is modified by several other processes that operate during the sedimentation cycle. From the moment the minerals are released from their host rocks, a series of processes come into effect, operating until the assemblages are extracted from the sediment for study. The significance of factors likely to affect the reliability of heavy minerals analyses and their interpretation have been discussed in many publications (Mackie, 1923; van Andel, 1959; Blatt ,1967; Hubert, 1971; Pettijohn et al., 1972; Morton, 1985).

The most important parameters are (Figure 3.1.):

(a) physiographic setting and climate of the source area. These factors largely control the pre-selection of the mineral grains during host-rock weathering and thus determine the original input of heavy mineral species into the sedimentary system;

(b) abrasion and mechanical destruction during transport. These are related to mechanical durability of the grains themselves;

(c) hydraulic factor. This operates during transport and is controlled by the conditions of the particular hydraulic regime. Its effects result in selective grain sorting according the size, shape and density;

(d) post-depositional, diagenetic, effects. This results in progressive dissolution of the less unstable mineral due to “intrastratal dissolution”.

The last two parameters are especially important. The hydraulic factor decides which mineral grains will be deposited under certain hydraulic conditions and fractionates the relative abundance of minerals with different hydraulic behavior. Diagenesis reduces mineral diversity through progressive dissolution of the less stable mineral, and it influences the ultimate heavy mineral assemblages of a particular sediment. Abrasion during transport, instead, appears to cause negligible modifications of heavy mineral suites (Russel, 1937; Shukri, 1949).

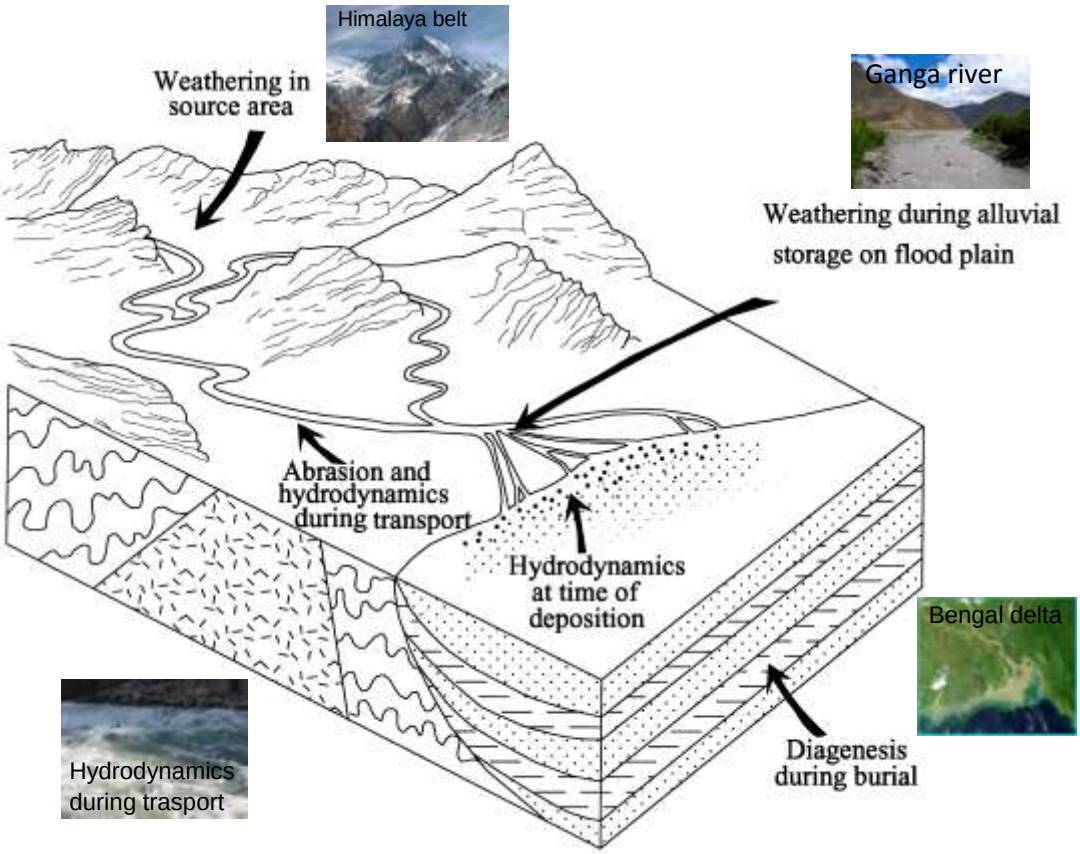

Figure 3.1. *Schematic diagram showing processes controlling heavy mineral assemblages in sandstones (modified after Morton and Hallsworth 1999).*

3.1. Heavy mineral concentration and suites in different source rocks

The concentration of heavy mineral grains in sand-sized terrigenous sediments may change considerably because of several factors, including provenance, sedimentary processes, and post-depositional dissolution (Mange and Maurer, 1992; Morton and Hallsworth, 1999). Concentrated heavy mineral assemblages, however, may result from density-sorting during erosion, transport, or deposition by tractive currents, which can segregate very effectively minerals with even small differences in density within distinct grain-size fractions and sedimentary environments. Deposits that show such heavy mineral enrichments, (e.g. black mixture of iron oxide, gold, platinum-group mineral, garnet) are defined “placers” (Komar and Wang, 1984; Reid and Frostick, 1985; Dickinson, 1994; Mallik at al., 1987;.Bryan et al., 2007; Ghosh et al., 2012). Conversely, depleted heavy mineral assemblages may result from severe diagenetic dissolution in ancient sandstones. Heavy mineral concentration may be depleted by an order of magnitude or more because of selective leaching of unstable species (Gazzi, 1965; Morton, 1985). In modern beaches and deltaic cusps, for instance, heavy minerals concentration is commonly observed to increase by an order of magnitude or more because of selective removal of lighter grains by wave erosion (Komar and Wang, 1984; Hughes et al., 2000).

Heavy mineral concentration in sediments primarily reflects the lithology of parent rocks, and specifically their composition, average density, and tectono-stratigraphic level. Sedimentary to very low-grade metasedimentary rocks and felsic plutonic rocks (e.g., metasandstone and granite), which characterise upper tectonostratigraphic levels of the Earth’s crust, have relatively low density (δ~2.70 g/cm^3; Daly et al., 1966). As a consequence they contain, and therefore can provide, only few heavy minerals. By contrast, ultramafic and mafic igneous rocks (e.g. peridotite, gabbro), or high temperature to high-pressure (e.g. amphibolite, granulite, eclogite) metamorphic rocks, that make up deeper tectono-stratigraphic levels of the lithosphere, are much denser (δ~2.80–3.45 g/cm^3), and therefore include and can supply a wealth of heavy minerals (Figure 3.2.).

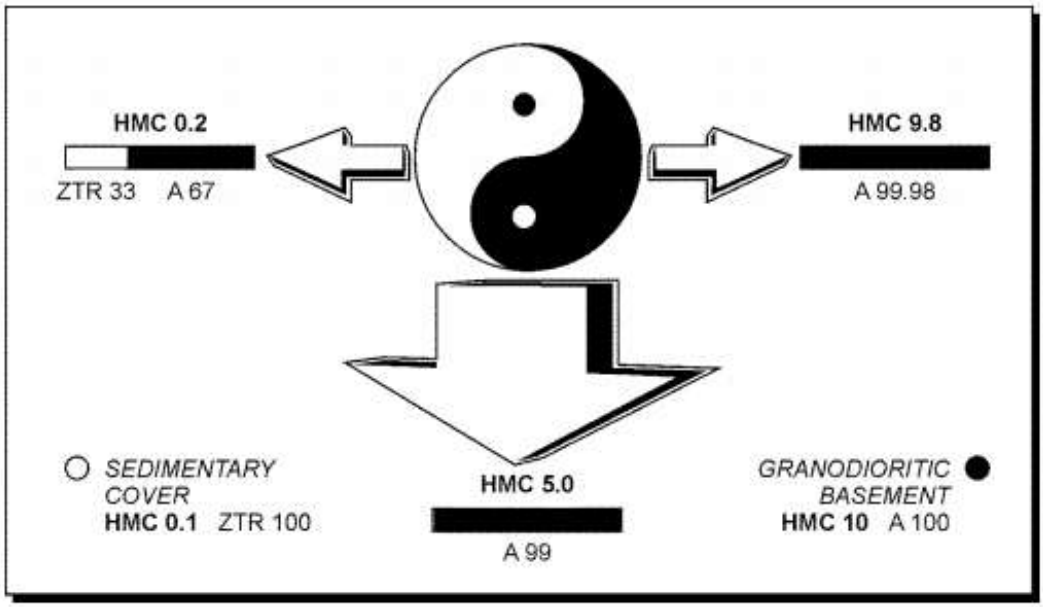

***Figure 3.2**. Asymmetric effect of a two-order-of-magnitude difference in heavy mineral concentration in detritus from basement and cover rocks. Granodioritic batholiths (dark yin) supply dominant amphiboles (HMC 10; A 100), whereas sedimentary successions (bright yang) only supply few recycled ultrastable minerals (HMC 0.1; ZTR 100). Where cover strata are widespread (left side of the Taiji Tu; e.g., "Undissected Craton subprovenance"), even a small basement high (black seed, representing 2% in outcrop area) is readily revealed by a low heavy mineral yield and an amphibole-rich assemblage. Instead, where basement is widespread (right side of the Taiji Tu; e.g., "Dissected Craton subprovenance"), locally preserved sedimentary strata (white seed, representing 2% in outcrop area) have an insignificant dilution effect on the heavy mineral assemblage. Even in the intermediate case (whole of the Taiji Tu; e.g., "Transitional Craton subprovenance"), the main effect of sedimentary covers (50% of outcrop area) is to halve the concentration of amphibole dominated heavy mineral assemblages (Garzanti and Andò, 2007a).*

Three primary sources of detritus are considered here: oceanic lithosphere, arc crust, and continental crust.

Oceanic lithosphere

Oceanic lithosphere displays a relatively simple stratigraphy; it commonly includes harzburgitic mantle peridotites at the base, layered gabbroic rocks followed by isotropic amphibole gabbros and plagiogranite sills of lower crust, sheeted diabase dikes, tholeiitic pillow basalts, and a thin pelagic sediment cover (Malpas et al., 1990; Boudier and Juteau, 2000).

Fresh harzburgites of oceanic mantle consist entirely of heavy minerals (75-85% olivine, 15-25% orthopyroxene, ≤2% spinel). Lower-crustal gabbroic rocks supply very rich, clinopyroxene-dominated heavy mineral assemblages including green to brown horneblende; higher crustal rocks are affected by actinolite-facies to prehnite-pumpellyite-facies metamorphism. Sheeted dykes shed pyroxenes, actinolite amphiboles and epidote, whereas pillow lavas provide mainly clinopyroxene. By contrast, thin pelagic covers are devoid of heavy minerals (Table 3.1.).

Arc crust

Arc crust includes gabbroic to granitic calc-alkaline batholiths at depth, and basaltic to rhyolitic lavas and pyroclastic deposits at the surface (Gill, 1981). Detritus from dissected arc batholiths is rich in heavy minerals and assemblages are dominated by blue-green and subordinately green and brown hornblende, with epidote, minor clinopyroxenes and green-pink hypersthene (Table 3.2. Transhimalayan belt). Undissected volcanic arcs shed heavy mineral assemblages dominated by green augite and yellow-green hypersthene, associated with either olivine or dark-brown to reddishbrown hornblende (oxyhornblende). Heavy mineral concentration, although fluctuating widely, is commonly high to extremely high.

Continental crust

Continental is characterized by a very complex and variable structure typically formed during its multistage geological evolution. The composition of orogenic sands also are complex because they are complex mixtures of detritus from several distinct tectono-metamorphic assemblages. Data from modern sands from distinct tectono-stratigraphic levels of continental crust and collision orogens across the world are reported in the Table 3.3.

Level	Lithology	Unit	n.	HMC	tHMC	ΔtHMC	SRD	%opHM	%udHM	%ZR	ZTR	T&	LgM	Gt	HgM	Hb	&A	CPX	OPX	OS	HCI	MMI
OBDUCTED OPHIOLITE NAPPE																						
Sediment cover	Remnant -ocean turbidites	Liguride flyshes	35	2	1	3,66	2,67	18	34	74	8	5	15	30	2	11	6	12	5	6	28	11
Upper crust	Basalts	Bela	1	17	9	3,41	2,8	8	0	33	1	0	9	0	0	7	1	81	1	0	n.d.	n.d.
Middle crust	Sheeted Dikes	Troodos	3	24	20	3,35	2,85	6	0	n.d.	0	0	45	0	0	4	7	40	3	0	31	n.d.
Middle crust	Sheeted Dikes	Kizildag	1	33	31	3,3	2,86	0	0	n.d.	0	0	4	0	0	6	10	69	11	1	19	n.d.
Lower crust	Gabbros	Internal Liguride	1	17	15	3,32	2,79	1	2	n.d.	0	0	1	0	0	1	2	94	0	1	n.d.	n.d.
Mantle	Harzburgites	Sama'il	2	17	12	3,34	2,84	26	2	n.d.	0	0	3	0	0	1	1	6	70	19	n.d.	n.d.
Mantle	Harzburgites	Kizildag	3	33	31	3,34	2,89	2	2	n.d.	0	0	0	0	0	0	0	3	56	41	n.d.	n.d.
SUBDUCTED CONTINENTAL-MARGIN UNITS																						
Lawsonite-carphholite facies	Metasediments	Saih Hatat	1	0.04	0,1	3,44	2,65	15	8	92	9	0	46	0	0	5	11	22	8	0	n.d.	n.d.
Blueschist facies	Metasediments	Saih Hatat	2	14	5	3,4	2,82	30	2	70	3	0	72	0	0	4	10	7	4	0	n.d.	n.d.
Eclogite facies	Metasediments	Saih Hatat	1	37	22	3,51	3,14	30	26	100	4	1	42	22	0	1	17	6	7	0	n.d.	n.d.

Table 3.1. *High heavy mineral concentration in detritus from serpentinised ultramafic and partly altered mafic rocks of the obducted oceanic lithosphere (modified after Garzanti and Andò, 2007a). Symbol are explained in 4.5.2. paragraph.*

Volcanic centre	Main volcanic produc	Age	n.	HMC	tHMC	ΔtHMC	SRD	%opHM	%udHM	%ZR	ZTR	T&	LgM	Gt	HgM	Hb	&A	CPX	OPX	OS	HCI	MMI
Active volcanic centre																						
Campi Flegrei	Tephrite	Holocene	1	20	19	3,31	2,79	3	1	n.d.	0	0	0	1	0	0	0	99	0	0	n.d.	n.d.
Vesuvio	Tephrite and phonolite	Holocene	1	58	54	3,32	3,05	6	2	n.d.	0	0	2	0	0	9	1	82	0	6	82	n.d.
Stromboli	High-K basalt to basaltic andesite	Holocene	3	59	53	3,31	3,05	9	0	n.d.	0	0	0	0	0	0	0	82	0	18	n.d.	n.d.
Panarea	Felsic andesite to rhyodacite	Holocene	1	53	44	3,32	3,02	17	0	n.d.	0	0	0	0	0	26	0	38	36	0	98	n.d.
Vulcano	Tephrite to rhyolite	Holocene	2	41	37	3,3	2,96	6	0	n.d.	0	0	0	0	0	0	0	94	0	6	n.d.	n.d.
Salina	High-Al basalt to dacite	Holocene	2	64	48	3,33	3,26	8	0	n.d.	0	0	0	0	0	1	0	64	27	8	72	n.d.
Lipari	Largely rhyolite	Holocene	3	16	15	3,31	2,76	6	0	n.d.	0	0	0	0	0	1	0	86	13	0	67	n.d.
Santorini	High-Al basalt to rhyolite	Holocene	1	21	18	3,35	2,8	13	0	n.d.	0	0	1	0	0	1	0	51	38	7	100	n.d.
Extinct Mesozoic to Cenozoic centers																						
Mt. Amiata	Rhyodacite	Quaternary	1	6	5	3,41	2,7	5	1	n.d.	0	0	0	1	0	0	0	3	96	0	n.d.	n.d.
Capraia	High-K andesite to rhyolite	Mio-Pliocene	1	5	4	3,33	2,69	17	0	n.d.	0	0	0	0	0	4	0	62	33	0	100	n.d.
S. Pietro	Peralkaline rhyolite	Miocene	1	3	1	3,43	2,69	15	12	100	1	10	10	3	0	6	36	21	12	0	64	n.d.
Lesvos	High-K basalt to rhyolite	Miocene	1	3	3	3,3	2,67	9	0	n.d.	0	0	0	0	0	4	0	94	2	0	92	n.d.
Dolomiti	Latite	Middle Triassic	1	34	32	3,3	2,89	2	0	n.d.	0	0	0	0	0	0	0	100	0	0	n.d.	

Table 3.2. *Heavy mineral concentration in modern sands from active and exstinct Mediterranean arcs (modified after Garzanti and Andò, 2007a). Symbol are explained in 4.5.2. paragraph.*

Level	Lithology	Unit	n.	HMC	tHMC	ΔtHMC	SRD	%opHM	%udHM	%ZR	ZTR	T&	LgM	Gt	HgM	Hb	&A	CPX	OPX	OS	HCI	MMI
Upper crust																						
Cover	Sediments	Orobie	5	0,7	0,4	3,51	2,66	24	26	33	5	4	25	22	8	30	3	3	1	0	32	40
Cover	Sediments	Levant/Nubia	17	0,8	0,4	3,6	2,66	31	23	61	30	4	28	6	8	17	1	5	1	0	11	40
Cover	Sediments	Gulf of Aden	19	0,9	0,6	3,58	2,66	27	28	77	14	1	38	15	1	22	2	4	2	1	32	31
Cover	Sediments	Indian Shield	2	1	0,8	3,73	2,67	20	38	51	45	7	26	5	2	13	2	0	0	0	11	67
Cover	Sediments + lavas	Dolomites	2	2	0,9	3,41	2,67	15	11	73	2	3	12	7	0	6	0	70	0	0	56	n.d.
Cover	Sediments + lavas	Levant/North Red Sea	26	1	0,7	3,52	2,67	23	12	68	15	3	13	2	2	16	0	45	0	3	15	36
Cover	Sediments + lavas	Gulf of Aden	6	2	1	3,4	2,67	12	7	61	4	1	19	3	1	25	2	33	7	4	32	39
Basement+cover		External Massifs	5	3	2	3,41	2,68	6	11	76	5	2	33	7	1	44	5	2	1	0	54	n.d.
Basement+cover		North Red Sea	22	4	2	3,42	2,69	23	8	73	7	3	22	3	2	42	1	20	0	0	14	37
Basement+cover		Gulf of Aden	8	3	3	3,41	2,68	13	9	87	5	1	43	4	0	35	3	6	2	0	28	32
Middle crust																						
Amphibolite facies	Metasediments	Serie dei Laghi	12	5	4	3,56	2,7	8	32	32	5	2	10	29	16	33	3	1	0	0	17	50
Amphibolite facies	Granitoids, metavolcanics	North Red Sea	11	9	5	3,39	2,76	27	6	77	6	9	12	1	1	53	1	16	0	0	11	39
Amphibolite facies	Granitoids, metavolcanics	South Red Sea	4	12	11	3,3	2,75	5	2	67	1	2	17	1	0	62	2	14	0	0	9	n.d.
Amphibolite facies	Granitoids, gneisses	Gulf of Aden	10	13	11	3,3	2,75	8	5	65	3	2	10	2	1	73	2	4	2	1	11	42
Amphibolite facies	Gneisses, granitoids	Indian Shield	5	7	6	3,39	2,71	8	15	84	2	3	9	13	2	61	1	7	1	0	18	59
Lower crust																						
Granulite facies	Kinzigites	Ivrea-Verbano	8	35	31	3,44	2,94	1	21	79	1	2	14	20	8	36	5	12	1	1	38	100
Granulite facies	Gabbros	Ivrea-Verbano	3	44	31	3,46	3,1	12	18	75	1	0	5	17	0	23	2	12	10	0	87	n.d.
Mantle	Peridotites	Ivrea-Verbano	1	70	57	3,33	3,15	2	2	n.n.	0	0	1	2	0	14	3	12	15	52	43	n.d.
Alps																						
Oceanic units																						
Non-metamorphic	Sediments	San Remo	4	0,2	0,1	3,7	2,65	12	42	69	24	4	23	22	2	14	2	5	3	1	28	51
Very-low grade	Metasediments	Ubaye-Parpaillon	2	0	0	3,92	2,65	51	56	66	73	0	8	8	0	2	2	6	2	0	n.d.	n.d.
Blueschist (carpholite zone)	Metasediments	Calcschists	3	1	0,3	3,39	2,66	6	3	25	2	6	49	0	0	8	25	9	0	0	43	0
Blueschist	Metasediments	Calcschists	5	3	2	3,46	2,67	9	13	58	8	1	57	8	1	8	15	2	1	0	21	7
Eclogite facies	Metaophiolites	Zermatt-Voltri	7	29	24	3,35	2,86	1	6	100	1	1	44	5	1	15	25	6	1	1	6	60
Continental units																						
Blueschist - carpholite zone	Metasediments	Ligurian Brianconnais	4	1	0,3	3,5	2,66	9	16	60	12	2	55	8	2	12	4	3	1	0	15	33
Blueschist - greenschist facies	Metasediments	Brianconnais	3	3	1	3,46	2,68	15	14	35	13	3	54	10	1	9	8	1	1	0	30	0
Blueschist - greenschist facies	Basement	Brianconnais	4	4	2	3,51	2,69	11	21	57	3	6	44	18	0	19	7	1	1	0	20	2
Amphibolite facies	Basement	Lepontine Dome	25	9	8	3,43	2,72	3	21	69	2	1	14	20	4	49	5	3	1	0	25	60
Eclogite - greenschist facies	Basement	Internal Massifs	5	7	6	3,67	2,73	3	42	71	4	2	45	39	1	6	2	1	0	0	5	17
Eclogite facies-very low grade	Basement	Sesia-Lanzo	7	16	14	3,53	2,8	1	22	100	1	3	59	21	0	7	8	1	0	0	12	n.d.
Granulite - greenschist facies	Lower crust	Dent Blanche	2	21	14	3,63	2,87	3	44	n.d.	1	1	25	43	6	12	2	5	5	0	55	99
Batholiths	Tonalite granodiorite	Periadriatic Zone	5	14	12	3,3	2,75	12	4	100	3	4	15	0	0	78	0	0	0	0	7	n.d.
Himalaya																						
Very-low grade	Metasediments	Tethys Himalaya	5	1	0,7	3,43	2,66	15	22	9	53	3	7	16	11	7	1	2	0	0	24	47
Very-low grade	Metasediments	Outer Lesser Himalaya	6	1	0,4	3,41	2,66	17	14	23	31	3	36	7	2	13	3	5	0	0	4	60
Greenschist facies	Metasediments	Inner Lesser Himalaya	2	7	6	3,52	2,73	13	33	42	5	1	18	31	3	38	4	0	0	0	3	67
Greenschist facies	Metasediments	North Himalaya	1	8	2	3,52	2,72	5	12	35	20	5	56	3	0	11	1	4	0	0	2	0
Amphibolite facies	Metasediments	Greater Himalaya	14	10	9	3,61	2,76	6	41	42	5	2	7	38	13	22	1	11	0	0	26	75
Batholiths	Gabbro-granite	Transhimalaya	5	25	20	3,28	2,84	8	1	83	1	3	16	0	0	69	3	4	4	0	16	n.d.

Table 3.3. *Heavy mineral concentration in modern sands from distinct tectono-stratigraphic levels of continental crust and collision orogens across the world (modified after Garzanti and Andò, 2007a). Symbol are explained in 4.5.2. paragraph.*

3.2 Plate tectonics and heavy mineral suites in modern sands

Different heavy mineral assemblages are produced in contrasting geodynamic settings (Garzanti and Andò, 2007b). In Figure 3.3. the provenance types of Dickinson and coworkers (Dickinson and Suczek, 1979; Dickinson, 1985; Ingersoll, 1990) and subsequently expanded by Garzanti and Andò (2007b) are reported.

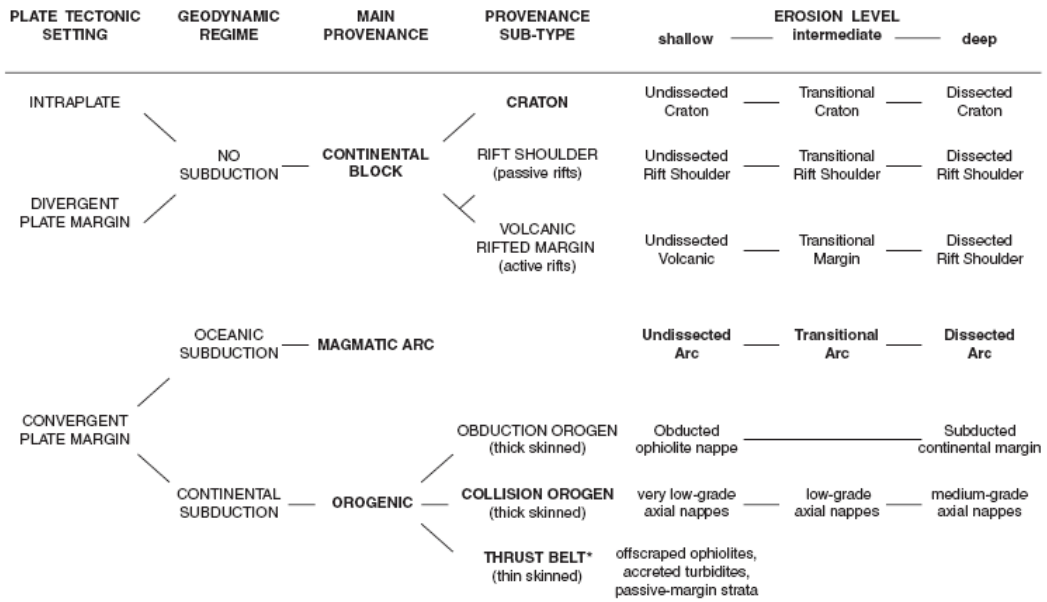

Figure 3.3. *Provenance scheme (terms introduced by Dickinson and Suczek, 1979; Dickinson, 1985; are in bold; Fig. 1. Garzanti and Andò, 2007b).*

Sands from "**Continental block**" provenance (Figure 3.4.) are characterised either by heavy-mineral-rich, horneblende dominated assemblages derived from amphibolite-facies basement rocks exposed along rift escarpments (''**Dissected Rift Shoulder subprovenance**'') or cratonic shields, or by heavy-mineral-poor suites with commonly rounded ultrastable grains recycled from cover strata (''**Undissected Rift Shoulder subprovenance**'').

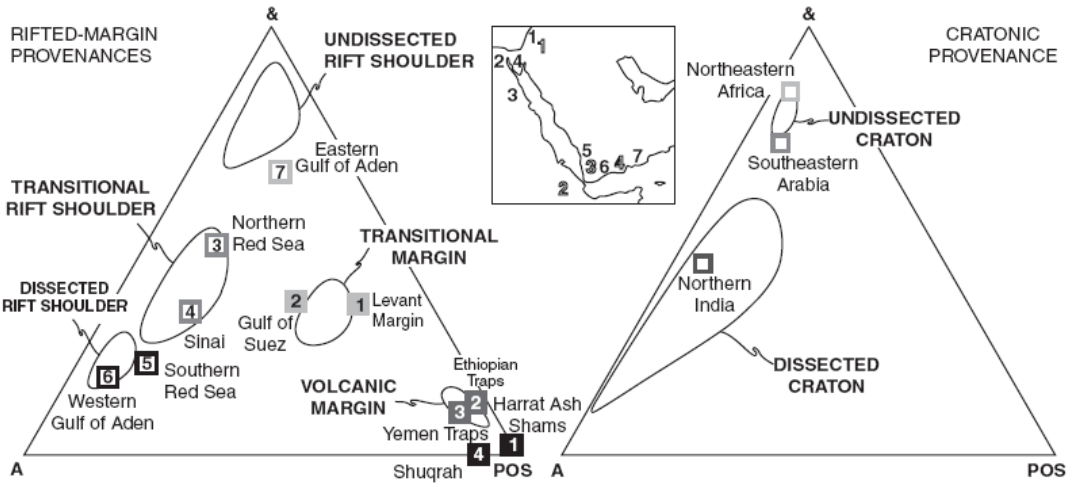

Figure 3.4. *Continental Block Provenance'' and heavy mineral suites. & = all transparent heavy minerals not included in the other two poles. A = Hb+&A = total amphiboles. POS = PX +OPX+OS =pyroxenes, olivine, and spinel (Fig. 3., Garzanti and Andò, 2007b).*

Detritus derived from "volcanic arcs" is typified by pyroxene-dominated heavy mineral assemblages (''**Undissected Arc subprovenance**''). The two dominant minerals are augite, found in the vast majority of orogenic lavas, and hypersthene, absent in basalts but widespread in andesites. Olivine, ubiquitous in basalts, is found even in felsic andesites. Hornblende is common in medium- to high-K felsic andesites and dacites, frequently associated with biotite. The ratio of orthopyroxene to clinopyroxene phenocrysts typically increases with increasing silica contents, and orthopyroxene is generally antipathic with both olivine and hornblende (Gill, 1981). Other clinopyroxenes are pigeonite (tholeiitic andesites lacking olivine) and clinoenstatite (boninites). Magnetite (relatively Ti-poor titanomagnetite) is the dominant opaque mineral. Garnet and spinel (locally occurring as inclusions in olivine phenocrysts) are rare. Volcanic rift margin shed detritus with lilac-brown and green augite-dominated heavy mineral suite locally asoociated with olivine and brown horneblende.

Detritus from calc-alkaline batholiths, representing the remnants of eroded arcs, is hornblende-dominated (''**Dissected Arc subprovenance**'').

Mixed assemblages, including augite and hypersthene from volcanic covers, associated in various proportions with hornblende and subordinate epidote from the plutonic roots and metamorphic wallrocks of the arc massif (''**Transitional Arc subprovenance**'') are frequently found in Circum-Pacific sands (Figure 3.5.).

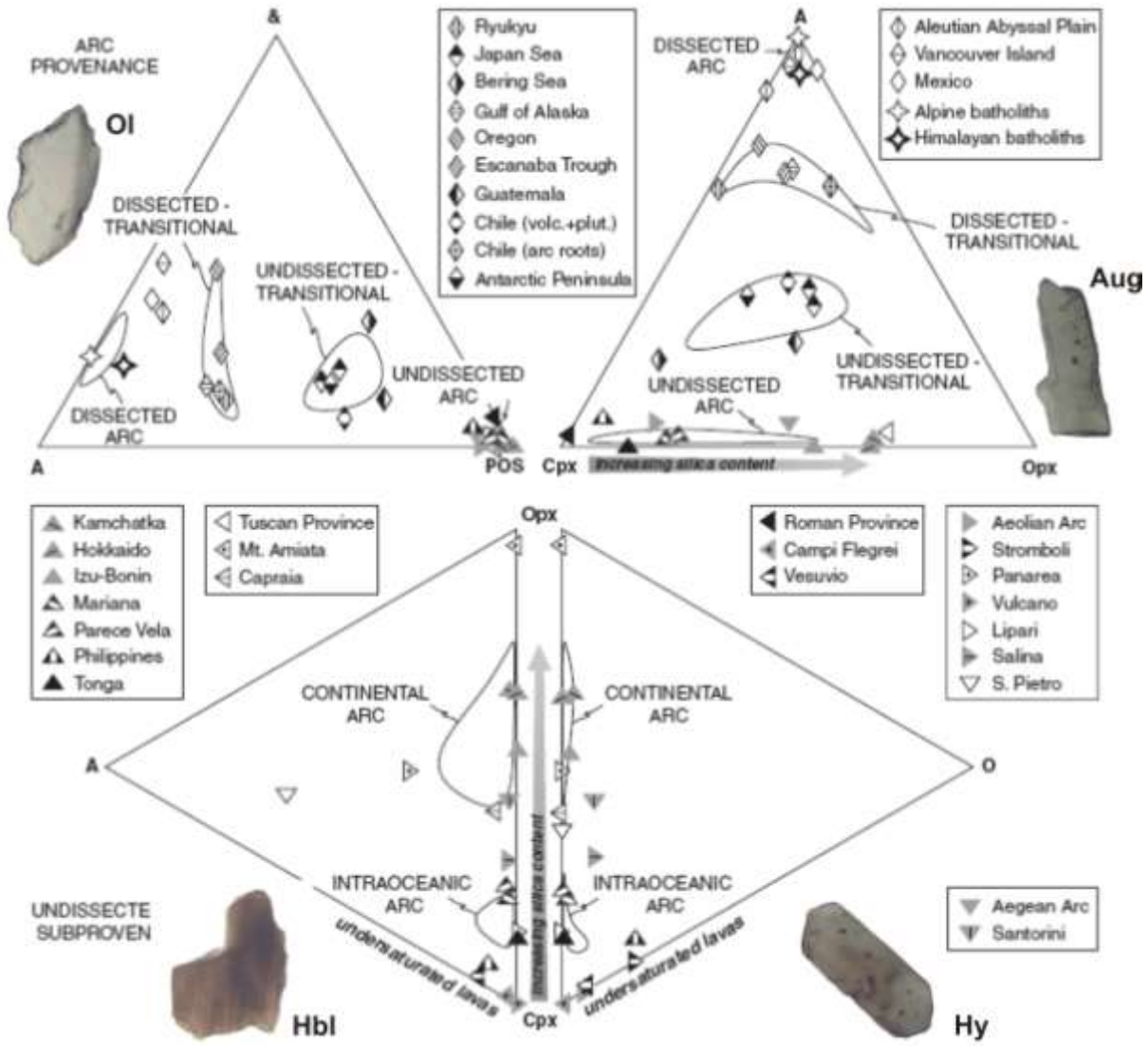

Figure 3.5. *''Magmatic Arc Provenance'' and heavy mineral suites. The double triangle below discriminates between intraoceanic (largely basalts and basaltic andesites) and continental (commonly felsic andesites to rhyolites) ''Undissected Arc subprovenance''. & =all transparent heavy minerals not included in the other two poles. A = Hb+&A = total amphiboles. POS = CPX+OPX+OS = pyroxenes, olivine, and spinel (modified after Garzanti and Andò, 2007b).*

Orogenic provenance is a complex subject, difficult to deal with in brief because each thrust belt has its own tectonic style, peculiar rock assemblage, and stacking pattern. Data of sands from Alps, Himalayas, Appennines and Oman belt are reported in Figure 3.6.

Sands of ''**Orogenic Provenance**'' include suites dominated by amphiboles, garnet, and epidote. The relative abundance of garnet (associated with subordinate staurolite, kyanite,

and sillimanite) and blue-green to green-brown hornblende increases with increasing metamorphic grade of the sedimentary or igneous protoliths, respectively. Oman-type obduction orogens shed abundant heavy minerals, dominated by mafic and ultramafic minerals derived from the obducted ophiolite nappe. Apennine-type thin-skinned thrust belts provide heavy-mineral-poor assemblages recycled from accreted passive-margin successions or foredeep turbidites. Pyroxenes, derived from offscraped ophiolitic sequences, can be locally present.

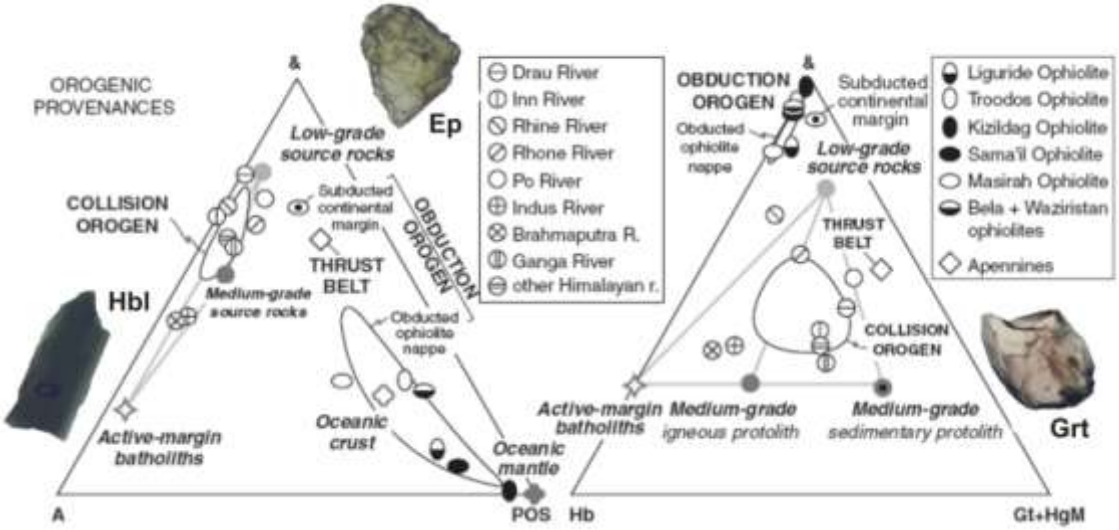

Figure 3.6. *''Orogenic Provenance'' and heavy mineral suites. & =all transparent heavy minerals not included in the other two poles. A = Hb+&A = total amphiboles. POS = CPX+OPX+ OS = pyroxenes, olivine, and spinel (modified after Garzanti and Andò, 2007b).*

3.3. Weathering of heavy minerals

The original composition of heavy mineral assemblages can be modified by weathering of parent rocks that prior to incorporation into transport system (Morton and Hallsworth, 1999). The degree to which heavy mineral assemblages are modified by weathering in the source area depends on three main factors: the original composition of the heavy mineral suite (controlled by the parent rock lithology), the physiographic setting, and the climate (precipitation and temperature; Suttner et al., 1981). The latter controls the extent to which soil formation occurs. If the transport processes removing weathered material are potentially more rapid than the weathering processes generating the material, erosion is said to be weathering-limited (Johnsson et al., 1991; Figure 3.7.a). Under such conditions, detritus is quickly removed without significant modification by chemical weathering, and thus the provenance signature of the parent rocks is likely to be largely transferred into the transport system. When, in contrast, the weathering rate exceeds the capacity of transport processes to remove material, then erosion is transport-limited (Johnsson et al., 1991; Figure 3.7.b). Under transport-limited conditions, weathering products have a longer time to react with soil and groundwaters, strongly affecting the composition of detritus. In this situation, extensive modification of the heavy mineral suites can occur before the sediment reaches the transport system.

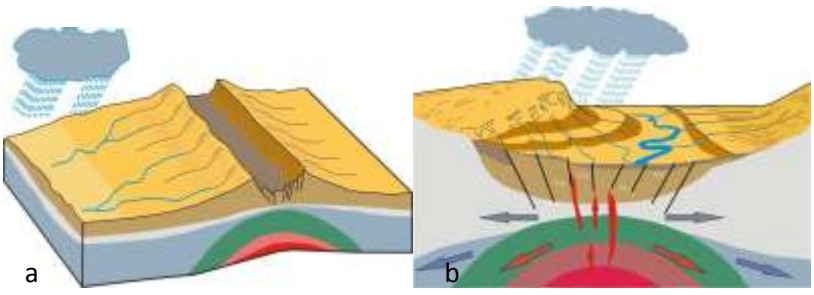

Figure 3.7. (a)"*Weathering-limited" regime,* ***(b)*** *"transport-limited regime".*

The generation of acidic groundwaters through bacterial degradation of organic matter (Burley et al., 1985) in well-vegetated humid environments under tropical or temperate climates causes strong evidence of corrosion, with etched grain surfaces and extensive dissolution of unstable heavy minerals (Friis and Johannesen, 1974). Red beds, in which

iron is in the ferric state, may form in either arid, desert conditions or in seasonal climates (Walker, 1967). Heavy mineral assemblages may be affected by non-marine weathering not only at the ultimate depositional site, but also during temporary alluvial storage, for example on river floodplains or in coastal dunes (Friis, 1978; Johnsson et al., 1988).

In general, the diversity of detrital heavy minerals in weathering profiles decreases from top (least weathered) to bottom (most weathered), due to dissolution or transformation of the less stable minerals. A comparison of the relative order of stability of heavy minerals in these profiles shows a reasonable degree of consistency, with zircon, rutile, tourmaline, kyanite, andalusite and sillimanite invariably showing higher stability, and apatite, olivine and pyroxenes showing very low stability. The intermediate group (garnet, calcic amphibole, staurolite and epidote) tends to vary in its relative stability among the various profiles (Table 3.4.) One possible explanation is that the stability variations result from compositional variations of amphibole, epidote and garnet between the different profiles. Another possibility is that there were variations in the composition and concentration of the groundwaters responsible for the leaching (Mitchell, 1975).

Chemical Stability

Gneiss Dolerite Amphibolite Northern USA Goldich (1938)	Crystalline schist Northern USA Dryden and Dryden (1946)	Granite Germany Piller (1951)	Terziary kaolinitic sand Germany Weyl and Werner (1951)	Bavarian molasse Germany Grimm (1973)	Calcareus sandstones Germany Lemcke et al. (1953)	Aeolian coversands England Bateman and Catt (1985)
 Zrn Garnet Calcic amphiboles Clinopyroxene Olivine	Zircon Sillimanite Monazite Kyanite Calcic amphiboles Staurolite  Grt Garnet Ortopyroxene	Zircon Tourmaline Garnet Apatite	 Ky Kyanite Staurolite Epidote Garnet Calcic amphiboles	Zircon, Rutile Tourmaline, Andalusite, Kyanite Staurolite Epidote Garnet, Apatite Calcic amphiboles Clinopyroxene Olivine	Zircon, Rutile, Tourmaline, Staurolite Kyanite, Epidote Calcic amphiboles Apatite Garnet	Zircon, Rutile, Tourmaline, Andalusite Titanite  St Garnet Epidote Clinopyroxene Ortopyroxene Calcic amphiboles Apatite

Table 3.4. *Relative stability of trasparent heavy minerals in weathering profiles (modified after Morton and Hallsworth, 1999).*

Changes of mineral surface textures can also underline the effect of weathering.

Mineral surface textures can be inherited (unmodified) from parent materials, modified or even completely destroyed and replaced by new surface textures during weathering.

The study of weathering morphological features produced by weathering can be analyzed in almost all species of heavy mineral. The best way to observe the weathering textures is investigated them at greater magnification, using the scanning electron microscope (Rahmani, 1973; Moral Cardona et al., 2005; Velbel, 1984; Velbel, 2007).

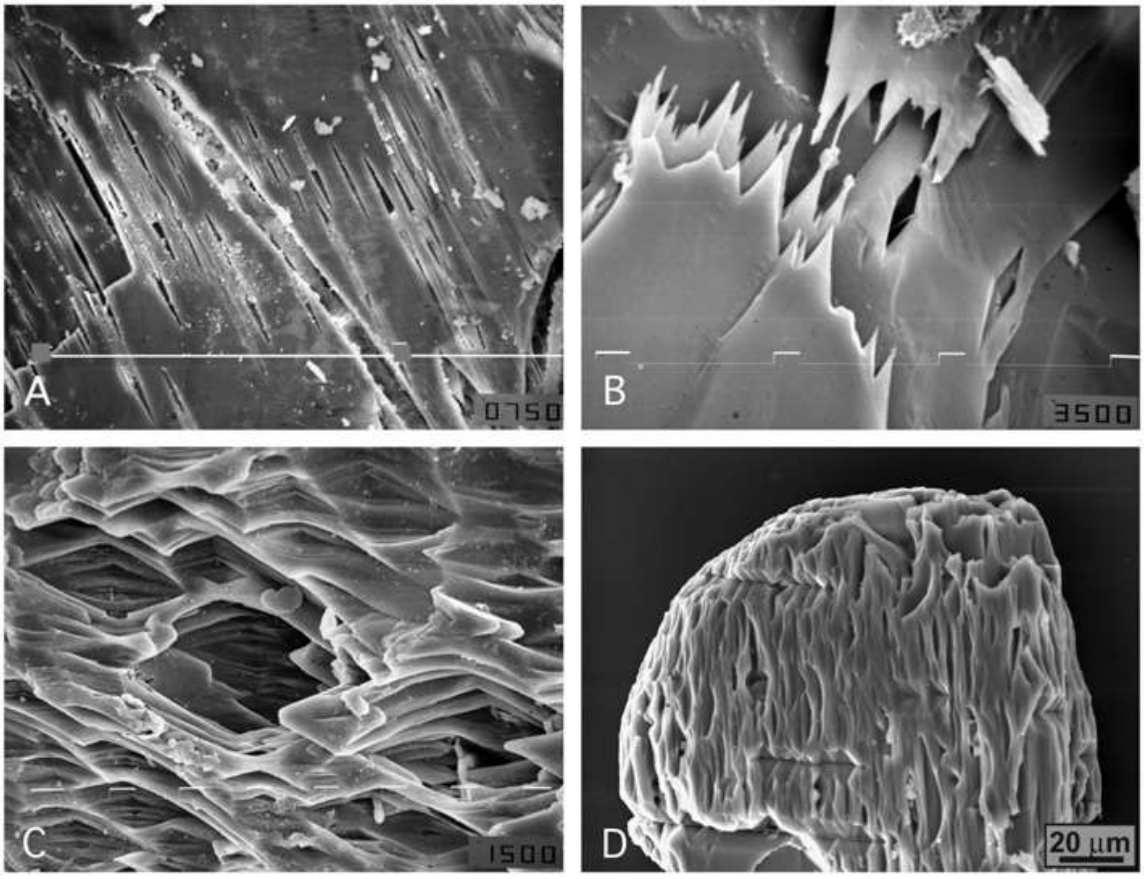

Figure 3.8. *Etch pits on various pyriboles weathered in different environments (Velbel, 2007).*

Corrosion morphologies depend on crystal structure. Individual etch pits and complex textures resulting from the coalescence and overlap of individual into more elaborate forms such as denticulated margins are observed on amphiboles and pyroxenes (Berner et al., 1980; Velbel, 2007).

Different surface textures of heavy minerals are analyzed during routine analysis under the polarizing microscope and turned into reproducible data in modern sediments produced of equatorial Africa, where weathering is extreme (Andò et al. 2012, Chapter 5.3.).

3.4. Hydraulic-sorting and grain-size

Detrital grains are sorted according to their size, density and shape, first when eroded and set in motion, then during transport by tractive currents, and last when finally deposited.
Sorting during erosion, transport, and deposition can change absolute and relative abundance of heavy mineral species in sediments (Flores and Shideler, 1978; Komar and Wang, 1984; Frihy et al., 1995). Heavy minerals in sediment have different hydrodynamic properties compared to light minerals like quartz and feldspar.
The phenomenon of size–density sorting has been recognized by pioneers of heavy-mineral studies (Udden, 1914; Mackie, 1923; Rittenhouse, 1943), highlighting that denser minerals concentrate in the fine tail of sorted sediments (Komar and Wang, 1984; Schuiling et al., 1985), and less dense or platy minerals in the coarse tail (Komar and Cui, 1984; Figure 3.9.).

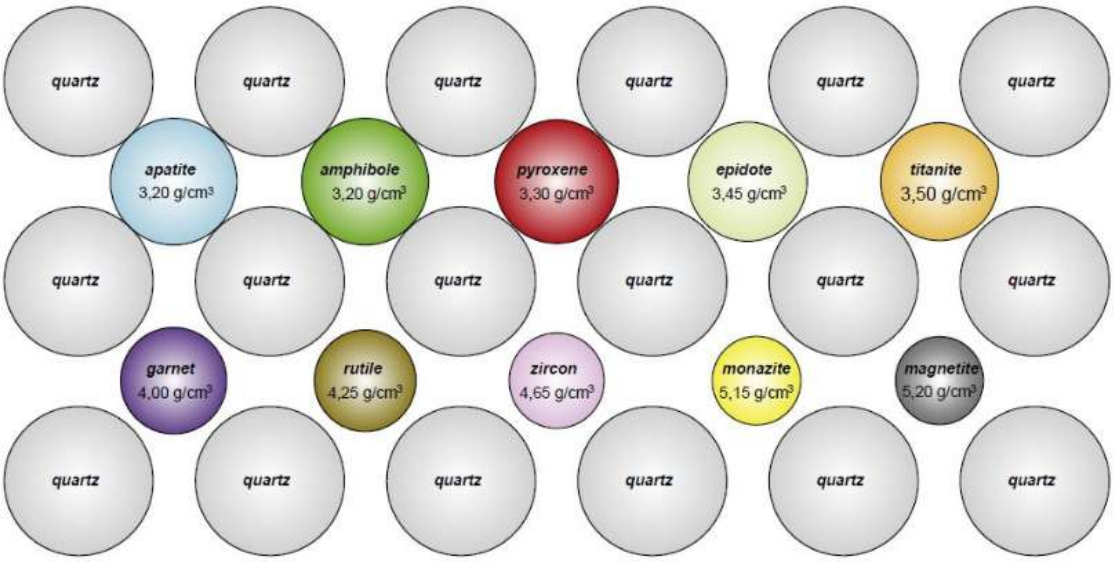

Figure 3.9. *Size relationships between quartz (2.65g/cm^3) and settling equivalent minerals of different densities (Resentini et al. 2013).*

In 1933 Rubey formulated the theory of hydraulic equivalence which states that grains of different size and densities, but of the same settling velocity, will be deposited together in subaqueous or subaerial environment. Sorting of heavy minerals by shape is as important as sorting by specific gravity (Schuiling et al., 1985).

The settling velocity of a detrital mineral in a fluid can be estimated by solving the balance between gravitational force and drag resistance (Figure 3.10.).

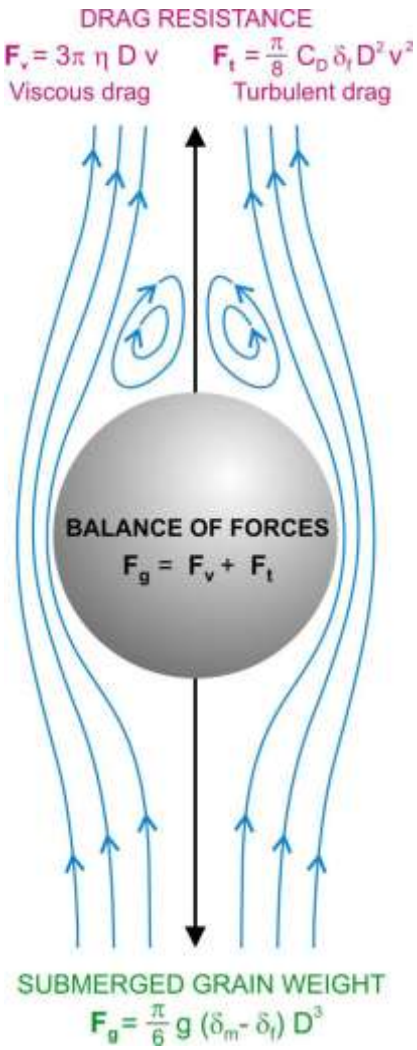

Figure 3.10. *Balanced force system form a settling spherical grain (Garzanti et al., 2008). In the figure F_v= viscous drag; F_t=turbulent drag; F_g=gravitational force; g=gravity; D=diameter of mineral; v=settling velocity; C_D drag coefficient; δ_m=mineral density; δ_f=fluid density; η=fluid viscosity. In freshwater, δ_f=1 g/cm^3 and η=0.01 g/cm s. In seawater, δ_f=1.025 g/cm^3 and η=0.0105 g/cm s. In air, δ_f=0.0012 g/cm^3 and η=0.00018 g/cm s.*

Size–density distributions in sand laid in water, where fluid viscosity plays an important role, can be predicted by empirical formulas, such that of Cheng (1997):

$$v = \left(\left(25 + 1.2\left((g \times \Delta_x \times D_x^3/\eta^2)^{2/3}\right)\right)^{1/2} - 5\right)^{3/2} \times \eta / D_x$$

$$SS_X = \log_2(\Delta_X/\Delta_{ref}) - 3/2 \log_2(\Xi_x/\Xi_{ref})$$

where v is settling velocity, g is gravity, Δ_x is the submerged density (mineral density δ_x—fluid density δ_f), D_x is the diameter of mineral grain x, η is the fluid viscosity.
SSx is the size-shift, i.e. the expected difference in size between a mineral x and the sediment mean size (Garzanti et al., 2008), where

$$\Xi = v/\eta + \left((v/\eta)^2 + 48(g \times \Delta_x/\eta^2)^{2/3}\right)^{1/2}$$

Theoretical size-shifts of different minerals relative to quartz are reported as a function of grain size in figure 3.12. The grain-size distribution in sand laid in air is influenced by fluid turbulence rather than fluid viscosity, and empirical results show that it can be described by the Impact law:

$$v = \left(2/3g \times \Delta_x \times D_x/\delta_f\right)^{1/2}$$
$$SS_x = \log_2\left(\Delta_x/\Delta_{ref}\right)$$

This formula can be applied to gravel.
Instead, for sediments laid in water and finer than 3.5 phi (i.e. very fine sand to silt), the turbulence effect is negligible and settling velocity and size shift can be calculated with the Stokes law:

$$v = g \times \Delta_x \times D_x^2/18\eta$$
$$SS_x = \log_2\left(\Delta_x/\Delta_{ref}\right)/2$$

Note that size shifts calculated with Stokes law are half of those calculated with the Impact law.

The effect of grain shape on settling velocities of heavy mineral grains was investigated by Briggs and coworkers (1962). Although shape plays a fundamental role (Komar and Cui.,1984), empirically its effect is measured only for platy or fibrous minerals (micas and fibrous sillimanite). Denser micas settle at lower velocity with respect of lighter quartz grains of the same size (Figure 3.11.)

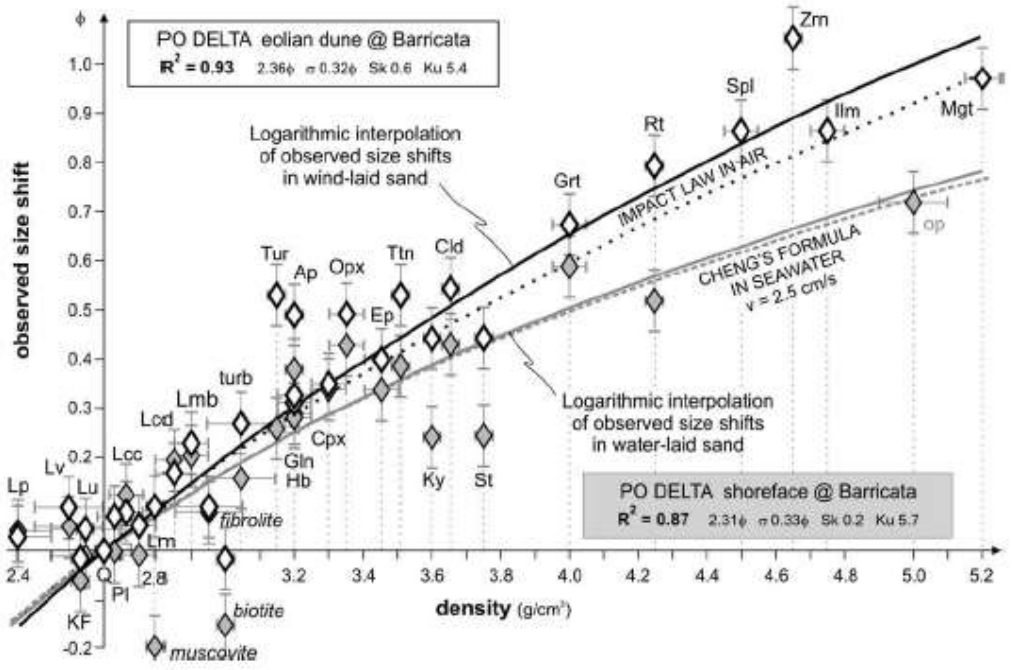

Figure 3.11. *Size–density sorting in water-laid versus wind-laid sands. Marine shoreface (grey-filled symbols) and eolian backshore sands (empty symbols), sampled at ~100 m distance along the same Po Delta beach profile, display nearly identical textures. Size shifts, accurately predicted by Cheng's formula in the former and by Impact formula in the latter, are systematically greater in the dune. Micas settle slower than quartz because of their shape (Garzanti et al., 2008).*

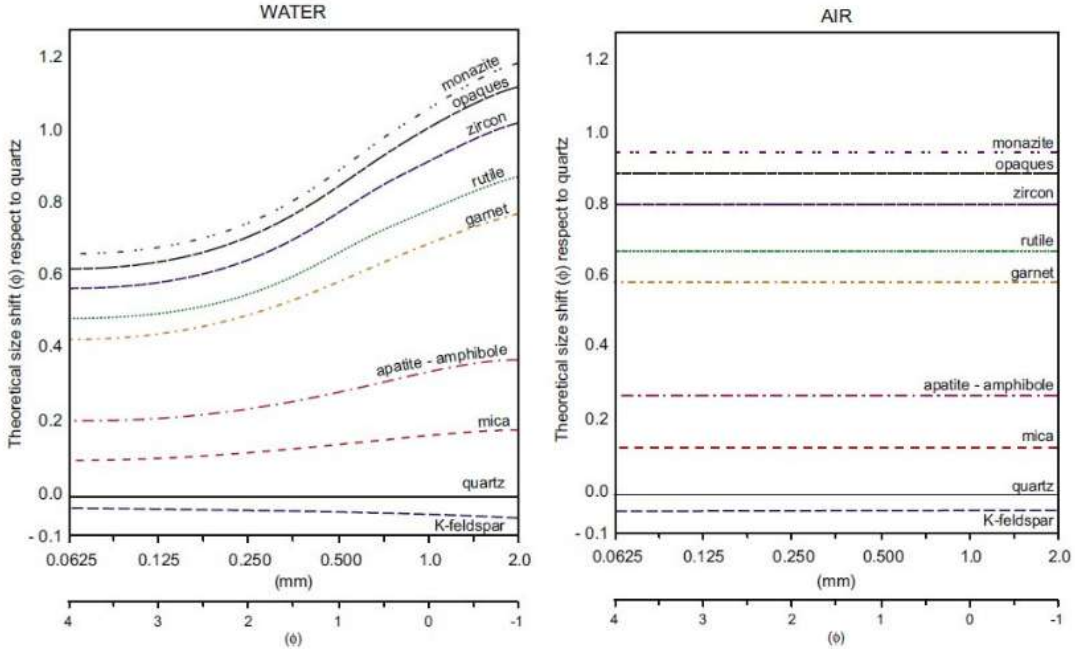

Figure 3.12. *Size-shift for different minerals as a function of grain size (Resentini et al. 2013).*

In all sorted sediments, common minerals like quartz, feldspars and calcite are thus associated with significantly smaller heavy minerals. The latter are enriched in the fine tail of the size distribution, the former make the bulk of the coarse tail.

Polymineral sediments size curves can be thus decomposed into several lognormal curves (one for each components), each of them ideally showing a better sorting then the bulk sediment (Figure 3.13.).

For such reason, theoretical sediments maximum sorting depends on the number of detrital species and their density contrast (Figure 3.14.).

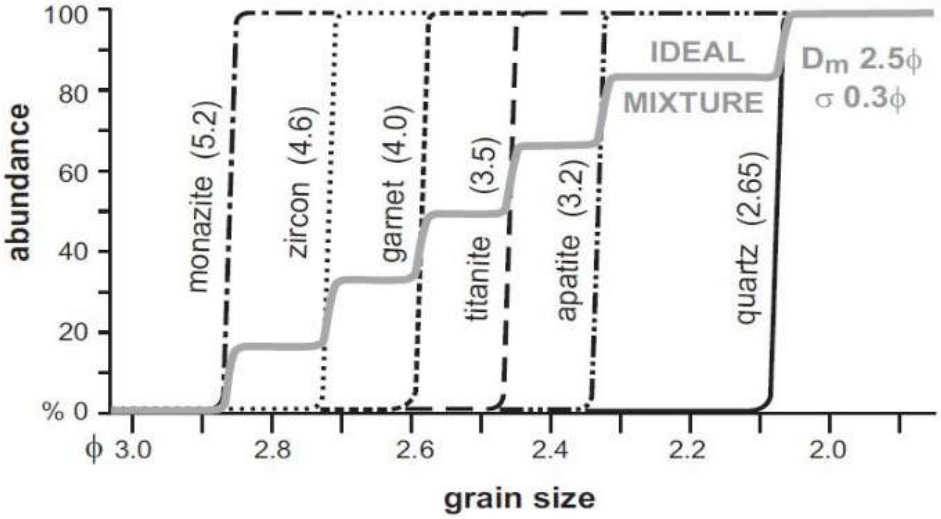

Figure 3.13. *Compound size distribution of polymineral sediments and lognormal distribution of each detrital component (Garzanti et al, 2008).*

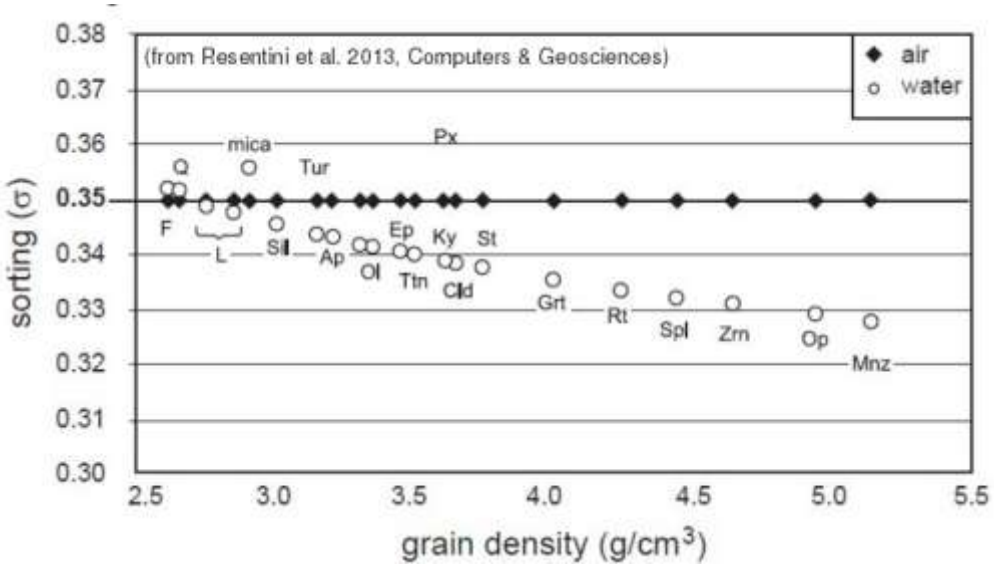

Figure 3.14. *Sorting of detrital minerals as a function of their density (Resentini et al. 2013).*

This knowledge helps us to provide a key to better understand sedimentary processes (Friedman, 1961), from hydraulic sorting during fluvial transport (Brush, 1965; Slingerland, 1984) to turbiditic sedimentation in the deep sea (Norman, 1969; Komar, 1985) for all sorted sediments deposited in subaerial to subaqueous environments. Settling-equivalence analysis of placer sands (Komar and Wang, 1984) allows us to predict the hydraulic behaviour of ultradense ore minerals (cassiterite grains, gold flakes; Tourtelot and Riley, 1973; Reid and Frostick, 1985) and to discriminate among diverse sedimentary processes leading to the formation of economic deposits (Slingerland and Smith, 1986).

A lot of works have been made in the last years on grain size and heavy minerals of modern sands. The effect of strong ocean waves, of the sedimentary processes in the depositional environment and of the seasonal discharge on the heavy mineral concentration was underlined in beach placers of Tonga (Dye and Dickinson, 1996), aeolian and beach sands of Arabia and river sands of the Blue Nile (Garzanti and Andò, 2007a).

3.5. Stability of heavy minerals during burial diagenesis

It has long been known that diagenesis exerts a major control on heavy mineral assemblages (Bramlette, 1941; Pettijohn, 1941; Morton, 1984; Milliken, 1988; Uddin and Lundberg, 1998; Cavazza and Gandolfi, 1992).

Heavy minerals react to burial diagenesis by overlapping corrosion textures on grain surface, dissolution of unstable phases and growth of secondary minerals. Although these secondary minerals have no bearing on provenance, they provide indications of the diagenetic regime. Some minerals are more stable than others. A mineral can be recognized as unstable on the basis of its surface textures and on its distribution in the subsurface (Morton and Hallsworth, 1999). Case studies from sedimentary basins worldwide show a rather uniform pattern of relative stability. The order of stability during burial diagenesis is olivine (least stable) < orthopyroxene, clinopyroxene < sodic pyroxene < calcic amphibole, andalusite, sillimanite < epidote < titanite < kyanite < sodic amphibole < staurolite < allanite < garnet, chloritoid < tourmaline, monazite, spinel < rutile, anatase, brookite, zircon, apatite (most stable, Morton and Hallsworth, 2007). The stability of minerals is not the only factor governing heavy mineral dissolution during deep burial. Porefluid temperature and composition, porefluid circulation, and time also influence heavy-mineral dissolution processes (Morton and Hallsworth, 2007).

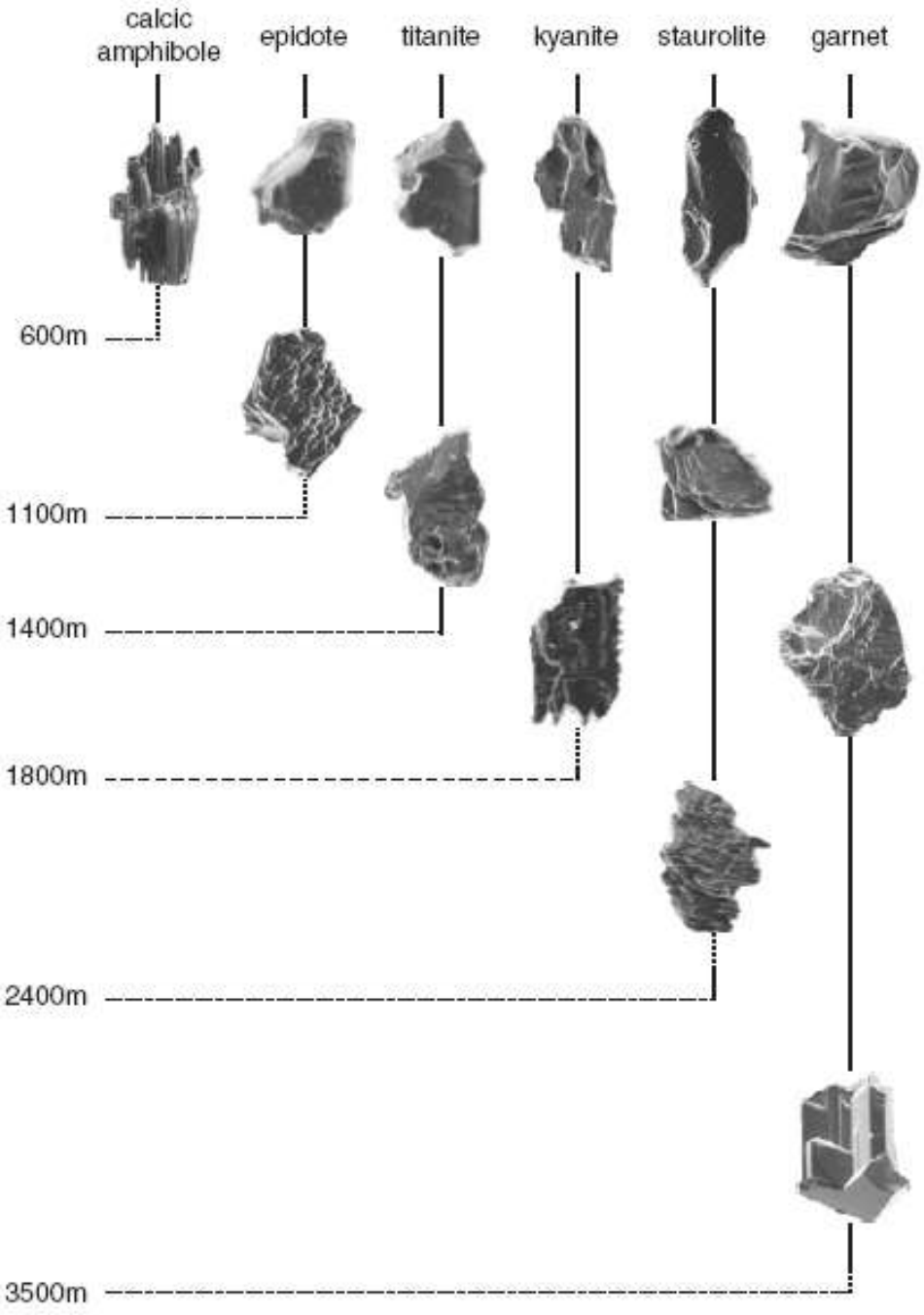

Figure 3.15. *Burial depth distribution of heavy minerals in Palaeocene-Eocene sandstones of the central North Sea, showing the decrease in mineral diversity with increasing burial caused by dissolution of unstable minerals (adapted from Morton, 1984, and Morton and Hallsworth, 1999).*

Intrastratal mineral dissolution in the subsurface can be recognised in three ways: by the presence of corroded surfaces on minerals, by the co-existence of high diversity and low diversity assemblages in adjacent high- and low-permeability sandstones, and by a decrease

in mineral diversity with increasing burial depth within the sedimentary basin (Morton and Hallsworth, 2007). The most direct indication of heavy-mineral dissolution is the presence of corrosion textures on grain surfaces. Differences in mineral composition and crystal structure yield different surface corrosion textures (Nickel, 1973; Berner et al., 1980; Turner and Morton, 2007).

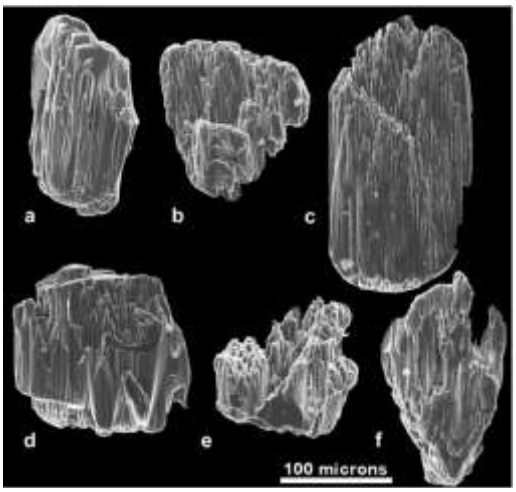

Figure 3.16. *Amphibole etching (Tuner and Morton, 2007).*

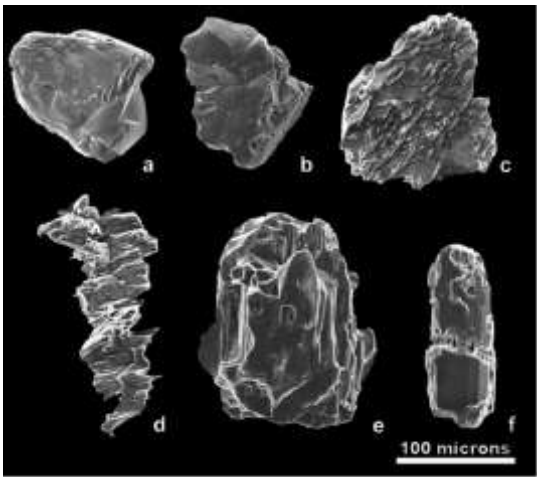

Figure 3.17. *Unetched (a), minor etch pitting (b) and etched (c) and high etched (d-e-f) epidote (Tuner and Morton, 2007).*

The effects of burial diagenesis and intrastatal dissolution can be quantified in basin where the source area has remained the same for long periods (i.e. the Alpine foreland or the Indus fan; Garzanti and Andò, 2007a).

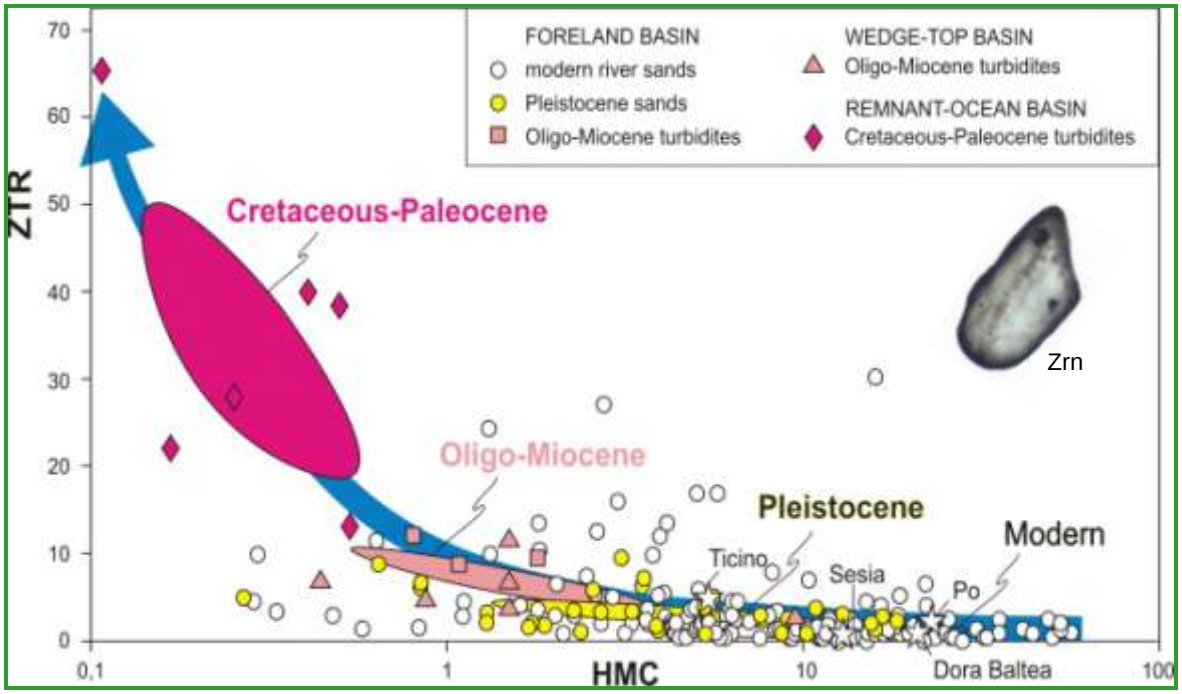

Figure 3.18. *Sharp discrepancy between heavy mineral suites in modern and ancient sediments derived from the Alps (Fig. 5. Garzanti and Andò, 2007).*

In the Po plain modern to Pleistocene fluvial sands chiefly derived from the Alps, have rich amphiboles-epidote-garnet heavy mineral suite. Oligo-Miocene turbidites, also mostly derived from the Alps and deposited in Alpine and Apenninic foredeeps (Valloni et al., 1991; Di Giulio, 1999; Carrapa and Di Giulio, 2001) have, by contrast, low garnet-dominated assemblages (Gazzi, 1965; Gandolfi et al., 1983). Late Cretaceous remnant-ocean turbidites yield low amounts of ultrastable species and garnet-dominated heavy mineral assemblages.
We can see that concentration (HMC index) steadily decreases, while chemical stability (ZTR index) progressively increases, from modern, to Pleistocene, to Oligo-Miocene, to Cretaceous-Palaeocene clastic wedges, testifying to progressive diagenetic dissolution.
In the Himalayan foreland the Indus and Brahmaputra Rivers carry heavy mineral-rich (HMC 7±8) hornblende-dominated sediment, containing epidote, garnet, and pyroxenes (Garzanti et al., 2004b, 2005). The Ganga, and other rivers, carry assemblages with lower heavy mineral concentration that include amphiboles, garnet, epidote, kyanite, sillimanite, and pyroxenes. Instead, Tertiary foreland basin sandstones from different stratigraphic units from Pakistan to Nepal contain mostly poor to very poor assemblages (HMC 0.8±0.8). dominated by ultrastables and garnet. These two comparisons demonstrate the overwhelming effect of diagenetic dissolution in ancient sandstones.

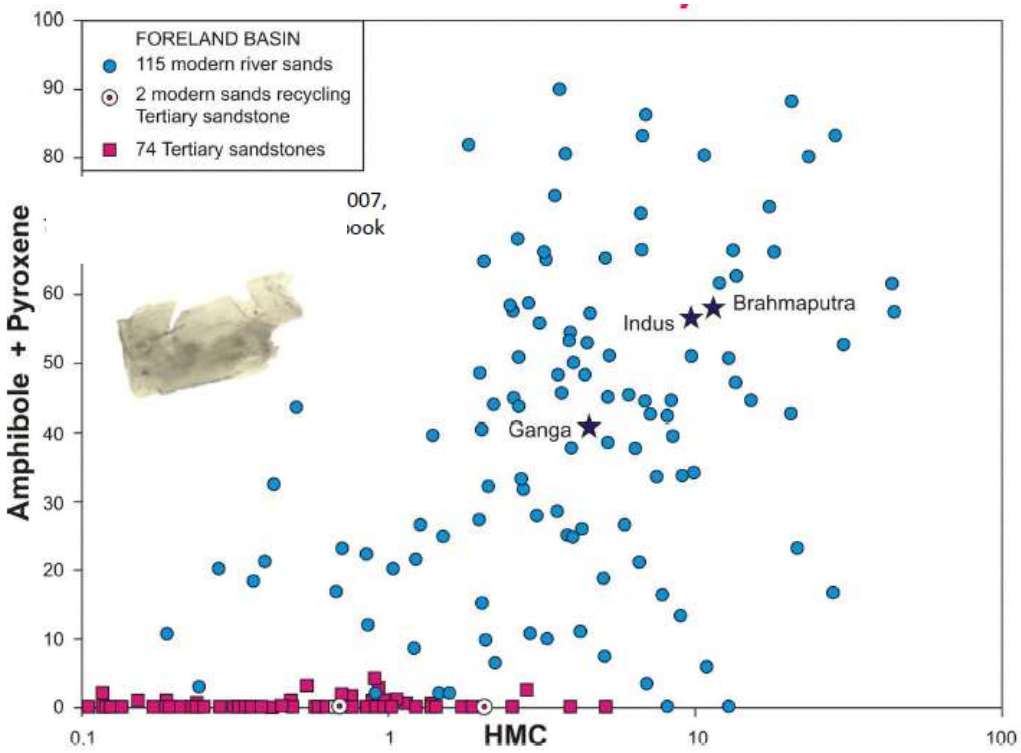

Figure 3.19. *Sharp discrepancy between heavy mineral suites in modern and ancient sediments derived from the Himalayas (Fig. 6. Garzanti and Andò, 2007).*

Corrosion features developed on surface of different heavy minerals and concentration of heavy minerals had been analyzed on a siliciclastic succession cored from the Bengal Basin in Bangladesh during my PhD. These data are relevant in the study of the chemical properties of minerals and of the diagenetic evolution of sedimentary successions, helping us to detect development of secondary porosity and occurrence of subsurface reservoirs for water and hydrocarbons (Andò et al., 2012; Chapter 5.4.).

4.Methods

4.1. Sampling for heavy mineral analyses

The accuracy of sampling largely influences the value analyses. For this reason sampling should be carefully planned and performed. Samples should be taken at regular intervals as well as after changes of stratigraphy, lithology, facies, texture, flow regime, bed configurations, etc. Usually the mass of each dry sample for heavy mineral analysis may vary between 1 g and 50 g.

As describe in previous paragraphs, heavy mineral composition may depend on grain size; usually the fine-to-medium grained sands or sandstones yield the most representative heavy mineral assemblages; siltstones and silty mudstones can often provide good results. They represent the largest amount of sediment on Earth and allow us to analyze depositional environment where they are present, as deltas and turbiditic currents to understand the evolution of collisional belts.

Specific hydraulic conditions can concentrate grains of normally high density and form heavy mineral rich layers. Deposits that show this heavy mineral enrichment, mostly black mixture of iron titanioum-oxide (magnetite, ilmenite and hematite) or zircon, or monazite, or garnet, or gold are defined placers (Komar and Wang, 1984; Reid and Frostick, 1985; Dickinson, 1994; Mallik at al., 1987;.Bryan et al., 2007; Ghosh et al., 2012). They are not representative of the overall heavy mineral content of the formation and therefore, sampling these accumulations alone should be avoided. Their study, instead, is interesting due to economic interest of these minerals.

4.2 Preparation of the samples

The required quantity of sediment for heavy mineral analysis depends on sample availability, its grain-size and geological setting. The characteristic of the source rocks, weathering and diagenesis, in fact, can modifiy heavy mineral concentration and assemblages (Chapter 3.).
Heavy minerals concentration and assemblages of modern sediments and sandstones and siltstones can usually be analyzed requiring small amount of material. Usually, about 20 g for poorly sorted sands and 10 g for well sorted sands can be used. The same quantity for each sample of sandstone (usually 30-50 g) or siltstone (usually 2-5 g) can be used after disaggregation of the rocks by crushing in a steel or agate mortar. If the whole sample is too large to be analyzed, splitting becomes necessary and this has to be performed precisely. Splitter (Krumbein and Pettijohn, 1938; Hutton, 1950) and Parfenoff's technique (Parfenoff, 1970) are efficient means of producing representative smaller portions for grain mounts.
Acid digestion to eliminate carbonate, remove organic substances, freeing the grains from clays and iron oxides-coating (Leith, 1950), authigenic minerals (Milner, 1962) sometimes can be usefull.
After chemical attacks, sieving is normally used to extract required size classes and to quantify the others fractions that have not been analyzed. Sieving can be performed with dry or wet techniques. The first method is used for fine-to-medium grained beach, dune and bar sands and the sieves are put on a mechanical shaker for about ten minutes (Figure 4.1.). The wet method is used for poorly sorted bank sands or loess with a significant amount of silt or clay and for sandstones and siltstones. This method allows us to avoid problems during the separation of heavy minerals.

Figure 4.1. *A mechanical shaker.*

4.3. Heavy mineral separation

Concentration of heavy minerals is mainly performed using high-density liquid. After immersion of a sample in a liquid of a given density minerals denser than the liquid will sink while minerals less dense will float. They are commonly called heavy and light fraction respectively. This separation is governed by the Stockes' law:

$$V_p = \frac{2gr_p^2(D_p - D_l)}{9\eta_l}$$

where V_p is mineral's settling velocity, g is gravity, r is the radius of mineral, D_p is the density of the mineral, D_l is the density of the fluid and η is the fluid viscosity.

High density liquid normally used for separation are bromofrom ($CHBr_3$, δ=2.89 g/cm^3 at 20°C) and the methylene iodide (CH_2I_2, δ=3.32 g/cm^3 at 20°C).

All of these liquids are highly toxic, so recently the non-toxic sodium polytungstate (SPT, $3Na_2WO_4*9WO_3*H_2O$, δ_{used}=2.90 g/cm^3) has been proposed (Callahan,1987). It is water-soluble and the heavy mineral separates can be cleaned with distilled water.

Two basic techniques are employed for heavy minerals separation: centrifuge separation and gravity settling (funnel separation).

4.3.1. Centrifuge separation

Dry samples are put into the test tubes, heavy liquid is added and the mixture is shaken. The sample volume should be in proportion to the capacity of the test tube. The best result are achieved when the ratio of sample to heavy liquid is 1:5. All the tubes must have the same weight to keep the centrifuge in equilibrium. Separation time depends on grain size of sediments. Five minutes allow the centrifuge separation for fine-to-medium sands, but it can be shorter for coarser sediments. Centrifuge speed is usually between 2000 and 3000 rpm (Figure 4.2.).

Figure 4.2. *Centrifuge separation*

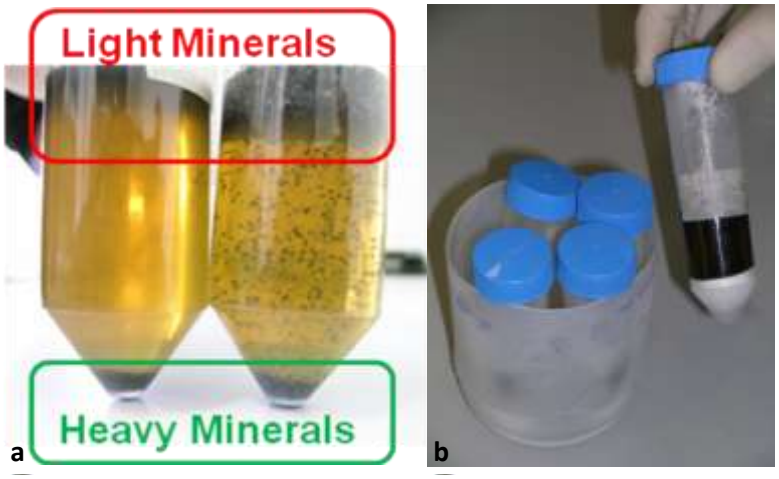

Figure 4.3. *(**a**) Two samples after the centrifuge separation. (**b**) Partial freezing with liquid nitrogen.*

While the centrifuge is in operation, two set of funnel and filter paper are arranged for each sample. When centrifuge has stopped, the test tubes are put into a beaker with liquid nitrogen (Figure 4.3.). The lower part of the test tube, which contains the heavy fraction will freeze in a few minutes. The non-frozen liquid, which contains light fraction is recovered in the "light" filter paper. When the heavy fraction will be unfrozen, it can be recovered in the "heavy" filter paper (Figure 4.4.). Each fraction can be cleaned with distilled water and dried in a oven. The diluited liquid, can be re-used after water evaporation.

Figure 4.4. *Equipment for recovering heavy and light fractions.*

4.3.2. Funnel separation

The Figure 4.5. shows the arrangement of equipment used for separation by gravity settling. The heavy liquid is filled in the separating funnel, the dry and weighted sample is then added to the liquid. Heavy minerals will accumulate at the bottom of the funnel above the lower pinch clip. When the denser grains are sunk, the upper clip is closed and the lower is opened slowly, allowing the heavy fraction to pour onto a filter paper in the lower funnel. A new funnel, with filter paper is placed under the separating funnel and the light fraction can be drained into the new funnel. Light and heavy fractions are washed with acetone. The used heavy liquid and washing are collected in a bottle. The heavy liquid can be re-used.
This method is used for separation with methylene iodide. All must be done inside a fume cupboard to limit the exposure to hazardous and/or unpleasant fumes.

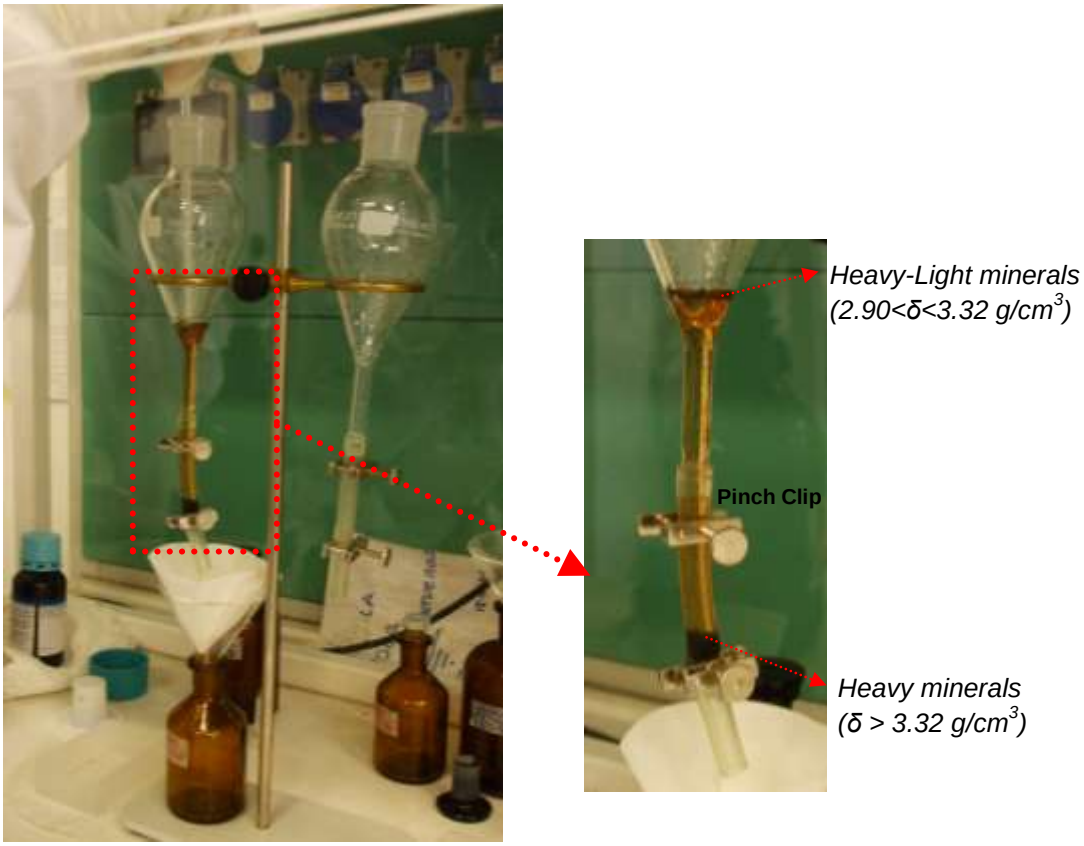

Figure 4.5. *Gravity separation with methylene iodide.*

4.4. Preparation for optical analyses

If the heavy fraction is too abundant to be mounted on a single microscope slide, splitting becomes necessary. Microsplitter are efficient means of producing statistically consistent small portions for grain mounts.
Collodin (Spencer, 1960), gelatin (Nayudu, 1962), gum Arabic (Gazzi et al., 1973), are used for temporary mount, while Canad balsam (n= 1.538), Meltmount (n=1), Araldite (n=1.54) are the most common resins for permanent mounts. The mounting of heavy minerals can be made on a hot plate, heated at ~115°C. Other synthetic resin with low refractive index, Eukitt (n=1.54), Lakeside (n=1.54), Permount (n=1.567), and Entellan (n=1.490-1.500) can be used. Grains are placed on the microscope slide with Canada balsam and covered with a cover glass; cold water allows the crystallization and spearing grains on the slide. Overlapping of grains should be avoided for a good optical analysis under the microscope.

4.5. Microscopic identification

William Nicol invented the nicol prism in 1828. This allowed Talbot and Sorby to build the first microscope in the mid-nineteenth century. Since this moment the microscope became and is still now the principal instrument for the recognition of minerals.
Many publications deal with the identification of minerals by their optical properties (Troger, 1959; Parfenoff et al., 1970; Mange and Maurer, 1992; Mange and Wright 2007).
In this paragraph the optical properties used for the recognition of heavy minerals are described. Each mineralogical species can be confidently recognized by diagnostic combination of optical properties. Form, color, pleochroism, relief, cleavage and inclusions are observed with one nicol; birefringence, interference figures, extinction and elongation with two nicols. In convergent light interference patterns and optical sign are analyzed and detected (Table 4.1.).

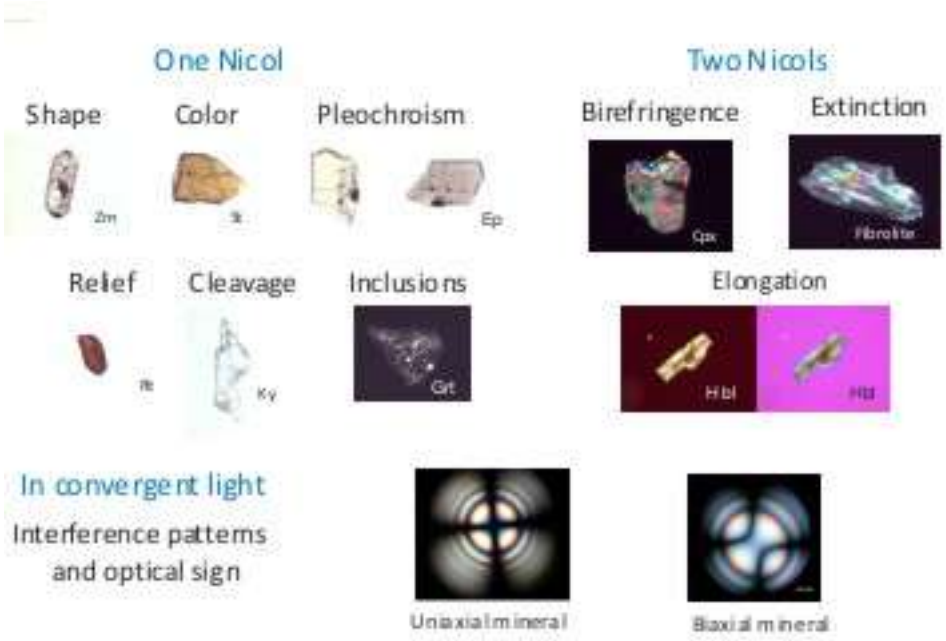

Table 4.1. *Optical properties analyzed under the microscope.*

4.5.1. Grain counting

To determine the relative abundance of heavy minerals in a sample, four different point counting methods are used (van Harten, 1965; Galehouse 1969, 1971).

Fleet method (Fleet, 1926): requires all grains in the mount to be counted. It is time consuming and the precision of the analysis does not significatively improve once 200-300 grains have been analyzed (Dryden, 1931; van Andel, 1950).

Line counting: the slide is moved along a line and all the grains intersected by the crosshair are identified and counted. As larger grains have larger chances to be hit by the crosshair, this method can lead to frequency distortion in favor of larger grains.

Area (or ribbon) method (Galehouse, 1969): all grains contained in randomly selected areas (ribbons) of the slide are analyzed and counted. Such approach ensures independence of results from minerals grain size (provided that analyzed ribbons width are larger than the maximum size of crystals) and mineral number frequencies can be converted

into number percentages. This method appears to be the most widely accepted in heavy mineral analysis.

Point counting: a slide of heavy minerals is prepared using a larger amount of grains to facilitate and speed up analyses. The mount is progressively moved, with the aid of a stage, by a fixed distance and grains hit by the microscope crosshair are identified and counted. This method is appropriate when sediments are poorly sorted and big grains (e.g. tourmaline) are mixed with very small grains (e.g. zircon) in the same suite.

4.5.2. Parameters

A few parameters by which heavy mineral concentration in sediments and sedimentary rocks can be expressed quantitatively and related with average density of source rocks are defined in this section. They are also helpful because some anomalies of concentration parameters can be caused by either hydraulic sorting or diagenetic dissolution.

The HMC Index (Garzanti and Andò, 2007a)
The ‘‘Heavy Mineral Concentration index’’ (HMC) defines the abundance of heavy minerals (transparent, opaque, and unidentifiable turbid grains denser than 2.90 g/ cm^3) contained in the analyzed fraction of terrigenous extrabasinal loose sediment or lithified sedimentary rock. It is defined as:

$$HMC = \frac{\left(\frac{W_D}{W_T}\right)\left(\frac{D_T}{D_D}\right)\left(1-\frac{s}{h}\right)}{1-\frac{d}{t}} * 100$$

where W_D/W_T indicates the ratio between the weight of the mineral fraction denser than 2.90 g/cm^3 and the weight of the sediment fraction considered, D_T/D_D the ratio between the weighted average densities of total framework grains and total dense grains, s/h the relative abundance of spurious grains in the dense fraction (carbonates, phyllosilicates, dense

inclusion-filled light minerals…), and d/t the relative abundance of allochemical and orthochemical components.

The tHMC Index (Garzanti and Andò, 2007a)

Since most heavy mineral studies focus only on transparent grains (which can be identified under a polarizing microscope), HMC can be converted into tHMC (transparent Heavy Mineral Concentration Index) according to the following formula:

$$tHMC = HMC\ (1 - \%opaque - \%turbid)$$

where % opaque and % turbid are the percentages of opaque and turbid heavy minerals over total heavy minerals, respectively.

The tHMC index is needed to integrate complementary provenance information from bulk petrography and heavy mineral analyses (Garzanti et al., 2004b, 2005, 2006a, 2006b). HMC and tHMC values are generally close in detritus from high-grade metamorphic rocks, whereas in detritus from very low-grade and retrogressed metamorphic rocks, contributing abundant turbid and opaque grains, tHMC may be half than HMC or less.

The SRD Index

Another parameter that can help in determining source rocks crustal level and in highlighting hydraulic effects on sediments composition, is the Source Rock Density (SRD) index (Garzanti and Andò, 2007a), calculated as:

$$SRD = \frac{\left[D_{tHMC}\left((1-\%opaque) + 5.00 * \%\ opaque\right) HMC + 2.65\ (100 - HMC)\right]}{100}$$

where D_{tHM} is the weighted average density of transparent dense mineral, 5 is the average density (g/cm^3) for opaque grains (intermediate between that of magnetite and ilmenite), HMC is the heavy mineral concentration index and 2.65 is the average density (g/cm^3) of "light" grains.

In order to reveal the effects of hydraulic sorting and diagenetic dissolution we consider also (Garzanti and Ando', 2007a),

% opaque = the percentage of opaque grains (δ: 4.50 to 5.30: ilmenite, magnetite, hematite) over total heavy minerals;
% ultradense= the percentage of ultradense transparent grains (δ ≥3.80) over total identified transparent heavy minerals;
% ZR= the percentage of ultradense ultrastable grains (zircon and rutile) over total ultrastable grains (zircon, tourmaline, and rutile; Hubert, 1962).

The **hornblende colour index HCI** (Garzanti et al., 2004a) and the metasedimentary minerals index (MMI) are other two parameters helpful in the study of orogenic sediments to estimate the average metamorphic grade of source rocks.

The first is defined as:

$$HCI = \frac{(1/3\ green\ horneblende\ +\ 2/3\ greenbrown\ +\ brown\ horneblende\ )}{horneblende * 100}$$

For medium- to high–grade metaigneous source rocks, hornblende color represents a useful indicator of average source rock grade. Analysis of modern river sediments drained from the Central European Alps (Garzanti et al., 2004a) showed that blue-green hornblende are dominant in heavy mineral suites from staurolite-grade rocks below 600°C, and are progressively replaced by green, green-brown, and brown grains as metamorphic grade of source rocks increases towards sillimanite-grade parageneses.

The **Metamorphic Mineral Index** is defined as

$$MMI = \frac{(1/3\ staurolite\ +\ 2/3\ kyanite + sillimanite)}{(chloritoid + staurolite + kyanite + sillimanite)} * 100$$

MMI and HCI indices vary from 0 in greenschistfacies to lowermost amphibolite-facies rocks (yielding chloritoid and blue-green amphibole), to 100 in granulite-facies rocks (yielding sillimanite and brown hornblende).

4.6. Raman Spectroscopy

Raman spectroscopy represents a new user-friendly technique to obtain detailed comprehensive information on heavy-mineral assemblages. It is much more time-effective, cheap and easy to use than the classical microprobe techniques. It allows, on one side, to routinely determine mineral chemistry on a great number of grains previously identified by polarizing microscope and, on the other side, to identify mineral grains that are difficult to be recognized only on the basis of optical properties. We can distinguish among Ti-Oxide polymorphs and minerals containing OH^- groups and identify altered and opaque minerals. Moreover, this analytical technique can be applied directly on thin sections and grain mounts without any particular preparation (e.g., polishing, carbon coating; Andò et al., 2009).

The identification of the granules is based on the position of the diagnostic peaks and the comparison with spectra of reference (RRUFF, www.rruff.info; University of Parma, www.fis.unipr.it/phevix/ramandb.php; University of Siena, www.dst.unisi.it/geofluids/raman/spectrum_frame.htm; Università of Lyon (www.ens-lyon.fr/LST/Raman/index.php); Database of Romania (www.rdrs.uaic.ro).

Some spectra of different heavy minerals taken during my PhD are reported in the tables below (Table 4.2., 4.3., 4.4, 4.5.).

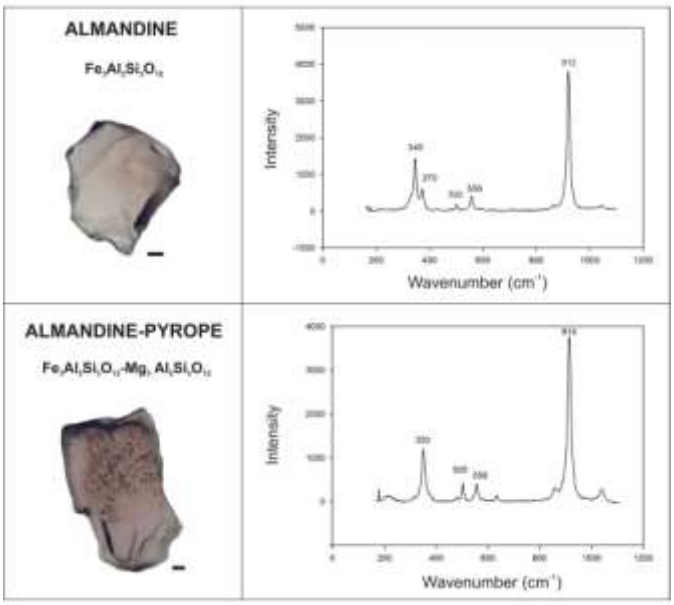

Table 4.2. *Raman discrimination of garnet-group minerals.*

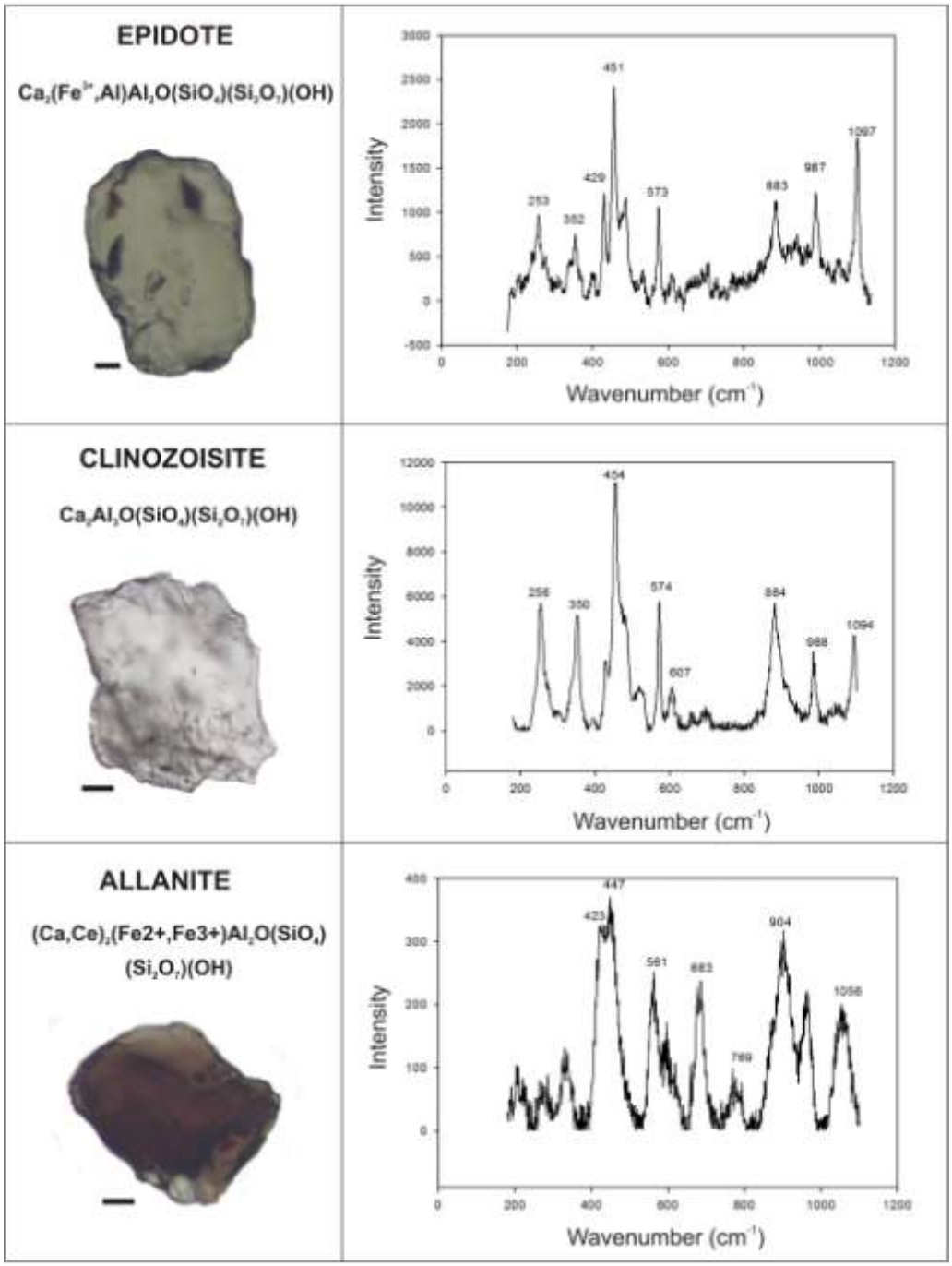

Table 4.3. *Raman discrimination of epidote-group minerals.*

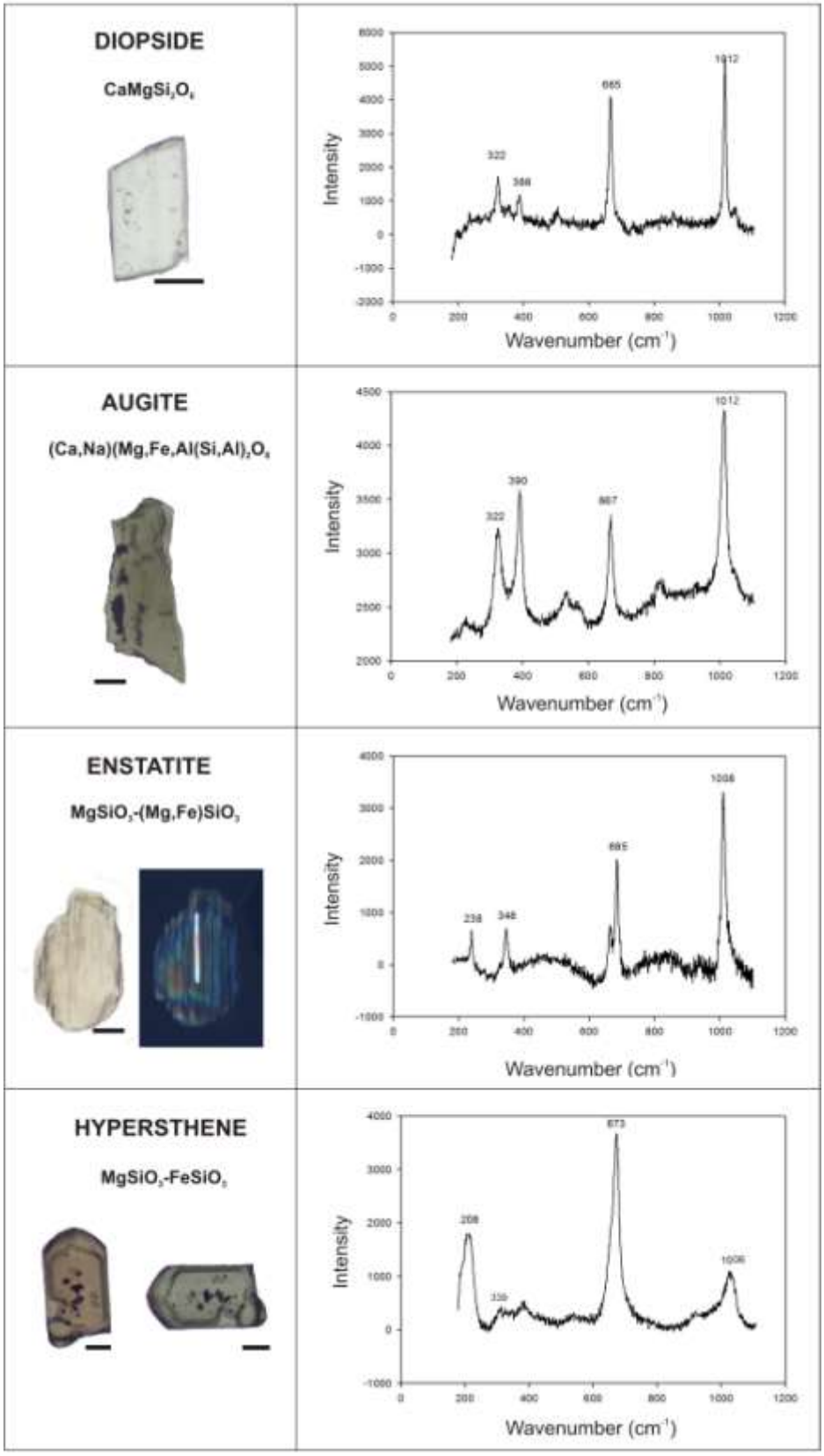

Table 4.4. *Raman discrimination of clinopyroxenes and orthopyroxenes.*

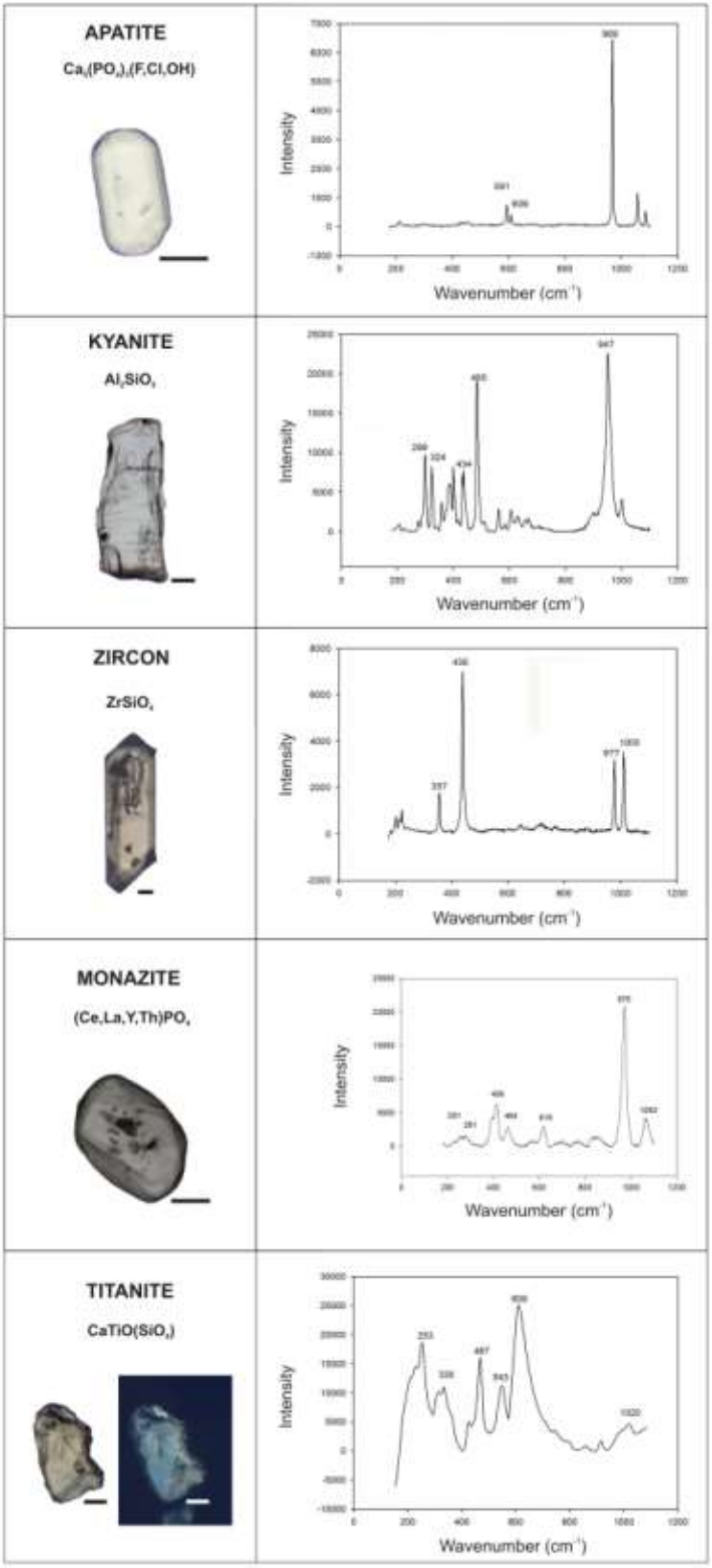

Table 4.5. *Raman discrimination of other different heavy minerals.*

4.7. Other auxiliary techniques

Although the petrographic microscope remains the fundamental tool in heavy mineral identification, in recent years additional advanced techniques (such as X-ray diffraction, electron microprobe, scanning electron microscopy, cathodoluminescence and Raman spectroscopy) have also been employed, assisting optical identification. Use of these techniques provides information on chemical composition, structural and textural characteristics, and increases the accuracy of heavy mineral analyses. However for same of these techniques sample preparation may be laborious (hand-picking).

X-ray diffraction (XRD) identifies mineral by providing data on crystal structure; it is useful for indentifying opaque grains (Harrison, 1973) and for obtaining a general knowledge on bulk heavy mineral composition (Pryor and Hester, 1969).

X-ray fluorescence spectrometry (XRF) relies upon bombardment and excitation of elements by means of a primary X-ray beam; this result in the emission of X-rays with characteristic wavelengths for each element. The radiation is detected by an X-ray spectrometer and then is used to identify and estimate the concentration of elements in samples (Norrish and Chappell, 1977).

Electron-probe microanalysis helps us to recognize ambiguous grains distinguishing between individual members of a mineral group or series by providing the data on crystal chemistry (Morton, 1984).

The scanning electron microscope (SEM) is equipped with an energy-dispersive X-ray spectrometer which analyzes the general morphological characteristics and the surface textures of heavy minerals.

Cathodoluminescence (CL) is the property of certain minerals to emit energy in the form of light when bombarded by electrons; it is useful for studying only a few heavy minerals as apatite (Smith and Stenstrom, 1965; Mariano and Ring, 1975).

Quantitative Evaluation of Minerals by SCANning Electron Microscopy (QEMSCAN) is a fully automated, non-destructive, micro-analysis system that provides rapid, statistically reliable and repeatable, mineralogical and petrographic data. This technology is used for obtaining high-resolution mineral/chemical information on solids combining the benefits of high-

resolution electron microscopy with the exponentially growing power of data interpretation in one linked system. Four high-speed, nitrogen-free energy dispersive detectors gather and merge element x-ray data to identify minerals. The mineral digital images permit users to quantify any desired aspect of the sample abundances and mineral associations, grain size distribution, grain morphology with unprecedented precision, accuracy and speed. QEMSCAN technology has seen applications in mining, metallurgy and mineral exploration, oil and gas exploration (Hoal et al., 2007; Ayling et al., 2012), coal, environmental geology (Kennedy ey al., 2002; Speir et al., 2008), and forensic geosciences (Pirrie et al., 2004).

5. Corrosion of heavy minerals during weathering and diagenesis: A catalog for optical analysis

published in the Sedimentary Geology, v. 280, p. 165-178. "Corrosion of heavy minerals during weathering and diagenesis: A catalog for optical analysis" by Sergio Andò, Eduardo Garzanti, Marta Padoan, Mara Limonta.

5.1. Introduction

Heavy-mineral assemblages in terrigenous sediments include a variety of species, most of which originally formed at temperature and pressure conditions markedly different from those of the Earth's surface. In the sedimentary environment, detrital minerals are consequently exposed to weathering, which is most extensive in warm humid climates where chemical reactions proceed at a faster rate (White and Blum, 1995; Brantley, 2003). In soil profiles developed at low latitudes (Oliva et al., 1999; Thomas et al., 1999; Horbe et al., 2004), severe dissolution affects not only unstable minerals such as olivine or garnet, but also quartz, tourmaline, and even zircon (Carroll, 1953; Crook, 1968; Cleary and Conolly, 1972; Colin et al., 1993; Van Loon and Mange, 2007; Van Loon, 2009), traditionally considered as stable or even "ultrastable" (e.g., Pettijohn et al., 1972 p. 305). In modern sediments produced in subequatorial settings, surface textures of detrital minerals range from incipient corrosion to deep etching, reflecting progressively increasing degree of alteration. After deposition, corrosion continues during diagenesis, which may include multiple stages with total duration of tens to hundreds of millions of years (Turner and Morton, 2007). Least stable minerals dissolve faster and ultimately disappear at relatively shallow burial depths; more stable minerals dissolve at slower rates and disappear last. The original detrital association is thus progressively depleted in both variety and concentration. Corrosion morphologies depend on crystal structure. Etch patterns are evident and similar in prismatic amphibole and pyroxene (Berner et al., 1980; Velbel, 2007), but not in garnet, epidote, or staurolite.

Investigating dissolution of diverse minerals helps us to read climate in the stratigraphical record, and to check whether and to what extent the original detrital assemblage has been modified by diagenesis. Such insight allows us to avoid gross mistakes in provenance diagnosis, and at the same time to infer temperature and geochemical conditions during burial.

The aim of the present study is to describe and classify the variety of surface textures displayed by the diverse heavy minerals found in modern river sediments of equatorial Africa, where weathering is extreme (Figure 5.1.). Presented with a series of color plates for visual comparison, such simple but complete classification helps us to objectively and systematically record all kind of potentially meaningful surface-textural attribute during routine analysis under the polarizing microscope. In the last part of the article we will finally show how the same classification can be used also in the study of ancient diagenized sediments, as illustrated in a case study on a siliciclastic succession cored for hydrocarbon exploration in the Bengal Basin.

In spite of different geochemical conditions and therefore different relative stability of diverse minerals (Morton and Hallsworth, 2007), there are great similarities between textures produced by dissolution during weathering and during burial diagenesis (Velbel, 2007). Our practical catalog can thus be used profitably also in the study of heavy-mineral assemblages found in diagenized ancient sandstones. The classification of grain morphologies proposed here helps us in fact to accurately and reproducibly describe corrosion features formed in any environment, including those produced artificially in the laboratory. The analysis can be carried out on any grain-size range, and potential grain-size dependence of corrosion features thus investigated. Data must be interpreted by taking into full account the heavy-mineral concentration in the sample (Garzanti and Andò, 2007a), which reveals potential depletion caused by chemical dissolution either prior to or after deposition. Detailed assessment of dissolution features is relevant in the study of the chemical properties of minerals and of the diagenetic evolution of sedimentary successions, helping us to detect development of secondary porosity and occurrence of subsurface reservoirs for water and hydrocarbons.

5.2. The morphology of mineral weathering

Corrosion features have been reported since the dawn of sedimentary petrology by Salmojraghi (1892) and Artini (1927), who documented deeply etched hornblende in fluvial sediments of the Po Plain. Etch pits, surface mamillae, facets, ragged edges, and hacksaw terminations were subsequently described in detail by Edelman and Doeglas (1932, 1934).
Extensively studied both in soils and in simulated laboratory experiments (Brantley et al., 1986; Velbel, 1993a), dissolution processes develop through progressive etching or replacement. In nature, as in laboratory experiments, orthosilicate weathering proves to be fundamentally controlled by the length and strength of bonds between major non-tetrahedral cations and structural oxygen (Velbel, 1999). Reaction rates may be markedly influenced by diverse factors, such as the development of a protective surface layer hampering dissolution of almandine garnet (Velbel, 1993b). Incipient dissolution is revealed by corroded rims and small etch pits on the surface of affected minerals. If the process continues, ragged edges, deep parallel grooves, and finally skeletal outlines are produced (Grimm, 1973; Mange and Maurer, 1992). Further detailed observations are obtained under the scanning electron microscope, where surface textures can be investigated at greater magnification (Rahmani, 1973; Moral Cardona et al., 2005).

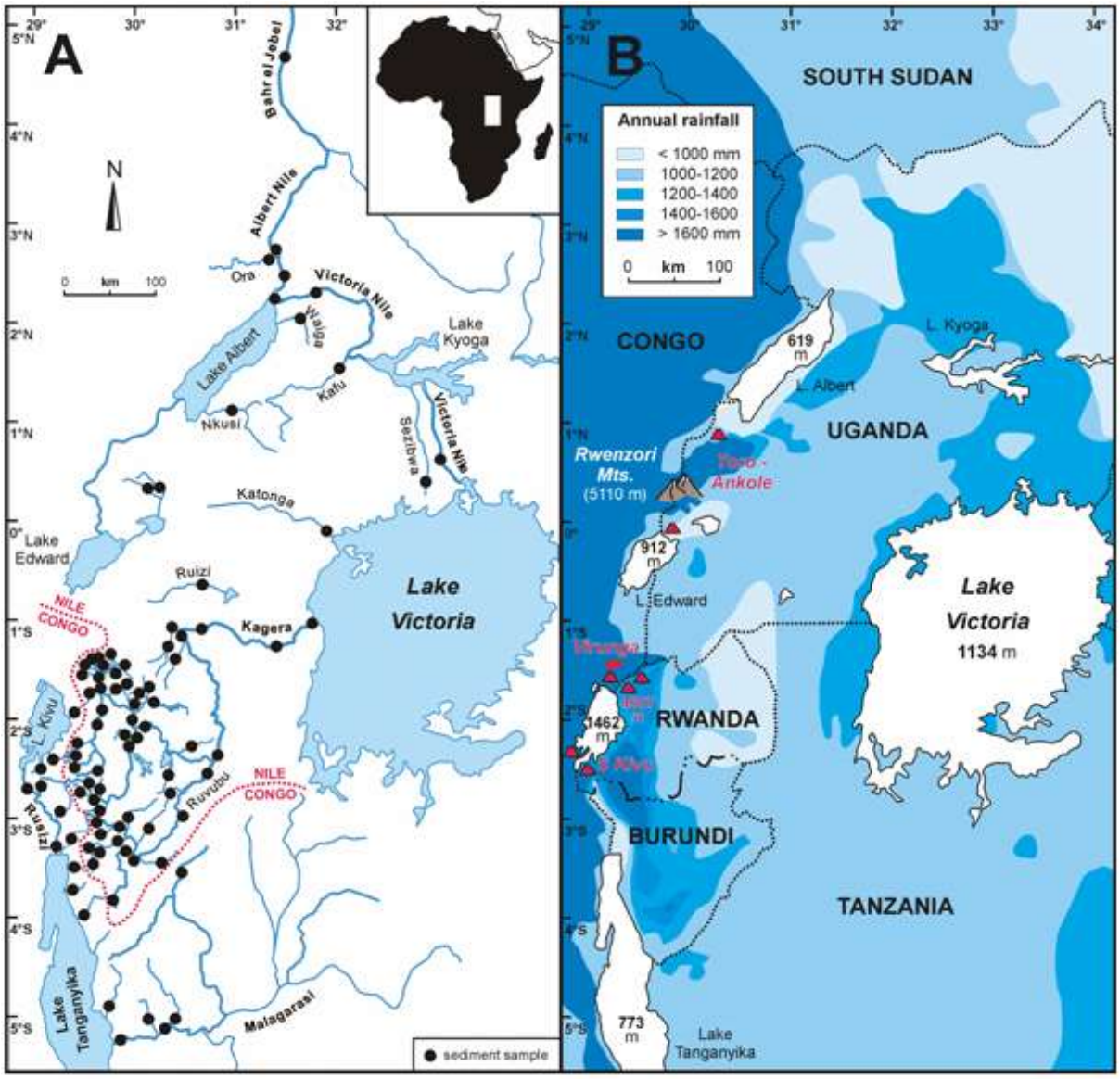

Figure 5.1. *Location map of the study region in equatorial central Africa. A) Studied river systems and sampling sites. The water divide between the upper catchments of Rivers Congo (including Lakes Kivu and Tanganyika) and Kagera-Nile (including Lakes Victoria, Kyoga, Edward and Albert) is shown. B) Rainfall map. The location of the Rwenzori Mountains and of the Toro-Ankole, Virunga and South Kivu volcanic fields is shown. Elevation (in m a.s.l.) is given for major lakes and for highest mountains and volcanoes in the region.*

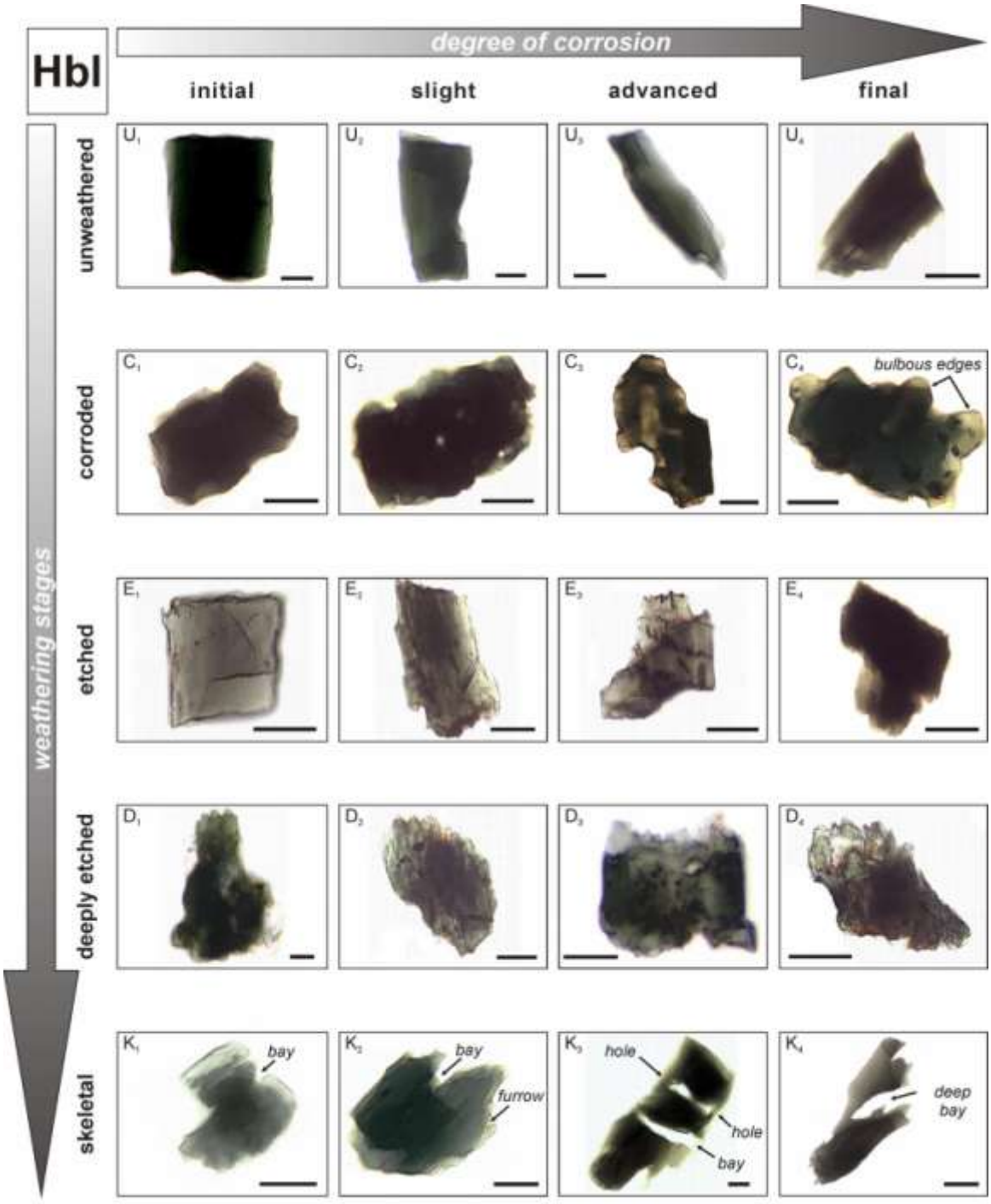

***Figure 5.2**. Visual classification of surface textures in hornblende grains from equatorial river sands. Weathering increases from top to bottom; within each stage, degree of corrosion increases progressively from left to right. Localities: Lake Albert drainage (Uganda: K1); Lake Kyoga drainage (Uganda: C2, C4, K2); Lake Kivu drainage (Rwanda: D1); Lake Tanganyika drainage (Burundi: U3, D3); Virunga volcanic field (Rwanda: U2); Kagera drainage (delta: C1, K4; Rwanda: all other grains). Scale bar 63 μm for all grains.*

5.2.1. Classification of weathering textures

In order to accurately determine the degree of chemical weathering of diverse minerals, we devised a classification of weathering textures aimed at collecting reproducible data during grain-counting under the polarizing microscope. Because the degree of corrosion may not be classified coherently at different magnification scales (e.g., a grain with incipient corrosion may appear unweathered at low magnification), the same objective (e.g., 20×) is better used consistently during optical observation. Incipient corrosion features are more easily identified when the microscope diaphragm is partially closed. Sticking to the existing nomenclature (Mange and Maurer, 1992 p. 9; Morton and Hallsworth, 2007; Turner and Morton, 2007),we have systematically identified the various morphologies displayed by diverse heavy minerals in many hundred sand and sandstone samples from different geological settings. This allowed us to characterize recurrent categories, and to rank them in a scale of progressive corrosion. Based on the appearance of diagnostic textural characters, five successive stages of weathering were thus defined (unweathered, corroded, etched, deeply etched, skeletal), which can be identified for detrital minerals of any lattice structure and chemical composition. Within each weathering stage, four degrees of progressive corrosion were distinguished, based on increasing evidence of features displayed by grain outlines. The final degree of corrosion of one stage (e.g., degree 4 of the corroded stage) does not necessarily indicate less intense weathering than the initial degree of corrosion of the successive stage (e.g., degree 1 of the etched stage), because different features may reflect different chemical processes.

Figure 5.3. *Visual classification of surface textures in actinolite grains from equatorial river sands. Weathering increases from top to bottom; within each stage, degree of corrosion increases progressively from left to right. Localities: Kagera drainage (delta: K2; Rwanda: all other grains). Composite image of grain K3 was required to have both parts of this thick grain properly focused. Scale bar 63 µm for all grains.*

The several plates presented in this article, illustrating the successive weathering stages and progressive degrees of corrosion for most common heavy minerals, provide a helpful reference standard, thus allowing an accurate and reproducible classification of corrosion features by visual comparison. The first three plates (hornblende, Figure 5.2.; actinolite, Figure 5.3.; augite, Figure 5.4.) illustrate how, in spite of different chemistry and stout to elongated prismatic crystal habit, the most common detrital inosilicates show analogous weathering sequences principally controlled by crystallographic structure (Velbel, 2007; Velbel and Losiak, 2010). The same weathering sequence can be identified for staurolite (Figure 5.5.), a relative stable mineral showing peculiar crystallographically-related features (e.g., limited development of etch pits because of poorer cleavage along the c-axis, appearance first of mamillae and then of cockscomb terminations at a more advanced stage of weathering; Velbel et al., 1996). Other heavy minerals do not display the same variety of surface textures, and consequently the same successive weathering stages are not easily identified. We could thus distinguish only among degrees of progressive corrosion, as illustrated in Figures. 5.6. and 5.7. Kyanite grains are characterized by perfect cleavage along one prism direction {100} and good cleavage along the {010} plane, and when weathered they thus tend to split along linear steps before etch pits sufficiently deep to be revealed could develop. Chloritoid also has strong cleavage, and typically displays tabular shape. Similar difficulties are met with minerals that do not show marked preferential crystallographic directions, such as isotropic garnet or epidote, which is not elongated along the c-axis and rarely prismatic (Figure 5.6.). Finally, some detrital minerals seldom show deep etch pits because they are relatively stable. Sillimanite prisms may be corroded only at their extremities and not along their lateral faces. Conversely, titanite may show corrosion along the surface, whereas the outline appears preserved (Figure 5.7.). Andalusite commonly displays bulbous edges. Monazite grains are usually rounded, with corrosion features distributed along their surface. Less extensive are corrosion features on tourmaline (Van Loon and Mange, 2007), rutile, or zircon (preferentially altered if metamictic; Colin et al., 1993). Even these “ultrastable” minerals, generally dominating heavy-mineral suites in ancient sandstones (Hubert, 1962), undergo dissolution during equatorial weathering and burial diagenesis (Figure 5.7.).

5.2.2. Definition of weathering stages

5.2.2.1. Unweathered stage (U)

The surface of the grain is uncorroded, with continuous outline without etch pits or re-entrants. Angular marks caused by mechanical rupture may occur. Detrital minerals may have any habit or degree of roundness, ranging from subhedral to euhedral, and from angular to rounded.

5.2.2.2. Corroded stage (C)

The original surface of the grain is recognized, but corrosion pits and re-entrants characterize the entire outline, and become progressively deeper with increasing degree of corrosion.

5.2.2.3. Etched stage (E)

The original grain surface can still be recognized, but hacksaw terminations appear, initially at the extremity of prismatic crystals along preferential crystallographic directions (e.g., c-axis in amphiboles and pyroxenes). Initially isolated, etch pits and denticles are arranged in rows and groups at higher degrees of corrosion. Finally, enlargement and coalescence of laterally adjacent pits produce lozenge-shaped textures affecting a significant part of the grain.

5.2.2.4. Deeply etched stage (D)

The entire grain outline is affected by extensive corrosion. Etch pits are significantly larger and deeper than in the previous stage. Angular embayments become evident.

5.2.2.5. Skeletal stage (K)

Grain shape is completely transformed by corrosion. Furrows, grooves, holes and articulate embayments cutting deep across the grain are developed.

Figure 5.4. *Visual classification of surface textures in augite grains from equatorial river sands. Weathering increases from top to bottom; within each stage, degree of corrosion increases progressively from left to right. Localities: Kagera drainage (Rwanda: U1, E3, E4, D1, D2, D4, K1, K4); Virunga volcanic field (Rwanda: all other grains). Scale bar 63 µm for all grains.*

5.2.3. Polymodal distribution of weathering textures

In the same sample, grains of the same mineral may display even the full suite of weathering stages (e.g., unweathered euhedral to deeply etched augite from the Virunga volcanoes coexist in river sand of northern Rwanda). This may reflect provenance from multiple and differently weathered sources (Nesbitt et al., 1997), including bedrock and soil profiles of various type and maturity, eroded by diverse processes (e.g., rill to gully erosion, landslides), in areas of the catchment characterized by contrasting climatic and geomorphological conditions (e.g., rainfall, temperature, relief, vegetation). Whenever the analysis reveals a polymodal distribution of surface textures, correlating such corrosion modes to specific sources and processes will be hardly feasible in the lack of suitable information (Stieglitz and Rothwell, 1978). Nevertheless, a complete, accurate, and reproducible description of the variety of surface textures observed will be of great help to correctly assess modifications of sediment composition induced by climate or diagenesis.

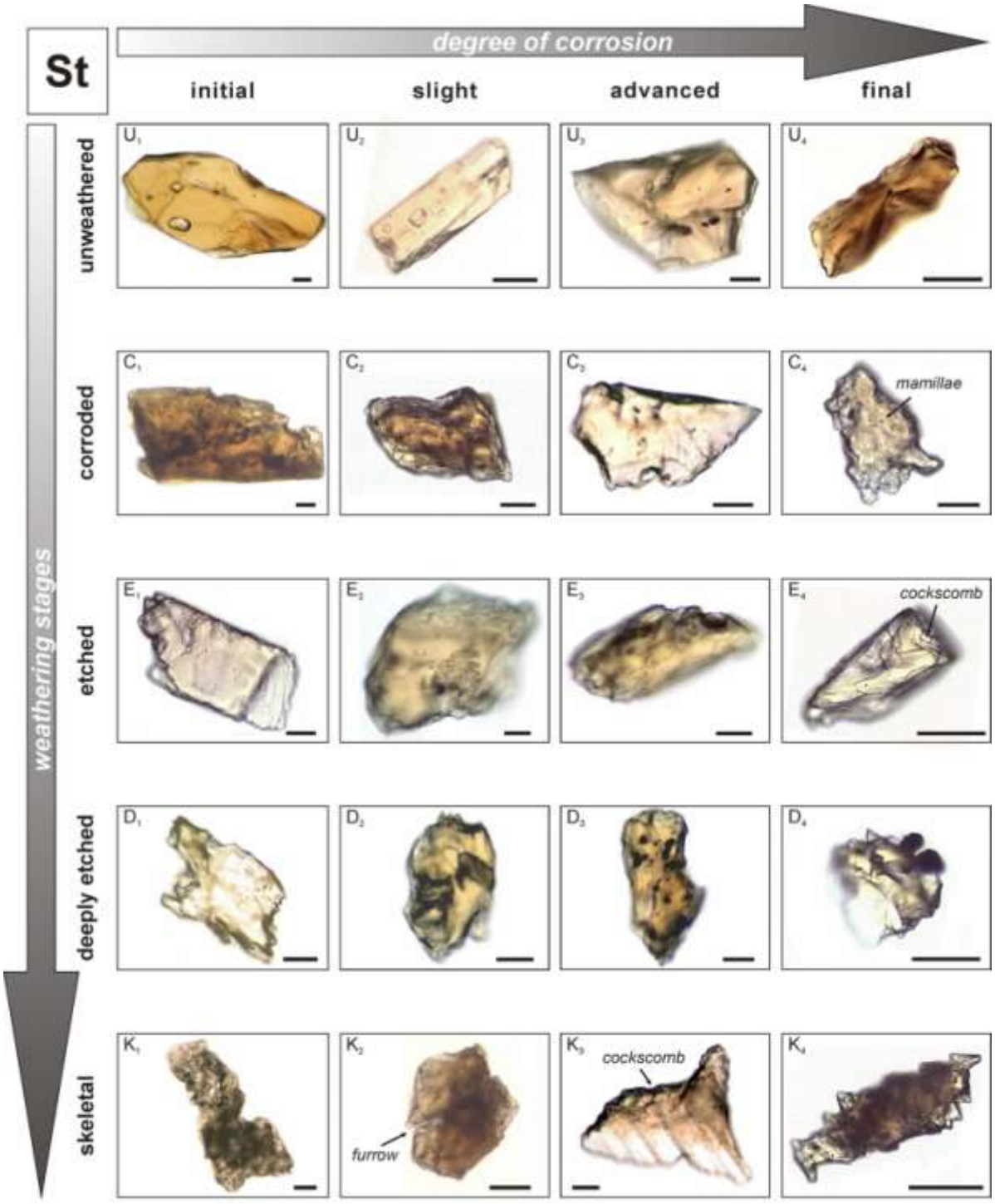

Figure 5.5. *Visual classification of surface textures in staurolite grains from equatorial river sands. Weathering increases from top to bottom; within each stage, degree of corrosion increases progressively from left to right. Localities: Kagera drainage (delta: U4, D1, K1; all other grains from Rwanda). Scale bar 63 µm for all grains.*

5.2.4. Composite grains

Heavy-mineral separates may contain grains including two species of the same mineral group (e.g., zoned augite, hornblende overgrown by actinolite) or made of diverse components (e.g., augite-bearing rock fragments in volcaniclastic sands, epidote-bearing rock fragments in metamorphiclastic or ophioliticlastic sands; Garzanti et al., 2000; 2006b; 2010b). Such composite grains, commonly dealt with cursorily during counting, provide us with the unique opportunity to observe selective weathering effects on different minerals that, belonging to the same grain, have shared the same history of weathering and transport. In grains including two different amphiboles (Figure 5.8.A) or pyroxenes (Figure 5.8.B), for instance, the higher-temperature phase typically displays more extensive corrosion. Within rock fragments, we can also compare the external part of a crystal, free to react with circulating fluids, with the internal part of the same crystal, protected from the outer environment (Figure 5.8.C). In rock fragments within fresh ash-fall deposits, for instance, euhedral faces of augite crystals are typically preserved where embedded in volcanic glass, but commonly display corroded outline along the free interface.

5.2.5. Chemical weathering versus mechanical abrasion

Rounding of detrital grains may be equally produced by weathering in tropical soils (Crook, 1968), abrasion (Dott, 2003), or recycling (Garzanti et al., 2003; Mehring and McBride, 2007). Such diverse origins are hard to distinguish under the polarizing microscope. Moreover, new surface textures can be variously superposed on older ones during the sedimentary cycle (Stieglitz and Rothwell, 1978). Grains weathered chemically in soils may be rounded mechanically later on, for instance during eolian transport. Vice versa, grains rounded by mechanical abrasion may be chemically etched since early burial stages (Pye and Mazzullo, 1994), or irregularities of the grain surface produced by mechanical processes may be enhanced by etch features developed during subsequentweathering or diagenesis (Mange and Maurer, 1992 p. 9). The same grain can be exhumed and recycled more than once during long multistep geological evolution, and occasionally preserve textures inherited from previous cycles (Velbel et al., 2007). Although unraveling all of these complexities is hardly feasible, the accurate inspection of surface textures can add useful information to verify doubts and avoid mistakes during interpretation. In order to define grain roundness, we

followed the same terminology as in Powers (1953), adapted for heavy minerals, and illustrated with examples offered by detrital zircon, tourmaline, and rutile (Figure 5.9.). These stable minerals are frequently rounded in ancient sandstones, because they commonly survive through more than one sedimentary cycle. Peculiar is the case of broken grains (Krumbein, 1941), displaying rounded or subrounded outline but with sharp edges on one side, thus revealing subsequent mechanical rupture (Figure 5.9.). When textures caused by both weathering (e.g., etch pits) and abrasion (e.g., rounded outline) are observed on the same grain, it is seldom possible to ascertain which preceded which. Nevertheless, it is important to record the coexistence of both characters, by using a simple and consistent nomenclature as shown in Figure 5.10. There, the illustrated detrital amphiboles and pyroxenes display all possible combinations of chemical and mechanical modifications of grain outlines, from unweathered (U) to corroded (C) and etched (E), and from angular (a), to subrounded (s) and rounded (r). Detrital minerals displaying different degrees of roundness and corrosion can thus be classified effectively, and consuming very little additional time during grain-counting under the microscope.

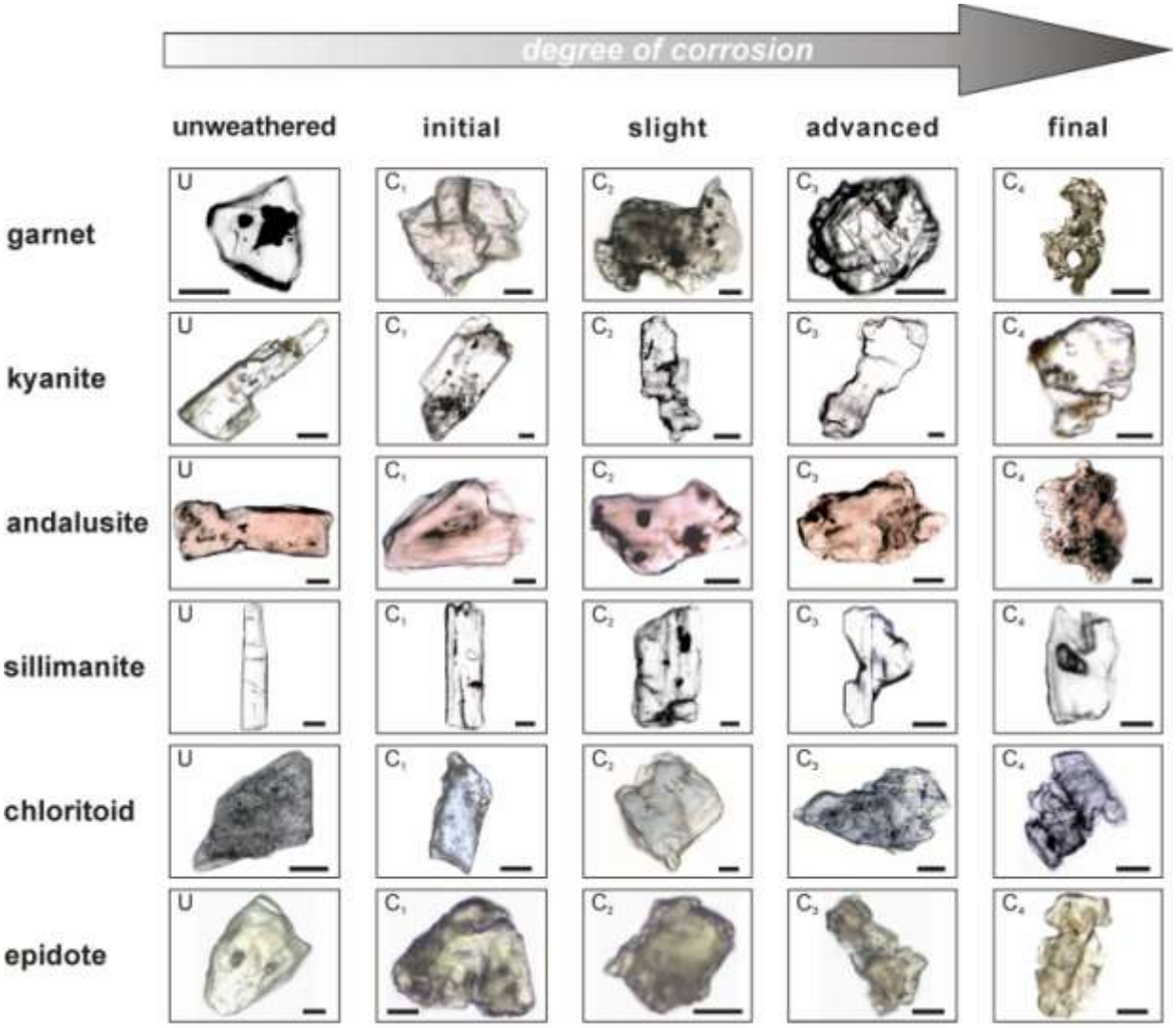

Figure 5.6. *Visual classification of surface textures in low to high grade metamorphic minerals. Degree of corrosion increases progressively from left to right. Localities: all grains from the Kagera drainage, but for unweathered garnet (Lake Tanganyika drainage, Burundi) and C4 garnet (Tertiary sandstones, northern Corsica). Scale bar 63 µm for all grains.*

5.3. Use of the catalog in the study of equatorial weathering

5.3.1. Study area

The study area follows the western branch of the East African rift (Ebinger, 1989) and straddles the equatorial belt, from a latitude of S5°13′ in NW Tanzania to a latitude of N4°51′ in South Sudan (longitude between 29°E and 33°E; Figure 5.1.). Uplifted along the rift shoulders are medium- to high grade crystalline rocks formed during successive Mesoarchean to Paleoproterozoic orogenic events. Intensely deformed metasediments intruded by granites and subordinate gabbros during the Mesoproterozoic are widely exposed in Burundi and Rwanda, whereas less-deformed siliciclastic successions and sub-tabular sedimentary rocks with intercalated basalts of Neoproterozoic age run along the Tanzania/Burundi boundary from Lake Tanganyika to Lake Victoria (Tack et al., 2010). Rift-related basins are punctuated by volcanic fields and filled by Neogene fluvial to lacustrine sediments. Volcanism, begun at ~12 Ma and restricted to three accommodation zones between extensional basins, shows a northward increase in alkaline character and CO_2 content. Tholeiites and alkali basalts of the S Kivu field were produced by fault-related activity dominated by fissure eruptions (Furman and Graham, 1999). Two active volcanoes and six extinct cones reaching up to 4507 m a.s.l. form the potassic Virunga field, straddling the Rwanda–Uganda–Congo border (Ebinger and Furman, 2003). The active Toro-Ankole field, aligned parallel to active faults east of the Rwenzori mountains, includes exceptionally silica-undersaturated melts and carbonatites (Rosenthal et al., 2009). Because of rift-related uplift, the region has considerable elevation and relief. Altitude of the numerous lakes, representing erosion base level, ranges from 619 m (Albert) and 772 m (Tanganyika) to 1134 m (Victoria) and 1462 ma.s.l. (Kivu), whereas the Rwenzori massif touches 5110 m (Figure 5.1.). The rift shoulder, marking the drainage divide between the Nile and Congo Rivers from Burundi to Rwanda, reaches between 2500 and 3000 m. West of this ridgeline, the land slopes abruptly toward Lakes Kivu and Tanganyika, joined along the rift axis by River Rusizi. The eastern slopes, drained by the diverse branches of River Kagera in Burundi (Ruvubu, Ruvyironza) and Rwanda (Nyabarongo, Akanyaru) are less steep, with rolling hills extending across central uplands to the low hills and papyrus swamps grading into Lake Victoria. Average air temperatures, ranging from 15 °C to 30 °C with minor seasonal and diurnal

variation, are markedly influenced by altitude. Freezing nights characterize the rugged Rwenzori mountains, where the highest peaks are permanently covered by snowfields and small rapidly retreating glaciers. Delivered during the passage of the intertropical convergence zone by humid masses blown by the southeasterly monsoon from the Indian Ocean, rainfall is distributed in two rainy seasons in autumn and spring. Annual precipitation ranges from ~1 m along the eastern shore of Lake Tanganyika to ~2 m on rift-shoulder reliefs in Burundi to Rwanda. Along the eastern Rwenzori slopes, it decreases sharply from 2.5 m on the mountains, where rain or snow falls nearly every day, to 0.75 m in the rain shadow at the foot of the range. Rain forests cover a small part of the territory in rift and volcanic highlands, and grade through subhumid acacia woodland to more arid shrubland and grassland. Soil temperature and moisture regimes vary from udic isothermic/isomesic on Rwanda and Burundi highlands to ustic isohyperthermic in savannah lowlands. Because of widespread development of thick red-brown ferrallitic soils and extensive vegetation cover, outcrops are rare and limited to most resistant lithologies (e.g., quartzite, amphibolite; Moeyersons, 2003). Where exposed, Mesoproterozoic metasediments are generally transformed into saprolite; sparse hillocks remain as isolated witnesses of large granitoid intrusions.

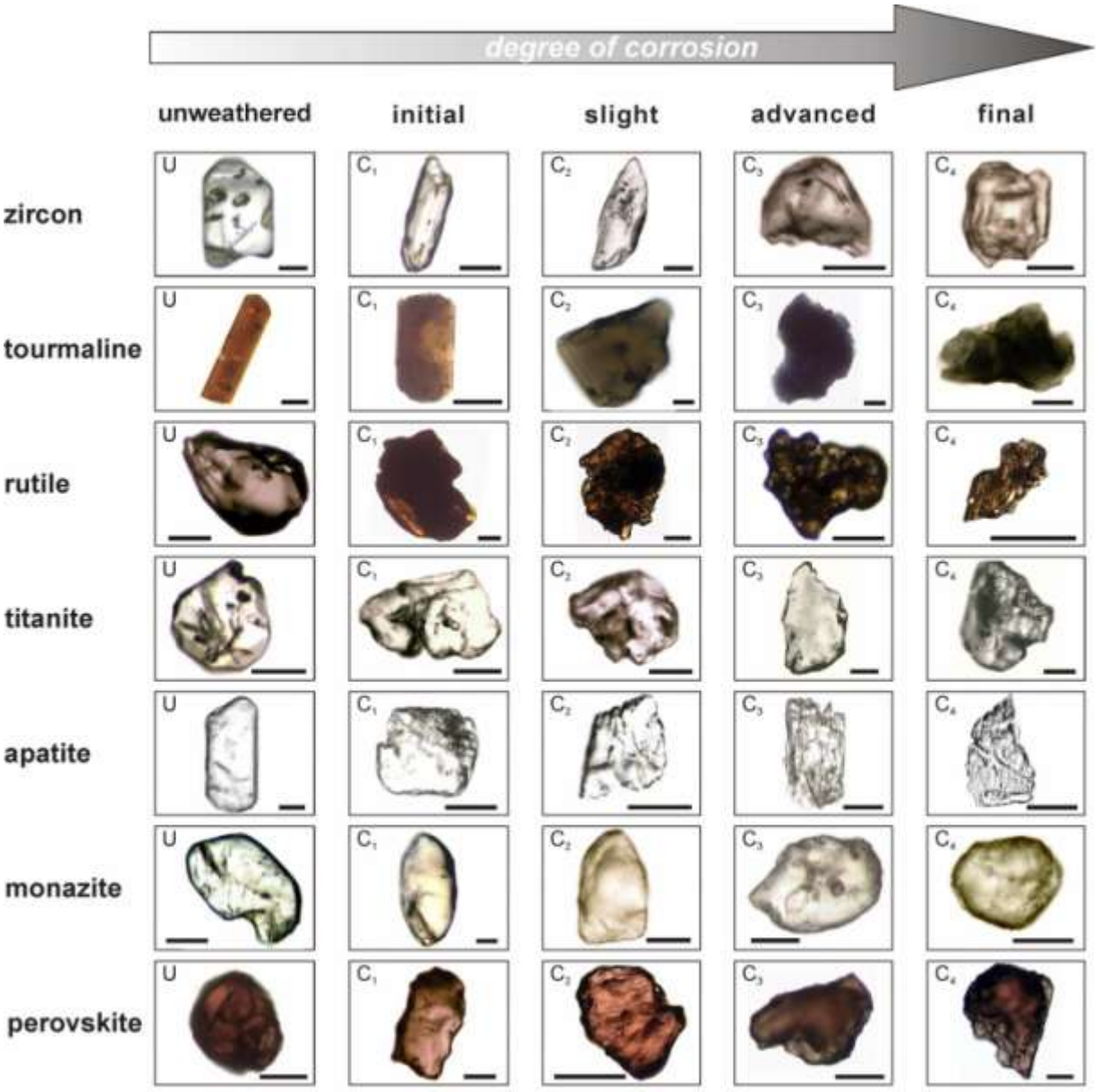

Figure 5.7. *Visual classification of surface textures in other heavy minerals. Degree of corrosion increases progressively from left to right. Localities: all grains from the Kagera drainage, but for C2 tourmaline (Victoria Nile drainage, Uganda), C1 rutile (Lake Albert drainage, Uganda), C1 monazite (Lake Tanganyika drainage, Burundi), and all apatite grains (Tertiary sandstones, northern Corsica). Scale bar 63 μm for all grains.*

5.3.2. Methods

Corrosion features of derital minerals were studied systematically in 170 sand samples collected from the active bed, bars or banks of the most significant 155 rivers in the upper Nile and Congo basins (Garzanti et al., 2013b). Surface textures were determined on 27,791 transparent heavy-mineral grains overall (see Appendix Table A1). Particular care was dedicated to sampling first order catchments with different climate, bedrock lithology and relief, from swampy lowlands to rift-shoulder highlands and volcanic fields. In order to assess the relative importance of weathering in soils at the source and during stepwise transport versus downstream changes caused by supply from successive tributaries, river sediments were collected upstream and well downstream of major confluences along the whole Kagera Basin, from the headwaters to the delta in Lake Victoria.

Samples were sieved, and a quartered part of the 63–250 μm class was treated with sodium ditionite–citrate–bicarbonate to remove iron-oxide coatings, an efficient grain-cleaning procedure which produces minimal damage on silicate grains (Cremeens et al., 1987).

Dense minerals were next separated by centrifuging in sodium metatungstate (density 2.90 g/cm^3), and recovered by partial freezing with liquid nitrogen. Corrosion features were studied on all detrital components and on all grain-size fractions, from very fine sand to granules and pebbles.

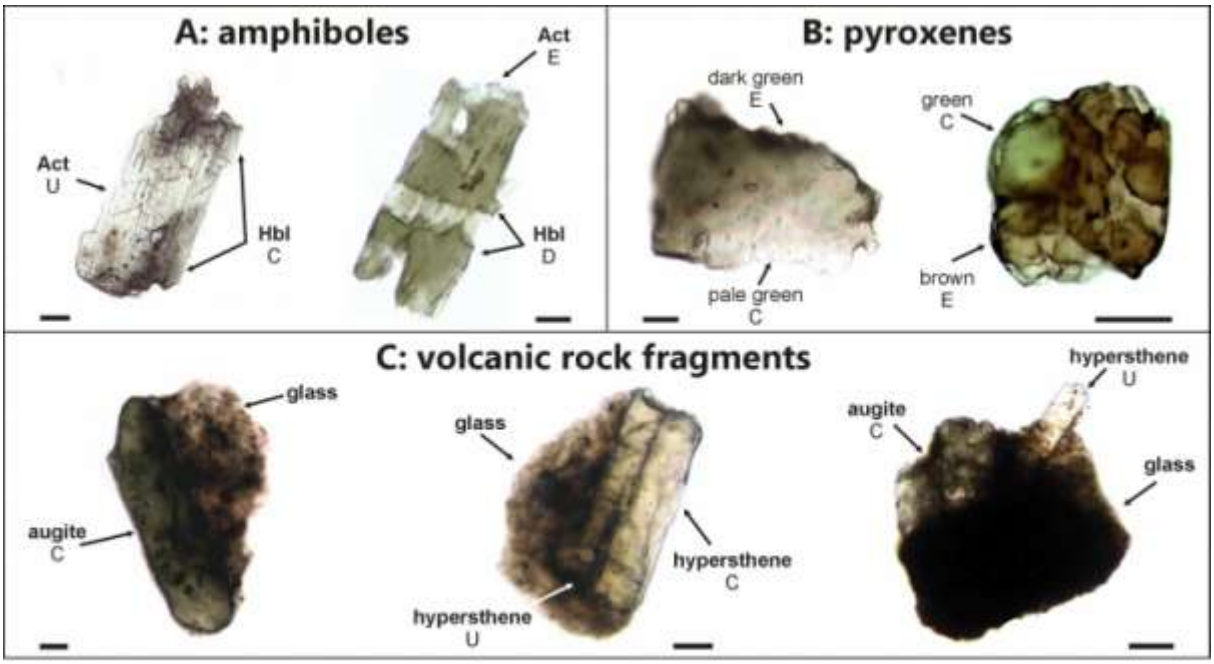

Figure 5.8. *Selective weathering in composite grains. In the same grain, less stable hornblende is more corroded than actinolite (A; Kagera drainage), brown titanian augite than green augite (B; Virunga volcanic field and Nile delta), volcanic groundmass than pyroxene phenocrysts, and augite than hypersthene (C; Virunga volcanic field). The same hypersthenes crystal, unweathered where secluded in glass, shows incipient corrosion where exposed. Scale bar 63 μm for all grains.*

5.3.3. Weathering in equatorial Africa

The degree of alteration attained in different parts of the studied region depends both on the intensity of weathering, primarily controlled by climate (precipitation, temperature), and on the amount of time over which weathering operates. This is markedly longer in transport-limited denudation regimes where weathering rate exceeds the ability of transport processes to remove material, than in weathering-limited erosion where the opposite occurs (Gilbert, 1909; Johnsson, 1993). For example, compositional modifications caused by weathering effects are remarkably small for detritus shed by the rugged central part of the Rwenzori massif, but may be extreme in humid Rwanda and Burundi rift highlands as well as in hot and swampy savannah lowlands (Garzanti et al., 2013c). In transport-limited regimes, detritus may be reduced to a nearly pure quartzose residue, with laterite clasts representing

most of the coarsest fraction. Most quartz grains display deep embayments or rounded corners, the mark of extensive dissolution in equatorial soils. Even in sediments derived entirely from granitoid rocks, feldspars may be few and largely represented by relatively stable although intensely corroded microcline. Even more sporadic are rock fragments, including extensively lateritized phyllite grains with quartz and dravitic tourmaline, and granitoid or gneissic grains with sericitized feldspars, slightly altered muscovite, chloritized to vermiculitic biotite, Fe–Ti oxides, amphibole, titanite, or epidote. Whereas micaschist pebbles are invariably rotten with completely decomposed garnet porphyroblasts, amphibolite pebbles may be remarkably fresh with tightly interlocked crystals of unaltered plagioclase and amphibole. Quartz– tourmaline pebbles are locally common. Basaltic rock fragments are extensively altered in the South Kivu field, but mostly fresh in the Virunga field, characterized by higher altitude and drier climate. Among detrital micas, muscovite generally appears as relatively fresh, whereas biotite is commonly altered.

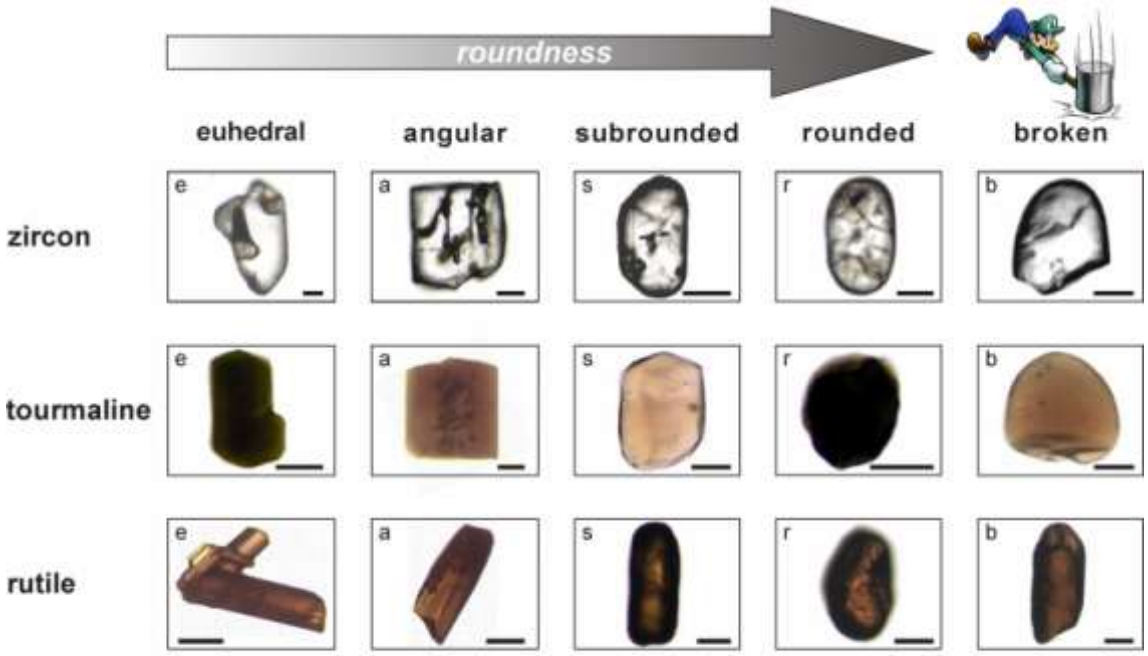

Figure 5.9. *Roundness scale for stable heavy minerals (following similar criteria as in Krumbein, 1941; Powers, 1953). Zircon grains are from the Kagera drainage (Burundi), but for the subrounded grain (River Rusizi, Congo). Tourmalines are from the Kagera drainage (Rwanda), but for the broken grain (Nile delta, Egypt). Rutiles are from the Nile delta (Egypt), but for the euhedral (Kagera drainage, Rwanda) and angular (Lake Albert drainage, Uganda) grains. Scale bar 63 µm for all grains.*

5.3.4. Corrosion of heavy minerals

Different heavy minerals display different responses to weathering. Although widely considered as highly unstable (Pettijohn et al., 1972 p. 305; Morton, 1985), olivine is preserved and traced downstream for at least 30 km of fluvial transport in detritus from the Virunga volcanoes. Olivine is more strongly weathered in South Kivu (only 8% uncorroded grains) than in Virunga volcaniclastic sands (22% uncorroded grains). In the same samples, colorless forsteritic grains and more ferriferous yellowish grains (as determined by Raman spectroscopy) both range from unweathered to etched. Instead, apatite grains derived from the Virunga volcanoes, characterized by grayish core, frequently display euhedral outline and only incipient corrosion. Pyroxene and amphibole grains commonly display corroded outlines, denticulated margins parallel to the c-axis, etch pits, and skeletal textures, with weathering products developed both between etch pits and on grain surfaces. In South Kivu volcaniclastic sands, half of identifiable pyroxenes are etched or skeletal (51±9%), and a minority unweathered (18±8%). Instead, pyroxene grains fromthe Virunga field appear commonly unweathered (42±9%), and a minority etched or skeletal (19±14%). Strongly corroded (25% unweathered, 44% etched) is also detrital pyroxene found in the northern Rwenzori (Fort Portal) area, and sparsely across northern Rwanda to southernmost Uganda. Green augite appears less weathered than brown augite. Amphiboles seldom appear unweathered even in detritus from the Rwenzori mountains, where half of them are corroded and the rest etched; most amphibole grains are etched to skeletal in the Kagera basin (Figure 5.11.). Among opaque detrital minerals, ilmenite mostly includes Si and Al impurities and displays poor Raman signal. Chromite grains may show a characteristic etch feature with sharp edges and wholly corroded surface, which is also observed in peridotites of the Southern European Alps and may thus as well be a post magmatic feature caused by late circulation of aggressive fluids through bedrock. Garnet grains are much rarer than expected in sediments derived from amphibolite-facies metasedimentary rocks. The few survivors commonly show corroded outlines, orange-peel surfaces, and largescale facets. Most epidote grains are corroded, but seldom deeply etched and never skeletal. Staurolite grains are rarely unweathered, and show corroded to deeply etched and skeletal outline. Chloritoid grains are mostly corroded, but less frequently etched. Among Al_2SiO_5 polymorphs, kyanite grains frequently show corroded rims and etch pits, starting within fractures and propagating laterally. Whereas a significant minority of prismatic sillimanite grains are unweathered, andalusite grains with common carbonaceous inclusions (shed in abundance from the extensive aureoles that surround mafic–ultramafic Kibaran intrusions; Tack et al., 2010)

almost invariably display corroded outlines. Less frequently weathered are andalusite grains including large and commonly euhedral minerals or lacking inclusions, which may derive from the periphery of peraluminous granites and pegmatites (Clarke et al., 2005). Perovskite grains, also possibly crystallized during the Kibaran event and characterized by intense orange-brownish color, high relief, low birefringence and anomalous interference colors, mainly display corroded rims and pitted surface. Titanite grains are commonly corroded, and in particular those with strong yellow color indicating higher concentration in REE. Among relative stable minerals, yellow-brown dravitic tourmaline is much more common in the Kagera basin and less frequently weathered than pinkish to green-blue schorlitic tourmaline, confirming a non-uniform response of various tourmaline color-varieties to the intensity of weathering (van Loon and Mange, 2007). Corroded rutile and brookite grains locally occur, and even zircon occasionally shows corrosion, and preferentially so metamictic grains.

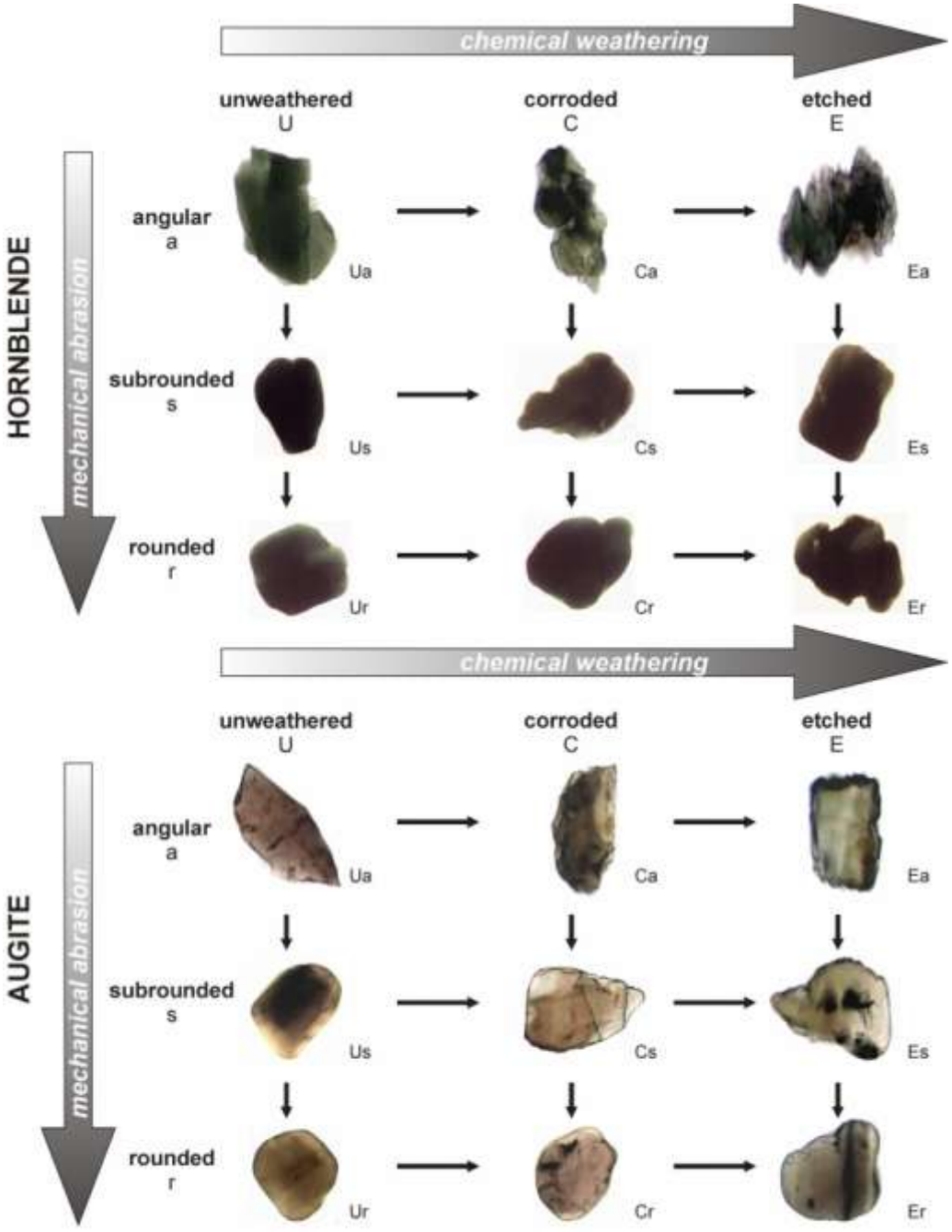

Figure 5.10. *Visual classification of surface textures caused by both weathering and mechanical abrasion. Weathering increases from left to right, roundness from top to bottom. Determining the temporal sequence (rounding ->etching versus etching ->rounding) requires detailed observation, and cannot be generally done during routine analysis. Angular grains are all from Rwanda (hornblende from the Kagera drainage, augite grains from the Virunga volcanic field); subrounded and rounded grains all from the Nile delta (Egypt).*

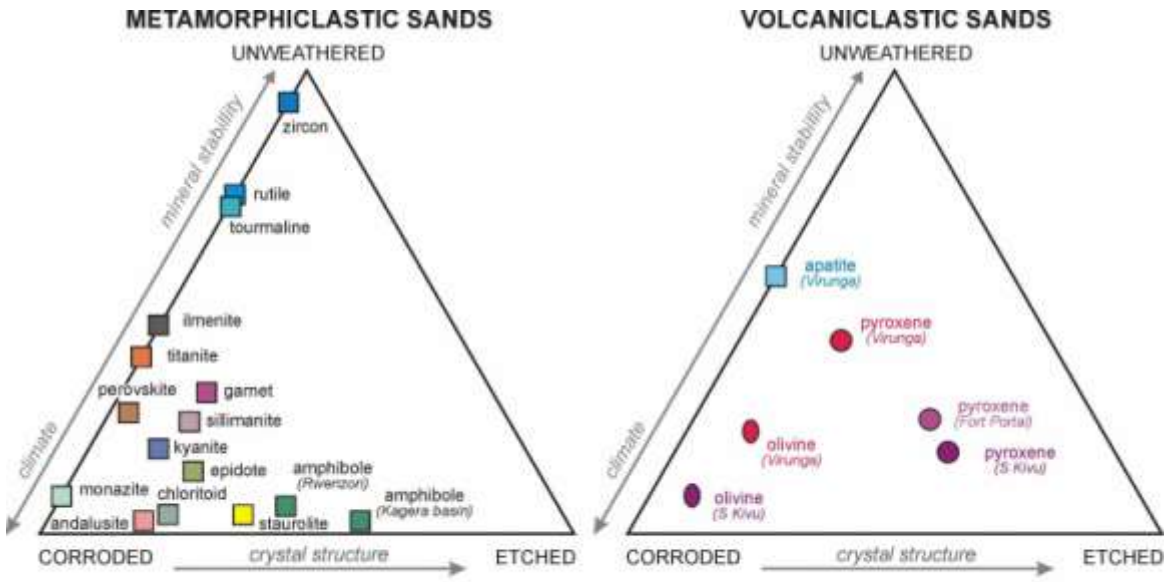

Figure 5.11. *Different response to weathering of heavy minerals from equatorial river sands. Frequency and type of surface textures depend not only on mineral stability (zircon least weathered, olivine most weathered) and climate (drier in Virunga than South Kivu volcanic provinces), but also on crystallography (deep etching develops on cleavable pyroxenes and amphiboles, but less easily on other minerals). Corrosion features on opaque ilmenite grains were assessed at SEM.*

5.4. Application potential of the catalog in the study of diagenesis

The striking discrepancies between modern sands and ancient sandstones in both variety and concentration of heavy-mineral assemblages demonstrate the overwhelming effect of post-depositional dissolution (Bramlette, 1941; Pettijohn, 1941; Gazzi, 1965; Morton, 1985). Diagenetic dissolution has a much more drastic effect than weathering because of much higher temperatures and longer available time. When analyzing provenance of ancient clastic wedges it is thus essential to investigate and ascertain how much and which part of the original detrital assemblage has been dissolved. Valuable information for this critical task can be obtained by carefully recording the occurrence of various corrosion features observed on diverse minerals, which can be carried out consistently and systematically with the help of the practical classification scheme illustrated here. Although direct observations can tell us only the state of what is preserved and not what was destroyed, such crucial guess can be attempted if frequencies of corrosion features are systematically correlated with relative mineral abundances and heavy-mineral concentration (HMC and tHMC indices). The HMC index is calculated as the volume percentage of total heavy minerals in the bulk sample, whereas the tHMC index represents the volume percentage of the transparent heavy minerals only (i.e., it does not consider opaque and turbid grains; Garzanti and Andò, 2007a).

Although potentially influenced by diverse factors such as hydraulic sorting, the HMC index provides the decisive key to detect and ultimately demonstrate the selective loss of unstable species, and to identify diagenetic suites fundamentally controlled by the different chemical stabilities of detrital minerals. Following this quantitative approach, we can ideally monitor the sequence of corrosion features developed on diverse minerals while detrital assemblages are transformed by diagenetic dissolution. This was done through the up to 22 km-thick Cenozoic succession of the Bengal Basin in Bangladesh (Figure 5.12.; Curray et al., 2003), as observed both in outcrop (Najman et al., 2008, 2012) and in the subsurface (Morton and Hallsworth, 2007 p. 224–225). We have studied 53 samples of Paleocene–Eocene to Pleistocene sandstones from various outcrops, and with particular detail 15 samples collected down to a depth of 2890 m in a subsurface core, on which corrosion features were determined on 2346 transparent heavy-mineral grains (see Appendix Table A2). The same preparation and analytical methods as described in Section 3.2 have been used. Lithified samples were gently disaggregated in a steel mortar, taking all possible care to avoid

grinding of single grains. Grain density of 3 modern river sands, derived from the Chittagong Hills (Bangladesh) and from the Arakan Yoma (Myanmar), and of 8 subsurface ancient sand samples was measured with a hydrostatic balance (method described in Garzanti et al., 2012; see Appendix Table A3).

The Ganga–Brahmaputra fluviodeltaic system, supplying Himalayan derived litho-feldspatho quartzose metamorphiclastic detritus with rich and varied amphibole–epidote–garnet suites (HMC 6±2, ZTR 5±2; Garzanti et al., 2010a, 2011; ZTR index after Hubert, 1962), has represented the dominant axial source of sediment throughout the Neogene (France-Lanord et al., 1993). Additionally, largely recycled lithic to feldspatho-litho-quartzose sedimentaclastic detritus with much poorer, epidote-dominated or epidote–amphibole–garnet suites with tourmaline, rutile, zircon, staurolite, kyanite, and chloritoid (HMC 1±1, ZTR 10±10; Garzanti et al., 2007a) was being fed transversally from the Indo-Burman Ranges, bordering the eastern side of the basin.

In the Neogene subsurface succession, heavy-mineral assemblages show systematic progressive changes with burial depth (Figure 5.13.). Below 0.5 km, pyroxene becomes very rare. Between 1 and 2 km, amphibole decreases rapidly, and consequently assemblages are relatively enriched in garnet and epidote. Between 2 and 3 km, amphibole and sillimanite completely disappear, and epidote is progressively attacked and dissolved; assemblages are thus relatively enriched further in garnet, which displays progressively more extensive corrosion features (HMC<1, ZTR 10±5). Between 3 and 4 km, kyanite and titanite first, staurolite next, and finally chloritoid are extensively dissolved, leaving a very poor, garnet-dominated heavy-mineral residue (HMC<0.5, ZTR 15±5). Corroded tourmaline occurs at any depth, and corroded zircon at depths ≥1 km. Because of decreasing heavy-mineral content, grain density also progressively decreases with depth and age ($r=-0.89$; sign. lev. 1%). Although older clastic units had with all likelihood significantly different sources and thus primitive mineralogy, the trend is continued in the upper Eocene/lower Miocene Barail Formation exposed in Bangladesh, invariably yielding very poor suites dominated by occasionally corroded zircon, tourmaline or Ti-oxides, with minor and occasionally corroded monazite and Cr-spinel. Corroded to skeletal chloritoid and staurolite are still common in Middle and Upper Barail strata (HMC<0.4, ZTR 39±19), whereas corroded garnet and chloritoid only sporadically occur in lower Barail strata (HMC<0.2, ZTR 56±20). Uddin and Lundberg (1998 p. 467–470) concur that “heavy-mineral content increases systematically through time (Eocene–Oligocene 0.2%), and is much higher in the Miocene and younger units (Bhuban 0.5%, Boka Bil 1.0%, Tipam 1.9%), and highest in the Dupi Tila sands (average 2.9 wt.% and as high as 7.5%)”, although their interpretation is altogether different:

"the vertical distribution of heavy minerals in the Bengal basin fill is not due to intrastratal solution during diagenesis".

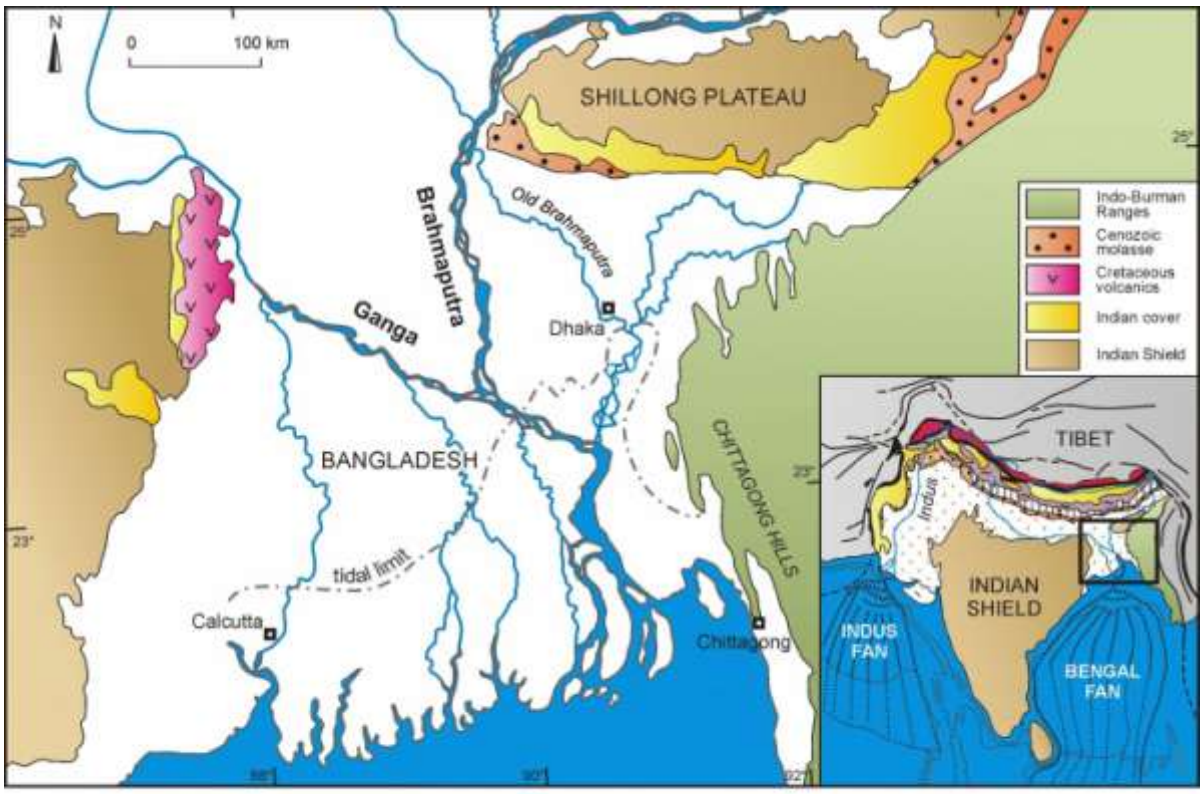

***Figure 5.12**. Location map of the Bengal Basin. The studied samples are from diverse outcrops of Cenozoic foreland-basin deposits in northern Bangladesh and from subsurface cores drilled in the Ganga–Brahmaputra estuary region of southern Bangladesh. Shown in inset are the Himalayan collision orogen with the associated sediment-transport routes and foreland to remnant-ocean basins.*

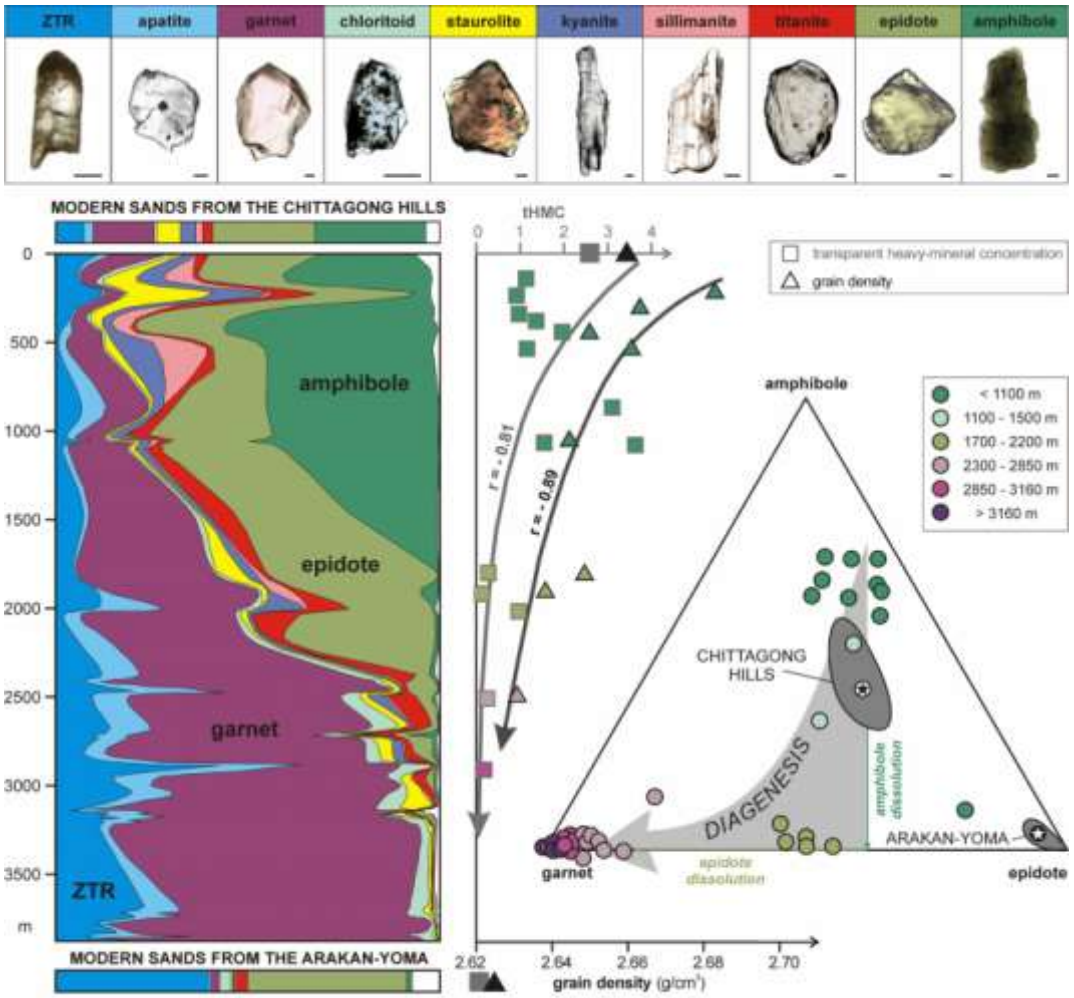

Figure. 5.13. *Vertical distribution of heavy minerals in cores from the Bay of Bengal. Note progressive decrease with depth and final disappearance of amphibole and sillimanite first, followed by epidote, kyanite, titanite, and staurolite. Garnet, chloritoid, apatite, rutile, tourmaline, and zircon are observed down to 4 km. Selective diagenetic dissolution causes a statistically significant downcore decrease (sign. lev. 1%) in both concentration of transparent heavy minerals (tHMC) and grain density. Downhole compositional trends are influenced by provenance changes as well. Feldspatho–quartzose sands at shallow depths compare well with modern sands from the Chittagong Hills (Bangladesh), largely recycled from Himalayan-derived turbidites of Neogene age. Coarser quartzo-lithic to lithic sands recurrent at greater depths, instead, closely resemble detritus from the Indoburman Ranges (Arakan Yoma, Myanmar; Garzanti et al., 2007), indicating erosion of more distal turbiditic mudrocks of Paleogene age, exposed in more eastern parts of the Indo-Burman Ranges (Allen et al., 2008). Extensive recycling is confirmed by subrounded outlines commonly displayed by heavy minerals at all burial depths. Scale bar 63 μm for all grains. Plotted compositions include data from Morton and Hallsworth (2007).*

5.5. Conclusion

An operational classification of surface textures, produced by chemical weathering and displayed by detrital minerals in modern equatorial sands as well as in diagenized Cenozoic sediments and sedimentary rocks, is presented here with the aim of enhancing the resolution potential of sediment-generation and provenance studies. Five stages of progressive weathering (unweathered, corroded, etched, deeply etched, and skeletal) are systematically identified and cataloged. Color plates illustrating increasing degrees of corrosion for each of these five weathering stages in diverse heavy-mineral species are specifically prepared to assist in the classification and data recording during optical analysis. Usage of visual-comparison standards effectively minimizes operator variation and enhances reproducibility. A wealth of information indispensable for a correct diagnosis of paleoclimatic setting or diagenetic conditions can thus be collected readily, without losing much additional time during routine grain-counting under the microscope. Such a practical tool proved to be of substantial help in assessing the incidence of climatic and diagenetic processes on the mineralogy of sediments deposited in various climatic and geodynamic settings, including the East African rift and the Bengal Basin, and ranging in size from silt to sand and in age from present day to Paleogene.

6. Subduction complexes at convergent plate boundaries

Subduction zones occur where the lithosphere descends into the astenospheric mantle along the Benioff zone. Subduction involves a lower downgoing plate and an upper overriding plate, both of which can be either oceanic or continental.

Their typical expression are fold and thrust belts or accretionary wedges. They are the area where material of both the footwall and hangingwall plate is juxtaposted and shortened. The processes of transferring material from the footwall to the hangingwall plate is termed “accretion”, whereas the processes of transferring material from the hangingwall to the footwall plate is defined as “erosion”(Von Huene and Lallemand, 1990). Material eroded and transported down into the subduction though may eventually be re-exhumed and exposed. The final stage of oceanic subduction is the collision of two continental margins and consequently the formation of a collisional orogen. The orogens have variable width which is mainly fuction of the age of the subduction, depth of the decollement planes, and polarity of subduction.

Subduction zones behaviour appears primarily controlled by the polarity of their downgoing slab, i.e., W-directed or E- to NNE-directed, probably due to the westward drift of the lithosphere relative to the asthenosphere (Doglioni et al., 1999).

Westward subductions are steeper and deeper with respect to those directed to the east which are shallower and less steep (Isacks and Barazanghi, 1977; Lundgren and Giardini, 1994).

Westward subductions produce thin-skinned, low-relief orogens, mainly with a single “eastward” vergence (or southeast or northeast) of the accretionary prism, chiefly consisting of volcanic or sedimentary cover rocks (West Pacific arcs, Lesser Antilles, Apennines, Carpathians). Eastward/northeastward subductions, instead, give rise to thick-skinned, high-relief and doubly-vergent orogens where deep-seated neometamorphic and igneous rocks are widely exhumed (Himalaya, Andes, Alps, Caucasus; Doglioni et al,. 2006).

Also decollement planes behave differently in these two end-members. In W-directed subduction zones, the decollement of the plate to the east is warped and subducted,

whereas in the E- to NNE-directed, it is ramping upward at the surface. The different decollements in the two end-members of subduction should make different PT-paths and, therefore, generate variable metamorphic assemblages in the associated accretionary wedges and orogens.

HP/LT metamorphism is typical of the frontal thrust belt of E- or NE-directed subduction zones, whereas the HT/LP metamorphism is typical of the hanging wall of W-directed subduction zones where the astenosphere replaces the slab at shallow levels (Doglioni, et al., 1999).

Different magmatic products are associated with these different subduction zones. Calc-alkaline and alkaline–tholeiitic volcanic products are typical of the island arc and the back-arc basin of the W-directed subduction zones, whereas calc-alkaline– shoshonitic suites, with large volumes of batholithic intrusions and porphyry copper ore deposits are associated with E- or NE-directed subduction zones (Thorpe, 1982).

Other differences may be highlighted by analysis of topographic profiles associated with satellite free air gravimetric anomalies profiles along subduction zones (Harabaglia and Doglioni, 1998).

They have been interpreted in term of different age of the subjecting lithosphere, dimension, composition and velocity of the plates (Hager and O'Connel, 1978), relative eastward mantle flow (Uyeda and Kanamori, 1979) or as a function of the geophysical and geological differences along the subduction zones of the world (Doglioni, 1990).

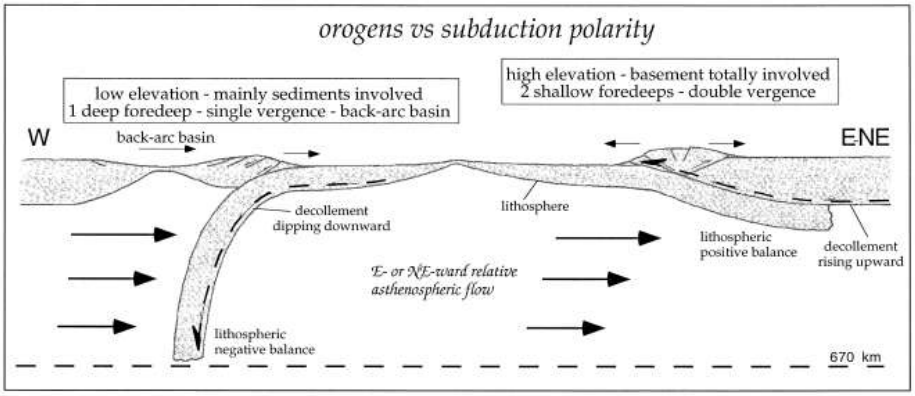

Figure 6.1. *Differences between W-directed and E-NE or NNE-directed subduction zones (Doglioni et al.,1999).*

By considering all possible combinations (oceanic vs. continental origin of the lower and upper plates; westward vs. eastward/northeastward subduction polarity), the types of plate convergence are reduced to eight end-members (Figures 6.2. and 6.3.):

- Westward Intraoceanic Subduction (e.g. Marianas-type intraoceanic arc, Figure 6.2. panel A),
- Westward Subduction of Oceanic beneath Continental Lithosphere (e.g. New Zealand-type boudinaged belt and prism, Figure 6.3. panel B),
- Westward Subduction of Continental Lithosphere beneath Oceanic Lithosphere (e.g. Appennine-type boudinaged belt and prism, Figure 6.3. panel C),
- Westward Subduction of Continental beneath Continental Lithosphere (e.g. Carpathian-type boudinaged belt and prism, Figure 6.3. panel D),
- Eastward Intraoceanic Subduction (e.g. Andaman-type intraoceanic prism, Figure 6.3. panel E),
- Eastward Subduction of Oceanic beneath Continental Lithosphere (e.g. Andean-type cordillera, Figure 6.3. panel F),
- Eastward Subduction of Continental beneath Oceanic Lithosphere (e.g. Oman-type obduction orogen, Figure 6.3. panel G),
- Eastward Subduction of Continental beneath Continental Lithosphere (e.g. Alpine-type collision orogen, Figure 6.3. panel H).

We focus our attention on westward subduction of the Atlantic Plate beneath the Caribbean Plate (Weber et al., 2001) since the middle Eocene and the formation of Barbados accretionary prism developing in the frontal part of the Lesser Antilles arc-trench system (westward subduction of oceanic beneath continental Lithosphere) and on the south Asia convergent plate margin, including the Himalayan orogen produced by continental collision in the west (Eastward Subduction of Continental beneath Continental Lithosphere) and the Sunda arc trench system produced by oceanic subduction in the east (Eastward Subduction of Oceanic beneath Continental Lithosphere).

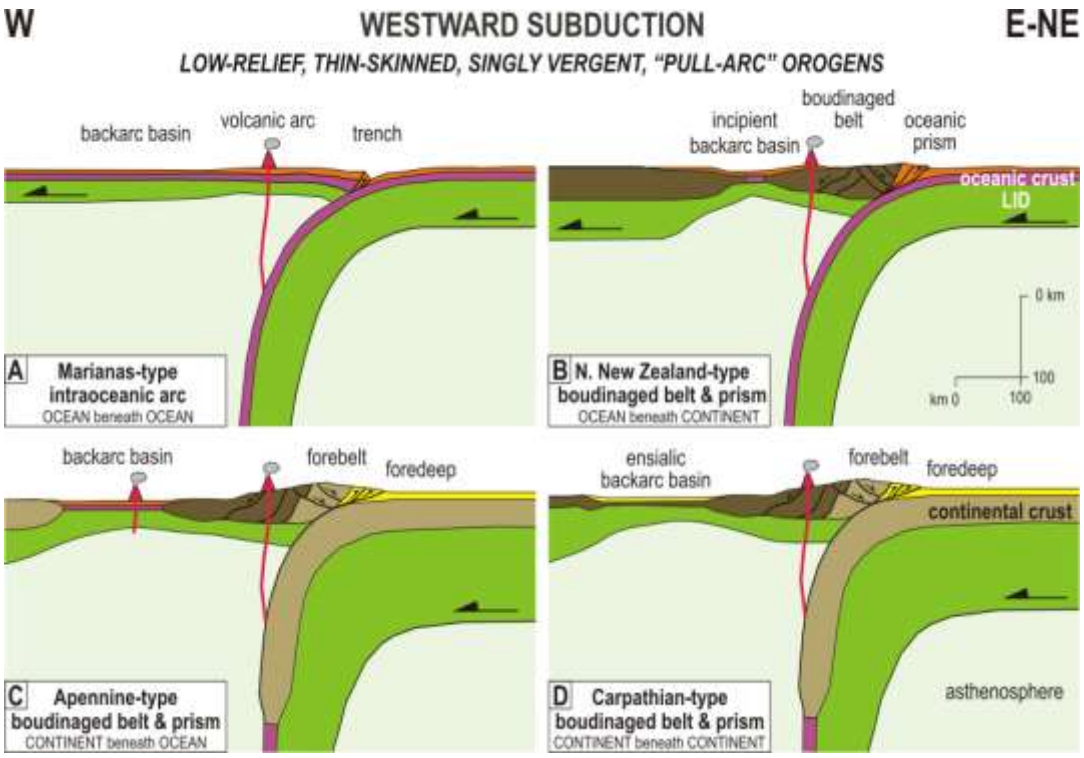

Figure 6.2. *The four cartoons illustrate different styles of orogenic deformation for the four identified scenarios of westward subduction (Garzanti et al., 2008 modified).*

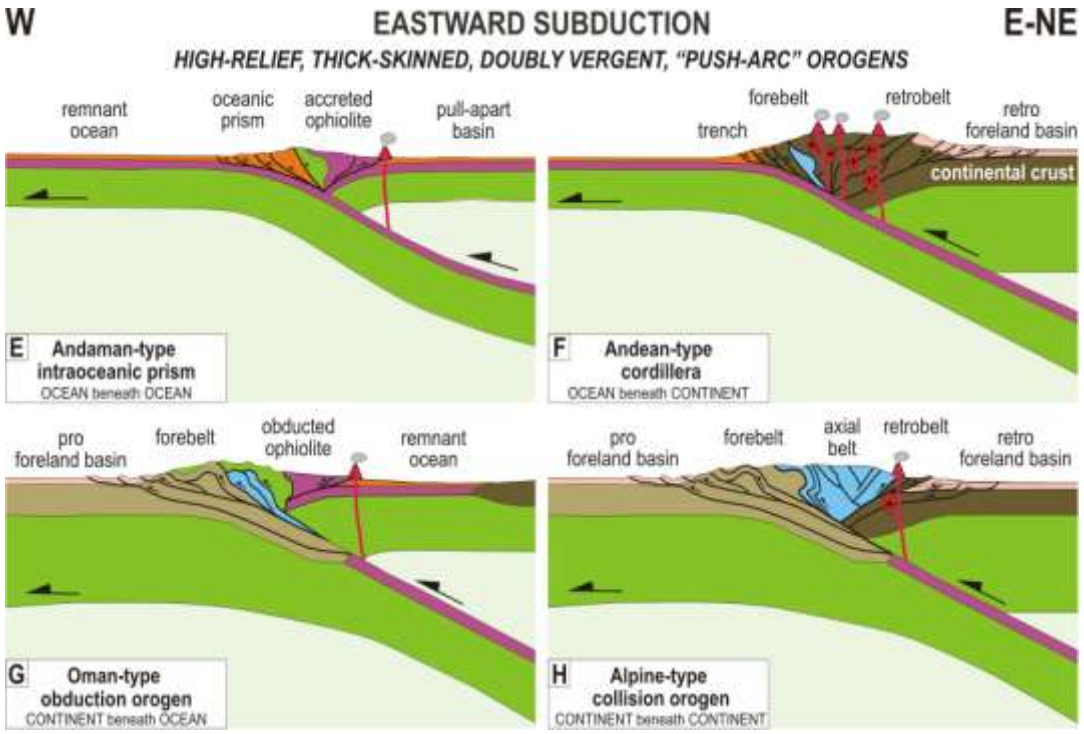

Figure 6.3. *The four cartoons illustrate different styles of orogenic deformation for the four identified scenarios of eastward subduction (Garzanti et al., 2008 modified).*

6.1. Provenance studies of modern sediments in subduction complexes.

Sediments sourced in large orogenic belts generated by oceanic or continental subduction are conveyed long-distance by major river systems crossing foreland basins, and eventually supplied to continental margins at specific deltaic or estuarine entry points (Potter, 1978; Dickinson, 1988; Hinderer, 2012). Sediment transport may continue via turbidity currents for hundreds to thousands of kilometers beyond the river mouth, and huge masses of sediment are thus transferred from the continent to the deep ocean (Ingersoll et al., 2003).

This typically occurs along the trend of high-relief major Himalayan-type continent–continent collision zones, where huge turbiditic successions accumulate on remnant-ocean floors that are fated to be subsequently subducted, while their clastic cover is detached and progressively accreted at the front of a growing fold-thrust belt (e.g., Indo-Burman Ranges; Morley et al., 2011).

When subduction complexes are tectonically uplifted and are large enough to be exposed subaerially they can become themselves sources of clastic detritus (Dickinson, 1988; Ingersoll et al., 2003; Morley et al., 2011).

Recycling of clastic rocks may occur extensively in plate tectonic settings (cratons, rifted margins, arc-trench-system and orogenic belts), but recycling of clastic rocks occurs systematically and at a larger scale in subduction complexes.

In chapters 7 and 8 two studies in sediment formation and recycling at convergence plate boundaries are shown.

Chapter 7 shows south Asia as the archetype example of such a convergent plate margin, including the Himalayan orogen produced by continental collision in the west and the Sunda arc trench system produced by oceanic subduction in the east (Hall and Smyth, 2008). Deep-sea fan turbidites largely fed from erosion of the mighty Himalayas, offscraped along the Indo-Burma–Sunda trench, are accreted to the Indo-Burman subduction complex and its southern prolongation, exposed on land in the Andaman–Nicobar Islands and beyond (Moore et al., 1982; Curray et al., 2003; Maurin and Rangin, 2009; Cochran, 2010).

Chapter 8 presents the geologically and geometrically distinct case of the Caribbean accretionary prism. Here detritus generated in the Andean Cordillera and carried along the Andean retro-belt basin by the Orinoco River finally reaches the transpressional setting of

Trinidad and is deposited via turbidity currents on Atlantic oceanic floors subducting towards the west beneath the Caribbean Plate (Velbel, 1985). Varied and complex trajectories in space and time are thus followed during multistep sediment transfer along and across convergent plate boundaries (Zuffa, 1987; Zuffa et al., 2000).

These two places, where a large accretionary prism is subaerially exposed, are the best suited natural laboratory in which investigate sediment formation and recycling at convergent plate margins. Only by thoroughly studying modern environments, where source-to-sink complexities can be physically traced and understood, can we acquire the necessary experience and sharpen our conceptual tools to solve the provenance conundrums posed by ancient clastic successions, where the original geometry of converging plates has been effaced by subsequent geological evolution. These studies also allow us to redefine the diagnostic mark of Subduction Complex Provenance as quite distinct from the original definition by Dickinson and Suczek (1979).

7. Sediment recycling at convergent plate margins (Indo-Burman Ranges and Andaman–Nicobar Ridge)

published in Earth-Science Reviews, v. 123, p. 113-132. "Sediment recycling at convergent plate margins (Indo-Burman Ranges and Andaman–Nicobar Ridge) " by Eduardo Garzanti, Mara Limonta, Alberto Resentini, Pinaki C. Bandopadhyay, Yani Najman, Sergio Andò, Giovanni Vezzoli.

7.1. Introduction

Recycling of clastic rocks may occur extensively in any plate tectonic setting, including stable cratons, rifted margins, arc-trench systems and orogenic belts. But nowhere on Earth sediment recycling occurs systematically and at a larger scale than in subduction complexes, where huge volumes of detritus shed from adjacent orogens, temporarily stored in remnant-ocean basins and subsequently rafted towards a subduction zone, are finally uplifted tectonically to become themselves sources of clastic detritus (Dickinson, 1988; Ingersoll et al., 2003; Morley et al., 2011). South Asia hosts the archetype example of such a convergent plate margin, including the Himalayan orogen produced by continental collision in the west and the Sunda arctrench system produced by oceanic subduction in the east (Hall and Smyth, 2008). Deep-sea fan turbidites largely fed from erosion of the mighty Himalayas, offscraped along the Indo-Burma–Sunda trench, are accreted to the Indo-Burman subduction complex and its southern prolongation, exposed on land in the Andaman–Nicobar Islands and beyond (Moore et al., 1982; Curray et al., 2003; Maurin and Rangin, 2009; Cochran, 2010). The eastern side of the Bengal Basin and Bengal Sea, extending across the tropical zone from 27°N in Assam to 7°N in Great Nicobar, thus appealed to us as the best suited natural laboratory in which to investigate sediment recycling at convergent plate margins (Figure 7.1.). In the present paper we challenge one of the thorniest problems in clastic petrology, that of sediment recycling, by studying the petrography and mineralogy of modern fluvial to beach sands derived from the Indo-Burman–Andaman–Nicobar accretionary prism, integrated with analyses of sandstone clasts and of Cenozoic parent sandstones exposed from Bangladesh to the Andaman Islands (Allen et al., 2007, 2008; Najman et al., 2008, 2012). Such a complete dataset allowed us to unravel the complex paths of multistep and

multicyclic sediment transfer along and across a classical example of convergent plate boundary (Ingersoll and Suczek, 1979; Moore, 1979; Velbel, 1985; Zuffa, 1987), and to obtain valuable information for a correct provenance diagnosis of terrigenous successions deposited in sedimentary basins associated with arc–trench systems and collision orogens.

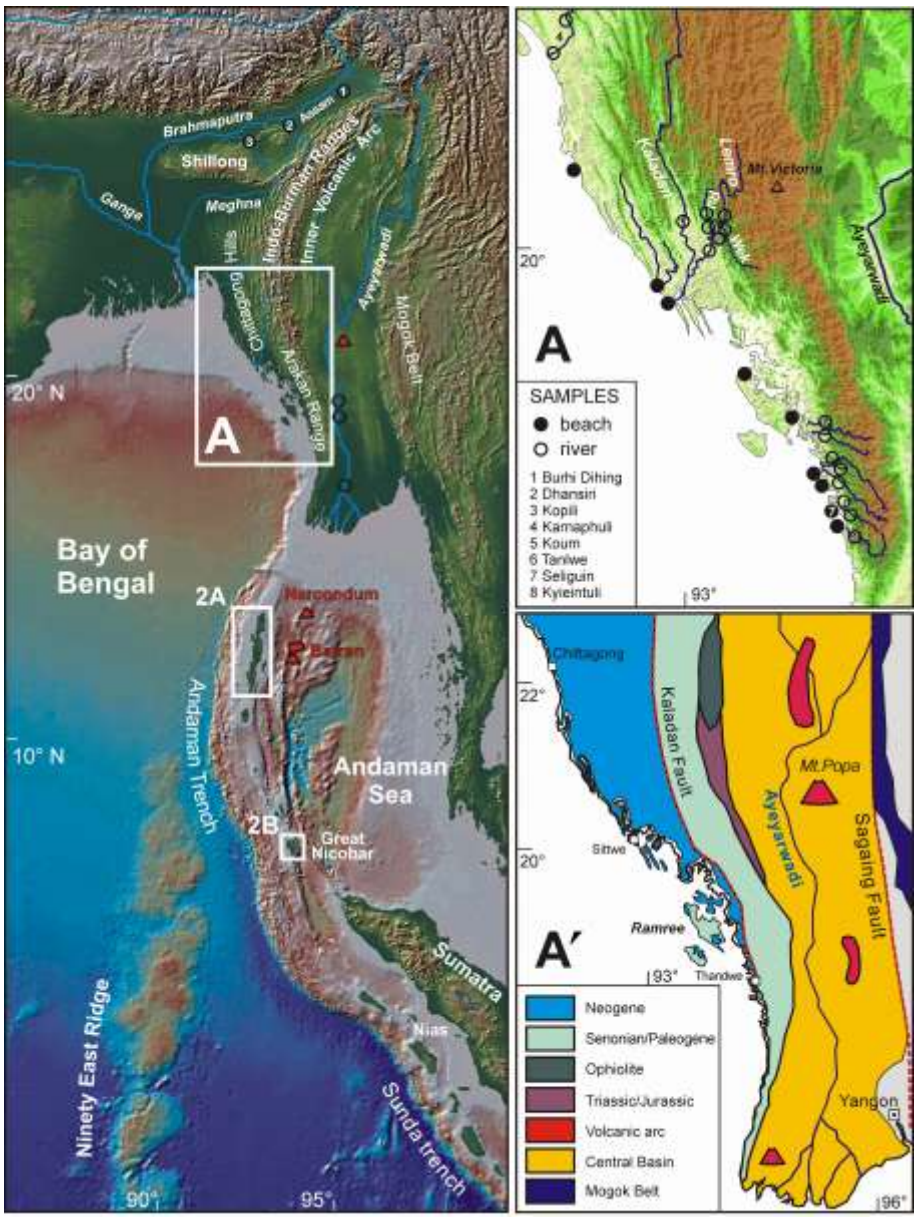

Figure 7.1. *The Indo-Burman collision zone. The Indo-Burman Ranges and the Andaman–Nicobar Ridge formed by tectonic accretion above the Arakan–Andaman trench, connecting southward to the Sunda trench. Note the occurrence of active (Barren Island) and dormant (Narcondum) volcanoes in the Andaman Sea, representing the southward prolongation of the late Cenozoic Burma volcanic arc (Stephenson and Marshall, 1984). A) Topography of the Chittagong Hills and Arakan Range with location of sampling sites in coastal Bangladesh and Myanmar. A') Geological sketch map of the Chittagong Hills and Arakan Range.*

7.2. The Indo-Burman–Andaman–Nicobar (IBAN) subduction complex

Active margins extend for over 30,000 km around the world, and huge piles of sedimentary rocks, deformed by continuing accretion and shale diapirism, are stored in their associated, wedge-shaped subduction complexes. New material is progressively accreted to the thin outer end of the wedge, while its oldest and thickest inner part can be thickened further, increased in volume by underplating, and consequently uplifted and exposed to form a chain of islands (Morley et al., 2011). Complex tectonic deformation with multiple episodes of folding and thrusting can be explained by critical taper theory (Dahlen, 1990), where outof-sequence faulting is necessary to keep thickening the internal part of the wedge so oceanward propagation of the thrust front can continue (Platt, 1986). Typically, the older, deeper parts of the accretionary prism have been exhumed in the islands. Out-of-sequence thrusting may also signify the onset of significant lithification, which permits slip to occur along discrete large-scale blocks (Moore et al., 2007).

7.2.1. The Indo-Burman Ranges

The eastern, inner part of the N–S trending Indo-Burman Ranges is composed primarily of Upper Cretaceous to Paleogene deep-water sediments and mélange containing blocks of gabbro, pillow basalt, serpentinite, chert, limestone and schist (Brunnschweiler, 1974; Mitchell, 1993). The western, outer part of the wedge consists instead of largely Neogene fluvio-deltaic sediments and turbidites primarily sourced from the Ganga–Brahmaputra river system and folded from the late Miocene to the recent (Figure 7.1.; Sikder and Alam, 2003). The accretionary prism developed initially as a result of N to NE-ward subduction of the Neotethys Ocean. Cretaceous to Paleogene deformation involved ophiolite obduction, uplift and erosion (Bhattacharjee, 1991; Acharyya, 2007), until collision of India with Eurasia and coupling with NW Burma terminated the early accretionary history (Morley, 2012). After collision, India has undergone highly oblique convergence with SE Asia, and is presently moving ~35 mm/a northwards relative to Sundaland. This motion is accommodated by distributed deformation on numerous faults across the Burma microplate, of which the dextral Sagaing Fault is the largest (Figure 7.1.; Vigny et al., 2003). Continuing growth of the

accretionary prism is fueled by active subduction beneath Bangladesh and western Myanmar, where the outer wedge is up to 150 km wide and covers onshore and offshore areas on oceanic crust (Steckler et al., 2008). In the north, sediments of the Ganga–Brahmaputra estuary, supplied by rapid erosion of the Himalaya, have prograded ~400 km off the Indian continental margin since the Eocene. Subducting oceanic lithosphere is thus covered by a sediment pile up to 20 km-thick at its northern edge (Curray et al., 2003). The Chittagong Hills fold belt of coastal Bangladesh consists of a >3 km-thick Neogene succession of turbidites, passing upward to shelfal and fluvio-deltaic deposits (Gani and Alam, 2003). By the late Miocene, the area was undergoing braidplain deposition, and folding developed in a continental environment. Much of the outer wedge presently exposed along coastal Myanmar, instead, still lay in deep water during the Pliocene, and folding took place only during the last 2 Ma. Due to a combination of tectonic uplift and infilling by southward progradation of the Bengal Fan, together with lesser input from the Indo-Burma Ranges in the east, the outer wedge has grown rapidly in the Quaternary, and its northern 550 km presently lies either in shallow water or onshore (Maurin and Rangin, 2009). The fold–thrust belt progressively narrows towards the south, until it is only 20 km-wide and composed of just 2–3 folds along a narrow slope bounded by a major transpressional fault in the west. Such a change in structural style indicates that deformation becomes increasingly focused offshore, on the oblique dextral Andaman subduction zone. Plate convergence, fully partitioned across the whole Burma microplate in the north, is taken up in equal amounts by the Andaman subduction zone and the Sagaing–W Andaman fault system near North Andaman (Nielsen et al., 2004). The Indo-Burman Ranges have a humid tropical climate. The summer monsoon brings heavy rains from June to September, whereas the winter season is mostly dry. Average annual rainfall exceeds 1.5 m and reaches as high as 5 m locally at the mountain front. Temperatures, warm throughout the year, range from 15 °C to 35 °C in summer and seldom drop below 4 °C in winter, although frost is common in the mountains. Devastating cyclones may form on the Bengal Sea during summer, with surging waves bringing huge damage and life losses to coastal Bangladesh (~500,000 casualties in September 1970). The Naga Hills, largely covered by wooded forest rich in flora and fauna, rapidly rise from the Brahmaputra Valley in Assam to ~600 m and more, reaching 3826 m a.s.l. at Mount Saramati in the southeast. Drainage is characterized by long fault controlled segments running parallel to structural strike, with shorter transversal tracts cutting across the axes of anticlines. The largest rivers are the Dhansiri in the north and the Kaladan in the south, with a length of ~350 km and a drainage area of ~30,000 km^2. The Arakan Range farther south acts as a barrier to humid air masses from the southwest, which bring

thunderstorms almost every day during the monsoon season, making their western slopes extraordinarily wet with >1 m of rain per month. The eastern slopes are much drier, and the central plain crossed by the Ayeyarwadi River (length ~ 2000 km, area ~ 400,000 km^3, annual sediment load ~ 330 10^6 tons) receives only 0.5–1 m of rain annually. The highest mountains, reaching 3053 m a.s.l. at Victoria peak in the north, are covered by winter snow.

7.2.2. The Andaman–Nicobar Ridge

Flanked by the Bay of Bengal on the west and the Andaman Sea on the east, the N/S trending arcuate Andaman–Nicobar archipelago includes 324 islands, covering 8249 km^2 land area and extending for ~700 km with a maximum width of ~31 km (Figure 7.2.). This outer ridge, characterized by numerous mud volcanoes, connects the Arakan Range of western Myanmar to the outer ridge of the Sumatran arc trench system, culminating in the Nias and Mentawai Islands (Samuel et al., 1997; Pal et al., 2003).

The Andaman–Nicobar subduction complex is forming above the W Sunda subduction zone due to oblique convergence between the Indo-Australian Plate and Eurasia (Guzman Speziale and Ni, 1996; Nielsen et al., 2004). Seismic sections outline an imbricate stack of E-dipping, W-vergent fold–thrust packets, capped by ophiolites along the eastern margin of Andaman and Nicobar (Roy, 1992). Farther to the east, the arc-trench system is delimited by a major composite dextral transform system, including the Sagaing Fault onland Myanmar and the Great Sumatran Fault in the south (Cochran, 2010). Between the two lies the Andaman Sea, a pull-apart basin which opened obliquely and stepwise since ~32 Ma, with active seafloor spreading recorded in the last ~4 Ma (Raju et al., 2004; Curray, 2005; Khan and Chakraborty, 2005). The active Barren Island and dormant Narcondum Island volcanoes, respectively characterized by basaltic to basaltic andesite and by andesite to dacite products, are part of the magmatic arc extending from Myanmar to Sumatra (Figure 7. 1.; Pal et al., 2007, 2010; Sheth et al., 2009).

The Andaman Islands include two contrasting geological domains (“Chaotic and Coherent terranes” of Bandopadhyay, 2012) separated by the Jarwa Thrust (Figure 7.2.). The Chaotic terrane, including obducted ophiolites and Mithakhari mélange, extends along the eastern side of South and Middle Andaman, covers the entire width of North Andaman, and occurs locally along the eastern margin of Great Nicobar. The Coherent terrane extends as thin strips along the western margin of Middle Andaman, becomes thicker and tectonically interleaved with slices of ophiolites and Mithakhari mélange in South Andaman, and covers

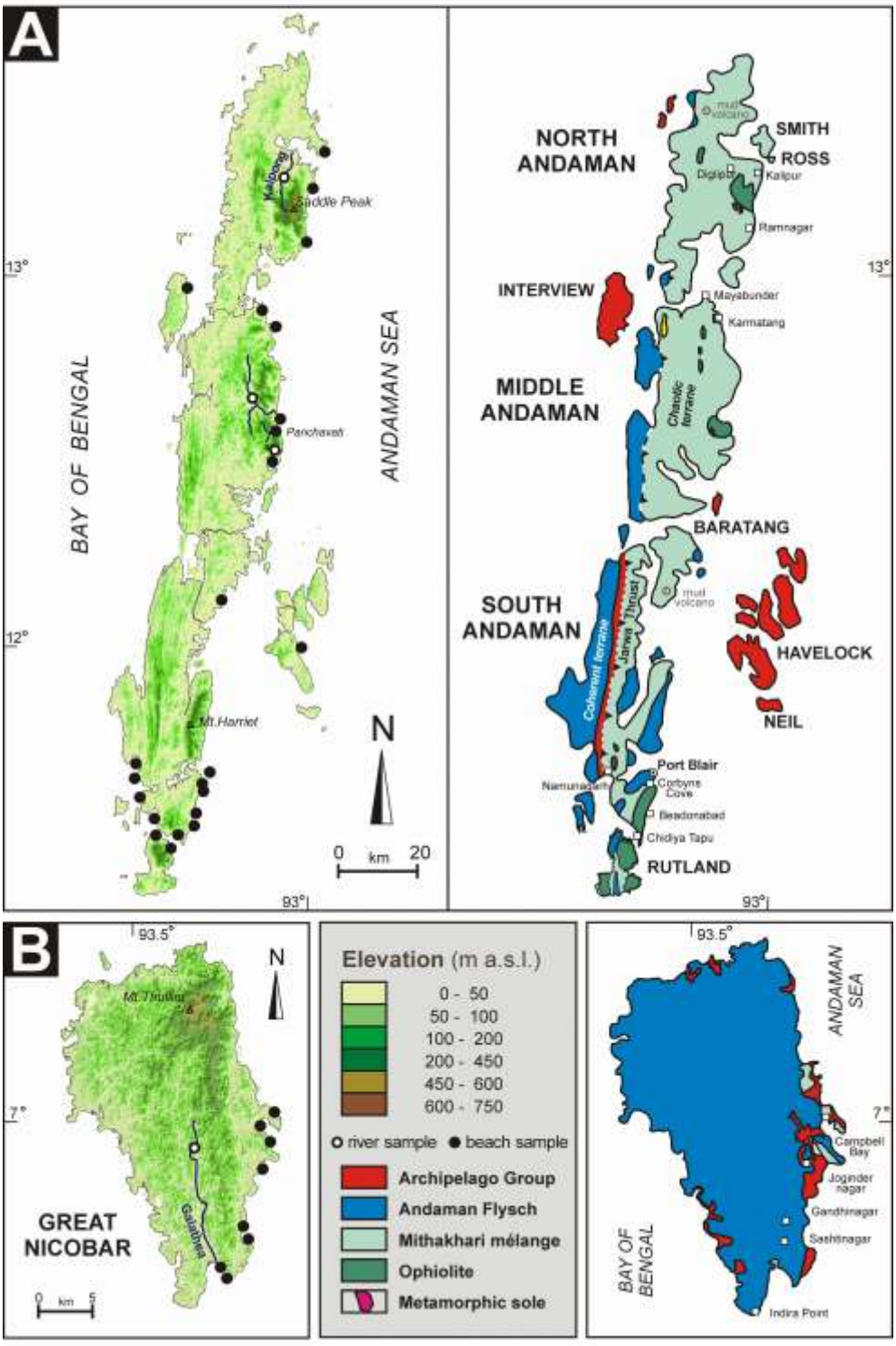

Figure 7.2. *The emergent Andaman–Nicobar subduction complex. A) Topography and geological sketch map of the Andaman Islands, with location of sampling sites. Mélange units cover most of Middle and North Andaman; ophiolites are exposed mainly along the eastern side, the Andaman Flysch mainly along the western side. Mio-Pliocene limestones, clastics and tuffs are exposed in minor islands on both sides. B) Topography and geological sketch map of Great Nicobar, with location of sampling sites. The Andaman Flysch is widely exposed; scattered outcrops of mélange units and Neogene strata occur along the coast.*

most of Great Nicobar. It consists of a regionally extensive succession of faulted and sheared turbiditic sandstones and mudrocks (Andaman Flysch). This distribution of geological units has been shown by drilling to continue offshore, with thick turbidites on the western side of North Andaman and chaotic assemblages off the east coast of Middle and North Andaman (Roy and Das Sharma, 1993).

The tectonically dismembered Andaman ophiolites include mantle harzburgites and crustal cumulates, gabbros, rare plagiogranites, sheeted dykes, basaltic pillow lavas and an andesite–dacite volcanic suite, overlain by lenses of multicolored mudrocks and radiolarian chert of Late Cretaceous to Paleocene age (Pal, 2011). South Andaman plagiogranites yielded late Cenomanian zircon U–Pb ages (95 ± 2, Pedersen et al., 2010; 94 ± 1 Ma, Sarma et al., 2010), similar to those of peri-Arabian ophiolites formed above subduction zones from Cyprus to Oman (Moores et al., 1984; Searle and Cox, 1999). This suggests that forearc spreading shortly followed the latest Albian/Cenomanian onset of subduction along the entire southernmargin of Eurasia (Garzanti and Van Haver, 1988; Pedersen et al., 2010).

Along the eastern side of the islands, the contact with the ophiolite is marked by heterogeneous blocks in sheared argillite matrix, including chertified marble, quartzite and garnet-bearing or actinolite chlorite schists, interpreted either as remnants of an older continental margin or as formed during low-grade, subduction-zone metamorphism possibly as the ophiolite sole (Sengupta et al., 1990; Pal and Bhattacharya, 2010). Limestone, chert, ophicalcite and sandstone also occur. The Mithakhari Group is a mélange unit generally described as including sediment-gravity flows deposited in an arc trench system, although the deformation may be largely ascribed to shale diapirism (Barber, 2013). The rarely exposed Lipa Black Shale is overlain by the Hope Town Conglomerate and volcaniclastic Namunagarh Grit, interbedded with foraminiferal limestones dated as late Paleocene to Eocene (Karunakaran et al., 1968). Petrographic and paleocurrent data suggest supply from an active volcanic arc, which prior to opening of the Andaman Sea was most likely located in coastal Myanmar (Bandopadhyay, 2005).

The unfossiliferous Andaman Flysch is largely ascribed to the Oligocene, with flute casts indicating southward sediment transport (Chakraborty and Pal, 2001). Most of Great Nicobar is composed of ≤5 km-thick Andaman Flysch, largely represented by distal turbiditic mudrocks (Karunakaran et al., 1975). The unconformably overlying Miocene–Pliocene Archipelago Group, widely exposed on Havelock and Interview Islands, includes bioclastic limestones, calcareous sandstones, marls, foraminiferal oozes and reworked felsic tuffs reflecting active volcanism (Pal et al., 2005). Folding of Archipelago Group strata took place during post-Pliocene uplift of the islands.

Climate in the Andaman–Nicobar Islands is tropical humid, with ~3 mm of annual rainfall mostly received during the southwest summer monsoon. Perennial streams (Kalpong in North Andaman, Galathea in Great Nicobar) flow along the regional north–south structural trend. The western coastline is fairly straight and gentle, whereas the eastern coastline is strongly indented and steep, with sandy beaches between headlands. Gravelly beaches occur where streams carry coarse sediments from high relief near the coast. Resistant ophiolitic or turbidite rocks form rugged mountains with steep slopes deeply incised by stream valleys. Saddle Peak, made of harzburgites and gabbros, reaches 732 m a.s.l. in North Andaman. The N/S trending ridges of Andaman Flysch peak at 360 m a.s.l. in South Andaman (Mt. Harriet) and at 642 m a.s.l. in Great Nicobar (Mt. Thullier). The Mithakhari mélange stands out as hills of moderate to low relief. Neogene formations exposed on offshore islands have very low relief surrounded by coral reefs and shallow seas.

7.3. Sampling and analytical methods

In order to investigate the compositional variability of sediments derived from the IBAN accretionary prism and the incidence of various controlling factors such as weathering, mechanical abrasion, hydraulic sorting and recycling, EG, YN and PCB collected 60 sand samples on active river bars and beaches from coastal Bangladesh, Andaman Islands and Great Nicobar during several expeditions between January 2005 and March 2010. We also collected 9 coarse sands to fine gravels and 4 silty sands from fluvial bars and levees of Arakan rivers, 1 ash fall layer during eruption of the Barren Island volcano, and 4 bar sands and 3 levee silty sands from the final 300 km of the Ayeyarwadi (Irrawaddy) River between Pyay and Yangon.

Our sample set was completed by 5 sands from beaches on other islands of the Andaman archipelago and 3 sands from rivers in Assam (NE India) kindly provided by other researchers.

Bulk-sand samples were impregnated with araldite, cut into standard thin sections, stained with alizarine red to distinguish dolomite and calcite, and analyzed by counting 400 points under the petrographic microscope (Gazzi–Dickinson method; Ingersoll et al., 1984). In order to better understand provenance and compositional variability of Arakan river sediments, we also counted 400 points on the 80–125 μm class obtained by dry-sieving from 3 levee samples, 150–200 granules on the 1–4 mm class of 8 coarse-sand samples, 300 points

within each of 5 sandstone pebbles from Lemro River gravel, and ≤ 300 points within each of 19 representative sandstone granules fromcoarse-sand samples of 3 southern Arakan rivers. Finally, in order to get indirect information on rocks exposed on Great Nicobar, we counted ~100 granules on the > 1 mm class of 2 coarse-sand samples, and ~50 points within each of 5 representative sandstone granules. Metamorphic grains were classified according to protolith composition and metamorphic rank. Average rank for each samplewas expressed by the Metamorphic Indices MI and MI*, which vary respectively from 0 (in detritus shed by exclusively sedimentary and volcanic cover rocks) or from 100 (in very-low-rank detritus shed by exclusively very low-grade metamorphic rocks) to 500 (in very-high-rank detritus shed by exclusively high-grade basement rocks; Garzanti and Vezzoli, 2003). Following a simple nomenclature scheme, sands were classified according to their main components (Q = quartz; F = feldspars; L = lithic fragments), considered if exceeding 10% QFL and listed in order of abundance (e.g., in a litho-feldspatho-quartzose sand Q > F > L > 10% QFL); an adjective reflecting the most common rock-fragment type may be added (e.g., volcaniclastic). Heavy-mineral analyses were carried out on a quartered aliquot of the 32–355 or 63–250 μm class of 67 sand samples and 3 coarse–silt to very-fine-sand-sized levee samples. Ayeyarwadi levee samples were analyzed in bulk. One fine-grained and well-sorted Ayeyarwadi sand sample was sieve-split into 0.5 φ classes, analyzed separately for both heavy minerals and bulk petrography. Heavy minerals were separated by centrifuging in sodium metatungstate (density ~ 2.90 g/cm^3), and recovered by partial freezing with liquid nitrogen. On grain mounts, ~200 transparent heavy-mineral grains were counted by the area method (Mange and Maurer, 1992). Dubious grains were checked by Raman spectroscopy (Andò and Garzanti, 2013). Diverse indices based on minerals that better resist diagenetic dissolution were used to trace provenance of recycled sand. The ZTR index (sum of zircon, tourmaline and rutile over total transparent heavy minerals; Hubert, 1962) defines the “mineralogical stability” of the detrital assemblage. The CZi and GZi indices (% Cr-spinel in total Cr-spinel plus zircon and % garnet in total garnet plus zircon; Morton and Hallsworth, 2007) provide information on the occurrence of ultimate mafic/ultramafic and metasedimentary versus felsic igneous sources, respectively. The Metasedimentary Mineral Index MMI (varying from 0 in detritus from low-grade rocks yielding chloritoid, to 50 in detritus from medium-grade rocks yielding staurolite, kyanite or andalusite, to 100 in detritus from high-grade rocks yielding sillimanite) estimates the average metamorphic grade of ultimate metasedimentary sources (Andò et al., 2013). Heavy-mineral concentration was calculated as the volume percentage of total (HMC) and transparent (tHMC) heavy minerals (Garzanti and Andò, 2007a). Heavy-mineral suites are defined as “extremely poor” (HMC >0.1), “very

poor" (0.1 ≤ HMC < 0.5), "poor" (0.5 ≤ HMC < 1), "moderately poor" (1 ≤ HMC < 2), "moderately rich" (2 ≤ HMC < 5), "rich" (5 ≤ HMC < 10), "very-rich" (10 ≤ HMC < 20) and "extremely rich" (20 ≤ HMC ≤ 50). Heavy-mineral-dominated placer sands (HMC > 50) also occur locally. Significant minerals are listed in order of abundance throughout the text.
Petrographic and heavy-mineral analyses were carried out by GV, AR, SA and ML at the University of Milano–Bicocca. Detailed information on location and provenance of modern-sand samples, and the complete bulk-petrography and heavy-mineral datasets for modern sands, Cenozoic sandstones, and sandstone pebbles and granules contained in modern sediments are provided in Appendix Tables A4 to A9.

7.4. Petrography and mineralogy of Cenozoic sandstones

Understanding the detrital modes of recycled sands is facilitated when we know the composition of their parent siliciclastic units. In this section we thus summarize the petrographic and heavy-mineral signatures of sandstones exposed along the IBAN intraocenic prism from Bangladesh to the Andaman Islands, investigated in several previous studies by the same operators and with the same analytical methods (Allen et al., 2007, 2008; Najman et al., 2008, 2012). Detrital modes of Paleogene turbidites exposed in the Arakan Range and on Great Nicobar could be obtained only indirectly from pebble and granule counts. The composition of Bengal Fan turbidites and of modern Ayeyarwadi River sand and silt (considered as a proxy of deep-sea turbidites for which data are not available) is also briefly described.

7.4.1. Cenozoic sandstones of the Bengal Basin

Sandstone composition changes through the thick Cenozoic Bengal Basin succession from quartzose for the Paleocene–Eocene Tura, Kopili and basal Barail Formations, to litho-quartzose metamorphiclastic for Oligocene Barail sandstones and finally feldspatho-litho-quartzose metamorphiclastic for the Miocene Bhuban and Boka Bil, Pliocene Tipam, and Pleistocene Dupi Tila Formations (Figure 7.3.; Najman et al., 2008, 2012). The Paleocene–

Eocene units, extremely poor to very poor heavy-mineral suites consist of tourmaline, zircon, titanium oxides and turbid grains, indicating complete dissolution of unstable species.

Heavy-mineral concentration and variety increase progressively upward. Barail sandstones may include chloritoid and staurolite, and Bhuban sandstones chloritoid, garnet, epidote, apatite, hornblende and titanite. Less stable species increase further in the poor to moderately poor suites of Boka Bil and Tipam sandstones, locally epidote dominated and including hornblende, garnet, staurolite, chloritoid, kyanite and occasionally sillimanite. Finally, moderately-poor to rich Dupi Tila suites are dominated by amphibole and epidote, associated with garnet, chloritoid, staurolite, kyanite and sillimanite. Inferred burial depths range from over 3 km for the Barail to less than 1 km for the Dupi Tila (Andò et al., 2012).

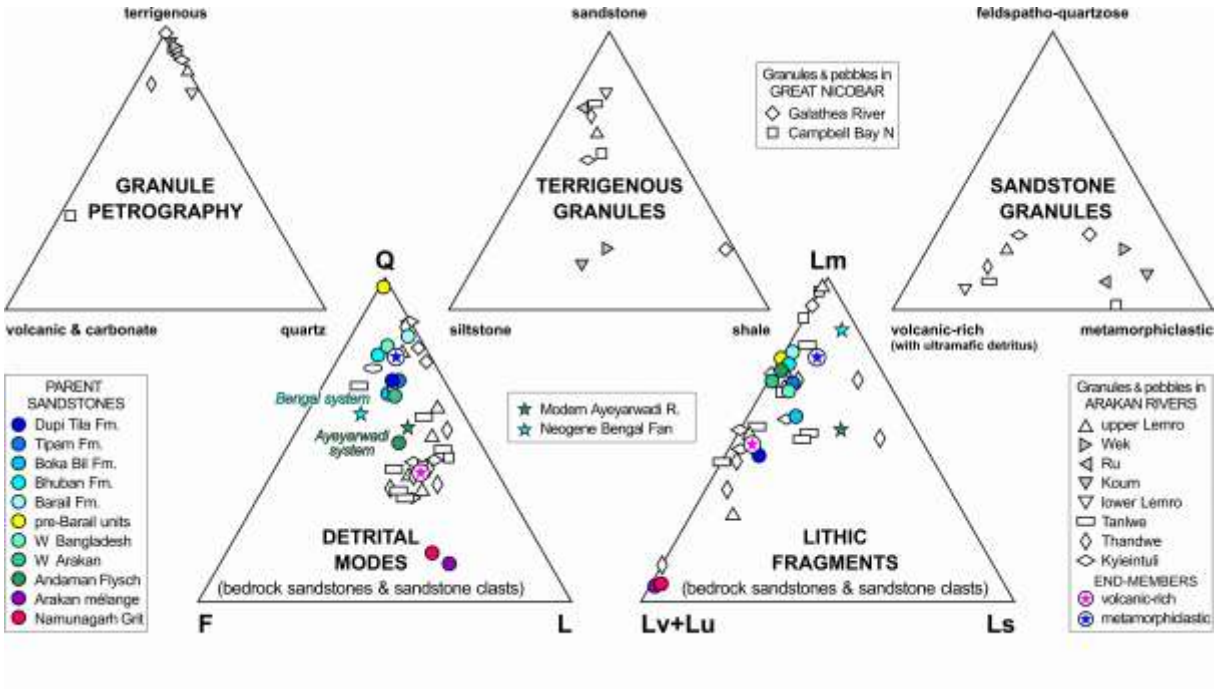

***Figure 7.3**. Clast petrography and composition of bedrock sandstones in the Indo-Burman–Andaman–Nicobar subduction complex. Arakan rivers carry pebbles and granules mostly derived from turbiditic source rocks. Two types of parent sandstones can be distinguished. Dominant in upstream reaches are feldspatho-quartzo-lithic to feldspatholitho- quartzose volcanic-rich clasts with minor chert and serpentinite grains (Figure 7.4.A), indicating ultimate provenance from the Burma active margin. Litho-quartzose metamorphiclastic clasts with composition similar to Barail-type Eohimalayan sandstones (Figure 7. 4.B) become common and locally dominant in the frontal part of the Arakan Range. Neohimalayan Bengal Fan sands (Ingersoll and Suczek, 1979) are closer to the metamorphiclastic end-member, whereas the Andaman Flysch exposed in E South Andaman (representing an Oligocene paleo-Ayeyarwadi deep-sea fan; Allen et al., 2007) is closer to the volcanic-rich end-member, thus reflecting additional contributions from the Burma arc. Detrital modes of parent-sandstone units from Bangladesh and Arakan (Allen et al., 2008; Najman et al., 2008) are plotted for comparison. Q = quartz; F = feldspars; L = lithic fragments (Lv = volcanic; Lu = ultramafic; Lm = metamorphic; Ls = sedimentary).*

7.4.2. Neogene turbidites of the Bengal Fan and Ayeyarwady River sediments

Himalayan-derived Bengal Fan sands are mostly litho-feldspathoquartzose metamorphiclastic (Ingersoll and Suczek, 1979). Amphibole dominated suites include pyroxene in the uppermost 100 m, but ferromagnesian minerals tend to progressively dissolve in the first km downsection (corr. coeff. −0.77, sign. lev. 0.1%), and more stable tourmaline, epidote and garnet are thus relatively enriched (Thompson, 1974). Upper Miocene strata still contain ferromagnesian minerals, but pyroxene first and amphibole next disappear in the Lower Miocene, where staurolite and kyanite persist, garnet becomes more abundant than epidote, and zircon, tourmaline, rutile and apatite increase relatively (Yokoyama et al., 1990).

Sediments supplied today by the Ayeyarwadi River to the Andaman Sea are feldspatho-litho quartzose metamorphiclastic, with mainly felsic volcanic/metavolcanic, chert, shale/slate to siltstone/metasiltstone rock fragments, minor serpentinite grains and micas. Rich amphibole–epidote suites include garnet, pyroxenes, titanite, and rare chloritoid and kyanite. Composition is similar to Ganga–Brahmaputra sediments (Garzanti et al., 2010a, 2011), with more detritus from sedimentary and volcanic cover rocks and less from high-rank metamorphic rocks, as indicated by lower Metamorphic Index (MI 100 ± 25 vs. 270 ± 20). Ayeyarwadi heavy-mineral suites are consequently less rich, relatively high in stable zircon, tourmaline, rutile, Cr-spinel and lowgrade minerals (epidote, chloritoid), and poorer in medium/high-grade minerals (garnet, staurolite, sillimanite, amphiboles).

7.4.3. Neogene sandstones of Bangladesh and coastal Arakan

Neogene sandstones exposed in the Chittagong Hills are lithoquartzose to litho-feldspatho-quartzose metamorphiclastic (Figure 7.3.; Allen et al., 2008). Poor to moderately poor suites include garnet, tourmaline, apatite and chloritoid, which are more common in Miocene sandstones, and epidote, staurolite and kyanite, which are more common in Plio-Pleistocene sandstones. Epidote decreases and amphibole progressively disappears downsection, indicating diagenetic dissolution at burial depths exceeding 2 km (Andò et al., 2012).

Neogene sandstones exposed in northern coastal Arakan are feldspatho-litho-quartzose to litho-feldspatho-quartzose metamorphiclastic, with metapelite/metapsammite rock fragments,

micas and subordinate felsic to microlitic volcanic/subvolcanic/metavolcanic grains, indicating Himalayan provenance with minor supply from a magmatic arc. Besides aggregates of titanium oxides and turbid grains, very poor suites include tourmaline, garnet, apatite, zircon, rutile, chloritoid, epidote, titanite and Cr-spinel, indicating extensive diagenetic dissolution at burial depths exceeding 3 km.

7.4.4. Paleogene sandstones and sandstone clasts in the Arakan Range

Quartzo-feldspatho-lithic volcaniclastic sandstones exposed locally within Paleogene mélange in coastal Arakan consist chiefly of microlitic volcanic grains and plagioclase, indicating provenance from a largely undissected volcanic arc. Besides aggregates of titanium oxides and turbid grains, the very poor heavy-mineral suite contains only Cr-spinel, apatite, minor zircon, tourmaline and rutile, indicating complete diagenetic dissolution of less stable species.

Sandstone clasts collected in the farthest localities that we could reach upstream in the Lemro River and southern Arakan rivers provide us with information on the Upper Cretaceous to Paleogene turbidites exposed in the eastern part of the Arakan Range. They are mostly feldspatho-litho-quartzose to feldspatho-quartzo-lithic, with common plagioclase and rare K-feldspar, abundant felsic volcanic/metavolcanic and very-low to medium-rank metasedimentary rock fragments, minor chert, and strongly altered metabasite and ultramafite grains (Figure 7.4.A). This volcaniclastic/metasedimentaclastic signature reflects mixed provenance, including supply from a volcanic arc and ophiolites located along the Burma active continental margin in the east (“volcanic-rich endmember” in Figures. 7.3. and 7.4.A; Mitchell, 1993; Suzuki et al., 2004; Allen et al., 2008). Arakan river gravels also contain clasts of mudrocks, vein quartz and tuffite, as well as litho-quartzose metamorphiclastic sandstone clasts (“metamorphiclastic end-member” in Figures. 7.3. and 7.4. B) that become dominant in tributaries and shorter rivers draining only the western part of the range.

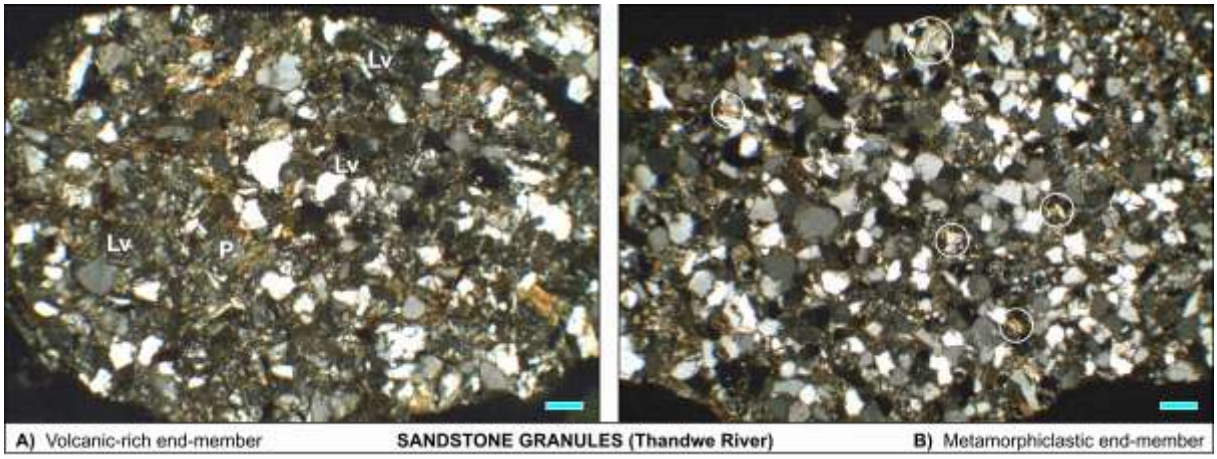

Figure 7.4. *Contrasting composition of sandstone clasts in southern Arakan river sands. A) Feldspatho-quartzo-lithic volcaniclastic granule 3197E, indicating provenance from a Burma derived Protohimalayan sandstone (P = plagioclase; Lv = volcanic lithics). B) Litho-quartzose metamorphiclastic granule 3197D, indicating provenance from a Barail-type Eohimalayan turbidite (encircled are micas and micaceous metasedimentary lithics). Photos with crossed polars; blue bar = 250 µm.*

7.4.5. Cenozoic sandstones and sandstone clasts in the Andaman and Nicobar Islands

Quartzo-feldspatho-lithic to feldspatho-lithic volcaniclastic Paleogene sandstones of the Namunagarh Formation exposed in South and North Andaman consist chiefly of plagioclase, felsitic, microlitic and lathwork volcanic grains, indicating provenance from a largely undissected volcanic arc. Chert, shale/slate, siltstone/metasiltstone and minor metabasite and serpentinite grains occur. Poor to moderately poor suites include clinopyroxene and epidote, with subordinate titanite, green–brown hornblende and Cr-spinel. Mineralogy and corrosion features indicate only moderate diagenetic dissolution.

Oligocene sandstones of the Andaman Flysch exposed along the east coast of South Andaman are litho-feldspatho-quartzose to feldspatholitho- quartzose metamorphiclastic with metapelite/metapsammite, mainly felsitic volcanic, and a few sedimentary rock fragments and micas, indicating provenance from a collision orogen with subordinate contributions from a volcanic arc (Figure 7.3.). Very poor to poor heavy mineral suites include Ti oxides, garnet, chloritoid, apatite, tourmaline, epidote, zircon, Cr-spinel and titanite. Corrosion features, absence of amphibole and partial resetting of apatite fission-track ages indicate burial depths of 3–4 km. More intense diagenetic dissolution than for the Namunagarh Formation is

consistent with the different depositional setting (basin-floor turbidites originally deposited onto the subducting Indian Plate and later accreted tectonically to the Andaman ridge versus Burma forearc basin above the subduction zone; Allen et al., 2007). Sandstone granules found in modern sands of Great Nicobar range from feldspatho-litho-quartzose and garnet bearing (Campbell Bay beach) to litho-quartzose and micaceous (Galathea River), with common low-rank metasedimentary and a few volcanic rock fragments (Figure 7.3.).

7.5. Modern sands from the IBAN subduction complex: a tale of multiple sources

Sands shed by the Indo-Burman–Andaman–Nicobar accretionary prism display a wide compositional range, reflecting mixing in variable proportions of detritus from mineralogically distinct source rocks (Figure 7.5.; Garzanti et al., 2007). These include a thick stack of deformed, largely turbiditic sandstones and mudrocks (Recycled Clastic Provenance), ophiolitic allochthons comprising both ultramafic mantle and mafic crustal rocks (Ophiolite Provenance), mélange units including volcaniclastic sandstones, as well as active or dormant volcanoes (Volcanic Arc Provenance). Siliciclastic detritus is mixed with subordinate calcareous allochems in beaches of coastal Bangladesh and northern Arakan, whereas bioclasts (mollusks, red algae, benthic foraminifera, corals, bryozoans, echinoderms, hydrozoans) are commonly overwhelming in beaches of the Andaman and Nicobar islands. Anomalously high heavy-mineral concentration in some South Andaman, Rutland and Nicobar beach samples, with local occurrence of chromite placers, resulted from selective entrainment effects, as revealed by systematic enrichment in ultradense Fe–Ti–Cr oxides, zircon and garnet (Garzanti et al., 2009).

Figure 7.5. *End-member sources of sand in the Indo-Burman–Andaman–Nicobar subduction complex. A) Shale/siltstone rock fragments (Ls) derived from turbiditic mudrocks (Galathea River). B) Quartz (Q) with subordinate feldspar (F) and micas (m) derived from turbiditic sandstones (Karnaphuli River mouth). C) Basaltic (Lv) and chert (ch) grains derived from pillow lavas of the oceanic crust and their pelagic cover strata (Beadonabad beach). D) Mostly cellular serpentinite grains (Lu) derived from mantle rocks (Panchavati River mouth). E) Neovolcanic detritus (P = plagioclase; Lv = volcanic lithics; p = pyroxene). F) Paleovolcanic detritus and calcareous grains (stained with alizarine red; Lc) recycled from Neogene strata. Photos with crossed polars; blue bar = 250 m. Sample locations given in Figures.7.1. and 7.2.*

7.5.1. Recycled Clastic Provenance

Turbiditic sandstones and mudrocks are by far the most widespread and significant source of detritus all along the IBAN accretionary prism. Because of the complex and locally chaotic tectonic structure of subduction complexes, however, recycled detritus is commonly mixed with ophiolitic and volcanic detritus even at the scale of the single catchment ("first-order sampling scale" of Ingersoll, 1990). Bulk petrography and heavy-mineral suites vary considerably along strike. In fluvial-bar sands of central to southern Arakan and Great Nicobar, lithic to quartzo-lithic compositions dominated by shale/slate with subordinate siltstone/sandstone/metasandstone rock fragments, little quartz, very few feldspars and virtually no micas reflect dominant mudrocks in the source (Figure 7.5.A). Levee silts and silty sands are also quartzo-lithic and show the same heavy-mineral suite, but are somewhat richer in quartz and feldspars and lack identifiable volcanic rock fragments and chert. Conversely, feldspatho-quartzose and even quartzose compositions with shale/slate, siltstone/sandstone/ metasandstone and a few higher-rank metamorphic rock fragments, feldspars and micas in Kopili River sand, in river and beach sands of coastal Bangladesh, and in beach sands of Ramree, western South Andaman, Baratang, NW Rutland and Great Nicobar islands reflect abundant sandstones in the source (Figure 7.5. B). Provenance from both mudrocks and sandstones is reflected by quartzo-lithic to litho-quartzose sands of the Dhansiri and Kaladan Rivers, and of northern Arakan beaches. Instead, quartzo-lithic to litho-quartzose composition of beach sand in southern Arakan, where mudrock sources are dominant, reflects selective mechanical destruction of non-durable shale and slate grains in wave-dominated coastal settings and consequent relative enrichment in quartz. Subordinate volcanic/metavolcanic or ophiolitic detritus, represented by mostly felsic to intermediate volcanic, very-low-rank metarhyolite/ metadacite, plagioclase, epidote and Cr-spinel grains, scarcely represented in Assam south of the Burhi Dihing River, becomes significant in coastal Bangladesh and increases progressively from northern to southern Arakan, reflecting southward increasing supply from Upper Cretaceous to Paleogene units of mixed arc orogenic provenance ultimately derived from the Burma active continental margin. Volcanic detritus is again negligible in beaches of western South Andaman and in Galathea River sand in Great Nicobar.

In sands from Assam, coastal Bangladesh and northern Arakan, very poor to moderately rich heavy-mineral suites include epidote, amphibole, garnet, zircon, Ti oxides, tourmaline, staurolite, kyanite or chloritoid. In sands from Ramree Island and southern Arakan, instead,

very poor suites are dominated by epidote or zircon, and invariably include Cr-spinel, rutile and tourmaline. Garnet and amphibole are invariably minor, and chloritoid, staurolite, kyanite or sillimanite only sporadically recorded. Corundum occurs in Lemro sands, and dominates the heavy-mineral suite of its Koum tributary. Altered grains consisting of Fe-oxide aggregates of pedogenetic origin dominate the dense fraction in all Arakan samples.

The very poor to moderately rich suites of western South Andaman beaches include epidote, garnet, zircon, staurolite, tourmaline, rutile and titanite. Garnet-rich beach sandswith staurolite and locally kyanite characterize the southeastern coast of Great Nicobar, whereas the very poor suite of Galathea River sand is epidote-rich with tourmaline, chloritoid, amphibole, garnet, zircon, rutile and titanite. Besides local hydraulic-sorting effects or occurrence of mélange units, such differences are accounted for by the different provenance of turbiditic source rocks and by the different intensity of the diagenetic processes they have undergone, as discussed in Section 7.6 below.

7.5.2. Ophiolite Provenance

Detritus from obducted ophiolites, significant in Burhi Dihing sand at the northernmost tip of the Indo-Burman Ranges but negligible in sands of coastal Bangladesh, Arakan and Great Nicobar, is most common and locally dominant, although never pure, along the eastern side of major Andaman Islands. A mafic crustal source, best approximated by beach sands of SE South Andaman (Figure 7.5.C), is readily distinguished from an ultramafic mantle source, best approximated by Panchavati sand (Figure 7.5.D).

Lithic, feldspatho-lithic or quartzo-feldspatho-lithic beach sands in SE South Andaman are dominated by lathwork volcanic, diabase/metadiabase, gabbro/pyroxenite/amphibolite, plagiogranite rock fragments and plagioclase, reflecting provenance from basalts, sheeted dikes and intrusive rocks of the oceanic crust. Radiolarian chert is also common. Rich to very rich heavy-mineral suites are dominated by clinopyroxene, actinolite, epidote and hornblende. Plagioclase, lathwork volcanic and diabase grains, associated with chert, clinopyroxene or actinolite, are mixed with detritus recycled from the Andaman Flysch in other beach samples from South Andaman.

Instead, the lithic Panchavati sand from Middle Andaman is dominated by cellular serpentinite rock fragments, with a few diabase/ metadiabase and arenaceous rock fragments, reflecting provenance from ultramafic mantle rocks with minor contributions from mafic igneous rocks and turbidite units. The rich heavy-mineral suite contains enstatite,

diopsidic clinopyroxene, hornblende, garnet, epidote, actinolite and Cr-spinel. Serpentinite rock fragments and enstatite, with minor olivine or Cr-spinel and associated with detritus from mafic rocks of the oceanic crust are significant in several other river and beach samples from Middle and North Andaman. In the N Rutland beach placer, dominant chromite is associated with a few olivine, clinopyroxene and orthopyroxene grains, revealing provenance from peridotite tectonites and overlying ultramafic crustal cumulates formed in supra-subduction settings (Ghosh et al., 2009, 2012).

7.5.3. Volcanic Arc Provenance

Besides basaltic rocks of the oceanic crust, sources of volcanic detritus in the IBAN accretionary prism include both active volcanoes (neovolcanic sources) and volcaniclastic sandstones and mélanges (recycled paleovolcanic sources; Zuffa, 1987). Pure neovolcanic detritus characterizes Barren and Narcondum Islands. Barren Island sands are feldspatho-lithic, with exclusively lathwork grains and a moderately rich, olivine-dominated suite with common clinopyroxene and no amphibole, reflecting provenance from basaltic rocks. Instead, Narcondum beach sand is litho-feldspathic, with lathwork to microlitic and minor felsitic rock fragments; plagioclase typically displays oscillatory zoning, and biotite is common (Figure 7.5.E). The very rich heavy-mineral suite is dominated by reddish-brown oxy-hornblende associated with green–brown kaersutite, augitic clinopyroxene and minor hypersthene, olivine and opaques, reflecting provenance from andesites and dacites (Figure 7.6.).

In the other islands of the Andaman archipelago, detritus is mainly paleovolcanic and recycled from either Paleogene (Namunagarh Grit) or Neogene volcaniclastic units (Archipelago Group) that have undergone limited burial diagenesis. Bioclastic beach sands of Interview and Havelock Islands are litho-feldspatho-quartzose with dominant plagioclase; poor heavy-mineral suites, dominated by hypersthenes and clinopyroxene, include kaersutitic hornblende (Figure 7.5.F). Bioclastic beach sands in Smith and Ross Islands are felspatho quartzo-lithic volcaniclastic with plagioclase and terrigenous rock fragments; very poor to moderately poor suites, including Cr-spinel, epidote and garnet, or zircon, tourmaline, chloritoid and garnet, indicate recycling of diverse Cenozoic units.

Peculiar composition is displayed by the quartzo-lithic Mayabunder beach sand at the northern tip of Middle Andaman, characterized by radiolarian chert associated with felsic to mafic volcanic, subvolcanic and metavolcanic rock fragments, shale and siltstone/sandstone

grains, plagioclase, and a poor suite dominated by epidote with Cr-spinel, clinopyroxene and hypersthene. Provenance from mélange units including deep-water radiolarites and volcanic/metavolcanic rocks is indicated.
Very-low-rank metarhyolite/metadacite rock fragments and Cr-spinel are common in sands from Baratang and Middle Andaman to North Andaman and Smith Island, where the Mithakhari mélange is widely represented (Figure 7.2.), as well as in southern Arakan where mélange including volcaniclastic forearc turbidites is also exposed.

7.6. Subduction Complex Provenance revisited

Subduction Complex Provenance (i.e., detritus from emergent ridges made of oceanic rocks deformed in a subduction zone) was originally defined by Dickinson and Suczek (1979 p.2176) as the subtype of Recycled Orogen Provenance characterized by “an abundance of chert grains, which exceed combined quartz and feldspar grains … by a factor of as much as two or three”. This criterion, however, is not met by any of our samples. Chert is mostly minor, and remains less abundant than quartz even in the chert-rich Mayabunder beach. Sand suites shed by thrust belts capped by oceanic allochthons (e.g., Cyprus, Apennines, Oman) document that chert-dominated detritus, rather than derived from offscraped oceanic slivers and abyssal-plain sediments stacked in intraoceanic prisms, is chiefly supplied by outer-continental-margin successions accreted at the front of the orogenic belt during a later collisional stage (Garzanti et al., 2000, 2002a, 2002b).
Subduction complexes large enough to be subaerially exposed and thus represent an effective source of sediment need be associated laterally with a large Himalayan-type or Andean-type mountain range formed above an east-directed subduction zone (Garzanti et al., 2007), from where huge volumes of orogenic detritus are conveyed via a major fluvio deltaic-turbiditic system to feed the rapidly growing accretionary prism (Velbel, 1985; Ingersoll et al., 2003; Morley et al., 2011). In such settings, detritus is dominantly recycled from offscraped turbiditic units (Figure 7.6.).

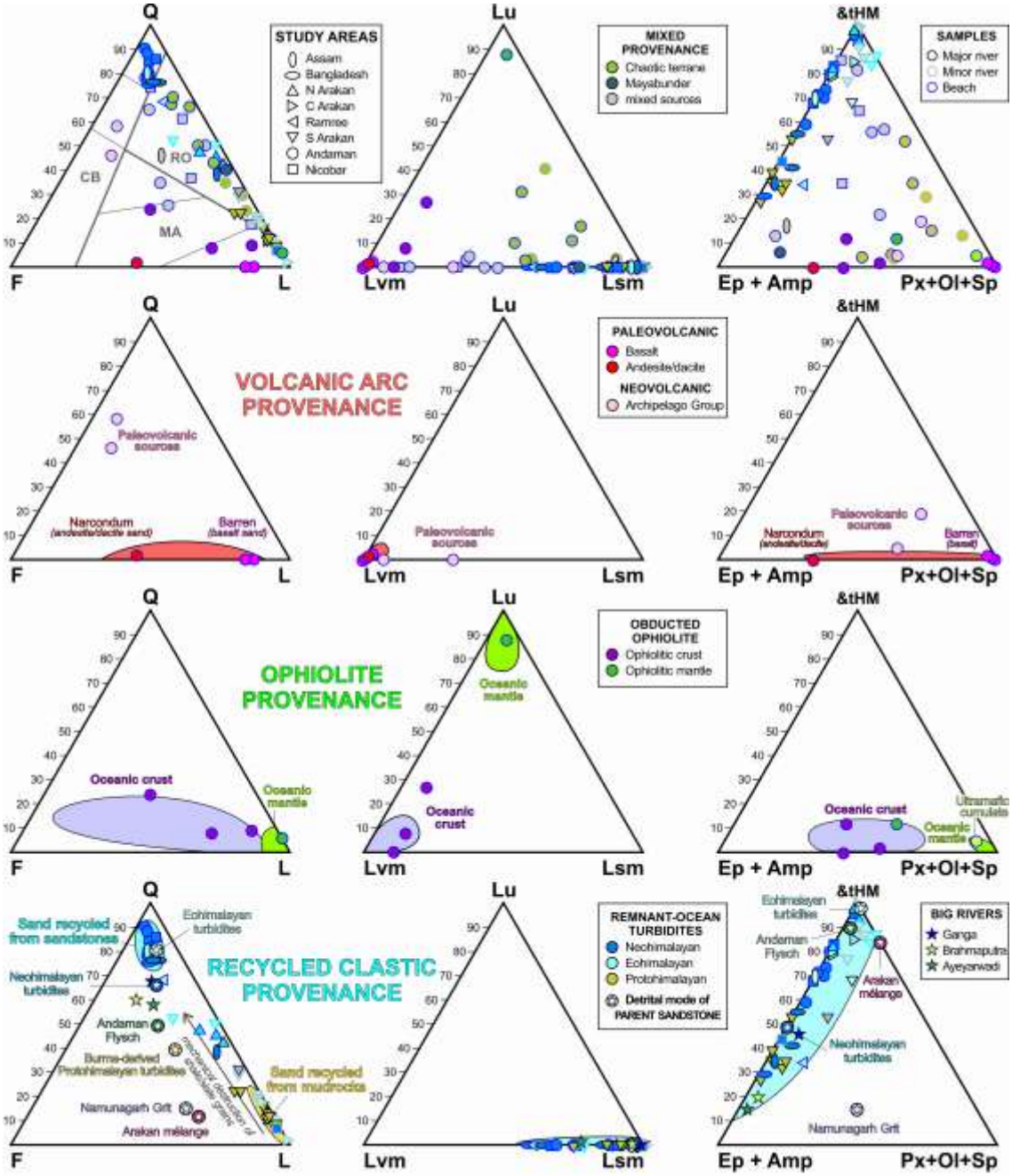

Figure 7.6. *Composite Subduction Complex Provenance decomposed in primary Volcanic Arc, Ophiolite and Recycled Clastic Provenances. Sands from the IBAN accretionary prism are mixtures of recycled detritus from accreted remnant-ocean turbidites, first-cycle detritus from obducted ophiolites, and both first-cycle neovolcanic and recycled paleovolcanic arc detritus. Sands recycled from Neohimalayan turbiditic sandstones are enriched in quartz relative to their source rocks, whereas sands recycled from Protohimalayan and Eohimalayan turbiditic mudrocks are enriched in lithics relative to their source rocks. The quartz/lithic ratio is higher in beach than in river sands, indicating selective mechanical destruction of labile shale/slate grains by waves. Fields of Dickinson (1985) (CB = Continental Block; MA = Magmatic Arc; RO = Recycled Orogen) are inadequate to sort out provenance at this level of complexity (Garzanti et al., 2007). Q = quartz; F = feldspars; L = lithic fragments (Lvm = volcanic and metavolcanic; Lu = ultramafic; Lsm = sedimentary and metasedimentary). Ep = epidote; Amp = amphibole; Px = pyroxene; Ol = olivine; Sp = Cr-spinel; &tHM = other transparent heavy minerals.*

7.6.1. The recycling effect on framework petrography

The recycling problem (i.e., “the evaluation of the abundance of detritus of first-cycle as opposed to polycyclic origin”) represents a long-standing and exceedingly difficult challenge in quantitative provenance analysis of sand and sandstone (Blatt, 1967). The importance of the issue can hardly be over-emphasized, considering that sedimentary rocks cover two thirds of the Earth's land surface and may supply up to 80% of detritus globally (Blatt and Jones, 1975; Garrels, 1986).

Reliable criteria to distinguish between detritus derived directly from igneous and metamorphic rocks or recycled from older sediments are few and largely qualitative (Zuffa, 1987; Dott, 2003). Enrichment in mechanically and chemically stable grains (e.g., quartz) at the expense of more labile components (e.g., plagioclase and rock fragments) is generally held to be a most obvious effect of polycyclicity (Johnsson, 1993; Cox and Lowe, 1995). Although it may appear to unescapably contain at least some sort of statistical truth, the idea owes its popularity more to plausibility of reasoning than to observational evidence. Actualistic case studies tell us that this is not necessarily the case. Recycled daughter sands may be even extremely quartz-poor, and markedly enriched instead in shale/slate, siltstone/metasiltstone or calcareous lithic fragments derived from mudrocks interlayered with sandstone beds in the source area (Zuffa, 1987; Johnsson et al., 1991 p.1639; Garzanti et al., 1998; Di Giulio et al., 2003). Instead of differentiating daughter sands from parent sandstones, the new sedimentary cycle may actually restore the original parent-rock composition by selective destruction of such labile mudrock grains, either mechanically during transport (Cavazza et al., 1993) or chemically in black swampy soils (Fontana et al., 2003). This is clearly shown by southern Arakan beach sands, which are petrographically much closer to parent sandstones than river sands, because the nondurable shale/slate grains derived in abundance from mudrock sources are selectively destroyed in coastal environments (Figure 7.6.).

Great Nicobar sands recycled from the Andaman Flysch are the extreme case: Galathea River sand is dominated by shale/slate grains and contains only 7% quartz, whereas beach sands contain 77 ± 2% quartz and only a few shale/slate grains.

Wherever mechanical abrasion and comminution is extensive, in temperate climates as in glacial environments (Nesbitt and Young, 1996 p.355), recycled sand is eventually compositionally similar to the original sandstone source. In the northern Apennines, river sands recycled entirely from Cenozoic sandstones show virtually the same composition as their source rocks (Cavazza et al., 1993; Fontana et al., 2003). The final product of the new

cycle may thus replicate that of the previous cycle because of (rather than in spite of) intense modifications in the sedimentary environment. Much of the complexities involved in sediment recycling remains to be investigated in order to understand and discriminate the effects of physico-chemical processes within each sedimentary cycle from that of diagenetic dissolution between successive cycles.

7.6.2. The recycling effect on heavy minerals

Most of the heavy minerals characterizing orogenic sediments tend to be selectively dissolved during diagenesis, and efficiently eliminated wherever burial depth exceeds ~1 km (pyroxene), ~2 km (amphibole) or ~3 km (epidote). At greater burial depths also titanite, kyanite, staurolite, and finally garnet and chloritoid are dissolved, and the residual suite dominantly consists of zircon, tourmaline, titanium oxides, apatite and, if originally present, Cr-spinel (Morton and Hallsworth, 2007). The effect of recycling thus depends primarily on – and is proportional to – the intensity of diagenetic dissolution, and thus to the sedimentary or tectonic burial depth reached by source rocks.

Heavy-mineral suites of daughter sands, however, do not necessarily mirror those of parent sandstones. Major discrepancies may be caused by chemical weathering (e.g., selective dissolution of unstable garnet or apatite in soil profiles; Morton and Hallsworth, 1999) or hydraulic sorting (e.g., concentration of denser minerals in placer deposits; Komar, 2007).

7.6.3. Sediment cycling along a convergent plate margin

The careful joint inspection of petrographic and heavy-mineral data (Figure 7.6.) allows us to differentiate diverse sources of recycled siliciclastic detritus along the IBAN accretionary prism (Figure 7.7.). The variability of petrographic composition is principally influenced by the sandstone/mudrock ratio within turbiditic source units, which is a rough index of originally proximal versus distal deep-sea fan deposition.

In order to interpret this piece of information correctly, we must consider that turbiditic fans prograde in time (Figure 7.8.). In the earlier Eocene–Oligocene “soft” stage of India-Asia collision (“Eohimalayan phase” of Hodges, 2000), when erosion rates were low, sand was largely confined to the foreland basin adjacent to the nascent Himalayan belt, whereas mud

was predominant in the deep sea (Najman and Garzanti, 2000; Alam et al., 2003; DeCelles et al., 2004; Najman et al., 2008). Sand lobes prograded rapidly and progressively southward since the earliest Miocene onset of “hard” continent–continent collision (“Neohimalayan phase” of Hodges, 2000), a major turning point in the erosional history of the orogen dated at ~20 Ma (Najman et al., 2009).

At any given site, the oldest turbidite packages offscraped and stacked at earlier times on top of the accretionary prism are thus expected to be mudrock-dominated. If a longer time elapsed before accretion, and such older turbidites were buried deeply beneath sandier turbidites deposited during a more advanced orogenic stage, then they may have experienced more prolonged and intense diagenetic dissolution than the overlying beds. We must also consider that shale/slate rock fragments are less durable mechanically than quartz and feldspars, and therefore prone to be destroyed selectively during high-energy transport in wave-dominated coastal settings (Garzanti et al., 2002a). And in particular we must take into full account that recycled heavy-mineral suites are an extensively mutilated residual of the detrital assemblage originally contained in parent sandstones, derived selectively of unstable species particularly where deeply buried (Garzanti and Andò, 2007a; Morton and Hallsworth, 2007).

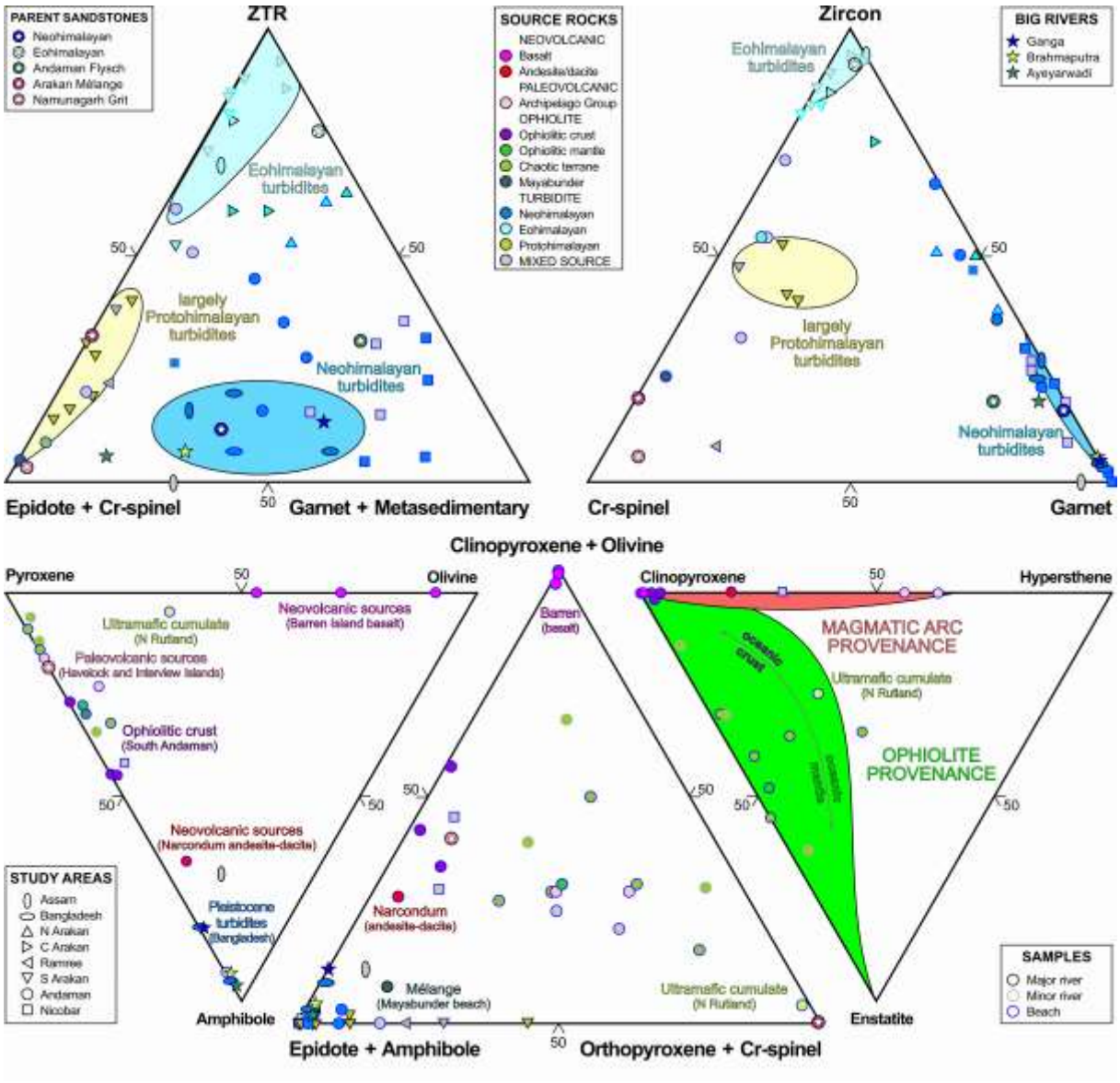

Figure 7.7. *Heavy-mineral tracers of Subduction Complex Provenance. Heavy minerals allow us to distinguish three end-members of Recycled Clastic Provenance: I) Cr-spinel and epidote-bearing sands largely recycled from Burma-derived Protohimalayan turbidites exposed along the eastern part of the Indo-Burman Ranges; II) zircon-bearing sands recycled from Eohimalayan turbidites exposed along the central part of the range; III) garnet and staurolite-bearing sands recycled from Neohimalayan turbidites exposed in the westernmost part of the range (e.g., Chittagong Hills). Distinguished are also suites shed by mantle serpentinites, oceanic crust, and basaltic versus andesite dacite neovolcanic and calc-alkaline paleovolcanic source rocks exposed in the Andaman Archipelago. ZTR = zircon + tourmaline + rutile. Metasedimentary minerals = chloritoid + staurolite + andalusite + kyanite + sillimanite.*

7.6.4. Recycling in the Indo-Burman Ranges

The composition of coastal Bangladesh sands almost perfectly mimics that of post-20 Ma (Neohimalayan) sandstones exposed along the adjacent Chittagong Hills, originally derived from the Himalaya via the paleo-Ganga–Brahmaputra fluvio-deltaic system (Allen et al., 2008). Heavy-mineral suites with subequal amphibole and epidote are somewhat less depleted than in the studied parent sandstones, indicating that modern sands are largely derived from the frontal range where source rocks have undergone only partial dissolution of unstable minerals at average burial depths of 1–1.5 km (Andò et al., 2012). Bulk petrography and heavy-mineral suites of Dhansiri River sand in Assam are compatible with recycling of largely distal, fine-grained turbidites fed by a paleo-Brahmaputra system affected by diagenetic dissolutionat similarly shallow burial depths.

Northern Arakan sands, intermediate in composition between coastal Bangladesh and southern Arakan sands, reflect mixed provenance from post-20 Ma sand-rich turbidites exposed in the western part of the range and pre-20 Ma mud-dominated distal turbidites, partly arc-derived and exposed in the eastern part of the range (Allen et al., 2008). Ramree sand is petrographically similar to sands of coastal Bangladesh, reflecting provenance largely from Neohimalayan sandrich turbidites, but with more abundant felsic volcanic/metavolcanic detritus. Heavy-mineral suites with epidote and Cr-spinel are the same as those of southern Arakan sands, indicating contribution from locally exposed Paleogene mélange (Maurin and Rangin, 2009).

The composition of southern Arakan sands reflects provenance from thrust packages of pre-20 Ma, mud-dominated distal turbidite packages. We calculate that recycling of sandstone beds provides one fourth of modern river sand, the remaining three/fourths being supplied by the largely predominant interbedded mudrocks. The strongly depleted, recycled heavy-mineral suites are characterized by epidote and Crspinel, inferred to have been ultimately supplied to their parent turbidites principally by altered arc-related or oceanic volcanic rocks of the Burma active margin. The other half of the suite consists of recycled stable species and very minor garnet, inferred to have been ultimately derived largely from the Himalayas. Garnet, chloritoid and amphibole become negligible, and staurolite, kyanite and sillimanite disappear towards the south, where the zircon/epidote ratio is distinctly higher in sands of minor rivers draining only the outer part of the range and beaches adjacent to their mouths.

Such compositional trends, displayed by modern sands from north to south and from east to west, reflect the present distribution of remnant-ocean-turbidite source rocks in space along

and across the Indo-Burman Ranges, controlled in turn by the progressive southward and outward growth of the accretionary prism and southward progradation of the Bengal deep-sea fan in time (Figure 7.8.). The solution of such four-dimensional puzzle is facilitated if ancient sandstones and modern sands are characterized by using indices based on relatively stable heavy minerals.

In Himalayan-derived strata of the Bengal Basin, MMI and GZi (petrographic and mineralogical indices defined in Section 3 above) progressively decrease with increasing age, from respectively 54 ± 15 and 98 ± 3 in Pleistocene Dupi Tila sandstones to 9 ± 11 and 13 ± 17 in Upper Eocene to Lower Miocene Barail sandstones (Table 7.1.).

This reflects unroofing of garnet and staurolite-bearing metamorphic rocks of the Greater Himalaya since ~20 Ma (White et al., 2002; Najman et al., 2009), as well as stronger diagenetic dissolution in deeply buried older units. The same pattern of values is displayed by modern sands and ancient sandstones in space, from coastal Bangladesh (MMI 49 ± 7 and GZi 90 ± 11 in sands vs. MMI 26 ± 20 and GZi 60 ± 41 in sandstones) to northern Arakan (MMI 0 ± 0 and GZi 8 ± 7 in sands vs. MMI 0 ± 0 in sandstones of the lower Kaladan catchment and GZi 3 ± 3 in sandstones of the lower Lemro catchment; Table 7.1.).

Such trends faithfully mirror the progressive southward increase in the average age of exposed Himalayan-derived sandstones. The virtual disappearance of garnet, staurolite and other metasedimentary minerals in southern Arakan sands reflects the absence of post-20 Ma Neohimalayan sandstones exposed on land (Figure 7.7.). Zircon-rich sands of minor rivers and beaches adjacent to their mouths indicate the occurrence of Eohimalayan Barail-type turbidites only in the outermost part of the range, whereas its inner part consists of Protohimalayan Upper Cretaceous to Paleogene deep-water units and volcaniclastic to ophioliticlastic mélange originally derived from the Burma active margin (Figure 7.8.; Mitchell, 1993).

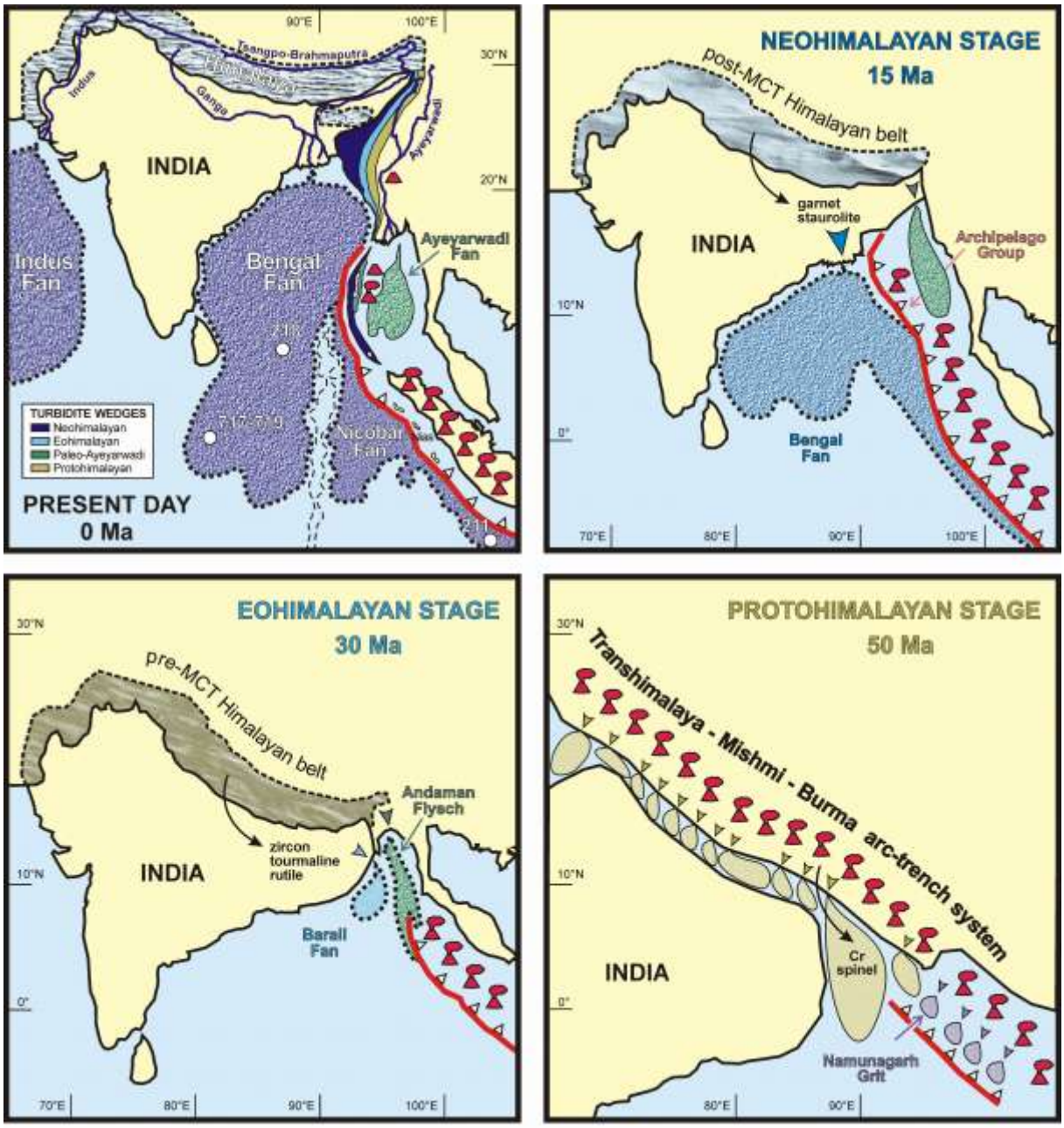

***Figure 7.8**. Evolution of the Himalayan collision zone and progressive growth of the Indo-Burman–Andaman–Nicobar subduction complex in space and time. Distinct petrographic and heavy-mineral signatures characterize detritus produced during the Protohimalayan (Upper Cretaceous–Early Eocene), Eohimalayan (Middle Eocene–Oligocene), and Neohimalayan (Neogene) phases of the Himalayan orogeny as defined in Hodges (2000). The Main Central Thrust (MCT), activated around the Oligocene/Miocene boundary (~23 Ma), led to rapid erosion of Greater Himalaya neometamorphic rocks in the Early Miocene (White et al., 2002; Najman et al., 2009). Reconstructed positions of India and southeast Asia relative to stable Siberia at 50, 30 and 15 Ma after Replumaz and Tapponnier (2003) and Replumaz et al. (2004). Progressive growth of deep-sea fans in time is poorly constrained because of limited data. Positions of DSDP Leg 22 sites 211 and 218 (Thompson, 1974; Ingersoll and Suczek, 1979) and ODP Leg 216 sites 717–719 (Yokoyama et al., 1990) are indicated in the upper left panel.*

7.6.5. Recycling on Andaman and Nicobar Islands

Beach sands of western South Andaman, NW Rutland and Great Nicobar contain much more quartz, less feldspars and rock fragments (along with somewhat more epidote and staurolite, and less apatite chloritoid and Cr-spinel) than the studied Andaman Flysch sandstones exposed along the eastern coast of South Andaman. Chemical weathering in soils of the richly vegetated subequatorial islands might explain the scarcity of apatite in modern sands (Morton and Hallsworth, 1999; Hall and Smyth, 2008), but other discrepancies can hardly be ascribed to a different intensity of diagenetic processes in source rocks on different sides of the islands. Mineral indices sensitive to post-depositional dissolution, for instance, are roughly similar for Oligocene sandstones (ZTR 25 ± 3, GZi 79 ± 3) and modern sands (ZTR 30 ± 12, GZi 47 ± 25). Distinct petrography is displayed by Galathea River sand, which together with the N Campbell Bay sample indicates provenance chiefly from turbiditic mudrocks as well as lack of severe mechanical destruction of labile shale/slate grains by waves. The Galathea suite is much richer in epidote and contains amphibole and rare clinopyroxene, which may be explained by minor direct or indirect contribution from arc-related volcanic or oceanic rocks.

7.6.6. Andaman Flysch: paleo-Irrawaddy or Bengal Fan?

Data from modern sands provide additional information for unraveling provenance of their parent sandstones, and sheds new light on the long-standing controversy concerning the origin of the Andaman Flysch exposed on Andaman and Nicobar Islands (Pal et al., 2003; Curray, 2005). The best mineral tracer for this task is relatively stable staurolite, associated with garnet in post-20 Ma Neohimalayan sandstones (Najman et al., 2009) but virtually absent in Ayeyarwadi sediments (Table 7.1.). Staurolite is negligible in both parent sandstones (St 0.3 ± 0.6% tHM) and daughter sands (St 0% tHM) along the eastern side of the Andaman Islands, but invariably common (St 6 ± 3% tHM) in beach sands from western South Andaman and NW Rutland to Great Nicobar, where garnet represents half of the heavy-mineral suite (Table 7.1.). Such regional distribution of garnet and staurolite suggests that the Andaman Flysch exposed in the west and south largely consists of post-20 Ma Neohimalayan turbidites originally representing the eastern part of the Bengal Fan (Figure

7.8.). Instead, turbidites exposed along the eastern side of South Andaman with all likelihood represent part of the Oligocene Ayeyarwadi deep sea fan (Allen et al., 2007), offscraped at an earlier growth stage in the rear of the accretionary prism (Figure 7.8.). Along the eastern side of the Andaman Islands, CZi indices of parent sandstones (42 ± 7) and daughter sands (35 ± 10) are compatible with those of modern Ayeyarwadi sediments (32 ± 25), revealing significant contribution from mafic/ultramafic rocks of the Burma arc-trench system. Instead, CZi indices are invariably lower in Himalayan-derived sediments, including Cenozoic sandstones from Bangladesh to Arakan (6 ± 4) and modern sands from the Ganga–Brahmaputra (3 ± 2; Garzanti et al., 2010a) to western South Andaman, NW Rutland and Great Nicobar (6 ± 4).

7.7. Provenance of Cr-spinel

Cr-spinel is a key mineral in provenance studies, generally held as a tracer of Ophiolite Provenance because it commonly occurs as a minor accessory in ultramafic to mafic rocks (Mange and Morton, 2007). Being chemically stable and mechanically durable, it can survive the sedimentary cycle easily and is concentrated, while the associated mafic silicates are first attacked chemically during weathering and later dissolved selectively during diagenesis (Morton and Hallsworth, 2007). As any other stable mineral, however, Cr-spinel can be recycled several times, and thus be a tracer of Recycled Clastic Provenance as well (Garzanti et al., 2002a). Distinguishing between first-cycle and polycyclic Cr-spinel is crucial for a correct provenance diagnosis.

The present study provides good clues to investigate this issue in detail. To this aim, it is useful to distinguish the volume concentration of Cr-spinel relative to the transparent heavy-mineral population (relative concentration = Sp/tHM%, which is the one generally used in heavy-mineral studies), from the volume concentration of Crspinel in the bulk sample (absolute concentration = Sp/bulk sample%, which is instead seldom considered). In this section we will show how diverse sedimentary processes determine different and identifiable patterns of relative and absolute Cr-spinel concentrations. Such theoretical trends will be compared with mineralogical data from Cr-spinel-bearing sands generated along the IBAN accretionary complex, in order to assess the physical and chemical processes that regulate the concentration of Cr-spinel in different settings. Cr-spinel was not observed in any of the

studied sands from Narcondum and Barren Islands, although it may locally occur in trace in sands of Volcanic Arc Provenance (Garzanti and Andò, 2007b).

7.7.1. First-cycle Cr-spinel of Ophiolite Provenance

Cr-spinel is a common accessory in mantle peridotites, mostly representing ≤ 2% of the bulk rock (e.g., Lippard et al., 1986). Because fresh peridotites consist entirely of dense minerals (olivine, orthopyroxene, clinopyroxene), this value represents the absolute as well as the relative concentration of Cr-spinel in the sand they shed. With progressive serpentinization and thus destruction of olivine and pyroxene in source rocks, the relative concentration of Cr-spinel increases in the sand, whereas its absolute concentration does not change. But only with virtually complete serpentinization of the ultramafic source can the relative concentration of Cr-spinel increase markedly in the sand and finally approach 100% tHM, whereas its absolute concentration remains constant and heavy-mineral-concentration linearly decreases (Figure 7.9.).

In modern sands derived entirely from peri-Arabian and peri- Mediterranean mantle ophiolites, typically displaying degrees of serpentinization between 50% and 80% (e.g., Lippard et al., 1986), enstatite remains predominant, and the relative concentration of Cr-spinel does not exceed 10% tHM (Garzanti et al., 2000, 2002b). The enstatite/Cr-spinel ratio (an index of the degree of serpentinization of source rocks) is ~7 in ophioliticlastic sands of Middle and North Andaman, a value intermediate between that of sands derived from the moderately serpentinized Sama'il Ophiolite and from the strongly serpentinized Masirah Ophiolite in Oman (Garzanti and Andò, 2007a).

A different case is outlined by the chromite placer sand of N Rutland, where absolute and relative concentrations of Cr-spinel are both extreme (Figure 7.9.). Besides local provenance from ultramafic cumulates (Ghosh et al., 2012), this indicates strong enrichment by hydraulic sorting in beach environments. Cr-rich spinel may be even denser than zircon (Mange and Maurer, 1992), and thus concentrated markedly by selective-entrainment processes (Garzanti et al., 2009). In summary, detritus derived from ultramafic mantle rocks is characterized by high absolute/low relative concentrations of Cr-spinel (e.g., Panchavati sand). High absolute/high relative concentrations indicate hydraulic-sorting effects (e.g., N Rutland chromite placer). Low absolute/high relative concentrations, instead, indicate selective destruction of unstable ferromagnesian silicates in source rocks, due to very

extensive serpentinization or even extreme weathering, as observed in detritus shed by mafic/ultramafic layered intrusions in equatorial Africa (Garzanti et al., 2013b).

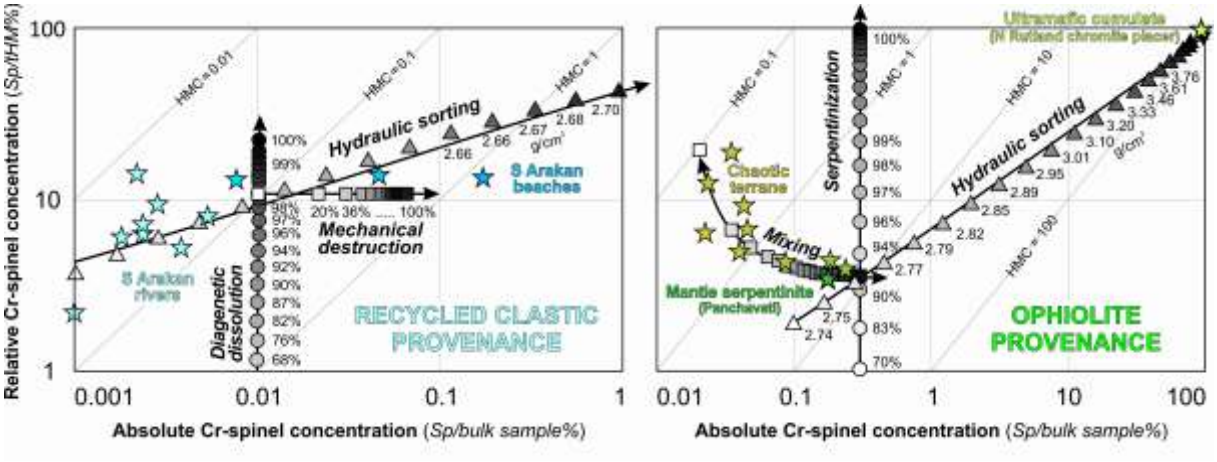

Figure 7.9. *Factors controlling absolute and relative concentrations of Cr-spinel in Recycled Clastic and Ophiolite Provenances. Selective entrainment in the depositional environment causes an increase in both absolute and relative concentrations of ultradense Cr-spinel, reaching maximum values for the chromite beach placer of N Rutland. Selective diagenetic dissolution in parent sandstones or serpentinization of mafic silicates in ultramafic source rocks, instead, cause an increase in relative concentration only, with negligible increase in absolute concentration. The opposite effect is caused by mechanical destruction of labile shale/slate grains, as displayed by Arakan beach sands. Mineralogical trends in ophioliticlastic sands shed by the Chaotic terrane in Middle and North Andaman are explained by mixing in various proportions with detritus from turbiditic sources that have lower absolute but higher relative Cr-spinel concentrations. Total heavy-mineral concentration and bulk-sediment grain density in g/cm3 (HMC and SRD indices of Garzanti and Andò, 2007a) are also indicated.*

7.7.2. Polycyclic Cr-spinel of Recycled Clastic Provenance

Polycyclic sands may display higher relative concentration of Cr-spinel than ultramaficlastic sand, although with very low absolute concentration (Garzanti et al., 2002a). This is because Cr-spinel is part of the meager stable residue that survived drastic diagenetic dissolution in parent sandstones, as indicated by exclusive association with other stable minerals such as zircon and quartz, shed instead by felsic source rocks. Selective diagenetic dissolution of unstable heavy minerals can increase the relative concentration of Cr-spinel by up to two orders of magnitude, with only very minor increase in its absolute concentration (Figure 7.9.). In southern Arakan sands, for instance, the relative concentration of Cr-spinel exceeds 10% tHM in five samples (one river sand out of ten, and all four studied beach sands). It may thus be higher than in ultramaficlastic sands of Middle and North Andaman, although the absolute

concentrations are lower by an order of magnitude (0.02 ± 0.05% vs. 0.5 ± 0.5%; Figure 7.9.). Besides imprecision in the determination of a rare component such as Cr-spinel, the high variability of these values suggests that the concentration of Cr-spinel is locally influenced by environmental processes to various degrees, and enhanced in beach relative to river sands.

Destruction of shale/slate grains occurs extensively in high-energy coastal environments, as shown by systematic petrographic differences between river and beach sands (Figure 7.6.). Such a mechanical process can account for a linear increase in the absolute concentration of heavy minerals – including Cr-spinel – by up to an order of magnitude if labile lithic fragments are completely destroyed, but without any increase in relative concentration (Figure 7.9.). Selective-entrainment effects, instead, determine an increase in both absolute and relative concentration of Cr-spinel, as well as of other ultradense minerals such as zircon (e.g., Seliguin beach).

	N°	Q	KF	P	Lvm	Lu	Lc	Lch	Lsm		tHMC	ZTR	Ap	Ttn	Ep	Grt
MODERN SANDS																
RECYCLED CLASTIC PROVENANCE																
Coastal Bangladesh	**3**	**76**	**7**	**4**	**4**	**0**	**0**	**1**	**9**	100,0	**1,6**	**8**	**2**	**2**	**27**	**16**
		1	*2*	*2*	*2*	*0*	*0*	*0*	*3*		*0,4*	*5*	*2*	*1*	*2*	*3*
N Arakan	**3**	**45**	**2**	**3**	**4**	**0**	**0**	**0**	**46**	100,0	**0,05**	**64**	**1**	**2**	**6**	**16**
		3	*2*	*1*	*2*	*0*	*0*	*0*	*7*		*0,02*	*6*	*1*	*1*	*7*	*6*
Lemro River	6	**11**	**0**	**1**	**1**	**0**	**0**	**0**	**87**	100,0	**0,03**	**74**	**4**	**2**	**8**	**2**
		6	*0*	*1*	*2*	*0*	*0*	*0*	*7*		*0,02*	*17*	*3*	*3*	*9*	*1*
Ramree Island	1	68	5	6	8	0	0	2	11	100,0	0,5	24	0	2	41	4
S Arakan rivers	**10**	**17**	**1**	**3**	**5**	**0**	**0**	**0**	**75**	100,0	**0,02**	**47**	**2**	**2**	**39**	**2**
		7	*1*	*2*	*4*	*0*	*0*	*0*	*5*		*0,01*	*26*	*2*	*2*	*27*	*2*
S Arakan beaches	**3**	**43**	**3**	**2**	**12**	**0**	**0**	**1**	**39**	100,0	**0,04**	**67**	**2**	**2**	**15**	**1**
		11	*5*	*2*	*4*	*0*	*0*	*1*	*11*		*0,50*	*19*	*3*	*3*	*6*	*8*
W South Andaman	**4**	**84**	**5**	**4**	**1**	**0**	**0**	**0**	**5**	100,0	**3**	**30**	**1**	**3**	**29**	**25**
NW Rutland		*6*	*1*	*3*	*1*	*0*	*0*	*0*	*2*		*4*	*12*	*0*	*3*	*6*	*8*
Great Nicobar	**3**	**83**	**5**	**3**	**2**	**0**	**0**	**2**	**5**	100,0	**4**	**15**	**0**	**2**	**13**	**53**
		4	*4*	*1*	*1*	*0*	*0*	*1*	*2*		*4*	*13*	*0*	*3*	*10*	*10*
Galathea River	1	7	1	1	0	0	0	0	92	100,0	0,1	24	0	2	48	7
OPHIOLITE PROVENANCE																
Oceanic crust	**3**	**14**	**0**	**23**	**49**	**7**	**0**	**4**	**3**	100,0	**11**	**0**	**0**	**0**	**20**	**4**
(South Andaman)		*9*	*1*	*14*	*22*	*10*	*1*	*4*	*1*		*5*	*0*	*0*	*0*	*2*	*6*
Panchavati mouth	1	6	0	0	4	83	0	1	5	100,0	5	0	1	0	8	10
VOLCANIC PROVENANCE																
Narcondum Island	1	2	0	54	44	0	0	0	0	100,0	14	0	0	0	0	0
Barren Island	3	**0**	**0**	**14**	**86**	**0**	**0**	**0**	**0**	100,0	**1,1**	**0**	**0**	**0**	**1**	**0**
		0	*0*	*2*	*2*	*0*	*0*	*0*	*0*		1,8	*0*	*0*	*0*	*1*	*0*
MIXED PROVENANCE																
Chaotic terrane	**10**	**43**	**1**	**4**	**10**	**14**	**0**	**6**	**22**	100,0	**2,0**	**13**	**0**	**1**	**15**	**3**
(Middle/North Andaman)		*21*	*1*	*2*	*5*	*26*	*0*	*12*	*17*		*2,3*	*14*	*0*	*2*	*22*	*3*
Havelock/Interview I.	**2**	**52**	**2**	**35**	**8**	**0**	**0**	**1**	**1**	100,0	**1,4**	**3**	**0**	**0**	**12**	**7**
		9	*1*	*5*	*0*	*0*	*0*	*1*	*1*		*1,6*	*4*	*0*	*0*	*8*	*7*
Smith/Ross Islands	**2**	**30**	**0**	**30**	**28**	**0**	**1**	**0**	**11**	100,0	**0,8**	**26**	**2**	**1**	**14**	**14**
		7	*0*	*1*	*13*	*0*	*0*	*1*	*8*		*0,8*	*30*	*2*	*1*	*20*	*2*
AYEYARWADI RIVER	**7**	**57**	**10**	**11**	**6**	**0**	**0**	**1**	**15**	100,0	**2,5**	**4**	**1**	**2**	**40**	**8**
		6	*2*	*1*	*3*	*0*	*0*	*1*	*2*		*0,5*	*3*	*1*	*1*	*8*	*4*
PARENT SANDSTONES (Cenozoic)																
Dupi Tila	7	**68**	**8**	**6**	**8**	**0**	**0**	**2**	**8**	100,0	**1,7**	**4**	**0**	**1**	**29**	**3**
Pleistocene		*14*	*2*	*3*	*3*	*0*	*0*	*2*	*3*		*1,6*	*1*	*1*	*1*	*10*	*2*
Tipam	7	**68**	**7**	**5**	**5**	**0**	**0**	**1**	**13**	100,0	**0,8**	**10**	**1**	**2**	**44**	**5**
Pliocene		*14*	*3*	*4*	*1*	*0*	*0*	*1*	*4*		*0,5*	*3*	*2*	*2*	*8*	*6*
Boka Bil	2	**64**	**10**	**7**	**6**	**0**	**0**	**3**	**11**	100,0	**0,7**		**4**	**2**	**37**	**13**
Miocene		*7*	*1*	*0*	*2*	*0*	*0*	*2*	*1*		*0,7*	*5*	*6*	*3*	*24*	*15*
Bhuban	11	**76**	**9**	**5**	**2**	**0**	**0**	**0**	**7**	100,0	**0,2**	**48**	**7**	**2**	**6**	**17**
Miocene		*5*	*2*	*2*	*1*	*0*	*0*	*0*	*1*		*0,2*	*17*	*7*	*3*	*9*	*17*
Barail	16	**81**	**2**	**1**	**3**	**0**	**0**	**0**	**12**	100,0	**0,1**	**89**	**0**	**1**	**0**	**1**
U.Eocene-L-Miocene		*10*	*2*	*1*	*1*	*0*	*0*	*0*	*5*		*0,1*	*17*	*0*	*1*	*0*	*2*
Pre-Barail	4	**97**	**2**	**0**	**0**	**0**	**0**	**0**	**1**	100,0	**0,07**	**89**	**0**	**2**	**2**	**1**
Paleocene-Eocene		*2*	*2*	*1*	*0*	*0*	*0*	*0*	*2*		*0,04*	*26*	*0*	*2*	*3*	*1*
Coastal Bangladesh	13	**78**	**7**	**3**	**3**	**0**	**0**	**1**	**7**	100,0	**0,4**	**32**	**5**	**1**	**16**	**16**
Neogene		*10*	*2*	*3*	*2*	*0*	*0*	*1*	*2*		*0,4*	*10*	*7*	*2*	*17*	*19*
Coastal Arakan	4	**64**	**10**	**5**	**6**	**0**	**0**	**0**	**14**	100,0	**0,1**	**65**	**13**	**1**	**2**	**14**
Neogene		*7*	*7*	*0*	*1*	*0*	*0*	*1*	*3*		*0,1*	*17*	*7*	*1*	*1*	*17*
Andaman Flysch	3	**49**	**13**	**9**	**8**	**0**	**0**	**1**	**20**	100,0	**0,2**	**45**	**13**	**2**	**7**	**14**
Oligocene		*2*	*4*	*3*	*1*	*0*	*0*	*1*	*5*		*0,1*	*4*	*3*	*2*	*10*	*1*
Namunagarh Grit	5	**15**	**1**	**29**	**50**	**0**	**0**	**1**	**3**	100,0	**0,6**	**2**	**2**	**11**	**34**	**1**
Paleocene-Eocene		*8*	*1*	*8*	*9*	*0*	*0*	*1*	*1*		*0,4*	*1*	*1*	*8*	*19*	*1*
Arakan Mélange (Eoc.)	1	12	2	25	57	0	0	1	3	100,0	0,2	75	8	0	0	0

Table 7.1. *Petrographic and mineralogical composition ofmodern daughter sands and Cenozoic parent sandstones of the Indo-Burman–Andaman–Nicobar subduction complex (mean values in bold, standard deviations in italics). Composition of Ayeyarwadi River sediments is also given. N° = number of samples; Q = quartz; KF = K-feldspar; P = plagioclase; L = lithic fragments (Lvm = volcanic and metavolcanic; Lu = ultramafic; Lc = carbonate; Lch = chert; Lsm = sedimentary and metasedimentary). tHMC = transparent-heavy-mineral concentration. ZTR = zircon, tourmaline and Ti oxides; Ap = apatite; Ttn = titanite; Ep = epidote-group minerals; Grt = garnet; Cld = chloritoid; St = staurolite; Ky = kyanite; Sil = sillimanite; gHb = blue-green and green hornblende; bHb = brown hornblende; oxyHb = oxy-hornblende; &A = other amphiboles; Cpx = clinopyroxene; Hy = hypersthene; En = enstatite; Ol = olivine; Sp = Cr-spinel; and &tHM = other transparent heavy-minerals.*

7.8. Conclusions

Turbiditic sandstones and mudrocks are by far the most widespread and significant source of sediments along the Indo-Burman–Andaman– Nicobar accretionary prism. Because of the locally chaotic tectonic structure of subduction complexes, however, recycled detritus is mixed in various proportions with ophiolitic and neovolcanic to paleovolcanic detritus. “Subduction Complex Provenance” (Dickinson and Suczek, 1979) is thus composite, as invariably is the case with orogenic sediments (Figure 7.6.).

In spite of the necessary connection along strike with an Himalayan or Andean-type orogenic belt, from which the parent material is mostly derived (Velbel, 1985; Morley et al., 2011), sharp differences exist between first-cycle neometamorphic detritus that characterizes collision orogens (Axial Belt Provenance; Garzanti et al., 2010b) and recycled orogenic detritus (Recycled Clastic Provenance). Recycled products provide in fact a distorted image of the original source for various reasons. First and foremost, diagenesis modifies drastically and irreversibly the original detrital suite by systematically erasing less stable minerals to a degree that primarily depends on stratigraphic or tectonic burial depth. Next, contrary to what is generally believed, daughter sand may be much less “mature” petrographically than parent sandstones, due to the locally overwhelming supply of shale/slate fragments from interbedded mudrocks. A replica of parent-rock composition can be reconstituted only through the mechanical or chemical processes that destroy selectively such labile grains in the sedimentary environment (Figure 7.6.). Last but not least, a considerable compositional mismatch may derive from the up-to tens- of-million-years time lag between the initial generation of parent sediments in the orogen and their final incorporation in the accretionary prism (Figure 7.8.). Parent sandstones reflect an earlier orogenic or even pre-orogenic stage, when medium to high-grade neometamorphic rocks were not yet exposed along the axial belt of the young orogen. The detritus produced was then stored in the adjacent foreland basin or proximal parts of the nascent deep-sea fan, whereas distal regions received little or no sediment from the growing orogen and were rather supplied from distinct transverse sources, as it is partly the case for Paleogene turbiditic mudrocks and mélange units of the inner Indo-Burman Ranges and Andaman Islands.

Sediment petrography and mineralogy effectively mediate the lithological structure of source areas and the effects of their diverse physical and chemical controls over vast regions. The representative quantitative information they provide helps us to illuminate the multistep transfer of material operated by sedimentary and tectonic processes, along and across plate

boundaries at the scale of thousands of km and tens of millions years (Dickinson, 1988; Ingersoll et al., 2003). All relevant factors that impact on the sedimentary system can be scrutinized at our will in modern settings, although the precise discrimination among the effects of each may remain hard to attain in intrinsically complex nature (Leeder, 2011). Compositional data from modern sediments offer us a valid key to reveal how the Earth's surface is continuously shaped by the interaction among the endogenous and exogenous forces that create and eventually destroy mountain relief, and represent the firmest starting point from which to proceed in the challenging task of interpreting provenance of ancient sedimentary successions.

8. Heavy-mineral evidence of ash-fall dispersal in arc-trench systems (Barbados, Lesser Antilles)

Limonta et al. in prep

8.1. Introduction

Neovolcanic detritus derived from active or dormant volcanoes and transported across the forearc region, as well as paleovolcanic detritus recycled from older volcaniclastic units, commonly occurs in accretionary prisms. Mineralogical signatures characterized by augitic clinopyroxene frequently associated with abundant and even dominant hypersthene reflect the calc-alkaline character of subduction-related magmas (Garzanti and Andò, 2007b). Extensive basaltic products may be revealed by local predominance of olivine over pyroxene and of glass-rich lathwork lithics over plagioclase, reflecting lower abundance of plagioclase phenocrysts in mafic parent lavas. Presence of oxy-hornblende or kaersutitic amphibole and biotite testify to occurrence of andesitic and more felsic products.

In this article we focus on petrographic composition and heavy-mineral assemblages characterizing beach sediments of Barbados Island, one of the places in the world where an active accretionary prism is subaerially exposed (Speed, 1994, 2002). We present a regional provenance study on compositional variability and long-distance multicyclic transport of terrigenous sediments along the convergent plate boundaries of Central America, from the northern termination of the Andes to the Lesser Antilles arc-trench system (Figure 8.1.). This new study represents a complement of the thorough investigation carried out with the same methodologies, rationale and goals on sediments produced along the Himalayan collision system and recycled along and across its eastern side, from the Bengal Basin to the Indo-Burman Ranges and the Andaman and Nicobar islands (Garzanti et al., 2013). The comparison of modern sands on Barbados with those shed by larger accretionary prisms such as the Indo-Burman Ranges redefines the diagnostic mark of Subduction Complex Provenance as quite distinct from the original definition by Dickinson and Suczek (1979). It is

invariably composite and chiefly consists of detritus recycled from orogen-derived turbidites transported long distance (Recycled Clastic Provenance), with local supply from ultramafic and mafic rocks of forearc lithosphere (Ophiolite Provenance) or recycled paleovolcanic to neovolcanic sources (Volcanic Arc Provenance).

We concentrate our attention on “Volcanic Arc Provenance” and heavy-mineral evidence of ash-fall dispersal in arc-trench systems analyzing heavy-mineral concentration, assemblages, size, corrosion features and roundness in modern sediments of Barbados island. The ash-fall dispersal in this area depend on trade winds and anti trades winds, two essential parts of the atmosphere's primary circulation (Bjerknes, 1935).

8.1.1. Trade winds versus anti trade winds

The trade winds (also called trades) are the prevailing pattern of easterly surface winds found in the tropics, within the lower portion of the Earth's atmosphere, in the lower section of the troposphere near the Earth's equator. The trade winds blow predominantly from the northeast in the Northern Hemisphere and from the southeast in the Southern Hemisphere. In the Northern Hemisphere they begin as north-northeast winds at about latitude 30°N in January and latitude 35°N in July, gradually veering to northeast and east-northeast as they approach the equator. Antitrades, instead, are westerly (blowing in the opposite direction from and above the trades) winds in the troposphere above the surface trade winds of the Tropics (Bjerknes, 1935). The present climate of Barbados is of the trade-wind littoral type, characterized by modest changes in temperature through the year. Mean annual temperature ranges from 24° to 28°C. Precipitation occurs in all months, but there is a distinctive dry season lasting from about December to May (Rouse and Watts, 1966). High-elevation terraces have more rainfall, lower temperatures, and lower potential evapo-transpiration than low elevation terraces. Precipitation on the low-elevation terraces is as low as 1100 mm/yr, compared to 2120 mm/yr in the Scotland District, where the highest elevations on the island are found.

In our area of study low-level trade winds have little effect on ash dispersal, whereas antitrades, at 7 to 16 km height, play a dominant role (Carey and Sigurdsson, 1978; Bonadonna et al., 2002). The 7 May 1902 eruption of the Soufrière on St. Vincent has become a textbook example of the production of pyroclastic flows from a vertical eruption column (Hay, 1959). Pyroclastic flows, however, represent only a small proportion of the total erupted products (6%), whereas the majority of the ejecta (94%) consists of air-fall tephra. A

minimum of 28 % of the air-fall tephra was transported into the Atlantic by the prevailing antitrade winds at altitudes of 7 to 16 km.

The importance of trade and antitrade winds in sediment dispersal pattern in Barbados Island is also testified to by the soils composition (Muhs, 2001). Potential soil parent materials in this region, external to the carbonate substrate, include volcanic ash from the island of St. Vincent (near Barbados), volcanic ash from the islands of Dominica and St. Lucia (somewhat farther from Barbados), the fine-grained component of distal loess from the lower Mississippi River Valley, and wind-transported dust from Africa. Volcanic ash from the island of St. Vincent appears to have been the most important influence, but African dust is a significant contributor (Muhs, 2001; Kallos et al., 2006; Karyampudi,1979; Karyampudi et al., 1999; Prospero et al., 1981).

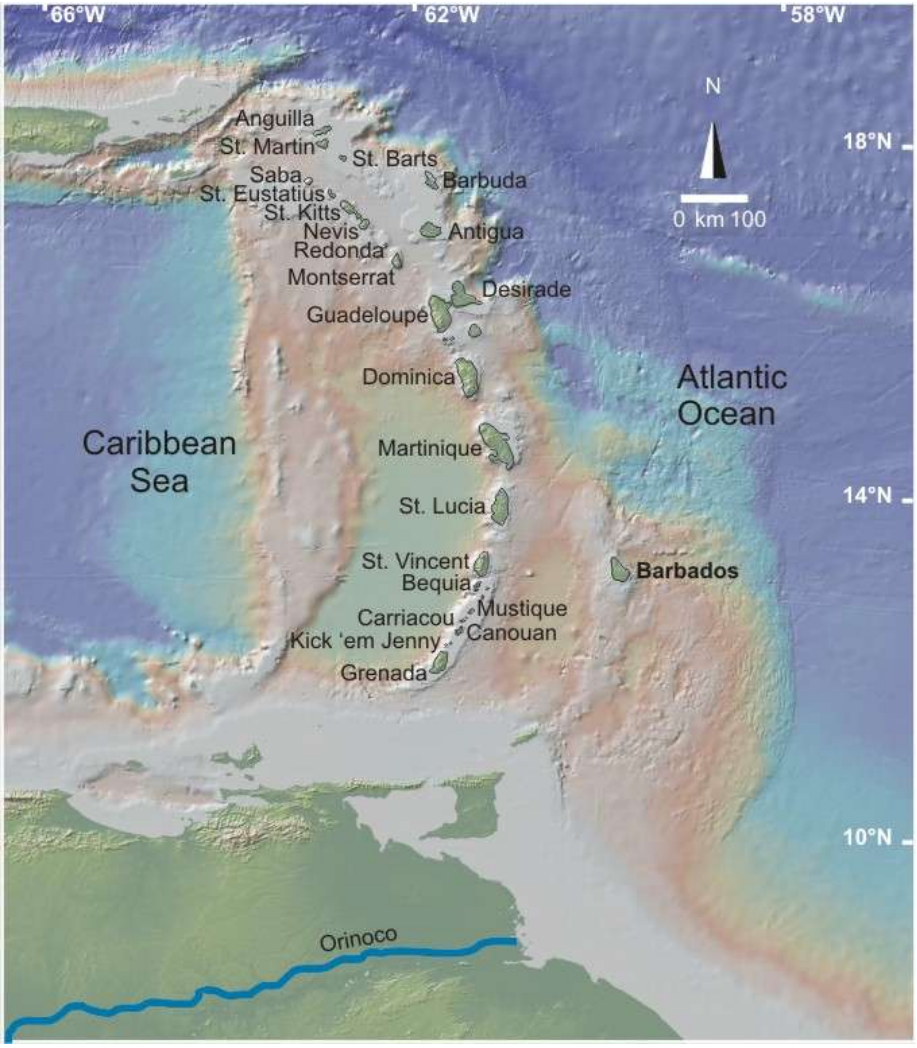

Figure 8.1. *Location map and tectonic scheme for the Lesser Antilles and Barbados Island (DEM modified from www.geomapapp.org).*

8.2.Geological framework

8.2.1. Lesser Antilles

The ~800 km-long Lesser Antilles volcanic arc extends from Grenada in the south to Saba in the north (Figure 8.1.). The bifurcation north of Martinique separates the active western Volcanic Caribees from the inactive eastern Limestone Caribees. The eastern arc was active mainly from Eocene to mid-Oligocene, whereas activity in the western arc began in the Early Miocene (Bouysse et al., 1990). Three groups of volcanic islands can be distinguished petrologically (Rea, 1982; Macdonald et al., 2000). The northern group (Saba to Montserrat) is dominated by andesites, with minor dacite and rare rhyolites; small volumes of basalt (0–5 km^3) are locally recorded as blocks in pyroclastic deposits (Rea and Baker, 1980). The central group includes the largest islands (Guadeloupe, Dominica, Martinique, St. Lucia) and is also characterized by predominant andesites, with some basalts, dacites and rare rhyolites. Larger volumes of volcanic products may reflect their older age as well as higher rates of volcanic production over the past 0.1 Ma (Wadge, 1984). The southern group includes St. Vincent, dominated by basalt and basaltic andesite, and the Grenadine islands, where rock types range from picritic or ankaramitic basalts through andesite to rare dacite; more magnesian rocks are silica-undersaturated.

8.2.2 The Orinoco River

The Orinoco River catchment occupies ~1.1*106 km^2 in northern South America. The Andean and Coastal fold-thrust belts in the west and north (~15% mountainous part of the basin) have strong relief with steep slopes and sharp peaks with active alpine glaciers. They include terrigenous and carbonate sediments and metasediments, along with felsic to mafic plutonic rocks. Orogeny began in the late Oligocene and peaked in the Pliocene, exerting a major influence in the development of the Amazon and Orinoco River systems. The Guiana Shield (~35% of the basin) is largely of low relief with dense vegetation and deeply-weathered soils, but locally reaches 3000 m a.s.l. It consists of felsic to intermediate granitoids and gneisses overlain by quartzites (Gibbs and Barron, 1983). The Llanos region

(50% of the basin) is a foreland basin filled with sediments derived mostly from the rising Andean orogen in the west and reworked widely by fluvial processes during the flood season and by eolian processes during the dry winter season (Johnsson et al., 1991). Lowland and delta regions have a strongly seasonal tropical climate with uniform temperatures throughout the year (25-28°C) and annual rainfall ranging from 120 to 360 mm. Sediment flux (~86 106 tons/a) consists of 80% mud and 20% sand (Warne et al., 2002).

Orinoco sands is quartzose, with a few feldspars (K-feldspar >> plagioclase) and metasedimentary to minor plutonic and sedimentary rock fragments (Potter, 1978; Johnsson et al., 1988; 1991). Sands of the Apure River tributary are quartzo-lithic in the Andean upper reaches, with epidote, amphibole, zircon and garnet as main heavy minerals. Due to reworking of weathered foreland-basin sediments, unstable components are progressively depleted with increasing distance from the mountain front, and sand becomes eventually quartzose as that of the Orinoco, although with more feldspars, rock fragments and higher K-feldspar/plagioclase ratio (Johnsson et al., 1988). Epidote and amphibole do not show downstream changes, whereas zircon tends to be enriched and apatite and garnet selectively depleted (Morton and Johnsson, 1993). Heavy-mineral analysis of modern sediments on the Guiana Shelf allowed recognition of different provinces (Nota, 1958; Imbrie and Van Andel, 1964): I) the area offshore of the Orinoco Delta, characterized by an epidote-amphibole suite; II) the adjacent shelf in the west offshore Trinidad, characterized by a zircon-epidote suite; III) the area offshore the Guiana Shield in the east, characterized by a staurolite-rich suite. Other heavy minerals, found also further east offshore the Essequibo and Demerara deltas, include sillimanite, tourmaline, rutile and andalusite. Garnet and kyanite are minor; hypersthene occurs locally.

8.2.3. Barbados Island

Barbados Island is the only emerged part of the accretionary prism, narrowing from 250 km in the south to 100 km in the north (Figure 8.1.; Moore et al., 1990). The marked change in thickness of Cenozoic sediments, decreasing northwards from > 6 km on the Venezuelan passive margin to 0.5 km on the Tiburon ridge that constitutes a topographic barrier for turbidites, reflects dominant supply from the Orinoco Delta (Faugères et al., 1993). Turbiditic mudrocks and sandstones, interbedded with pelagic oozes and more abundant during the Middle Eocene to Late Oligocene but continuing throughout the Neogene, are being deposited on the floor of piggyback basins bounded by anticlinal ridges, and are fed by

erosional canyons cutting through the tectonic structures (Beck et al., 1990; Mascle et al., 1990; Faugères et al., 1991).

With the exception of minor volcanic ash, the rock succession in Barbados is entirely sedimentary in origin, demonstrating its geological independence from the volcanic arc of the Lesser Antilles. About 15% are the deformed deep-marine Cenozoic sediments of the oceanic complex, exposed over an area of 40 km^2 in a triangular region of NE Barbados called the Scotland District (Figure 8.3.). Two tectono-stratigraphic levels can be identified: a) the Basal Complex and its cover strata; b) the overlying allochthonous oceanic units (Speed and Larue 1982). The remaining 85% is represented by the unconformably overlying Pleistocene calcarenite cap. The Basal Complex includes the quartzose turbiditic sandstones and mudrocks of the "Scotland Formation" and the mélange of the Joes River Formation, overlain by radiolarite and hemipelagite deposits (Senn, 1940). These rocks, originally deposited in deep-sea fan and trench settings and subsequently offscraped and accreted to form the accretionary prism around the end of the Eocene, have undergone modest tectonic deformation since then (Speed et al., 1991).

The Barbados accretionary prism is unconformably capped by a SW-ward-dipping arch of Pleistocene calcarenite strata (Mesolella et al., 1970; Schellman and Radtke, 2004). These upraised coral reefs, completely eroded in the Scotland District, include three main terraces formed during the long-term uplift of the Barbados Ridge and documenting Late and Middle Pleistocene glacio-eustatic highstands. The older coral reefs are locally folded and reach their highest elevation in the central-northern part of the island (Taylor and Mann, 1991). The two main reef steps are known as the First High Cliff, located close to the coastline at 20 to 60 m a.s.l., and the Second High Cliff at 130 to 200 m a.s.l..

8.3. Sediment composition

In July 2011 to March 2013 we collected 15 sand samples on beaches from Barbados Island. From a quartered aliquot of the 32-355 □m class obtained by dry-sieving, heavy minerals were separated by centrifuging in Na polytungstate (density ~2.90 g/cm^3) and recovered by partial freezing with liquid nitrogen. 200 to 250 transparent heavy-mineral grains were counted by the area method on grain mounts. Different corrosion features and roundness of turbiditic-derived and volcanic arc-derived heavy mineral grains are analyzed (Figure 8.4.).

Beach sands on Barbados Island can be subdivided into two main compositional groups. Terrigenous sands in the Scotland District are dominantly quartzose, reflecting provenance principally from the Basal Complex (Figure 8.2B). Predominant monocrystalline quartz commonly shows rounded outlines and deep etching features (Figure 8.2B), reflecting both recycling and chemical weathering in subequatorial climate. Calcareous grains derived from the Pleistocene calcarenite cap may be quite abundant (≤ 55% of bulk sediment), as well as shale/siltstone grains recycled from turbidite units. A few plagioclase and K-feldspars are invariably present, and low-rank metasedimentary, volcanic and radiolarian-chert grains also frequently occur. Heavy-mineral assemblages have extremely poor concentration (tHMC ≤0.1) and include, in order of abundance, pyroxenes (hypersthene ≈ green augite), stable minerals (zircon > tourmaline >> rutile), metasedimentary minerals (andalusite, garnet, staurolite, kyanite, chloritoid, sillimanite), epidote, and minor amphiboles (hornblende and oxy-hornblende), olivine, titanite, apatite, monazite (Figure 8.3.).

In contrast, beach sands along the northern, western and southern coast consist monotonously of reworked bioclasts and other allochemical detritus, reflecting provenance from upraised Pleistocene reef terraces (Figure 8.2A). These calcareous sands include poor to extremely poor heavy-mineral assemblages (tHMC mostly ≤0.5) dominated by augitic clinopyroxene and hypersthene in subequal amounts. Subordinate hornblende occurs in the northeast, whereas olivine is most abundant in beach sands to the west, south and southeast (Figure 8.3.). Ferromagnesian minerals are commonly euhedral and less corroded that stable and metasedimentary minerals (Figure 8.4.; Andò et al., 2012).

Beach	Sample	tHM%w	Zrn	Tur	Ttn	Ap	Ep	Grt	Cld	St	And	Ky	Sil	Amp	Cpx	Hy	Ol	&	Total	Rt	TiOx	monazite	&
River Bay	S4239	0,5	0	0	0	0	4	0	0	0	0	0	0	2	59	32	1	0	100,0	0,0	0,0	0,0	0,0
Creek Pie Corner	S4240	0,4	1	0	0	0	2	1	1	1	0	1	0	4	46	40	6	0	100,0	0,0	0,0	0,0	0,0
Pico Tenerife	S4242	0,2	0	0	0	0	2	0	0	0	0	0	0	3	60	31	3	0	100,0	0,0	0,0	0,0	0,0
Morgan Lewis	S4243	0,07	14	8	2	0	27	6	2	2	3	2	0	6	14	17	0	0	100,0	0,0	0,0	0,0	0,0
Windy Hill	S4247	0,1	25	7	1	0	8	5	1	3	8	1	0	0	18	21	1	0	100,0	0,0	0,0	0,5	0,0
Cattlewash	S4249	0,07	33	14	1	1	5	7	1	4	20	3	0	0	4	8	0	1	100,0	1,1	0,0	0,0	0,0
Bathsheba	S4251	0,06	7	7	1	1	15	6	1	1	9	1	2	0	26	23	2	0	100,0	0,0	0,0	0,0	0,0
St Martin's	S4252	0,8	9	0	0	0	0	1	0	0	0	0	0	0	13	20	2	55	100,0	0,0	0,0	0,0	55
Bath	S4253	0,03	0	1	0	0	1	0	1	0	0	0	0	0	60	35	2	0	100,0	0,0	0,0	0,0	0,0
Bottom Bay	S4254	0,04	0	0	0	0	0	0	0	0	0	0	0	1	44	54	1	0	100,0	0,0	0,0	0,0	0,0
Foul Bay	S4255	0,004	0	0	0	1	0	0	0	0	0	0	0	1	43	46	8	0	100,0	0,0	0,0	0,0	0,0
Oistins	S4256	0,3	0	1	0	0	0	0	0	0	0	0	0	1	44	38	15	0	100,0	0,0	0,0	0,0	0,0
Fitt's Village	S4257	0,3	0	1	0	0	1	1	0	0	0	0	0	1	27	63	8	0	100,0	0,0	0,0	0,0	0,0
St Francis	S4259	0,1	0	0	0	0	1	0	0	0	0	0	0	0	30	52	16	0	100,0	0,0	0,0	0,0	0,0
Smithon's Bay	S4261	0,04	0	1	0	0	4	1	0	0	0	0	0	2	41	40	10	1	100,0	0,5	0,5	0,0	0,0
Orinoco	20%	0,6	38	6	0	0	19	3	0	1	2	0	3	24	2	0	0	4	100,0	3	1,2	0,0	0
Orinoco diagenizzato		0,5	51	8	0	0	26	3	0	2	2	0	3					5	100,0	26			
Scotland District beaches		**0,09**	**20**	**9**	**1**	**0**	**14**	**6**	**1**	**2**	**10**	**1**	**0**	**2**	**15**	**17**	**1**	**0**	100,0				
		0,04	*11*	*3*	*0*	*1*	*10*	*1*	*0*	*2*	*7*	*1*	*1*	*3*	*9*	*6*	*1*	*1*					
		0,20	**0**	**0**	**0**	**0**	**1**	**0**	**0**	**0**	**0**	**0**	**0**	**2**	**45**	**43**	**7**	**0**					
		0,19	*0*	*0*	*0*	*0*	*2*	*0*	*0*	*0*	*0*	*0*	*0*	*1*	*12*	*10*	*6*	*0*					

Table 8.1. *Heavy mineral composition of Barbados beach sands.*

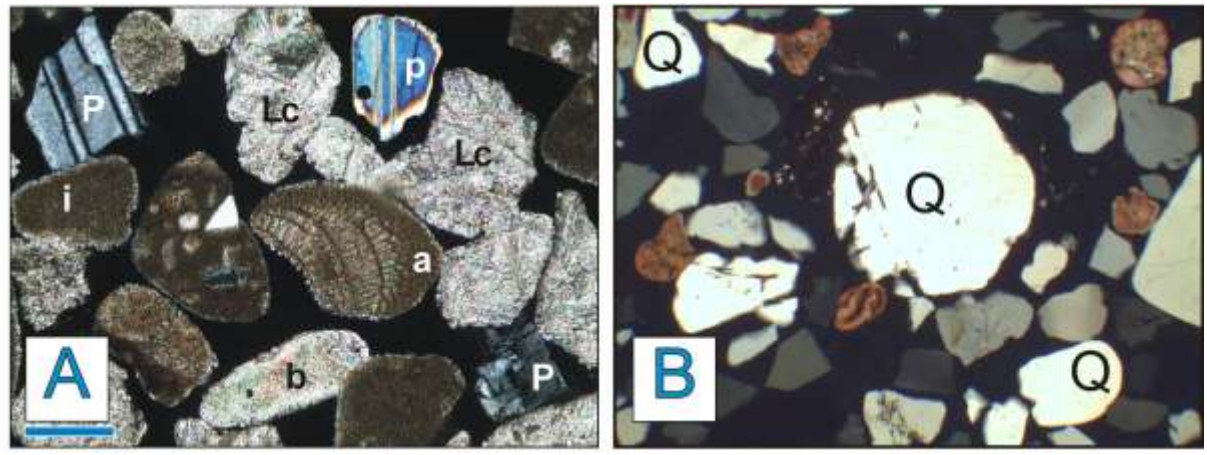

Figure 8.2. *Beach sands on Barbados Island. A) Calcareous grains recycled from Pleistocene carbonate rocks (Lc), mixed with euhedral plagioclase (P) and pyroxene (p) derived from interbedded volcanic ash layers and with allochems (a= coralline red algae; b= bioclasts; i= intraclasts) in beach sand of western Barbados (Fitt's Village). B) Recycled quartz grains displaying deep etching and lobate outline indicative of extensive chemical weathering in subequatorial soils, documenting recycling of turbidites fed long distance by the Orinoco River (Windy Hill). All photos with crossed polars; blue bar = 250 μm.*

8.4.Multiple heavy-mineral sources

Modern sands on Barbados Island reflect mixing in various proportions of detritus from Basal Complex quartzose turbidites and their stratigraphic and tectonic cover (Scotland District), from the Pleistocene calcarenite cap, and from volcanic ash layers ultimately derived from the Lesser Antilles. Sediment of Barbados are partly derived from erosion of rocks exposed on the island (including turbidites derived long-distance from South America; Velbel, 1985), and partly transported by winds from external sources. A lot of works highlight the importance of long-range transport of dust and indicate that large quantities of dust are being carried out of the North Africa and across the Atlantic by trade winds (Prospero and Lamb, 2003; Prospero et al., 2002; Kallos et al., 2006; Muhs, 2001).

The eruptions of active volcanoes of the Lesser Antilles arc system also contribute with ash-fall tephra carried out by anti-trade winds (eruption of the Soufrière of St. Vincent in 1902, Carey and Sigursson, 1978; explosive eruption of the Soufriere of St. Vincent in 1979, Brazier et al., 1982; Muhs, 2001)**.**

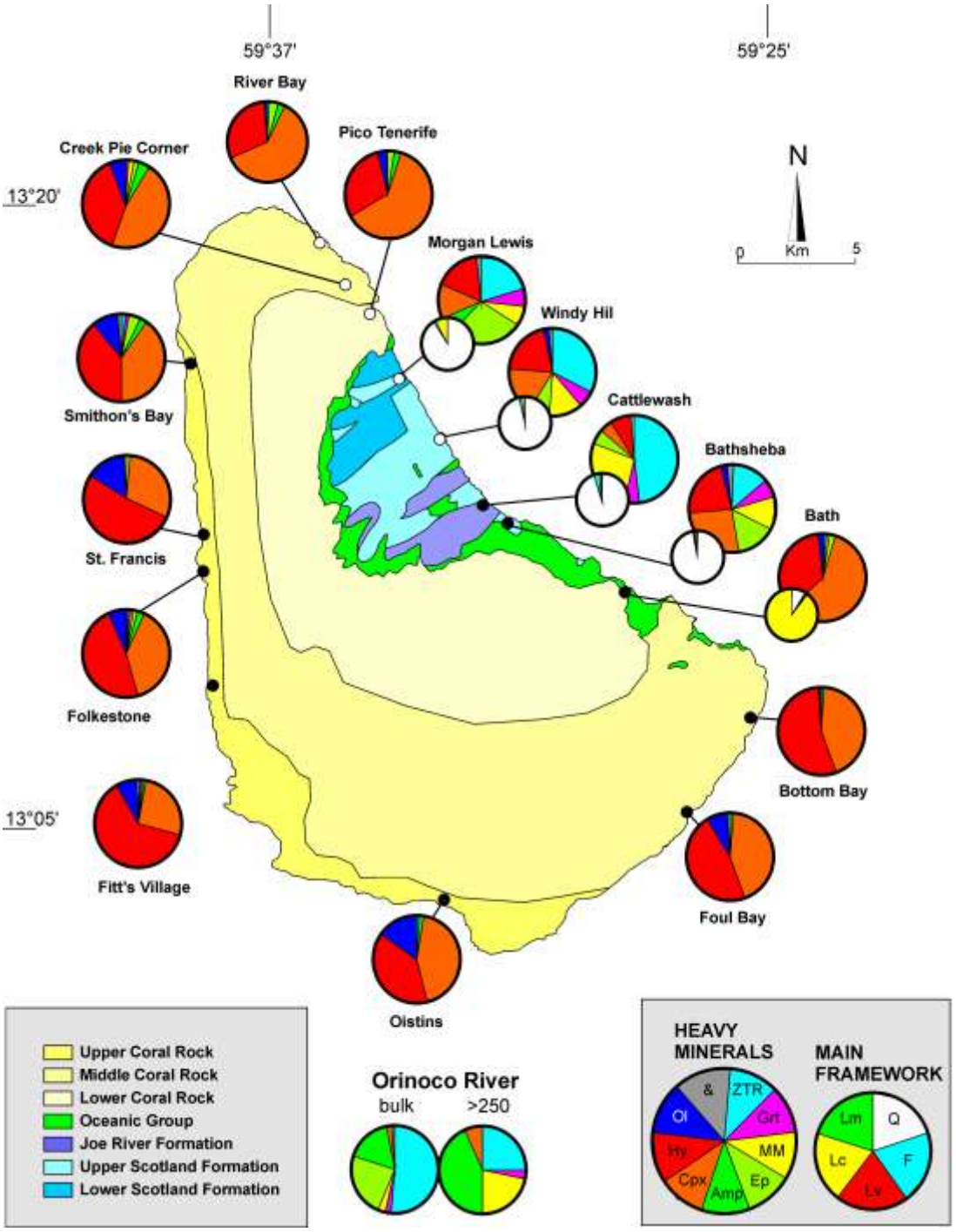

Figure 8.3. *Petrographic composition and heavy minerals of modern beaches on Barbados Island. Location of studied samples is shown. Q= quartz; F= feldspar; L= lithic grains (Lv= volcanic; Lc= carbonate; Lm= metamorphic). ZTR= zircon + tourmaline + rutile; Grt= garnet; MM= chloritoid + staurolite + andalusite + kyanite + sillimanite; Ep= epidote-group minerals; Amp= amphibole; Cpx= clinopyroxene; Hy= hypersthene; Ol= olivine; &= other minerals (mainly titanite and apatite).*

8.4.1 The turbiditic source (Recycled Clastic Provenance)

Most minerals are recycled from accreted orogen-derived Orinoco turbidites (Figure 8.5.; Faugères et al., 1991).

Turbiditic rocks that represent the bulk of material accreted in subduction complexes range from generally older mud-dominated distal-fan units to generally younger sand-dominated proximal-fan units (Garzanti et al., 2013); calcareous turbidites may also be prominent, as for the the Helminthoid Flysch of the northern Apennines (Zuffa, 1987; Garzanti et al., 1998; 2002a; Di Giulio et al., 2003). The mineralogy of such parent rocks is controlled not only by their original provenance but also strongly by the intensity of chemical processes undergone during weathering prior to deposition and subsequently during diagenesis (Johnsson, 1993; Morton and Hallsworth, 2007). Significant incidence of both weathering in the subequatorial Orinoco catchment (Johnsson et al., 1988; 1991) and intrastratal dissolution in Basal Complex sandstones is reflected in the quartzose composition of modern sands, containing mostly monocrystalline quartz with rounded outline or deep etching (Figure 2A) and depleted heavy-mineral assemblages with mainly stable and semi-stable minerals (epidote, zircon, tourmaline and rutile). Petrographic observations indicate that epidote grains in sandstones are detrital in origin and virtually invariably corroded, thus ruling out locally extensive authigenic growth, and rather indicating strong influence of intrastratal dissolution. It has long been known that heavy-mineral suites in ancient sandstones may be severely depleted during burial diagenesis (Morton and Hallswoth, 2007).

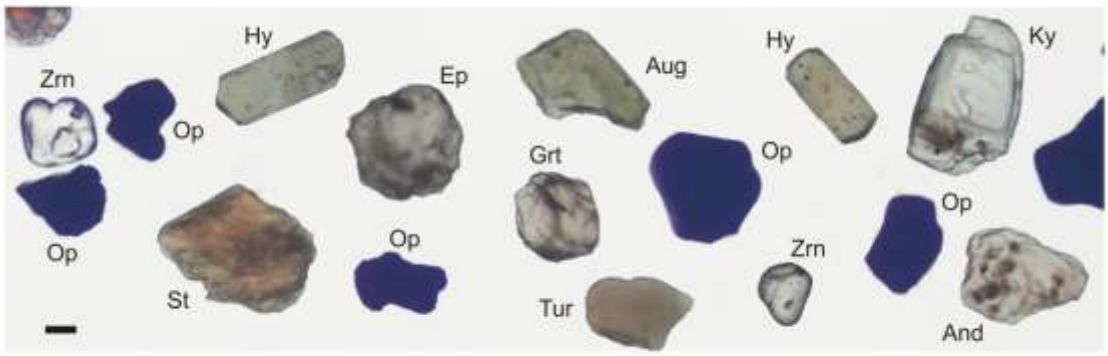

Figure 8.4. *Different behaviour of heavy minerals from beach sand of Windy Hill (Scotland District). Pyroxenes (augite and hyperstene), from volcanic arc, are commonly euhedral and less corroded and less rounded and subrounded that stable and metasedimentary minerals, from turbiditic source (zircon, tourmaline, garnet, epidote, kyanite, andalusite, staurolite). Photo with one nicol; black bar = 63 μm.*

8.4.2 The volcanic source (Magmatic Arc Provenance)

Mineralogical signatures characterized by augitic clinopyroxene frequently associated with abundant and even dominant hypersthene reflect the calc-alkaline character of subduction-related magmas (Garzanti and Andò, 2007b). Heavy-mineral distribution in beaches of Barbados Island reflects the trend displayed along the Lesser Antilles arc: from dominant andesites and subordinate felsic products in the central group of islands (e.g., St. Lucia), highlighted by the presence of oxy-hornblende or kaersutitic amphibole and biotite in the northern modern sediments of Barbados, to increasing incidence of basalts in the southern group of islands (e.g., St. Vincent) revealed by local predominance of olivine over pyroxene and of glass-rich lathwork lithics over plagioclase in the southernmost beaches of Barbados (Figure 8.5.).

The same pyroxene types (augitic pyroxenes and hyperstene) occur all around the island and are mixed with detritus produced by erosion of local source rocks in beach sands of the Scotland District. This reveals reworking of widespread volcaniclastic layers originally deposited as ash fall derived from the central part of the Lesser Antilles arc.

Figure 8.5. *Ash-fall dispersal pattern and long distance transport from Orinoco river.*

8.5. Conclusion

As invariably is the case with orogenic sediments, “Subduction Complex Provenance” is composite. Sand dominantly recycled from accreted orogen-derived turbidites mixes with subordinate amounts of detritus from sources including ophiolitic mélange, arc-related volcanic layers and shallow-water calcarenites widespread in tropical settings. Local contribution from Lesser Antilles volcanic arc can be dominant (up to 98% of the heavy mineral suite) as highlighted by widespread occurrence of olivine and pyroxenes usually lacking in the turbidites (2% of Orinoco-derived heavy minerals).

The most evident distinction from the main type of orogenic provenance (i.e., sediments shed from Alpine-Himalayan collision orogens) is the lack of first-cycle detritus from metamorphic rocks. Barbados Island consists in fact entirely of deformed deep-sea sediments offscraped at the trench and unconformably overlain by Pleistocene coral reefs as indicated by poor to extremely poor heavy mineral assemblages (tHMC never exceeding 1).

References

Acharyya, S.K., 2007. Collisional emplacement history of the Naga–Andaman ophiolites and the position of the eastern Indian suture. Journal of Asian Earth Sciences 29, 229–242.

Alam, M., Alam, M.M., Curray, J.R., Chowdhury, M.L.R., Gani, M.R., 2003. An overview of the sedimentary geology of the Bengal Basin in relation to the regional tectonic framework and basin-fill history. Sedimentary Geology 155, 179–208.

Allen, R., Carter, A., Najman, Y., Bandopadhyay, P.C., Chapman, H.J., Bickle, M.J.,Garzanti, E., Vezzoli, G., Andò, S., Foster, G.L., Gerring, C., 2007. New constraints on the sedimentation and uplift history of the Andaman–Nicobar accretionary prism, South Andaman Island. In: Draut, A., Clift, P.D., Scholl, D.W. (Eds.), Formation and applications of the sedimentary record in arc collision zones: Geological Society of America, Special Paper, 436, pp. 223–255.

Allen, R., Najman, Y., Carter, A., Barfod, D., Bickle, M.J., Chapman, H.J., Garzanti, E., Vezzoli, G., Andò, S., Parrish, R.R., 2008. Provenance of the Tertiary sedimentary rocks of the Indo-Burman Ranges, Burma (Myanmar): Burman arc or Himalayanderived? Journal of the Geological Society of London 165, 1045–1057.

Andò, S., Garzanti, E., 2013. Raman spectroscopy in heavy-mineral studies. In: Scott, R., Smyth, H., Morton, A., Richardson, N. (Eds.), Sediment Provenance Studies in Hydrocarbon Exploration and Production, 386. Geological Society London, Special Publication. http://dx.doi.org/10.1144/SP386.2.

Andò, S., Bersani, D., Vignola, P., Garzanti, E., 2009. Raman spectroscopy as an effective tool for high-resolution heavy-mineral analysis: Examples from major Himalayan and Alpine fluviodeltaic systems. Spectrochimica Acta Part A: Molecular and Biomolecular Spectroscopy 73, 450-455.

Andò, S., Garzanti, E., Padoan, M., Limonta, M., 2012. Corrosion of heavy minerals during weathering and diagenesis: a catalogue for optical analysis. In: von Eynatten, H., Critelli, S., Ingersoll, R.V., Weltje, G.J., Actualistic Models of Sediment Generation. Sedimentary Geology 280, pp. 165-178.

Andò, S., Morton, A., Garzanti, E., 2013. Metamorphic grade of source rocks revealed by chemical fingerprints of detrital amphibole and garnet. In: Scott, R., Smyth, H., Morton, A., Richardson, N. (Eds.), Sediment Provenance Studies in Hydrocarbon Exploration and Production, 386. Geological Society London, Special Publication. http://dx.doi.org/10.1144/SP386.5.

Artini, E., 1891. Intorno alla composizione mineralogica delle sabbie del Ticino. Giornale di Mineralogia, Cristallografia e Petrologia (Pavia) 2, 177-195.

Artini, E., 1927. Osservazioni mineralogiche sui materiali incontrati da due trivellazioni profonde recentemente seguite a Milano. Atti Società Italiana Scienze Naturali, 66. Museo Civico di Storia Naturale, Milano, pp. 1–13.

Ayling, B., Rose, P., Petty, S., Zemach, E., Drakos, P., 2012. QEMSCAN (quantitative evaluation of minerals by scanning electron microscopy): capability and application to fracture characterization in geothermal systems. PROCEEDINGS, Thirty-SeventhWorkshop on Geothermal Reservoir EngineeringStanford University, Stanford, California, January 30-February1, 2012 SGP-TR-194.

Bandopadhyay, P.C., 2005. Discovery of abundant pyroclasts in the Namunagarh Grit, South Andaman: evidence for arc volcanism and active subduction during the Palaeogene in the Andaman area. Journal of Asian Earth Sciences 25, 95–107.

Bandopadhyay, P.C., 2012. Re-interpretation of the age and environment of deposition of Paleogene turbidites in the Andaman and Nicobar Islands, Western Sunda Arc. Journal of Asian Earth Sciences 45, 126–137.

Barber, A.J., 2013. The origin of mélanges: cautionary tales from Indonesia. Journal of Asian Earth Sciences. http://dx.doi.org/10.1016/j.jseaes.2012.12.021.

Barrell, J., 1908. Relations between climate and terrestrial deposits. Journal of Geology 16, 159-190. 255-295. 363- 384.

Basu, A., 1985. Influence of climate and relief on compositions of sands released at source areas. In: Provenance of arenite. G.G. Zuffa (ed), NATO-ASI serie C, 148, Dordrecht, 408 p.

Berner, R.A., Sjöberg, E.L., Velbel, M.A., Krom, M.D., 1980. Dissolution of pyroxenes and amphiboles during weathering. Science 207, 1205–1206.

Bernet, M., Brandon, M.T., Garver, J.I., and Molitor, B., 2004. Downstream changes of Alpine zircon fission-track ages in the Rhône and Rhine Rivers. Journal of Sediment Research 74, 82-94.

Bhattacharjee, C.C., 1991. The ophiolites of northeast India — a subduction zone ophiolite complex of the Indo-Burman orogenic belt. Tectonophysics 191, 213–222.

Blatt, H., 1967. Provenance determinations and recycling of sediments. Journal of Sedimentary Petrology 37, 1031–1044.

Blatt, H., Jones, R.L., 1975. Proportions of exposed igneous, metamorphic, and sedimentary rocks. Geological Society of America Bulletin 86, 1085–1088.

Boswell, P. G. H., 1933. On the mineralogy of sedimentary rocks. London: Thomas Murby.

Boudier, F., Juteau, T., 2000. The ophiolite of Oman and United Arab Emirates. Marine Geophysical Researches 21, 145–407.

Bramlette, M.N., 1941. The stability of minerals in sandstone. Journal of Sedimentary Petrology 11, 32–36.

Brammal, A., 1928. Dartmoor detritals: a study in provenance. Proceedings of the Geological Association 39, 27-48.

Brantley, S.L., 2003. In: Drever, J.I., Holland, H.D., Turekian, K.K. (Eds.), Reaction kinetics of primary rock-forming minerals under ambient conditions. Treatise on Geochemistry, 5. Elsevier, Amsterdam, pp. 73–117.

Brantley, S.L., Crane, S.R., Crerar, D.A., Neumann, R., Stallard, R., 1986. Dissolution at dislocation etch pits in quartz. Geochimica et Cosmochimica Acta 50, 2349–2361.

Briggs, L.I., McCulloch, D.S., Moser, F., 1962. The hydraulic shape of sand particles. Journal of Sedimentary Petrology 32, 645–656.

Brunnschweiler, R.O., 1974. Indoburman Ranges. Geological Society of London, Special Publication 4, 279–299.

Brush, L.M., Jr., 1965. Sediment sorting in alluvial channels: In: Middleton, G.V. (Ed.), Primary Sedimentary Structures and their Hydrodynamic Interpretation. Society of Economic Paleontologists and Mineralogists Special Publication 12, pp. 25–33.

Bryan, K.R, Robinson, A., Briggs, R. M. 2007 Spatial and temporal variability of titanomagnetite placer deposits on a predominantly black sand beach. Marine Geology 236, 1-2, 45-59.

Burley, S.D., Kantorowicz, J.D., Waugh, B., 1985. Clastic diagenesis. In: Brenchley, P.J., Williams, B.P.J. (Eds.), Sedimentology: Recent Developments and Applied Aspects. Geology Society of London, Special Publications 18, 189–226.

Callahan, J. 1987. A non-toxic heavy liquid and inexpensive filters for separation of mineral grains. Journal of Sedimentary Petrology. 57, 765-6

Carey, S. N., Sigurdsson, H., 1978. Deep-sea evidence for distribution of tephra from the mixed magma eruption of the Soufriere on St. Vincent, 1902: Ash turbidites and air fall. Geology 6, 271– 274.

Carrapa, B., Di Giulio, A., 2001. The sedimentary record of the exhumation of a granitic intrusion into a collisional setting: the lower Gonfolite Group, Southern Alps, Italy. Sedimentary Geology 139, 217–228.

Carroll, D., 1953. Weatherability of zircon. Journal of Sedimentary Research 23, 106–116.

Cavazza, W., Gandolfi, G., 1992. Diagenetic processes along a basin-wide marker bed as a function of burial depth. Journal of Sedimentary Petrology 62, 261–272.

Cavazza, W., Zuffa, G.G., Camporesi, C., Ferretti, C., 1993. Sedimentary recycling in a temperate climate drainage basin (Senio River, north-central Italy): composition of source rock, soil profiles, and fluvial deposits. In: Johnsson, M.J., Basu, A. (Eds.), Processes Controlling the Composition of Clastic Sediments: Geological Society of America, Special Paper, 284, pp. 247–261.

Chakraborty, P.P., Pal, T., 2001. Anatomy of a forearc submarine fan: Upper Eocene–Oligocene Andaman flysch Group, Andaman Islands, India. Gondwana Research 4, 477–487.

Cheng, N.S.,1997. Simplified settling velocity formula for sediment particle. Journal of Hydraulic Engineering 123,149–152.

Clarke, D.B., Dorais, M., Barbarin, B., Barker, D., Cesare, B., Clarke, G., El Baghdadi, M., Erdmann, S., Förster, H.-J., Gaeta, M., Gottesmann, B., Jamieson, R.A., Kontak, D.J., Koller, F., Gomes, C.L., London, D., Morgan, G.B., Neves, L.J.P.F., Pattison, D.R.M., Pereira, A.J.S.C., Pichavant, M., Rapela, C.W., Renno, A.D., Richards, S., Roberts, M., Rottura, A., Saavedra, J., Sial, A.N., Toselli, A.J., Ugidos, J.M., Uher, P., Villaseca, C., Visonà, D., Whitney, D.L., Williamson, B., Woodard, H.H., 2005. Occurrence and origin of andalusite in peraluminous felsic igneous rocks. Journal of Petrology 46, 441–472.

Cleary, W.J., Conolly, J.R., 1972. Embayed quartz grains in soils and their significance. Journal of Sedimentary Petrology 42, 899–904.
Cochran, J.R., 2010. Morphology and tectonics of the Andaman Forearc, northeastern Indian Ocean. Geophysical Journal International 182, 631–651.

Colin, F., Alarcon, C., Vieillard, P., 1993. Zircon: an immobile index in soils? Chemical Geology 107, 273–276.

Cox, R., Lowe, D.R., 1995. A conceptual review of regional-scale controls on the composition of clastic sediment and the co-evolution of continental blocks and their sedimentary cover. Journal of Sedimentary Research 65, 1–12.

Cremeens, D.L., Darmody, R.G., Jansen, I.J., 1987. SEM analysis of weathered grains: pretreatment effects. Geology 15, 401–404.

Crook, K.A.W., 1968. Weathering and roundness of quartz sand grains. Sedimentology 11, 171–182.

Crook, K.A.W., 1974. Lithogenesis and geotectonics: the significance of compositional variations in flysch arenites (graywackes). In: Dott, J.R., and Shaver, R.H., (eds). Modern and ancient geosynclinals sedimentation. Society of Economic Paleontologists and Mineralogists, Special Publications 19, 304-310.

Curray, J.R., 2005. Tectonics and history of the Andaman Sea region. Journal of Asian Earth Sciences 25, 187–232.

Curray, J.R., Emmel, F.J., Moore, D.G., 2003. The Bengal Fan: morphology, geometry, stratigraphy, history, and processes. Marine and Petroleum Geology 19, 1191–1223.

Dahlen, F.A., 1990. Critical taper model of fold-and-thrust belts and accretionary wedges. Annual Review of Earth and Planetary Sciences 18, 55–99.

Daly, R.A., Manger, G.E., Clark, S.P., 1966. Density of rocks. Section 4, Handbook of Physical Constants. Geological Society of America Memoirs, 19–26.

DeCelles, P.G., Gehrels, G.E., Najman, Y., Martin, A.J., Carter, A., Garzanti, E., 2004. Detrital geochronology and geochemistry of Cretaceous–Early Miocene strata of Nepal: implications for timing and diachroneity of initial Himalayan orogenesis. Earth and Planetary Science Letters 227, 313–330.

De Filippi, F. 1839. Sulla costituzione geologica della pianura e delle colline della Lombardia. Annuali Universali di Statistica 59, 225-248.

Dick, A.B., 1887. On zircon and other minerals contained in sands. Nature 36, 1-92.

Dickinson, W.R., 1970. Interpreting detrital modes of greywacke and arkose. Journal of Sedimentary Petrology 40, 695-707.

Dickinson, W.R., 1974. Plate tectonics and sedimentation. In: Dickinson, W.R. (ed). Tectonics and sedimentation. Society of Economic Paleontologists and Mineralogists, Special Publications 22, 1-27.

Dickinson, W.R., 1985. Interpreting provenance relations from detrital modes of sandstones. In: Zuffa, G.G. (Ed.), Provenance of Arenites. NATO-ASI Series, 148. Reidel Publishing Company, Dordrecht, pp. 333–361.

Dickinson, W.R., 1988. Provenance and sediment dispersal in relation to paleotectonics and paleogeography of sedimentary basins. In: Kleinspehn, K.L., Paola, C. (Eds.), New Perspectives in Basin Analysis. Springer, New York, pp. 3–25.

Dickinson, W. R., 1994. Natural beach placer analogous to prehistoric island temper. The Journal of the Polynesian society 103, 2, 217-219.

Dickinson, W.R., Suczek, C.A., 1979. Plate tectonics and sandstone composition. American Association of Petroleum Geologists Bulletin 63, 2164–2172.

Dickinson, W. R. and Valloni, R., 1980. Plate setting and provenance of sand in modern ocean basin. Geology 8, 82-86.

Di Giulio, A., 1999. Mass transfer from the Alps to the Apennines: volumetric constraints in the provenance study of the Macigno-Modino source-basin system, Chattian-Aquitanian, northwestern Italy. Sedimentary Geology 124, 69–80.

Di Giulio, A., Carrapa, B., Fantoni, R., Gorla, L., and Valdisturlo, A., 2001. Middle Eocene to Early Miocene sedimentary evolution of the western Lombardian segment of the South Alpine foredeep (Italy). Int. Journal of Earth Sciences 90, 534-548.

Di Giulio, A., Ceriani, A., Ghia, E., Zucca, F., 2003. Composition of modern stream sands derived from sedimentary source rocks in a temperate climate (Northern Apennines, Italy). Sedimentary Geology 158, 145–161.

Doglioni, C., 1990. The global tectonic pattern. Journal of Geodynamics 12, 21-38.

Doglioni, C.; Harabaglia, P.; Merlini, S.; Mongelli, F.; Peccerillo, A.; and Piromallo, C., 1999. Orogens and slabs vs. their direction of subduction. Earth-Science Reviews 45, 167–208.

Doglioni, C.; Carminati, E.; and Cuffaro, M. 2006. Simple kinematics of subduction zones. International Geology Review 48, 479-493.

Dott, R.H., 2003. The importance of eolian abrasion in supermature quartz sandstones and the paradox of weathering on vegetation-free landscapes. Journal of Geology 111, 387–405.

Dryden, A. L., 1931. Accurancy on percentage representation of heavy mineral frequencies. Proceedings of the National Academy of Sciences 17, 233-8.

Dye, T.S., Dickinson, W.R., 1996. Sources of sand tempers in prehistoric Tongan pottery. Geoarchaeology 11, 141–164.

Ebinger, C.J., 1989. Tectonic development of the western branch of the East-African rift system. Geological Society of America Bulletin 101, 885–903.

Ebinger, C., Furman, T., 2003. Geodynamical setting of the Virunga Volcanic Province. Acta Vulcanologica 14, 1–8.

Edelman, C. H. 1931. Over bloedverwantschap van sedimenten in verban met het zware mineralen onderzoek. Geol. Mijnb 10, 122-124.

Edelman, C. H. 1933. Petrologische provincies in het nederlandsche Kwartair. Ph.. thesisi, Centen's Uitg Mij., Amsterdam. 104.

Edelman, C.H., Doeglas, D.J., 1932. Reliktstructuren detritischer Pyroxene und Amphibole. Tschermaks Mineralogische und Petrographische Mitteilungen 42, 482–490.

Edelman, C.H., Doeglas, D.J., 1934. Über Umwandlungserscheinungen an detritischem Staurolith und anderen Mineralien. Tschermaks Mineralogische und Petrographische Mitteilungen 44, 225–234.

Fleet, W. F., 1926. Petrological notes on the Old Red Sandstone of the west Midlands. Geological Magazine 63, 505-516.

Flores, R.M., Shideler, G.L., 1978. Factors controlling heavy mineral variations on the South Texas outer continental shelf, Gulf of Mexico. Journal of Sedimentary Petrology 48, 269–280.

Fontana, D., Parea, G.C., Bertacchini, M., Bessi, P., 2003. Sand production by chemical and mechanical weathering of well lithified siliciclastic turbidites of the Northern Apennines (Italy). In: Valloni, R., Basu, A. (Eds.), Quantitative Provenance Studies in Italy: Memorie Descrittive della Carta Geologica d' Italia, 61, pp. 51–60.

France-Lanord, C., Derry, L., Michard, A., 1993. Evolution of the Himalaya since Miocene time: isotopic and sedimentological evidence from the Bengal Fan. In: Treloar, P.J., Searle,M.P. (Eds.), Himalayan Tectonics. Special Publication, 74. Geological Society of London, pp. 603–622.

Friedman, G.M., 1961. Distinction between dune, beach, and river sands from their textural characteristics. Journal of Sedimentary Petrology 31, 514–529

Frihy, O.E., Lotfy, M.F., Komar, P., 1995. Spatial variations in heavy minerals and patterns of sediment sorting along the Nile delta, Egypt. Sedimentary Geology 97, 33–41

Friis, H., 1978. Heavy-mineral variability in Miocene marine sediments in Denmark: a combined effect of weathering and reworking. Sedimentary Geology 21, 169–188.

Friis, H., Johannesen, F.B., 1974. Late Tertiary weathering of fluvial deposits at La°sby, Denmark. Bulletin of The Geological Society of Denmark 23, 197–202.

Fuentes, F., DeCelles, P.G., and Gehrels, G.E., 2009. Jurassic onset of foreland basin deposition in northwestern Montana, USA: implications for along-strike synchroneity of Cordilleran orogenic activity. Geology 37, 379-382.

Furman, T., Graham, D., 1999. Erosion of lithosphericmantle beneath the East African Rift system: geochemical evidence from the Kivu volcanic province. Lithos 48, 237–262.

Galehouse, J. S., 1969. Counting grain mounts: number percentage vs. number frequency. Journal of Sedimentary Petrology 39, 812-15.

Galehouse, J. S., 1971. Point counting. In: Procedures in sedimentary petrology, R. E. Carver (ed), 385-407. New York: Wiley.

Gandolfi, G., Paganelli, L., Zuffa, G.G., 1983. Petrology and dispersal pattern in the Marnoso-Arenacea Formation (Miocene, Northern Apennines). Journal of Sedimentary Petrology 53, 493–507.

Gani, M.R., Alam, M.M., 2003. Sedimentation and basin-fill history of the Neogene clastic succession exposed in the southeastern fold belt of the Bengal Basin, Bangladesh: a high-resolution sequence stratigraphic approach. Sedimentary Geology 155, 227–270.

Garrels, R.M., 1986. Sediment cycling and diagenesis. In: Mumpton, F.A. (Ed.), Studies in Diagenesis: U.S. Geological Survey Bulletin, 1578, pp. 1–11.

Garzanti, E., Andò, S., 2007a. Heavy-mineral concentration in modern sands: implications for provenance interpretation. In: Mange, M.A., Wright, D.T. (Eds.), Heavy Minerals in Use. Developments in Sedimentology Series, 58. Elsevier, Amsterdam, pp. 517–545.

Garzanti, E., Andò, S., 2007b. Plate tectonics and heavy-mineral suites of modern sands. In: Mange, M.A., Wright, D.T. (Eds.), Heavy Minerals in Use. Developments in Sedimentology Series, 58. Elsevier, Amsterdam, pp. 741–763.

Garzanti, E., Van Haver, T., 1988. The Indus clastics: forearc basin sedimentation in the Ladakh Himalaya (India). Sedimentary Geology 59, 237–249.

Garzanti, E., Vezzoli, G., 2003. A classification of metamorphic grains in sands based on their composition and grade. Journal of Sedimentary Research 73, 830–837.

Garzanti, E., Scutellà, M., Vidimari, C., 1998. Provenance from ophiolites and oceanic allochthons:modern beach and river sands from Liguria and the Northern Apennines (Italy). Ofioliti 23, 65–82.

Garzanti, E., Andò, S., Scutellà, M., 2000. Actualistic ophiolite provenance: the Cyprus Case. Journal of Geology 108, 199–218.

Garzanti, E., Canclini, S., Moretti Foggia, F., Petrella, N., 2002a. Unraveling magmatic and orogenic provenances in modern sands: the back-arc side of the Apennine thrust-belt (Italy). Journal of Sedimentary Research 72, 2–17.

Garzanti, E., Vezzoli, G., Andò, S., 2002b. Modern sand from obducted ophiolite belts (Oman, U.A.E.). Journal of Geology 110, 371–391.

Garzanti, E., Andò, S., Vezzoli, G., Dell'Era, D., 2003. From rifted margins to foreland basins: investigating provenance and sediment dispersal across desert Arabia (Oman, UAE). Journal of Sedimentary Research 73, 572–588.

Garzanti, E., Vezzoli, G., Lombardo, B., Ando`, S., Mauri, E., Monguzzi, S., Russo, M., 2004a. Collision-orogen provenance (Western and Central Alps): detrital signatures and unroofing trends. Journal of Geology 112, 145–164.

Garzanti, E., Vezzoli, G., Ando` , S., France-Lanord, C., Singh, S.K., Foster, G., 2004b. Sediment composition and focused erosion in collision orogens: the Brahmaputra case. Earth and Planetary Science Letters 220, 157–174.

Garzanti, E., Vezzoli, G., Ando` , S., Paparella, P., Clift, P.D., 2005. Petrology of Indus River sands: a key to interpret erosion history of the Western Himalayan Syntaxis. Earth and Planetary Science Letters 229, 287–302.

Garzanti, E., Andò, S., Vezzoli, G., 2006a. The continental crust as a source of sand (southern Alps cross-section, northern Italy). Journal of Geology 114, 533-554

Garzanti, E., Andò, S., Vezzoli, G., Ali Abdel Megid, A., El Kammar, A., 2006b. Petrology of Nile River sands (Ethiopia and Sudan): sediment budgets and erosion patterns. Earth and Planetary Science Letters 252, 327–341

Garzanti, E., Doglioni, C., Vezzoli, G., Andò, S., 2007a. Orogenic belts and orogenic sediment provenances. Journal of Geology 115, 315–334.

Garzanti, E., Vezzoli, G., Andò, S., Lavè, J., Attal, M., France-Lanord, C., DeCelles, P., 2007b. Quantifying Sand Provenance and Erosion (Marsyandi River, Nepal Himalaya). Earth and Planetary Science Letters 258, 500-515.

Garzanti E., Vezzoli G., Andò S., 2008. Settling equivalence of detrital minerals and grain-size dependence of sediment composition. Earth and Planetary Science Letters 273, 138–151.

Garzanti, E., Andò, S., Vezzoli, G., 2009. Grain-size dependence of sediment composition and environmental bias in provenance studies. Earth and Planetary Science Letters 277, 422–432.

Garzanti, E., Andò, S., France-Lanord, C., Vezzoli, G., Najman, Y., 2010a. Mineralogical and chemical variability of fluvial sediments. 1. Bedload sand (Ganga–Brahmaputra, Bangladesh). Earth and Planetary Science Letters 299, 368–381.

Garzanti, E., Resentini, A., Vezzoli, G., Andò, S., Malusà, M.G., Padoan, M., Paparella, P., 2010b. Detrital fingerprints of fossil continental-subduction zones (Axial Belt Provenance, European Alps). Journal of Geology 118, 341–362.

Garzanti, E., Andò, S., France-Lanord, C., Galy,V., Censi, P., Vignola, P., 2011.Mineralogical and chemical variability of fluvial sediments. 2. Suspended-load silt (Ganga–Brahmaputra, Bangladesh). Earth and Planetary Science Letters 302, 107–120.

Garzanti, E., Resentini, A., Vezzoli, G., Andò, S., Malusà, M.G., Padoan, M., 2012. Forward compositional modelling of Alpine orogenic sand. Sedimentary Geology. doi:10.1016/ j.sedgeo.2012.03.012.

Garzanti, E., Limonta, M., Resentini, A., Bandopadhyay, P.C., Najman, Y., Andò, S., Vezzoli, G., 2013a. Sediment recycling at convergent plate margins (Indo-Burman Ranges and Andaman-Nicobar Ridge). Earth-Science Reviews 123, 113-132.

Garzanti, E., Padoan, M., Andò, S., Resentini, A., Vezzoli, G., Lustrino, M., 2013b. Weathering and relative durability of detrital minerals in equatorial climate: Sand petrology and geochemistry in the East African Rifts. Journal of Geology 121 (6), 547-580.

Garzanti E., M. Padoan, M. Setti, Y. Najman, L. Peruta, and I. M. Villa, 2013c. Weathering geochemistry and Sr-Nd fingerprints of equatorial upper Nile and Congo muds, Geochemestry Geophysics Geosystems 14, 292–316, doi:10.1002/ggge.20060.

Gazzi, P., 1965. On the heavy mineral zones in the geosyncline series, recent studies in the Northern Apennines, Italy. Journal of Sedimentary Petrology 35, 109–115.

Gazzi, P., Zuffa, G. G., Gandolfi, G. G., Paganelli, L., 1973. Provenienza e dispersione litoranea delle sabbie delle spiagge adriatiche fra le foci dell'Isonzo e del Foglia: inquadramento regionale. Memorie Della Società Geologica Italiana 12, 1-37.

Ghosh, B., Pal, T., Bhattacharya, A., Das, D., 2009. Petrogenetic implications of ophiolitic chromite from Rutland Island, Andaman—a boninitic parentage in supra-subduction setting. Mineralogy and Petrology 96, 59–70.

Ghosh, B., Morishita, T., Bhatta, K., 2012. Detrital chromian spinels from beach placers of Andaman Islands, India: a perspective view of petrological characteristics and variations of the Andaman ophiolite. Island Arc 21, 188–201.

Gilbert, C.M., 1954. Sedimentary rocks. In: Williams, H., Turner, F.J., and Gilbert, C.M., (eds). Petrography. San Francisco, W.H. Freeman and Co, 406 p.

Gilbert, G.K., 1909. The convexity of hilltops. Journal of Geology 17, 344–350.

Gill, J., 1981. Orogenic Andesites and Plate Tectonics. Springer-Verlag, Berlin, 390pp.

Grantham, J.H., Velbel, M.A., 1988. The influence of climate and topography on rock fragments abundance in modern fluvial sands of the southern Blue Ridge Mountains, North Carolina. Journal of Sedimentary Petrology 58, 219-227.

Grimm, W.D., 1973. Stepwise heavy mineral weathering in the Residual Quartz Gravel, Bavarian Molasse (Germany). : Contribution to Sedimentology, 1. Schweizerbart, Stuttgart, pp. 103–125.

Guzman-Speziale, M., Ni, J.F., 1996. Seismicity and active tectonics of the western Sunda arc. In: Yin, A., Harrison, T.M. (Eds.), The Tectonic Evolution of Asia. Cambridge University Press, pp. 63–84.

Hall, R., Smyth, H.R., 2008. Cenozoic arc processes in Indonesia: identification of the key influences on the stratigraphic record in active volcanic arcs. In: Draut, A.E., Clift, P.D., Scholl, D.W. (Eds.), Formation and Applications of the Sedimentary Record in Arc Collision Zones: Geological Society of America, Special Paper, 436, pp. 27–54.

Harrison, W. E., 1973. Heavy minerals of Horn Island, Northern Gulf of Mexico. Journal of Sedimentary Petrology. 43, 391-5.

Haughton, P.D. et al. 1991. Sedimentary provenance studies. Development in sedimentary provenance studies. Geology Society Special Publications 57, 1-11.

Heberer, B., Roser, G., Behrmann, J.H., Rahn, M., and Kopf, A., 2010. Holocene sediments from the Southern Chile Trench: a record of active margin magmatism, tectonics, and palaeoseismicity. Journal of Geology Society of London 167,539-553.

Hinderer, M., 2012. From gullies to mountain belts: A review of sediment budgets at various scales. Sedimentary Geology 280, 21-59.

Hoal, K. O., Botha, P., W.S.K., Forsyth, A., Butcher, A. R., 2007. Advanced mineralogy research: mineral characterization using QEMSCAN® techniques. GSA Denver Annual Meeting (28–31 October 2007).

Hodges, K.V., 2000. Tectonics of the Himalaya and southern Tibet from two perspectives. Geological Society of America Bulletin 112, 324–350.

Horbe, A.M.C., Horbe, M.A., Suguio, K., 2004. Tropical spodosols in northeastern Amazonas State, Brazil. Geoderma 119, 55–68.

Hubert, J.F., 1962. A zircon–tourmaline–rutile maturity index and the interdependence of the composition of heavy minerals assemblages with the gross composition and texture of sandstones. Journal of Sedimentary Petrology 32, 440–450.

Hubert, J.F., 1971. Analysis of heavy mineral assemblages. In: Carver, R.E. (Ed.), Procedures in Sedimentary Petrology. Wiley, New York, pp. 453–478.

Hughes, M.G., Keene, J.B., Joseph, R.G., 2000. Hydraulic sorting of heavy mineral grains by swash on a medium-sand beach. Journal of Sedimentary Research 70, 994–1004.

Hutton, C. O., 1950. Studies of heavy detrital minerals. Geological Society of America Bulletin 61, 635-710.

Illing, V. C., 1916. The oilfields of Trinidad. Proceedings of the Geological Association 27, 115.

Ingersoll, R.V., 1990. Actualistic sandstone petrofacies: discriminating modern and ancient source rocks. Geology 18, 733–736.

Ingersoll, R.V., Suczek, C.A., 1979. Petrology and provenance of Neogene sand from Nicobar and Bengal Fans, DSDP Sites 211 and 218. Journal of Sedimentary Petrology 49, 1217–1228.

Ingersoll, R.V., Bullard, T.F., Ford, R.L., Grimm, J.P., Pickle, J.D., Sares, S.W., 1984. The effect of grain size on detrital modes: a test of the Gazzi-Dickinson point-counting method. Journal of Sedimentary Petrology 54, 103-116.

Ingersoll, R.V., Dickinson, W.R., Graham, S.A., 2003. Remnant–ocean Submarine Fans: Largest Sedimentary Systems on Earth. In: Chan, M.A., Archer, A.W. (Eds.), Extreme depositional environments: mega end members in geologic time: Geological Society of America, Special Paper, 370, pp. 191–208.

Isacks, B.L., Barazangi, M., 1977. Geometry of Benioff zones: lateral segmentation and downward bending of the subducted lithosphere. In: Talwani, M., Pitman, W.M. III Eds, Island Arcs, Deep Sea Trenches and Back-arc Basins. AGU, Maurice Ewing Series 1, pp. 99–114.

Johnsson, M.J., 1993. The system controlling the composition of clastic sediments. In: Johnsson, M.J., Basu, A. (Eds.), Processes Controlling the Composition of Clastic Sediments: Geological Society of America, Special paper, 284, pp. 1–19.

Johnsson, M.J.; Stallard, R.F.; and Meade, R.H., 1988. First-cycle quartz arenites in the Orinoco River basin: Venezuela and Colombia. Journal of Geology 96, 263-277.

Johnsson, M.J., Stallard, R.F., Lundberg, N., 1991. Controls on the composition of fluvial sands from a tropical weathering environment: sands of the Orinoco River drainage basin, Venezuela and Colombia. Geological Society of America Bulletin 103, 1622–1647.

Kallos, G., Papadopoulos, A., Katsafados, P., Nickovic, S., 2006. Transatlantic Saharan dust transport: Model simulation and results. Journal of Geophysical Research 111, D09204, doi:10.1029/2005JD006207.

Karunakaran, C., Ray, K.K., Saha, S.S., 1968. Tertiary sedimentation in the Andaman–Nicobar geosyncline. Journal of the Geological Society of India 9, 32–39.

Karunakaran, C., Ray, K.K., Sen, C.R., Saha, S.S., Sarkar, S.K., 1975. Geology of Great Nicobar Island. Journal of the Geological Society of India 16, 135–142.

Karyampudi, V. M., 1979. A detailed synoptic-scale study of the structure, dynamics, and radiative effects of the Saharan air layer over the eastern tropical Atlantic during GARP Atlantic Tropical Experiment. M.S. thesis, 136 pp., Dep. of Meteorol., Pa. State Univ.

Karyampudi, V. M., et al., 1999. Validation of the Saharan dust plume conceptual model using Lidar, Meteosat, and ECMWF data, American Bulletin of Meteorological Society 80, 1045– 1075.

Kennedy, S.K., Walker, W., Forslund, B. 2002. Speciation and characterisation of heavy-metal contaminated soils using computer-controlled scanning electron microscopy. Environmental Forensics 3, 131-143.

Khan, P.K., Chakraborty, P.P., 2005. Two-phase opening of Andaman Sea: a new seismotectonic insight. Earth and Planetary Science Letters 229, 259–271.

Klein, G. DeV., 1963. Analisys and review of sandstone classifications in North American geological literature. Geological Society of America Bulletin. 74, 555-576.

Komar, P.D., 1985. The hydraulic interpretation of turbidites from their grain sizes and sedimentary structures. Sedimentology 32, 395–407.

Komar, P.D., 2007. The entrainment, transport and sorting of heavy minerals by waves and currents. In: Mange, M.A., Wright, D.T. (Eds.), Heavy Minerals in Use. Developments in Sedimentology Series, 58. Elsevier, Amsterdam, pp. 3–48.

Komar, P.D., Cui, B., 1984. The analysis of grain-size measurements by sieving and settling-tube techniques. Journal of Sedimentary Petrology 54, 603–614.

Komar, P. D. and Wang, C. 1984. Processes of selective grain transport and the formation of placers on beaches. The Journal of Geology, 92, 637-655.

Krumbein,W.C., 1941. Measurement and geological significance of shape and roundness of sedimentary particles. Journal of Sedimentary Petrology 11, 64–72.

Krumbein, W. C., Pettijohn, F. J., 1983. Manual of sedimentary petrography. New York: Appleton-Centuary.

Krynine, P.D., 1935. Arkose deposits in the humid tropics. A study of sedimentation in southern Mexico. American Journal of Science 29, 353-363.

Krynine, P.D., 1936. Geomorphology and sedimentation in the humid tropics. American Journal of Science 32, 292-306.

Krynine, P.D., 1941. Paleogeographic and tectonic significance of arkoses. Geological Society of America Bulletin 52, 1918- 1919.

Leeder, M., 2011. Complexity and the memory of landscape. Nature 469, 39.

Leith, C. J. 1950. Removal of iron oxide coating from mineral grains. Journal of Sedimentary Petrology 20, 174-176.

Lévy, M. 1878. Note sur quelques minéraux contenus dans les sables du Mesvrin, près Autun. Bulletin de la Société Française de Minéralogie et de Crystallographie 1, 39–41.

Lippard, S.J., Shelton, A.W., Gass, I.G., 1986. The Ophiolites of Northern Oman. Blackwell, London (178 pp.).

Lundgren, P., Giardini, D., 1994. Isolated deep earthquakes and the fate of subduction in the mantle. Journal of Geophysical Research 99, 15833–15842.

Mackie, W., 1923. The source of purple zircons in the sedimentary rocks of Scotland. Transactions of *the* Edinburgh Geological Society 11, 200–213.

Mackie, W., 1923. The principles that regulate the distribution of particles of heavy minerals in sedimentary rocks, as illustrated by the sandstones of the north-east of Scotland. Transactions of the Edinburgh Geological Society 11, 138–164.

Mallik, T. K., Vasudevan, V., Aby Verghese, P., Machado, T. 1987. The black sand placer deposits of Kerala beach, southwest India. Marine Geology 77, 1-2, 129-150.

Malpas, J., Moores, E., Panayiotou, A., Xenophontos, C., 1990. Oceanic crustal analogues. In: Proceedings of the Symposium ‘‘Troodos 1987’’, Geological Survey Department, Ministry of Agriculture and Natural Resources, Nicosia, 733pp.

Mange, M.A., Maurer, H.F.W., 1992. Heavy Minerals in Colour. Chapman and Hall, London (147 pp.).

Mange, M.A., Morton, A.C., 2007. Geochemistry of heavy minerals. In: Mange, M.A., Wright, D.T. (Eds.), Heavy Minerals in Use. Developments in Sedimentology Series, 58. Elsevier, Amsterdam, pp. 345–391.

Mariano, A. N., Ring, P. J., 1975. Europium activated cathodoluminescence in minerals. Geochimica et Cosmochimica Acta 39, 649-60.

Maurin, T., Rangin, C., 2009. Structure and kinematics of the Indo-Burmese Wedge: recent and fast growth of the outer wedge. Tectonics 28. http://dx.doi.org/10.1029/ 2008TC002276.

Mehring, J.L., McBride, E.F., 2007. Origin of modern quartzarenite beach sands in a temperate climate, Florida and Alabama, USA. Sedimentary Geology 201, 432–445.

Milliken, K.L., 1988. Loss of provenance information through subsurface diagenesis in Plio-Pleistocene sediments, northern Gulf of Mexico. Journal of Sedimentary Petrology 58, 992–1002.

Milner, H. B., 1962. Sedimentary petrography. London: Thomas Murby.

Mitchell, W.A., 1975. Heavy minerals. In: Gieseking, J.E. (Ed.), Soil Components II. Inorganic. Springer, New York, pp. 449–480.

Mitchell, A.H.G., 1993. Cretaceous–Cenozoic tectonic events in the western Myanmar (Burma) — Assam region. Journal of the Geological Society of London 150, 1089–1102.

Moeyersons, J., 2003. The topographic thresholds of hillslope incisions in southwestern Rwanda. Catena 50, 381–400.

Moore, G.F., 1979. Petrography of subduction zone sandstones from Nias Island, Indonesia. Journal of Sedimentary Petrology 49, 71–84.

Moore, G.F., Curray, J.R., Emmel, F.J., 1982. Sedimentation in the Sunda trench and forearc region. In: Leggett, J.K. (Ed.), Trench Forerarc Geology, 10. Geological Society London, Special Publication, pp. 245–258.

Moore, J.C., Rowe, C., Meneghini, F., 2007. How accretionary prisms elucidate seismogenesis in subduction zones. In: Dixon, T.H., Moore, J.C. (Eds.), The Seismogenic Zone of Subduction Thrust Faults. Columbia University Press, New York, pp. 288–313.

Moores, E.M., Robinson, P.T., Malpas, J., Xenophonotos, C., 1984. Model for the origin of the Troodos massif, Cyprus, and other mideast ophiolites. Geology 12, 500–503.

Moral Cardona, J.P., Gutierrez Mas, J.M., Sanchez Bellon, A., Domınguez-Bella, S., Martınez Lopez, J., 2005. Surface textures of heavy-mineral grains: a new contribution to provenance studies. Sedimentary Geology 174, 223–235.

Morley, C.K., 2012. Late Cretaceous–early Palaeogene tectonic development of SE Asia. Earth-Science Reviews 115, 37–75.

Morley, C.K., King, R., Hillis, R., Tingay, M., Backe, G., 2011. Deepwater fold and thrust belt classification, tectonics, structure and hydrocarbon prospectivity: a review. Earth-Science Reviews 104, 41–91.

Morton, A.C., 1984. Stability of detrital heavy minerals in Tertiary sandstones of the North Sea Basin. Clay Mineralogy 19, 287– 308.

Morton, A.C., 1985. Heavy minerals in provenance studies. In: Zuffa, G.G. (Ed.), Provenance of Arenites. : NATO-ASI Series, 148. Reidel, Dordrecht, pp. 249–277.

Morton, A.C., Hallsworth, C.R., 1999. Processes controlling the composition of heavy mineral assemblages in sandstones. Sedimentary Geology 124, 3–29.

Morton, A.C., Hallsworth, C.R:, 2007. Stability of detrital heavy minerals during burial diagenesis. In: Mange, M.A., Wright, D.T. (Eds.), Heavy Minerals in Use. Developments in Sedimentology Series, 58. Elsevier, Amsterdam, pp. 215–245.

Morton, A., and Chenery, S., 2009. Detrital rutile geochemistry and thermometry as guides to provenance of the Jurassic- Paleocene sandstones of the Norwegian Sea. Journal of Sediment Research 79, 540-553.

Muhs, D. R., 2001. Evolution of soils on Quaternary reef terraces, Barbados, West Indies, Quaternary Research 56, 66– 78.

Najman, Y., Garzanti, E., 2000. Reconstructing early Himalayan tectonic evolution and paleogeography from Tertiary foreland basin sedimentary rocks, northern India. Geological Society of America Bulletin 112, 435–449.

Najman, Y., Bickle, M., BouDagher-Fadel, M., Carter, A., Garzanti, E., Paul, M., Wijbrans, J., Willett, E., Oliver, G., Parrish, R., Akhter, S.H., Allen, R., Andò, S., Chisty, E., Reisberg, L., Vezzoli, G., 2008. The Paleogene record of Himalayan erosion: Bengal Basin, Bangladesh. Earth and Planetary Science Letters 273, 1–14.

Najman, Y., Bickle, M., Garzanti, E., Pringle, M., Barfod, D., Brozovic, N., Burbank, D., Andò, S., 2009. Reconstructing the exhumation history of the Lesser Himalaya, NW India, from a multitechnique provenance study of the foreland basin Siwalik Group. Tectonics 28. http://dx.doi.org/10.1029/2009TC002506 TC5018.

Najman, Y., Allen, R., Willett, E.A.F., Carter, A., Barfod, D., Garzanti, E., Wijbrans, J., Bickle, M.J., Vezzoli, G., Andò, S., Oliver, G., Uddin, M.J., 2012. The record of Himalayan erosion preserved in the sedimentary rocks of the Hatia Trough of the Bengal Basin and the Chittagong Hill Tracts, Bangladesh. Basin Research 24, 1–21.

Nayudu, Y. 1962. Rapid method for studying silt-size sediments and heavy minerals by liquid immersion. Journal of Sedimentary Petrology 32, 326-33.

Nesbitt, H.W., Young, G.M., 1996. Petrogenesis of sediments in the absence of chemical weathering: effects of abrasion and sorting on bulk composition and mineralogy. Sedimentology 43, 341–358.

Nesbitt, H.W., Fedo, C.M., Young, G.M., 1997. Quartz and feldspar stability, steady and non-steady-state weathering, and petrogenesis of siliciclastic sands and muds. Journal of Geology 105, 173–191.

Nickel, E., 1973. Experimental dissolution of light and heavy minerals in comparison with weathering and intrastratal solution. Contributions to Sedimentary Geology 1, 1–68.

Nielsen, C., Chamot-Rooke, N., Rangin, C., the Andaman Cruise Team, 2004. From partial to full partitioning along the Indo-Burmese hyper-oblique subduction. Marine Geology 209, 303–327.

Norman, T.N., 1969. A method to study the distribution of heavy-mineral grain abundance in a turbidite. Sedimentology 13, 263–280.

Norrish, K., and Chappell, B. W. 1977. X-ray fluorescence spectrometry. In Physical methods in determinative mineralogy, 2nd edn, J. Zussman (ed), 201-72. London: Academic Press.

Okada, H., 1971. Classification of sandstone: Analysis and proposal. Journal of Geology 79, 509–525.

Oliva, P., Viers, J., Dupré, B., Fortuné, J.-P., Martin, F., Braun, J.-J., Nahon, D., Robain, H., 1999. The effect of organic matter on chemical weathering: study of a small tropical watershed: Nsimi-Zoétélé site, Cameroon. Geochimica et Cosmochimica Acta 63, 4013–4035.

Pal, T., 2011. Petrology and geochemistry of the Andaman ophiolite: melt-rock interaction in a suprasubduction-zone setting. Journal of the Geological Society of London 168, 1031–1045.

Pal, T., Bhattacharya, A., 2010. Greenschist-facies sub-ophiolitic metamorphic rocks of Andaman Islands, Burma–Java subduction complex. Journal of Asian Earth Sciences 39, 804–814.

Pal, T., Chakraborty, P.P., Gupta, T.D., Singh, C.D., 2003. Geodynamic evolution of the outer arc-forearc belt in the Andaman Islands, the central part of the Burma–Java subduction complex. Geological Magazine 140, 289–307.

Pal, T., Gupta, T.D., Chakraborty, P.P., Das Gupta, S.C., 2005. Pyroclastic deposits of Mio-Pliocene age in the Arakan–Yoma–Andaman–Java subduction complex, Andaman Islands, Bay of Bengal, India. Geochemical Journal 39, 69–82.

Pal, T., Mitra, S.K., Sengupta, S., Katari, A., Bandopadhyay, P.C., Bhattacharya, A.K., 2007. Dacite–andesites of Narcondam volcano in the Andaman Sea — an imprint of magma mixing in the inner arc of the Andaman–Java subduction system. Journal of Volcanology and Geothermal Research 168, 93–113.

Pal, T., Raghav, S., Bhattacharya, A., Bandopadhyay, P.C., Mitra, S.K., Renjit, M.L., Sankar, M.S., Ghosh, B., 2010. The 2005–2006-eruption of the Barren Volcano, Andaman Sea: evolution of basaltic magmatism in island arc setting of Andaman–Java subduction complex. Journal of Asian Earth Sciences 39, 12–23.

Parfenoff, A., Pomerol, C., Tourenq, J., 1970. Les mine´raux en grains—me´thodes d'e´tude et de´termination. Masson, Paris, 578pp.

Pedersen, R.B., Searle, M.P., Carter, A., Bandopadhyay, P.C., 2010. U-Pb zircon age of the Andaman ophiolite: implications for the beginning of subduction beneath the Andaman-Sumatra arc. Journal of the Geological Society London 167, 1105-1112.

Pettijohn, F.J., 1941. Persistence of heavy minerals and geologic age. Journal of Geology 49, 610–625.

Pettijohn, F.J., Potter, P.E., Siever, R., 1972. Sand and Sandstone. Springer, New York. 618 p.

Pirrie, D., Butcher, A.R., Power, M.R., Gottlieb, P., Miller, G.L. 2004. Rapid quantitative mineral and phase analysis using automated scanning electron microscopy (QemSCAN);

potential applications in forensic geosciences. Geological Society, London, Special Publications 232,123-136.

Platt, J.P., 1986. Dynamics of orogenic wedges and the uplift of high-pressure metamorphic rocks. Geological Society of America Bulletin 97, 1037–1053.

Potter, P.E., 1978. Petrology and chemistry of modern big river sands. Journal of Geology 86, 423-449.

Powers, M.C., 1953. A new roundness scale for sedimentary particles. Journal of Sedimentary Petrology 23, 117–119.

Prospero, J. M., Glaccum, R.A., Nees, R.T., 1981. Atmospheric transport of soil dust from Africa to South America. Nature 289, 570– 572.

Prospero, J. M., Lamb, P. J., 2003. African droughts and dust transport to the Caribbean: Climate change implications. Science 302, 1024–1027.

Prospero, J. M., Ginoux, P., Torres, O., Nicholson, S. E., Gill, T. E., 2002. Environmental characterization of global sources of atmospheric soil dust identified with the Nimbus 7 Total Ozone Mapping Spectrometer (TOMS) absorbing aerosol product. Reviews of Geophysics 40(1), 1002, doi:10.1029/2000RG000095.

Pryor, W. A., Hester, N. C., 1969. X-ray diffraction analysis of heavy minerals. Journal of Sedimentary Petrology 39, 1384-9.

Pye, K., Mazzullo, J., 1994. Effects of tropical weathering on quartz grain shape: an example from northeastern Australia. Journal of Sedimentary Research 64, 500–507.

Rahmani, R.A., 1973. Grain surface etching features of some heavy minerals. Journal of Sedimentary Petrology 43, 882–888.

Raju, K.A.K., Ramprasad, T., Rao, P.S., Rao, B.R., Varghese, J., 2004. New insights into the tectonic evolution of the Andaman basin, northeast Indian Ocean. Earth and Planetary Science Letters 221, 145–162.

Reid, I., Frostick, L.E., 1985. Role of settling, entrainment and dispersive equivalence and of interstice trapping in placer formation. Journal of the Geological Society of London 142, 739–746.

Replumaz, A., Tapponnier, P., 2003. Reconstruction of the deformed collision zone between Indian and Asia by backward motion of lithospheric blocks. Journal of Geophysical Research 108. http://dx.doi.org/10.1029/2001JB000661.

Replumaz, A., Kárason, H., van der Hilst, R.D., Besse, J., Tapponnier, P., 2004. 4-D evolution of SE Asia's mantle from geological reconstructions and seismic tomography. Earth and Planetary Science Letters 221, 103–115.

Resentini, A., Malusà, M.G., Garzanti, E., 2013. MinSORTING:An Excels worksheet for modeling mineral grain-size distribution in sediments, with application to detrital geochronology and provenance studies. Computers and Geosciences 59, 90-97.

Rittenhouse, G., 1943. Transportation and deposition of heavy minerals. Geological Society of America Bulletin 54, 1725–1780.

Rosenthal, A., Foley, S.F., Pearson, D.G., Nowell, G.M., Tappe, S., 2009. Petrogenesis of strongly alkaline primitive volcanic rocks at the propagating tip of the western branch of the East African Rift. Earth and Planetary Science Letters 284, 236–248.

Rouse, W. R., Watts, D., 1966. Two studies in Barbadian Climatology. Climatological Research Series 1, McGill University, Montreal, 119 pp.

Roy, S.K., 1992. Accretionary prism in Andaman forearc. Geological Survey of India, Special Publication 29, 273–278.

Roy, S.K., Das Sharma, S., 1993. Evolution of Andaman forearc basin and its hydrocarbon potential. In: Biswas, S.K., et al. (Ed.), Proceedings of the 2nd Seminar on Petroliferous Basins of India. Indian Petroleum Publishers, Dehra Dun, pp. 407–435.

Rubey, W.W., 1933. The size-distribution of heavy minerals within a water-laid sandstone. Journal of Sedimentary Petrology 3, 3–29.

Russel, R. D. 1937. Mineral composition of Mississippi River sands. Geological Society of America Bulletin 48, 1307-1348.

Salmojraghi, F., 1892. Osservazioni geologiche sopra alcuni pozzi recentemente perforati nella provincia di Milano. Rendiconti Regio Istituto Lombardo. vol. 25.

Samuel, M.A., Harbury, N.A., Bakri, A., Banner, T.F., Hartono, L., 1997. A new stratigraphy for the islands of the Sumatran Forearc, Indonesia. Journal of Asian Earth Sciences 15, 339–380.

Sarma, D.S., Jafri, S.H., Fletcher, I.R., McNaughton, N.J., 2010. Constraints on the tectonic setting of the Andaman ophiolites, Bay of Bengal, India, from SHRIMP U–Pb zircon geochronology of plagiogranite. Journal of Geology 118, 691–697.

Schuiling, R.D., de Meijer, R.J., Riezebos, H.J., Scholten, M.J., 1985. Grain size distribution of different minerals in a sediment as a function of their specific density. Geologie en Mijnbouw 64, 199–203.

Schwab, F.L., 1975. Framework mineralogy and chemical composition of continental margin type sandstones. Geology, 3, 487-490.

Shukri, N.M., 1949. The mineralogy of Nile sediments. Journal of Geological Society of London 105, 511–529.

Searle, M.P., Cox, J., 1999. Tectonic setting, origin, and obduction of the Oman ophiolite. Geological Society of America Bulletin 111, 104–122.

Sengupta, S., Ray, K.K., Acharyya, S.K., de Smeth, J.B., 1990. Nature of ophiolite occurrence along the eastern margin of the Indian plate and their tectonic significance. Geology 18, 439–442.

Sheth, H.C., Ray, J.S., Bhutani, R., Kumar, A., Smitha, R.S., 2009. Volcanology and eruptive styles of Barren Island: an active mafic stratovolcano in the Andaman Sea, NE Indian Ocean. Bulletin of Volcanology 71, 1021–1039.

Sikder, A.M., Alam, M.M., 2003. 2-D modelling of the anticlinal structures and structural development of the eastern fold belt of the Bengal Basin, Bangladesh. Sedimentary Geology 155, 209–226.

Slingerland, R.L., 1984. The role of hydraulic sorting in the origin of fluvial placers. Journal of Sedimentary Petrology 54, 137–150.

Smith, J. V., Stenstrom, R. C., 1965. Electron-excited luminescence as a petrologic tool. Journal of Geology 73, 627-35.

Sorby, H. C. 1880. On the structure and origin of non-calcareus stratified rocks. Proc. Geol. Soc. London. 36, 46-92.

Speirs, J.C., McGowan, H. A., Neil, D. T., 2008. Polar eolian sand transport: grain characteristics determined by an automated scanning electron microscope (QEMSCAN). Arctic, Antarctic, and Alpine Research 40, 731-743.

Spencer, C. W., 1960. Method for mounting silt-size heavy minerals for identification by liquid immersion. Journal of Sedimentary Petrolgy 30, 498-500.

Steckler, M.S., Akhter, S.H., Seeber, L., 2008. Collision of the Ganges–Brahmaputra Delta with the Burma Arc: implications for earthquake hazard. Earth and Planetary Science Letters 273, 367–378.

Stephenson, D., Marshall, T.R., 1984. The petrology and mineralogy of Mt. Popa Volcano and the nature of the late-Cenozoic Burma Volcanic Arc. Journal of the Geological Society of London 141, 747–762.

Stieglitz, R.D., Rothwell, B., 1978. Surface microtextures of freshwater heavy mineral grains. Geoscience Wisconsin 3, 21–34.

Suttner, L.J., 1976. Sedimentary petrographic provinces: an evaluation. in Ross, C.A. (ed). Paleogeographic provinces and provinciality. Society of Economic Paleontologists and Mineralogists, Special Publications 21, 75-84.

Suttner, L. J.1989. Recent advances in study of the detrital mineralogy of sand and sandstone:implications for teaching. Journal of Geological Education 37, 235-240.

Suttner, L.J., Basu, A., and Mack, G.H., 1981. Climate and the origin of quartz arenites. Journal of Sedimentary Research 51, 1235-1246

Suzuki, H., Maung, M., Aung, A.K., Takai, M., 2004. Jurassic radiolaria from chert pebbles of the Eocene Pondaung Formation, central Myanmar. Neues Jahrbuch für Geologie und Palaeontologie Abhandlungen 231, 369–393.

Tack, L., Wingate, M.T.D., De Waele, B., Meerte, J., Belousova, E., Griffin, B., Tahon, A., Fernandez-Alonso, M., 2010. The 1375 Ma “Kibaran event” in Central Africa: prominent emplacement of bimodal magmatism under extensional regime. Precambrian Research 180, 63–84.

Thomas, M., Thorp, M., McAlister, J., 1999. Equatorial weathering, landform development and the formation of white sands in north western Kalimantan, Indonesia. Catena 36, 205–232.

Thompson, R.W., 1974. Mineralogy of sands from the Bengal and Nicobar fans, sites 218 and 211, eastern Indian Ocean. Initial Reports of the Deep Sea Drilling Project 22, 711–713.

Thorpe, R.S., (Ed) 1982. Andesites: Orogenic Andesites and Related Rocks. Wiley, Chichester, 724 pp.

Tourtelot, H.A., Riley, L.B., 1973. Sizes and shape of gold and platinum grains. In: Amstutz, G.L., Bernard, A.J. (Eds.), Ores in Sediments. Springer-Verlag, New York, NY, pp. 307–319.

Troger, W. E., 1969. Optische Bestimmung der gesteinsbildenden Minerale. Vol. 2: 2nd edn. Stuttgart: Schweizerbart'sche.

Turner, G., Morton, A.C., 2007. The effects of burial diagenesis on detrital heavy mineral grain surface textures. In: Mange, M.A., Wright, D.T. (Eds.), Heavy Minerals in Use. : Developments in Sedimentology Series, 58. Elsevier, Amsterdam, pp. 393–412.

Udden, J.A.,1914. Mechanical composition of clastic sediments. Geological Society of America Bulletin 25, 655–744.

Uddin, A., Lundberg, N., 1998. Unroofing history of the eastern Himalaya and the Indo-Burman ranges: heavy-mineral study of Cenozoic sediments from the Bengal Basin, Bangladesh. Journal of Sedimentary Research 68, 465–472.

Uyeda, S., and Kanamori, H., 1979. Back-arc opening and the mode of subduction. Journal of Geophysical Research 84 (3), 1049-1061.

Valloni, R., Lazzari, D., Calzolari, M.A., 1991. Selective alteration of arkose framework in Oligo-Miocene turbidites of the Northern Apennines foreland: impact on sedimentary provenance analysis. In: Morton, A.C., Todd, S.P., Haughton, P.D.W. (Eds.), Developments in Sedimentary Provenance Studies. In: Geological Society of London Special Publication, vol. 57, pp. 125–136.

Van Andel, T., H., 1950. Provenance, transport and deposition of Rhine sediments.Wageningen: H. Veeman en Zonen.

van Andel, T.H., 1959. Reflection on the interpretation of heavy mineral analyses. Journal of Sedimentary Petrology 29, 153–163.

van Harten, D., 1965. On the estimation of relative grain frequencies in heavy mineral slides. Geologie en Mijnbouw 44, 357-63.

Van Hise, R., 1885. Enlargements of Hornblende fragments. The American Journal of Science III 30, 231.

Van Loon, A.J., 2009. Unravelling the enigmas of the 'silver sands' in the Dutch/German/ Belgian border area. Netherlands Journal of Geosciences-Geologie en Mijnbouw 88, 133–145.

Van Loon, A.J., Mange, A.M., 2007. "In situ" dissolution of heavy minerals through extreme weathering, and the application of the surviving assemblages and their dissolution characteristics to correlation of Dutch and German silver sands. In: Mange, M.A., Wright,

D.T. (Eds.), Heavy Minerals in Use. : Developments in Sedimentology Series, 58. Elsevier, Amsterdam, pp. 189–213.

Velbel, M. A., 1984. Natural weathering mechanisms of almandine garnet: Geology 12, 631–634.

Velbel, M.A., 1985. Mineralogically mature sandstones in accretionary prisms. Journal of Sedimentary Petrology 55, 685–690.

Velbel, M.A., 1993a. Constancy of silicate-mineral weathering-rate ratios between natural and experimental weathering: implications for hydrologic control of differences in absolute rates. Chemical Geology 105, 89–99.

Velbel, M.A., 1993b. Formation of protective surface layers during silicate-mineral weathering under well-leached, oxidizing conditions. American Mineralogist 78, 408–417.

Velbel, M.A., 1999. Bond strength and the relative weathering rates of simple orthosilicates. American Journal of Science 299, 679–696.

Velbel, M.A., 2007. Surface textures and dissolution processes of heavy minerals in the sedimentary cycle: examples from pyroxenes and amphiboles. In: Mange, M.A., Wright, D.T. (Eds.), Heavy Minerals in Use. : Developments in Sedimentology Series, 58. Elsevier, Amsterdam, pp. 112–150.

Velbel, M.A., Losiak, A.I., 2010. Denticles on chain silicate grain surfaces and their utility as indicators of weathering conditions on Earth and Mars. Journal of Sedimentary Research 80, 771–780.

Velbel, M.A., Basso, C.L., Zieg, M.J., 1996. The natural weathering of staurolite: crystalsurface textures, relative stability, and the rate-determining step. American Journal of Science 296, 453–472.

Vigny, C., Socquet, A., Rangin, C., Chamot-Rooke, N., Pubellier, M., Bouin, M.N., Bertrand, G., Becker, M., 2003. Present-day crustal deformation around Sagaing Fault, Burma. Journal of Geophysical Research 108. http://dx.doi.org/10.1029/2002JB001999.

Von Huene, R., Lallemand, S., 1990. Tectonic erosion along the Japan and Peru convergent margins. Geological Society of America Bulletin 102(6), 704–720.

Walker, T.R.,1967,Formation of red bed sinmodern and ancient deserts. Bulletin of Geological Society of America 78, 353-368.

Weber, J.C., Dixon, T.H., Demets, C., Ambeh, W.B., Mattioli, P.J.G., Saleh, J., Selle, G., Bilham, R., Perez, O., 2001. GPS estimate of relative motion between the Caribbean and South American plates, and geological implications for Trinidad and Venezuela. Geology 29, 75–78.

White, A.F., Blum, A.E., 1995. Effects of climate on chemical weathering in watersheds. Geochimica et Cosmochimica Acta 59, 1729–1747.

White, N.M., Pringle, M., Garzanti, E., Bickle, M., Najman, Y., Chapman, H., Friend, P., 2002. Constraints on the exhumation and erosion of the High Himalayan Slab, NW India, from foreland basin deposits. Earth and Planetary Science Letters 195, 29–44.

Yokoyama, K., Amano, K., Taira, A., Saito, Y., 1990. Mineralogy of silts from the Bengal Fan. In: Cochran, J.R., Stow, D.A.V., et al. (Eds.), Proceedings of the Ocean Drilling Program: Scientific Results 116, pp. 59–73.

Zuffa, G.G., 1987. Unravelling hinterland and offshore palaeogeography from deepwater arenites. In: Leggett, J.K., Zuffa, G.G. (Eds.), Marine Clastic Sedimentology. Concepts and Case Studies. Graham and Trotman, London, pp. 39–61.

Zuffa, G.G., Normark. W.R.. Serra, F., Brunner, C.A., 2000. Turbidite megabeds in an oceanic rift valley recording Jökulhlaups of Late Pleistocene glacial lakes of the Western United States. Journal of Geology 108, 253-274.

Appendices

Research activity (2011-2013)

Publications:

2013: Garzanti, E., Limonta, M., Resentini, A., Bandopadhyay, P.C., Najman, Y., Andò, S., Vezzoli, G., 2013. Sediment recycling at convergent plate margins (Indo-Burman Ranges and Andaman–Nicobar Ridge). Earth-Science Reviews 123, 113-132.

Garcon, M., Chauvel, C., France-Lanord, C., Limonta, M., Garzanti, E. 2013. Removing the ‘‘heavy mineral effect’’ to obtain a new Pb isotopic value for the upper crust. Geochemestry Geophysics, Geosystem 14, 3324–3333.

Garcon, M., Chauvel, C., France-Lanord, C., Limonta, M., Garzanti, E. Which minerals control the Nd-Hf-Sr-Pb isotopic compositions of river sediments? Chemical Geology 364, 42-55.

Nagel, S., Castelltort, S., Garzanti, E., Mouthereau, F., Limonta, M., Adatte, T. Provenance evolution during arc-continent collision: Sedimentary petrography of Miocene to Pleistocene sediments in the Western Foreland Basin of Taiwan. Journal of Sedimentary Research. Submitted.

Munack, H., Korup, O., Resentini, A., Limonta, M., Garzanti, E., Blöthe, J.H., Scherler, D., Wittmann, H. and Kubik, P.W. Postglacial denudation of western Tibetan Plateau margin outpaced by long-term exhumation. GSA Bulletin. Submitted.

Limonta, M., Resentini, A., Bechstädt, T., Boni, M., Garzanti, E. Multistep sediment transfer along and across convergent plate boundaries (Barbados, Lesser Antilles). In prep.

2012: Andò, S., Garzanti, E,. Padoan, M., Limonta, M. Corrosion of heavy minerals during weathering and diagenesis: a catalogue for optical analysis. Sedimentary Geology 280, 165–178.

Schools:

2013: 1st School of Heavy Mineral Analysis. Dipartimento di Scienze dell’Ambiente, del Territorio e di Scienze della Terra, Università di Milano-Bicocca, Italia.

International School “Zircon: a key mineral for dating and tracking geological processes.” Università degli Studi di Pavia, Italia.

Short course “Geodynamics of mountain buildings and its interaction with climate.” Prof. Peter Molnar, University of Colorado. Dipartimento di Scienze, Università di Roma TRE, Italia.

2012: Sample preparation for geochemical analyses. CNRS, Université Joseph Fourier de Grenoble, France.

Short course “II Scuola di applicazione della Spettroscopia Raman alle Scienze della Terra”. Università degli Studi di Milano Bicocca. Dipartimento di Scienze dell’ambiente e del territorio e di Scienze della Terra.

2011: Short course “Applicazione della Spettroscopia Raman alle Scienze della Terra”. Università degli Studi di Siena, Dipartimento di Scienze della Terra.

Short course “An introduction to statistical methods for geoscientist”. PhD Raimon Tolosana-Delgado. Università degli Studi della Calabria, Dipartimento di Scienze della Terra.

Meetings:

2013: EGU General Assembly . Limonta, M., Resentini, A., Andò, S., Vezzoli, G., Bandopadhyay, P.C., Najman, Y., Boni, M., Bechstädt, T., Garzanti, E. “Subduction Complex Provenance redefined: modern sands from Indo-Burman-Andaman-Nicobar Ridge and Barbados Island”. Oral presentation.

1st School of Heavy Mineral Analysis. Limonta, M. “Corrosion of heavy minerals during diagenesis (Bengal fan)”. Oral presentation.

Appendix Table A4. —Frequency and type of heavy-mineral surface textures in river sands from equatorial Africa.

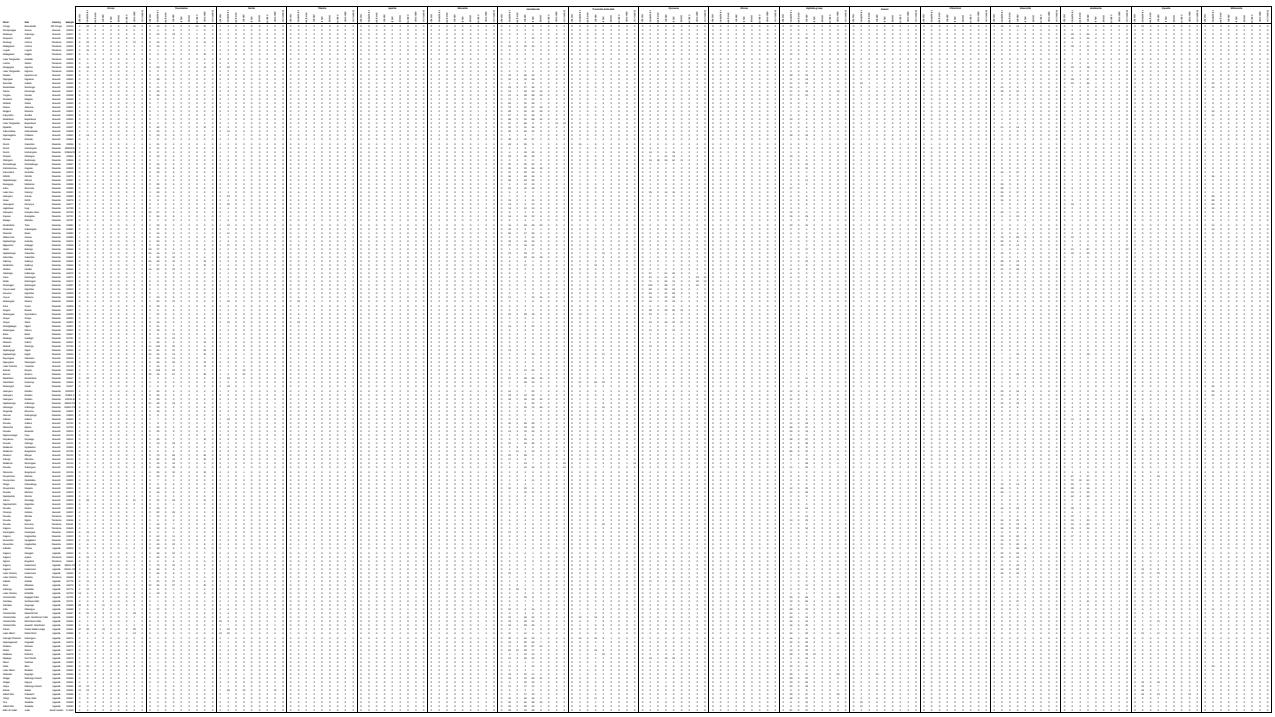

Appendix Table A2 - Frequency and type of heavy-mineral surface textures in modern and subsurface sands from the Bengal Basin

core depth (m)	Zircon									Tourmaline									Rutile									Titanite								
	euhedral	unweathered	weathered	corroded	etched	skeletal	rounded	subrounded	corr.rounded	euhedral	unweathered	weathered	corroded	etched	skeletal	rounded	subrounded	corr.rounded	euhedral	unweathered	weathered	corroded	etched	skeletal	rounded	subrounded	corr.rounded	euhedral	unweathered	weathered	corroded	etched	skeletal	rounded	subrounded	corr.rounded
modern sand	0	4	0	0	0	0	5	0	0	0	6	0	0	0	0	0	0	0	0	10	0	0	0	0	1	0	0	0	6	0	0	0	0	1	0	0
150-160	0	0	0	0	0	0	0	0	0	0	8	1	0	0	0	0	0	0	0	5	0	0	0	0	0	0	0	0	3	0	0	0	0	0	0	0
220-230	0	0	0	0	0	0	0	0	0	0	2	0	1	0	0	0	0	11	0	0	0	1	0	0	0	1	2	0	0	0	0	0	0	0	0	0
310-320	0	0	0	0	0	0	1	0	0	0	2	0	1	0	0	0	0	4	0	0	0	0	0	0	0	0	0	0	0	0	0	0	0	1	1	0
360-370	0	0	0	0	0	0	0	0	0	0	4	0	0	0	0	0	1	0	0	4	0	0	0	0	0	0	0	0	1	0	0	0	0	0	0	0
440-450	0	0	0	0	0	0	1	0	0	0	0	0	0	0	0	0	0	1	0	0	0	1	0	0	0	0	0	0	2	1	0	0	0	1	0	0
530-540	0	0	0	0	0	0	0	1	0	0	0	0	0	0	0	0	0	0	0	0	0	0	0	0	0	0	0	0	1	0	0	0	0	0	0	0
860-870	0	1	0	2	0	0	0	3	0	0	2	0	4	0	0	0	0	0	0	3	0	0	0	0	0	0	0	0	3	0	4	0	0	0	0	0
1050-1060	5	3	0	2	0	0	0	2	0	0	0	0	0	0	0	1	0	0	0	0	0	0	0	0	0	0	0	0	5	1	0	0	0	0	0	0
1070-1080	0	0	1	0	0	0	0	0	0	0	5	0	0	0	0	0	0	0	0	0	0	0	0	0	0	0	0	0	3	0	0	0	0	0	0	0
1790-1800	1	0	0	0	0	0	0	0	0	0	0	0	2	0	0	0	0	1	0	0	0	0	0	0	0	0	0	0	0	0	1	0	0	0	0	0
1890-1900	1	0	0	0	0	0	0	0	0	0	0	0	0	0	0	0	0	2	0	1	0	0	0	0	0	0	0	0	0	0	0	0	0	0	0	0
2000-2010	0	0	0	0	0	0	0	0	7	0	3	0	8	0	0	0	0	0	0	4	0	0	0	0	0	0	0	0	8	0	14	0	0	0	0	0
2470-2480	0	0	0	1	0	0	2	3	2	0	0	0	0	0	0	0	0	0	0	1	0	0	0	0	0	0	0	0	1	0	0	0	0	0	0	0
2880-2890	1	0	0	1	0	0	0	1	0	0	0	0	1	0	0	0	0	2	0	1	0	1	0	0	0	0	0	0	0	0	0	0	0	0	0	0

core depth (m)	Apatite									Monazite									Hornblende									Tremolite-Actinolite								
	euhedral	unweathered	weathered	corroded	etched	skeletal	rounded	subrounded	corr.rounded	euhedral	unweathered	weathered	corroded	etched	skeletal	rounded	subrounded	corr.rounded	euhedral	unweathered	weathered	corroded	etched	skeletal	rounded	subrounded	corr.rounded	euhedral	unweathered	weathered	corroded	etched	skeletal	rounded	subrounded	corr.rounded
modern sand	0	6	0	0	0	0	0	0	0	0	0	0	0	0	0	0	0	0	0	3	1	1	40	0	1	0	0	0	0	0	1	3	0	0	0	0
150-160	0	0	0	0	0	0	0	0	0	0	0	0	0	0	0	0	0	0	0	49	3	4	14	0	0	0	0	0	4	3	0	0	0	0	0	0
220-230	0	0	0	0	0	0	0	0	0	0	0	0	0	0	0	0	0	0	0	0	0	0	1	0	0	0	4	0	0	0	0	0	0	0	0	0
310-320	0	0	0	0	0	0	0	0	0	0	0	0	0	0	0	0	0	0	0	0	1	10	3	0	2	6	43	0	0	0	1	0	0	0	1	1
360-370	0	0	0	0	0	0	0	0	0	0	1	1	0	0	0	0	0	0	0	67	1	17	8	0	0	0	0	0	10	2	0	0	0	0	0	0
440-450	0	4	0	0	1	0	0	0	1	0	0	0	0	0	0	0	0	0	0	29	0	44	5	0	0	5	26	0	1	0	4	0	0	0	0	0
530-540	0	2	0	2	0	0	0	0	0	0	0	0	0	0	0	0	0	0	0	10	1	22	6	1	0	5	24	0	0	0	0	0	0	0	0	0
860-870	0	6	0	3	1	0	0	1	3	0	0	0	0	0	0	0	0	0	0	4	1	63	16	0	0	0	10	0	1	2	3	3	0	0	0	0
1050-1060	0	2	0	1	0	0	0	0	0	0	0	0	0	0	0	0	0	0	0	3	2	28	17	0	0	2	20	0	0	0	0	0	0	0	0	2
1070-1080	0	0	0	0	0	0	0	0	0	0	0	0	0	0	0	0	0	0	0	85	0	12	6	0	0	1	0	0	2	1	0	0	0	0	0	0
1790-1800	0	0	0	0	0	0	0	0	0	0	0	0	0	0	0	0	0	0	0	1	0	4	0	0	0	0	2	0	0	0	0	0	0	0	0	0
1890-1900	0	0	0	0	0	0	0	0	0	0	0	0	0	0	0	0	0	0	0	0	0	2	0	0	0	0	1	0	0	0	0	0	0	0	0	0
2000-2010	0	5	0	5	0	0	0	0	22	0	0	0	0	0	0	0	0	0	0	0	0	3	1	0	0	0	0	0	0	0	1	0	0	0	0	0
2470-2480	0	11	0	0	0	0	0	1	0	0	0	0	0	0	0	0	0	0	0	1	0	0	0	0	0	0	1	0	0	0	0	0	0	0	0	0
2880-2890	0	3	0	1	0	0	0	0	0	0	0	0	0	0	0	0	0	0	0	0	0	0	0	0	0	0	0	0	0	0	0	0	0	0	0	0

core depth (m)	Pyroxene									Epidote-group									Garnet									Chloritoid								
	euhedral	unweathered	weathered	corroded	etched	skeletal	rounded	subrounded	corr.rounded	euhedral	unweathered	weathered	corroded	etched	skeletal	rounded	subrounded	corr.rounded	euhedral	unweathered	weathered	corroded	etched	skeletal	rounded	subrounded	corr.rounded	euhedral	unweathered	weathered	corroded	etched	skeletal	rounded	subrounded	corr.rounded
modern sand	0	5	0	0	6	0	0	0	0	0	59	5	4	2	0	0	0	0	0	29	0	0	0	0	1	0	0	0	3	0	0	0	0	0	0	0
150-160	0	0	1	0	0	0	0	0	0	0	26	5	5	0	0	0	0	0	0	9	0	0	0	0	0	0	0	0	1	1	0	0	0	0	0	0
220-230	0	0	0	0	0	0	0	0	0	0	1	1	14	0	0	0	4	20	0	1	0	7	0	0	0	0	0	0	0	0	0	0	0	0	0	1
310-320	0	0	0	1	0	0	0	0	0	1	13	0	3	0	0	0	6	18	0	0	0	8	0	0	0	0	0	0	0	0	1	0	0	0	0	0
360-370	0	0	0	0	0	0	0	0	0	0	43	4	2	1	0	0	1	0	0	6	0	1	0	0	0	0	0	0	2	1	0	0	0	0	0	0
440-450	0	1	0	0	0	0	0	0	0	0	8	4	10	0	0	0	7	21	0	10	0	4	0	0	0	0	3	0	0	0	0	0	0	0	0	0
530-540	0	1	0	0	1	0	0	0	0	0	14	2	9	0	0	0	0	1	0	7	0	9	0	0	0	0	1	0	1	0	0	0	0	0	0	0
860-870	0	0	0	0	0	0	0	0	0	0	11	1	40	1	0	0	0	0	0	5	0	21	0	0	0	0	0	0	0	0	0	0	0	0	0	0
1050-1060	0	0	0	0	0	0	0	0	0	0	16	8	6	0	0	0	0	6	0	9	2	12	0	0	0	1	2	0	0	0	0	0	0	0	0	0
1070-1080	0	0	0	0	0	0	0	0	0	0	20	7	4	0	0	0	2	0	0	28	0	1	0	0	0	0	0	0	0	2	0	0	0	0	0	0
1790-1800	0	0	0	0	0	0	0	0	0	0	12	6	12	0	0	0	0	7	0	4	1	20	0	0	1	0	4	0	1	0	0	0	0	0	0	0
1890-1900	0	0	0	0	0	0	0	0	0	0	2	1	7	0	0	0	1	2	0	3	0	12	0	0	0	0	1	0	0	0	0	0	0	0	0	0
2000-2010	0	0	0	1	0	0	0	0	0	0	8	0	26	0	0	0	0	1	0	12	0	22	1	0	0	0	0	0	2	1	2	1	0	0	0	1
2470-2480	0	0	0	0	0	0	0	0	0	0	1	0	2	0	0	0	0	1	0	7	2	12	0	0	0	0	1	0	0	0	0	0	0	0	0	0
2880-2890	0	0	0	0	0	0	0	0	0	0	0	0	0	0	0	0	0	0	0	0	0	3	0	0	0	0	2	0	1	1	0	0	0	0	0	0

core depth (m)	Staurolite									Andalusite									Kyanite									Sillimanite								
	euhedral	unweathered	weathered	corroded	etched	skeletal	rounded	subrounded	corr.rounded	euhedral	unweathered	weathered	corroded	etched	skeletal	rounded	subrounded	corr.rounded	euhedral	unweathered	weathered	corroded	etched	skeletal	rounded	subrounded	corr.rounded	euhedral	unweathered	weathered	corroded	etched	skeletal	rounded	subrounded	corr.rounded
modern sand	0	0	6	0	0	0	0	0	0	0	1	0	0	0	0	0	0	0	0	4	0	0	0	0	0	0	0	0	1	0	0	0	0	0	0	0
150-160	0	17	0	1	1	0	0	0	0	0	1	0	0	0	0	0	0	0	0	15	0	0	0	0	0	0	0	0	17	0	0	0	0	0	0	0
220-230	0	0	0	19	1	0	0	0	14	0	0	0	0	0	0	0	0	3	0	7	0	4	0	0	0	0	12	0	2	0	4	0	0	0	0	10
310-320	0	0	0	4	0	0	0	0	9	0	0	0	0	0	0	0	0	0	0	2	0	0	0	0	0	2	3	0	5	0	0	0	0	0	5	0
360-370	0	6	0	1	0	0	0	0	0	0	0	0	0	0	0	0	0	0	0	2	3	0	0	0	0	0	0	0	12	0	0	0	0	0	0	0
440-450	0	2	0	0	0	0	0	0	0	0	0	0	0	0	0	0	0	0	0	4	2	0	0	0	0	1	0	0	7	0	0	0	0	0	1	0
530-540	0	0	1	4	0	0	0	0	0	0	0	0	0	0	0	0	0	1	0	17	0	0	0	0	0	1	1	0	21	0	0	0	0	0	2	0
860-870	0	0	0	1	0	0	0	0	1	0	0	0	0	0	0	0	0	0	0	2	0	3	0	0	0	0	0	0	0	0	0	0	0	0	0	0
1050-1060	0	1	0	0	0	0	0	1	0	0	0	1	0	0	0	0	0	0	0	1	0	0	0	0	0	0	2	0	2	0	0	0	0	0	0	0
1070-1080	0	1	0	1	0	0	0	0	0	0	0	0	0	0	0	0	0	0	0	4	0	0	0	0	0	0	0	0	0	0	0	0	0	0	0	0
1790-1800	0	0	0	5	0	0	0	0	0	0	0	0	0	0	0	0	0	0	0	2	0	0	1	0	0	0	0	0	1	0	0	0	0	0	0	0
1890-1900	0	0	0	1	0	0	0	0	0	0	0	0	0	0	0	0	0	0	0	0	0	0	0	0	0	0	0	0	2	0	0	0	0	0	0	0
2000-2010	0	0	0	0	0	0	0	0	0	0	0	0	0	0	0	0	0	0	0	3	12	6	0	0	0	0	1	0	0	0	0	0	0	0	0	0
2470-2480	0	1	0	0	0	0	0	0	0	0	0	0	0	0	0	0	0	0	0	0	0	0	0	0	0	0	0	0	0	0	0	0	0	0	0	0
2880-2890	0	0	0	0	0	0	0	0	0	0	0	0	0	0	0	0	0	0	0	0	0	0	0	0	0	0	0	0	0	0	0	0	0	0	0	0

Appendix Table A3 - Grain density of modern and subsurface sands from the Bengal Basin

River	Country	Sample	g/cm^3	g/cm^3	g/cm^3	g/cm^3	mean	*st.dev*
MODERN RIVER SANDS								
Chittagong	Bangladesh	SO188-2	2,673	2,659	2,651	2,649	**2,658**	*0,011*
Tanlwe	Myanmar	S3193	2,621	2,640	2,620	2,620	**2,625**	*0,010*
Pazumbye	Myanmar	S3191	2,629	2,623	2,612	2,601	**2,616**	*0,012*
	core depth (m)							
SUBSURFACE	220-230		2,685	2,681			**2,683**	*0,003*
SAMPLES	310-320		2,668	2,666	2,655		**2,663**	*0,007*
	440-450		2,666	2,654	2,646	2,633	**2,650**	*0,014*
	530-540		2,664	2,662	2,658		**2,661**	*0,003*
	1050-1060		2,659	2,644	2,632		**2,645**	*0,014*
	1790-1800		2,690	2,655	2,602		**2,649**	*0,044*
	1890-1900		2,642	2,640	2,633		**2,638**	*0,005*
	2470-2480		2,631				2,631	

Table A4. Location and provenance of modern sand samples (Indo-Burman-Andaman-Nicobar subduction complex)

river	locality	deposit	sample	main source rocks	provenance	region/island	country	latitude	longitude
Burhi Dihing	Deurigaon	bar	BR 13	Turbidites + ophiolite	Mixed orogenic	Assam	India	27°46' N	95°42' E
Dhansiri	Barahigaon	bar	BR 11	Turbidites	Recycled clastic	Assam	India	26°30' N	93°57' E
Kopili	Marigaon	bar	BR 68	Turbidites + molasse	Recycled clastic	Assam	India	26°12' N	92°21' E
Karnaphuli	Rangamati	bar	S3547	Turbiditic sandstones	Recycled clastic	Chittagong Hills	Bangladesh	22°39' N	92°10' E
Karnaphuli	Chittagong	mouth	SO188-2	Turbiditic sandstones	Recycled clastic	Chittagong Hills	Bangladesh	22°19' N	91°51' E
	Cox Bazar	beach	S3530	Turbiditic sandstones	Recycled clastic	Chittagong Hills	Bangladesh	21°25' N	91°58' E
Kaladan	Kyauktaw	bar	S3177	Turbidites	Recycled clastic	N Arakan	Myanmar	20°50'15N	92°59'09E
	Padali	beach	S3175	Turbidites	Recycled clastic	N Arakan	Myanmar	20°17'33N	92°51'23E
	Sittwe	beach	S3176	Turbidites	Recycled clastic	N Arakan	Myanmar	20°06'54N	92°53'45E
Lemro	Atet Than Htaung	bar	S3182	Turbiditic mudrocks	Recycled clastic	N Arakan	Myanmar	20°49'21N	93°18'58E
Wek	Atet Than Htaung	bar	S3181	Turbiditic mudrocks	Recycled clastic	N Arakan	Myanmar	20°49'01N	93°19'19E
Ru	Ru Chaung	bar	S3183	Turbiditic mudrocks	Recycled clastic	N Arakan	Myanmar	20°50'46N	93°14'32E
Koum	Koum Chaung	bar	S3179	Turbiditic mudrocks	Recycled clastic	N Arakan	Myanmar	20°44'35N	93°16'46E
Lemro	Mrauk U	bar	S3178b	Turbiditic mudrocks	Recycled clastic	N Arakan	Myanmar	20°39'39N	93°14'56E
Lemro	Mrauk U	levee	S3178a	Turbiditic mudrocks	Recycled clastic	N Arakan	Myanmar	20°39'39N	93°14'56E
	Kyaukphyu	beach	S3184	Turbidites	Recycled clastic	Ramree	Myanmar	19°24'36N	93°33'09E
Tanlwe	Migyaunglu	bar	S3193b	Turbiditic mudrocks	Recycled clastic	S Arakan	Myanmar	18°59'10N	94°15'24E
Tanlwe	Migyaunglu	levee	S3193a	Turbiditic mudrocks	Recycled clastic	S Arakan	Myanmar	18°59'10N	94°15'24E
Taunggok	Taunggok	bar	S3194	Turbiditic mudrocks	Recycled clastic	S Arakan	Myanmar	18°52'55N	94°15'14E
Tahde	Shwehle	bar	S3195	Turbiditic mudrocks	Recycled clastic	S Arakan	Myanmar	18°36'35N	94°20'39E
Pyunpye	Pyunpye	bar	S3196	Turbiditic mudrocks	Recycled clastic	S Arakan	Myanmar	18°30'19N	94°22'14E
Thandwe	Thandwe	bar	S3197	Turbiditic mudrocks	Recycled clastic	S Arakan	Myanmar	18°27'47N	94°23'56E
	Linn Thar	beach	S3186	Turbiditic mudrocks	Recycled clastic	S Arakan	Myanmar	18°24'01N	94°20'11E
Kyaukki	Kyaukki	bar	S3192	Turbiditic mudrocks	Recycled clastic	S Arakan	Myanmar	18°14'22N	94°28'38E
Pazunbye	Pazunbye	bar	S3191	Turbiditic mudrocks	Recycled clastic	S Arakan	Myanmar	18°10'09N	94°29'43E
	Seliguin	beach	S3190	Turbiditic mudrocks	Recycled clastic	S Arakan	Myanmar	18°03'44N	94°28'48E
Kyieintuli	Kalabyin	bar	S3188b	Turbiditic mudrocks	Recycled clastic	S Arakan	Myanmar	17°57'14N	94°33'09E
Kyieintuli	Kalabyin	levee	S3188a	Turbiditic mudrocks	Recycled clastic	S Arakan	Myanmar	17°57'14N	94°33'09E
Kyieintuli	delta	beach	S3189	Turbiditic mudrocks	Recycled clastic	S Arakan	Myanmar	18°00'50N	94°28'28E
Ayeyarwadi	Pyay	bar	S3198	*Trunk river*	Mixed orogenic	Ayeyarwadi	Myanmar	18°48'39N	95°12'22E
Ayeyarwadi	Pyay	levee	S3198A	*Trunk river*	Mixed orogenic	Ayeyarwadi	Myanmar	18°48'39N	95°12'22E
Ayeyarwadi	Shwedaung	bar	S3199	*Trunk river*	Mixed orogenic	Ayeyarwadi	Myanmar	18°42'05N	95°11'30E
Ayeyarwadi	Shwedaung	levee	S3199A	*Trunk river*	Mixed orogenic	Ayeyarwadi	Myanmar	18°42'05N	95°11'30E
Ayeyarwadi	Nyaungdoun	bar	S3200CS	*Trunk river*	Mixed orogenic	Ayeyarwadi	Myanmar	17°01'29N	95°33'03E
Ayeyarwadi	Nyaungdoun	bar	S3200FS	*Trunk river*	Mixed orogenic	Ayeyarwadi	Myanmar	17°01'29N	95°33'03E
Ayeyarwadi	Nyaungdoun	levee	S3200A	*Trunk river*	Mixed orogenic	Ayeyarwadi	Myanmar	17°01'29N	95°33'03E
Kalpong	Diglipur	bar	S3212	"Chaotic terrane"	Mixed	North Andaman	India	13°14'43N	92°58'41E
	Kalipur	beach	S3213	"Chaotic terrane"	Mixed	North Andaman	India	13°13'39N	93°03'04E
	Ramnagar	beach	S3220	"Chaotic terrane"	Mixed	North Andaman	India	13°04'33N	93°01'35E
	Mayabunder	beach	S3211	Mèlange	Mixed	Middle Andaman	India	12°52'59N	92°54'23E
	Karmatang	beach	S3210	"Chaotic terrane"	Mixed	Middle Andaman	India	12°50'53N	92°56'20E
Lisvolo	Billiground	dry bed	S3214	"Chaotic terrane"	Mixed	Middle Andaman	India	12°39'57N	92°53'22E
	Cuthbert Bay	beach	S3209	"Chaotic terrane"	Mixed	Middle Andaman	India	12°36'07N	92°57'22E
	Panchavati	beach	S3208	Mantle serpentinites	Ophiolite	Middle Andaman	India	12°33'12N	92°58'19E
Nimbutala	Nimbutala	dry bed	S3215	"Chaotic terrane"	Mixed	Middle Andaman	India	12°31'08N	92°57'53E
	Amkunj	beach	S3207	"Chaotic terrane"	Mixed	Middle Andaman	India	12°30'44N	92°57'58E
	Balu Dera	beach	S3206	Turbidites (+ oceanic crust)	Mixed	Baratang	India	12°08'01N	92°48'20E
	Collinpur	beach	S3216	Turbiditic sandstones	Recycled clastic	South Andaman	India	11°41'35N	92°35'55E
	Kurmadera	beach	S3217	Turbiditic sandstones	Recycled clastic	South Andaman	India	11°39'54N	92°35'43E
	Wandoor	beach	S4090	Turbiditic sandstones	Recycled clastic	South Andaman	India	11°35'47N	92°36'29E
	Corbyn's Cove	beach	S3201	Turbidites + oceanic crust	Mixed	South Andaman	India	11°38'29N	92°44'48E
	Manjeri	beach	S4088	Turbidites + oceanic crust	Mixed	South Andaman	India	11°32'43N	92°39'00E
	Beadonabad	beach	S3204	Oceanic crust	Ophiolite	South Andaman	India	11°34'34N	92°44'15E
	Barmanala	beach	S4089	Oceanic crust	Ophiolite	South Andaman	India	11°33'29N	92°43'47E
	Chidiya Tapu	beach	S3203	Oceanic crust	Ophiolite	South Andaman	India	11°29'56N	92°42'13E
	Barren	beach	BA1	Recent lavas	Neovolcanic	Barren	India	12°16' N	93°52' E
	Barren	beach	BA2	Recent lavas	Neovolcanic	Barren	India	12°16' N	93°52' E
	Barren	ash fall	BA3	*Volcanic eruption*	Neovolcanic	Barren	India	12°16' N	93°52' E
	Narcondum	beach	S4091	Recent lavas	Neovolcanic	Narcondum	India	13°26' N	94°15' E
	Interview	beach	S3222	Archipelago Group	Mixed	Interview	India	12°55' N	92°43' E
	Havelock	beach	S3223	Archipelago Group	Mixed	Havelock	India	12°00'17N	93°01'21E
	Smith	beach	S3221	Archipelago Gp. + turbidites	Mixed	Smith	India	13°18' N	93°04' E
	Ross	beach	S3218	Archipelago Gp. + turbidites	Mixed	Ross	India	11°40' N	92°46' E
	NW Rutland	beach	S4087	Turbiditic sandstones	Recycled clastic	Rutland	India	11°30' N	92°39' E
	N Rutland	beach placer	S4086	Ultramafic cumulates	Ophiolite	Rutland	India	11°29' N	92°40' E
	N Campbell Bay	beach	S4077	Turbidites + Archipelago Gp.	Mixed	Great Nicobar	India	6°59'56"N	93°56'16E
	Campbell Bay	beach	S4078	Turbidites + Archipelago Gp.	Mixed	Great Nicobar	India	7°00'13N	93°54'54E
	S Campbell Bay	beach	S4079	Turbiditic sandstones	Recycled clastic	Great Nicobar	India	6°59'23N	93°55'19E
	Jogindarnagar	beach	S4080	Archipelago Gp. + turbidites	Mixed	Great Nicobar	India	6°56'36N	93°54'58E
	Gandhinagar	beach	S4081	Archipelago Gp. + turbidites	Mixed	Great Nicobar	India	6°50'47N	93°53'34E
	Shastrinagar	beach	S4082	Turbiditic sandstones	Recycled clastic	Great Nicobar	India	6°50'20N	93°54'07E
	N Indira Point	beach	S4083	Turbiditic sandstones	Recycled clastic	Great Nicobar	India	6°48'43N	93°52'09E
	S Indira Point	beach	S4084	Turbiditic sandstones	Recycled clastic	Great Nicobar	India	6°48'11N	93°52'46E
Galathea	upper reaches	bar	S4085	Turbiditic mudrocks	Recycled clastic	Great Nicobar	India	6°57'55N	93°49'53E

Table A5. Bulk-petrography data for modern sands derived from the Indo-Burman-Andaman-Nicobar subduction complex

river	locality	deposit	sample	Grain Size (μm)	n°points	Q	KF	P	Lvf	Lvm	Lmv	Lu	Lch	Lc	Lp	Lms	Lm	mica	HM		MI*	MI
ASSAM																						
Burhi Dihing	Deurigaon	bar	BR 13	290	400	43	10	12	0	0	2	1	3	0	4	12	8	2	4	100,0	261	224
Dhansiri	Barahigaon	bar	BR 11	70	400	38	4	3	0	0	1	0	1	0	17	34	1	1	0	100,0	125	85
Kopili	Marigaon	bar	BR 68	80	400	77	8	3	0	0	0	0	0	0	3	5	0	1	2	100,0	224	170
COASTAL BANGLADESH																						
Karnaphuli	Rangamati	bar	S3547	270	400	76	8	2	1	1	3	0	1	0	3	3	1	1	1	100,0	209	151
Karnaphuli	Chittagong	mouth	SO188-2	135	400	74	4	5	1	1	0	0	0	0	10	1	1	1	1	100,0	n.d.	40
	Cox Bazar	beach	S3530	135	400	72	7	5	2	1	3	0	0	0	3	3	2	0	3	100,0	184	112
NORTHERN ARAKAN																						
Kaladan	Kyauktaw	bar	S3177	260	400	42	1	2	1	0	1	0	1	0	32	19	1	0	0	100,0	121	49
	Padali	beach	S3175	120	400	47	5	4	1	0	5	0	0	0	14	22	2	0	0	100,0	138	91
	Sittwe	beach	S3176	130	400	45	2	2	1	0	2	0	0	0	24	23	1	0	0	100,0	121	61
CENTRAL ARAKAN																						
Wek	Atet Than Htaung	bar	S3181	800	400	11	0	0	0	0	0	0	0	0	65	24	0	0	0	100,0	116	30
Ru	Ru Chaung	bar	S3183	530	400	18	0	2	0	0	0	0	0	0	69	11	0	0	0	100,0	123	17
Koum	Koum Chaung	bar	S3179	550	400	2	0	0	0	0	0	0	0	0	82	16	0	0	0	100,0	106	18
Lemro	Mrauk U	bar	S3178b	450	400	13	0	1	1	0	3	0	1	0	38	43	0	0	0	100,0	115	62
Lemro	Mrauk U	levee	S3178a	cl.80-125	400	11	1	2	0	0	0	0	0	0	70	15	0	0	0	100,0	116	21
RAMREE ISLAND																						
	Kyaukphyu	beach	S3184	120	400	67	5	6	4	0	3	0	2	0	1	7	3	0	1	100,0	176	130
SOUTHERN ARAKAN																						
Tanlwe	Migyaunglu	bar	S3193b	470	400	8	0	1	3	1	5	0	1	0	52	29	0	0	0	100,0	101	37
Tanlwe	Migyaunglu	levee	S3193a	cl.80-125	400	22	1	7	0	0	0	0	0	0	52	17	0	0	0	100,0	124	31
Taunggok	Taunggok	bar	S3194	240	400	11	0	3	1	1	4	0	0	0	36	43	0	0	0	100,0	106	58
Tahde	Shwehle	bar	S3195	340	400	12	0	1	2	1	4	0	1	0	34	45	0	0	0	100,0	107	59
Pyunpye	Pyunpye	bar	S3196	240	400	20	0	2	0	1	0	0	0	0	74	2	0	0	0	100,0	n.d.	5
Thandwe	Thandwe	bar	S3197	250	400	16	0	2	2	0	4	0	1	0	41	34	0	0	0	100,0	114	55
	Linn Thar	beach	S3186	360	390	49	11	5	0	6	0	0	0	4	24	0	0	0	0	100,0	n.d.	0
Kyaukki	Kyaukki	bar	S3192	160	400	29	2	2	1	1	0	0	0	0	60	5	0	0	0	100,0	116	9
Pazunbye	Pazunbye	bar	S3191	270	400	19	1	2	2	1	5	0	0	0	34	36	1	0	0	100,0	107	55
Kyieintuli	Kalabyin	bar	S3188b	260	400	10	0	1	4	2	6	0	0	0	33	43	0	0	0	100,0	105	58
Kyieintuli	Kalabyin	levee	S3188a	cl.80-125	400	22	2	5	0	0	0	0	0	0	60	11	0	0	0	100,0	140	22
Kyieintuli	mouth	beach	S3189	260	400	31	1	2	3	1	11	0	0	0	14	35	1	0	0	100,0	117	86
	Seliguin	beach	S3190	180	400	50	0	1	4	3	4	0	1	0	17	18	1	0	0	100,0	115	56
AYEYARWADI RIVER																						
Ayeyarwadi	Pyay	bar	S3198b	220	400	58	8	8	2	2	1	0	2	0	7	4	3	3	3	100,0	212	86
Ayeyarwadi	Shwedaung	bar	S3199b	220	400	61	8	11	0	1	0	0	2	0	5	5	3	1	2	100,0	243	130
Ayeyarwadi	Nyaungdoun	bar	S3200B	220	400	57	12	10	3	0	0	0	1	0	9	3	3	1	2	100,0	240	65
Ayeyarwadi	Nyaungdoun	bar	S3200b	145	400	47	11	11	5	1	3	0	1	0	6	9	3	3	2	100,0	213	121
Ayeyarwadi	Nyaungdoun	18% bulk	S3200b	cl.80-125	400	52	7	7	4	1	2	0	1	0	7	5	4	2	10	100,0	208	104
Ayeyarwadi	Nyaungdoun	68% bulk	S3200b	cl.125-180	400	46	12	12	5	0	3	0	1	0	6	10	3	2	1	100,0	192	116
Ayeyarwadi	Nyaungdoun	12% bulk	S3200b	cl.180-250	400	45	10	11	5	2	1	1	1	0	5	8	3	8	0	100,0	186	99
Ayeyarwadi	Nyaungdoun	12% bulk	S3200b	cl.180-250	400	46	10	13	3	2	1	0	1	0	6	7	1	8	0	100,0	161	73
NORTH ANDAMAN																						
Kalpong	Diglipur	bar	S3212	375	400	20	0	4	1	6	2	26	2	0	17	10	0	0	12	100,0	138	48
	Kalipur	beach	S3213	325	400	48	1	7	4	6	1	12	3	0	10	2	0	0	5	100,0	n.d.	22
	Ramnagar	beach	S3220	140	400	67	3	6	7	1	2	0	1	0	10	2	0	0	0	100,0	113	20
MIDDLE ANDAMAN																						
	Mayabunder	beach	S3211	480	400	40	0	3	4	6	3	0	38	0	4	1	0	0	0	100,0	139	45
	Karmatang	beach	S3210	140	400	71	3	4	5	3	1	2	2	0	6	2	0	0	0	100,0	n.d.	23
Lisvolo	Billiground	dry bed	S3214	370	400	35	1	5	8	12	3	2	2	0	28	4	0	0	1	100,0	120	15
	Cuthbert Bay	beach	S3209	290	400	42	0	6	3	6	1	6	6	0	23	6	0	0	1	100,0	104	17
	Panchavati	beach	S3208	510	400	5	0	0	0	1	2	75	1	0	4	1	1	0	10	100,0	233	125
Nimbutala	Nimbutala	dry bed	S3215	400	400	30	0	2	2	3	1	2	0	0	53	8	0	0	0	100,0	107	11
	Amkunj	beach	S3207	200	400	65	0	3	3	1	0	5	1	0	15	4	0	0	2	100,0	n.d.	30
BARATANG					400																	
	Balu Dera	beach	S3206	125	400	77	7	6	3	2	0	0	1	0	0	2	1	0	0	100,0	193	88
SOUTH ANDAMAN					400																	
	Collinpur	beach	S3216	180	400	79	7	4	1	0	0	0	1	0	2	4	1	0	1	100,0	184	109
	Kurmadera	beach	S3217	190	400	89	5	2	0	0	0	0	0	0	0	2	1	1	0	100,0	n.d.	n.d.
	Wandoor	beach	S4090	180	400	84	5	1	1	0	0	0	0	0	1	2	0	0	5	100,0	n.d.	88
	Corbyn's Cove	beach	S3201	220	400	50	3	3	8	16	3	1	7	1	3	5	0	0	0	100,0	n.d.	38
	Manjeri	beach	S4088	130	400	64	2	16	2	7	1	1	5	0	0	0	0	0	2	100,0	n.d.	39
	Beadonabad	beach	S3204	900	400	9	0	8	1	64	4	0	7	0	1	0	1	0	5	100,0	304	39
	Barmanala	beach	S4089	75	400	19	1	29	0	18	7	3	1	0	2	1	0	0	20	100,0	n.d.	65
	Chidiya Tapu	beach	S3203	750	400	8	0	23	0	18	23	18	2	1	1	2	0	0	4	100,0	145	86
OTHER ANDAMAN ISLANDS					400																	
	Barren	beach	BA1	330	400	0	0	15	0	84	0	0	0	0	0	0	0	0	1	100,0	n.d.	0
	Barren	beach	BA2	70	400																	
	Barren	ash fall	BA3	100	400	0	0	12	0	85	0	0	0	0	0	0	0	0	3	100,0	n.d.	0
	Narcondum	beach	S4091	340	400	2	0	45	1	36	0	0	0	0	0	0	0	5	12	100,0	n.d.	0
	Interview	beach	S3222	210	150	46	3	39	1	8	0	0	2	0	1	1	0	0	0	100,0	n.d.	16
	Havelock	beach	S3223	130	241	55	2	29	2	5	1	0	0	0	1	0	0	0	6	100,0	n.d.	n.d.
	Smith	beach	S3221	500	400	25	0	31	7	29	0	0	1	1	5	0	0	0	1	100,0	n.d.	4
	Ross	beach	S3218	570	90	35	0	28	2	16	0	0	0	1	15	1	0	0	1	100,0	n.d.	3
	NW Rutland	beach	S4087	100	400	61	3	6	1	0	1	0	0	0	2	3	1	0	22	100,0	250	167
GREAT NICOBAR																						
	N Campbell Bay	beach	S4077	700	400	18	1	4	1	9	0	0	0	0	47	20	0	0	0	100,0	100	23
	Campbell Bay	beach	S4078	380	400	72	5	7	9	2	0	0	0	0	1	1	0	0	3	100,0	n.d.	55
	S Campbell Bay	beach	S4079	230	400	75	1	3	1	1	0	0	0	0	2	2	1	0	12	100,0	n.d.	63
	Jogindarnagar	beach	S4080	450	400	37	3	15	4	23	3	0	8	1	5	0	2	0	0	100,0	n.d.	25
	Gandhinagar	beach	S4081	400	400	57	7	0	7	0	0	0	0	0	7	11	3	7	0	100,0	n.d.	n.d.
	Shastrinagar	beach	S4082	460	400	78	10	2	3	0	0	0	2	0	1	0	3	0	0	100,0	n.d.	n.d.
	S Indira Point	beach	S4084	390	400	78	4	4	0	0	1	0	2	0	1	2	1	0	8	100,0	n.d.	n.d.
Galathea	upper reaches	bar	S4085	520	400	7	1	1	0	0	0	0	0	0	54	37	0	0	0	100,0	100	39

Table A6. Heavy-mineral data for modern sands derived from the Indo-Burman-Andaman-Nicobar subduction complex

river	locality	deposit	sample	Operator	class (microns)	acid treatment	counting method	n°HM grains	HMC%w	% transparent	% opaque	% turbid	zircon	tourmaline	rutile	Ti oxide	apatite	titanite	epidote	garnet	chloritoid	staurolite	kyanite	sillimanite	b/g hornblende	g/b hornblende	& amphiboles	clinopyroxene	enstatite	hypersthene	olivine	spinel	others		HCl	MMI	ZTR	CZi	GZi
ASSAM																																								
Burhi Dihing	Deurigaon	bar	BR 13	S.Andò	63-250	oxalic/acetic	area	210	6,8	73%	8%	19%	0	0	0	0	0	1	32	14	0	0	0	0	25	5	4	5	4	1	5	1	0	100,0	21	n.d.	0	n.d.	100
Dhansiri	Barahigaon	bar	BR 11	S.Andò	63-250	oxalic/acetic	area	200	0,7	50%	18%	32%	5	3	4	1	0	2	43	12	5	3	1	0	18	0	2	2	1	0	0	0	1	100,0	5	17	13	0	73
Koplli	Marigaon	bar	BR 68	S.Andò	63-250	oxalic/acetic	area	206	2,1	57%	30%	13%	42	8	8	3	0	3	20	3	0	1	0	0	9	1	0	0	0	0	0	0	0	100,0	10	n.d.	62	0	6
COASTAL BANGLADESH																																								
Karnaphuli	Rangamati	bar	S3547	S.Andò	63-250	Na ditionite	area	210	4,0	71%	17%	12%	1	2	2	1	0	2	27	20	1	10	10	2	16	0	0	0	0	0	0	0	1	100,0	3	52	6	n.d.	96
Karnaphuli	Chittagong	mouth	SO188-2	M.Limonta	32-500	Na ditionite	area	207	4,0	67%	30%	3%	4	3	5	0	3	3	29	14	1	3	2	0	20	3	2	5	0	0	0	0	0	100,0	19	40	13	10	77
	Cox Bazar	beach	S3530	S.Andò	63-250	Na ditionite	area	207	2,8	80%	3%	17%	0	2	0	0	4	1	25	14	0	2	2	0	42	1	0	2	0	0	0	0	1	100,0	3	53	4	n.d.	97
NORTHERN ARAKAN																																								
Kaladan	Kyauktaw	bar	S3177	S.Andò	63-250	acetic	area	202	0,4	19%	8%	73%	20	20	14	16	0	0	2	19	4	3	0	0	0	0	0	0	0	0	0	0	0	100,0	n.d.	15	70	2	49
	Padali	beach	S3175	S.Andò	63-250	acetic	area	207	0,5	34%	7%	59%	5	23	12	17	0	2	14	8	7	5	1	0	3	0	0	0	0	0	0	0	0	100,0	n.d.	18	57	8	61
	Sittwe	beach	S3176	S.Andò	63-250	acetic	area	206	0,6	30%	11%	59%	24	17	12	11	1	2	2	19	4	1	0	0	0	0	0	0	0	0	0	4	0	100,0	n.d.	8	64	14	45
CENTRAL ARAKAN																																								
Lemro	Atet Than Htaung	bar	S3182	M.Limonta	32-355	none	area	163	0,7	7%	1%	93%	50	13	10	1	6	1	9	2	1	0	0	0	0	0	0	0	0	0	0	6	1	100,0	n.d.	n.d.	74	11	4
Wek	Atet Than Htaung	bar	S3181	M.Limonta	32-355	none	area	115	0,6	4%	2%	94%	25	39	17	0	1	0	2	1	9	0	0	0	0	0	0	0	0	0	0	1	6	100,0	n.d.	0	81	3	3
Ru	Ru Chaung	bar	S3183	M.Limonta	32-355	none	area	208	0,9	15%	1%	84%	30	45	15	0	1	0	1	2	4	0	0	0	0	0	0	0	0	0	0	0	0	100,0	n.d.	0	91	2	6
Koum	Koum Chaung	bar	S3179	M.Limonta	32-355	none	area	202	1,3	7%	1%	92%	5	6	0	0	0	0	0	4	1	0	0	0	0	0	0	0	0	0	0	0	83	100,0	n.d.	n.d.	12	0	45
Lemro	Mrauk U	bar	S3178b	S.Andò	63-250	acetic	area	5	1,1	1%	3%	96%	60	0	0	0	0	0	20	0	20	0	0	0	0	0	0	0	0	0	0	0	0	100,0	n.d.	n.d.	60	0	0
Lemro	Mrauk U	levee	S3178a	M.Limonta	63-250	none	area	70	0,2	7%	2%	92%	13	20	14	4	8	6	20	3	7	0	0	0	0	0	0	0	0	0	0	1	4	100,0	n.d.	n.d.	51	10	18
RAMREE ISLAND																																								
	Kyaukphyu	beach	S3184	S.Andò	63-250	acetic	area	201	0,5	56%	12%	32%	1	7	9	6	0	2	41	4	1	0	2	0	9	0	1	0	0	0	0	14	0	100,0	0	38	24	90	73
SOUTHERN ARAKAN																																								
Tanlwe	Migyaunglu	bar	S3193b	S.Andò	63-250	acetic	area	114	0,3	20%	10%	70%	7	2	5	11	0	4	61	4	0	0	0	0	0	0	0	0	0	0	0	7	0	100,0	n.d.	n.d.	25	50	33
Tanlwe	Migyaunglu	levee	S3193a	M.Limonta	63-250	none	area	176	0,3	20%	3%	77%	6	5	5	1	6	6	62	6	1	0	0	0	1	0	0	0	0	0	0	2	0	100,0	n.d.	n.d.	17	27	48
Taunggok	Taunggok	bar	S3194	S.Andò	63-250	acetic	area	34	0,2	9%	6%	85%	9	9	12	15	0	6	41	0	0	0	0	3	3	0	3	0	0	0	0	0	0	100,0	n.d.	n.d.	44	0	0
Tahde	Shwehle	bar	S3195	S.Andò	63-250	acetic	area	93	0,7	11%	10%	79%	0	3	9	9	1	3	71	2	0	0	0	0	0	0	0	0	0	0	0	2	0	100,0	n.d.	n.d.	20	100	n.d.
Pyunpye	Pyunpye	bar	S3196	M.Limonta	32-355	none	area	201	0,5	12%	11%	77%	61	8	11	1	4	0	4	0	0	0	0	0	0	0	0	0	0	0	0	9	0	100,0	n.d.	n.d.	82	13	0
Thandwe	Thandwe	bar	S3197	S.Andò	63-250	acetic	area	49	0,3	8%	9%	83%	20	8	10	18	2	4	16	4	0	0	0	0	2	0	0	0	0	0	0	14	0	100,0	n.d.	n.d.	57	41	17
	Linn Thar	beach	S3186	M.Limonta	32-355	none	area	39	0,0	####	0%	0%	54	13	13	0	8	0	0	0	0	0	0	0	0	0	0	0	0	0	0	13	0	100,0	n.d.	n.d.	79	19	0
Kyaukki	Kyaukki bar	bar	S3192	M.Limonta	32-355	none	area	208	0,6	23%	8%	69%	50	13	13	9	4	0	3	0	0	0	0	0	0	0	0	0	0	0	0	5	0	100,0	n.d.	n.d.	86	9	1
Pazunbye	Pazunbye	bar	S3191	S.Andò	63-250	acetic	area	213	0,7	16%	10%	74%	46	4	16	8	0	1	15	1	0	0	0	0	0	0	0	0	0	0	0	8	0	100,0	n.d.	n.d.	75	15	3
Kyleintuli	Kalabyin	bar	S3188b	S.Andò	63-250	acetic	area	18	0,5	3%	4%	93%	17	6	6	11	0	0	61	0	0	0	0	0	0	0	0	0	0	0	0	0	0	100,0	n.d.	n.d.	39	0	0
Kyleintuli	Kalabyin	levee	S3188a	M.Limonta	63-250	none	area	200	0,3	12%	5%	84%	6	6	14	1	5	1	58	3	1	0	0	0	1	0	0	1	0	0	0	6	0	100,0	n.d.	n.d.	26	50	29
Kyleintuli	mouth	beach	S3189	S.Andò	63-250	acetic	area	213	0,6	16%	7%	76%	13	6	10	16	0	5	34	1	0	0	0	0	0	0	0	0	0	0	0	13	0	100,0	n.d.	n.d.	46	50	10
	Seliguin	beach	S3190	M.Limonta	32-355	none	area	201	7,5	35%	35%	30%	69	3	8	0	0	0	3	1	0	0	0	0	0	0	0	0	0	0	0	13	0	100,0	n.d.	n.d.	82	16	1
AYEYARWADI RIVER																																								
Ayeyarwadi	Pyay	bar	S3198b	M.Limonta	32-355	none	area	200	6,0	71%	19%	10%	6	2	2	1	1	1	31	14	0	0	1	0	35	3	1	3	1	0	1	1	1	100,0	12	n.d.	10	14	69
Ayeyarwadi	Pyay	levee	S3198a	M.Limonta	bulk	none	area	225	3,1	80%	3%	17%	3	1	0	0	2	1	39	6	3	0	0	0	35	2	6	0	0	0	0	1	0	100,0	8	0	4	33	70
Ayeyarwadi	Shwedaung	bar	S3199b	M.Limonta	32-355	none	area	245	6,3	74%	11%	15%	1	1	1	0	1	4	38	12	0	0	1	0	31	5	4	1	0	0	0	0	0	100,0	12	n.d.	3	n.d.	91
Ayeyarwadi	Shwedaung	levee	S3199a	M.Limonta	bulk	none	area	198	4,0	70%	11%	19%	3	1	1	0	2	1	46	5	3	0	0	1	34	1	2	0	0	0	0	1	0	100,0	6	14	5	14	63
Ayeyarwadi	Nyaungdoun	bar	S3200B																																						
Ayeyarwadi	Nyaungdoun	levee	S3200a	M.Limonta	>15	none	area	212	3,2	78%	6%	16%	1	1	0	0	0	0	53	6	0	0	0	0	30	1	6	0	0	0	0	0	0	100,0	12	n.d.	3	n.d.	80
Ayeyarwadi	Nyaungdoun	bar	S3200b	S.Andò		Na ditionite	area		5,0	80%	7%	13%	0	0	1	1	0	3	37	7	1	0	0	0	43	1	2	2	1	0	0	0	0	100,0	4	n.d.	2	n.d.	97
Ayeyarwadi	Nyaungdoun	18% bulk	S3200b	S.Andò	80-125	Na ditionite	area	205	13,4	79%	13%	8%	0	0	0	1	1	1	3	42	6	1	0	0	0	38	1	1	1	0	0	0	1	0	100,0	4	n.d.	3	n.d.	93
Ayeyarwadi	Nyaungdoun	68% bulk	S3200b	S.Andò	125-180	Na ditionite	area	205	3,4	82%	1%	17%	0	0	0	0	0	3	33	7	0	0	0	0	48	1	2	2	2	0	0	0	0	100,0	4	n.d.	1	n.d.	100
Ayeyarwadi	Nyaungdoun	12% bulk	S3200b	S.Andò	180-250	Na ditionite	area	216	1,2	66%	1%	33%	0	0	0	1	0	3	33	2	0	0	0	0	49	2	5	4	1	0	0	0	0	100,0	6	n.d.	1	n.d.	n.d.
NORTH ANDAMAN																																								
Kalpong	Diglipur	bar	S3212	M.Limonta	32-355	none	area	225	4,5	72%	13%	15%	0	2	0	0	0	0	4	2	0	0	0	0	15	6	9	37	17	2	1	4	0	100,0	39	n.d.	2	91	n.d.
	Kalipur	beach	S3213	M.Limonta	32-355	none	area	201	10,6	78%	7%	16%	0	0	1	0	0	0	9	2	0	0	0	0	16	9	1	23	28	0	5	4	0	100,0	53	n.d.	1	100	n.d.
	Ramnagar	beach	S3220	M.Limonta	32-355	none	area	200	0,7	41%	26%	33%	21	3	7	1	1	0	9	4	0	0	0	0	2	1	2	20	14	6	0	13	0	100,0	n.d.	n.d.	30	39	16
MIDDLE ANDAMAN																																								
	Mayabunder	beach	S3211	M.Limonta	32-355	none	area	236	1,9	42%	20%	38%	3	0	1	0	0	0	73	0	0	0	0	0	1	0	0	8	0	3	0	9	0	100,0	n.d.	n.d.	5	76	13
	Karmatang	beach	S3210	M.Limonta	32-355	none	area	206	0,6	45%	27%	28%	26	3	9	2	0	7	5	3	0	0	0	0	1	1	0	8	7	6	0	19	0	100,0	n.d.	n.d.	40	43	10
Lisvolo	Billiground	dry bed	S3214	M.Limonta	32-355	none	area	203	2,5	50%	28%	22%	21	1	4	0	0	0	2	2	0	0	0	0	7	0	1	47	7	1	0	5	0	100,0	20	n.d.	26	19	11
	Cuthbert Bay	beach	S3209	M.Limonta	32-355	none	area	206	1,9	55%	19%	26%	6	0	2	0	1	1	8	4	0	0	0	0	2	1	5	42	18	1	0	7	0	100,0	n.d.	n.d.	9	52	41
	Panchavati	beach	S3208	M.Limonta	32-355	none	area	202	10,6	54%	8%	38%	0	0	0	0	1	0	8	10	0	0	0	0	15	0	6	26	26	1	1	3	0	100,0	2	n.d.	0	100	100
Nimbutala	Nimbutala	dry bed	S3215	M.Limonta	32-355	none	area	205	1,1	51%	22%	27%	4	1	5	0	0	1	1	0	1	0	0	0	3	1	1	24	46	3	1	6	0	100,0	n.d.	n.d.	10	62	0
	Amkunj	beach	S3207	M.Limonta	32-355	none	area	205	3,9	73%	10%	16%	0	1	1	0	0	0	27	1	0	0	0	0	13	0	5	24	18	2	1	4	0	100,0	5	n.d.	3	90	n.d.
BARATANG																																								
	Balu Dera	beach	S3206	M.Limonta	32-355	none	area	212	2,0	46%	37%	17%	31	4	8	0	0	6	9	4	4	0	0	0	1	2	0	9	0	0	0	22	0	100,0	n.d.	0	42	42	12
SOUTH ANDAMAN																																								
	Collinpur	beach	S3216	M.Limonta	32-355	none	area	209	3,8	59%	24%	17%	8	3	3	0	1	6	37	29	3	5	0	0	1	0	0	1	0	0	0	1	0	100,0	n.d.	21	15	11	78
	Kurmadera	beach	S3217	M.Limonta	32-355	none	area	215	1,1	45%	39%	16%	26	9	9	0	0	1	28	13	1	9	0	0	0	0	0	0	0	0	0	0	0	100,0	n.d.	33	44	2	34
	Wandoor	beach	S4090	M.Limonta	32-355	none	area	217	9,6	47%	45%	8%	19	3	4	0	1	5	24	31	2	6	0	0	0	0	0	0	0	0	0	2	0	100,0	n.d.	27	26	11	62
	Corbyn's Cove	beach	S3201	M.Limonta	32-355	none	area	147	5,8	40%	20%	40%	41	3	5	1	0	2	15	1	1	0	0	0	1	0	1	11	1	0	0	16	1	100,0	n.d.	50	28	3	
	Manjeri	beach	S4088	M.Limonta	32-355	none	area	207	2,9	64%	26%	10%	6	2	2	0	0	0	25	2	0	0	0	0	18	0	30	0	3	0	0	10	0	100,0	8	n.d.	10	64	29
	Beadonabad	beach	S3204	M.Limonta	32-355	none	area	203	16,8	73%	8%	19%	0	0	0	0	0	0	20	0	0	0	0	0	8	0	13	56	0	1	0	0	0	100,0	6	n.d.	0	n.d.	n.d.
	Barmanala	beach	S4089	M.Limonta	32-355	none	area	217	28,5	77%	9%	14%	0	0	0	0	0	0	19	0	0	0	0	0	14	1	22	43	0	2	0	0	0	100,0	20	n.d.	0	n.d.	n.d.
	Chidiya Tapu	beach	S3203	M.Limonta	32-355	none	area	205	41,4	63%	21%	16%	0	0	0	0	0	1	22	10	0	0	0	0	5	0	21	30	0	0	0	8	0	100,0	10	n.d.	0	100	100
OTHER ANDAMAN ISLANDS																																								
	Barren	beach	BA1	M.Limonta	32-355	none	area	217	5,2	12%	0%	88%	0	0	0	0	0	0	0	0	0	0	0	0	0	0	0	29	0	0	71	0	0	100,0	n.d.	n.d.	0	n.d.	n.d.
	Barren	beach	BA2	M.Limonta	32-355	none	area	195	3,8	8%	0%	92%	0	0	0	1	0	0	2	0	0	0	0	0	0	0	0	45	0	1	52	0	0	100,0	n.d.	n.d.	1	n.d.	n.d.
	Barren	ash fall	BA3	M.Limonta	32-355	none	area	205	5,8	73%	0%	26%	0	0	0	0	0	0	0	0	0	0	0	0	0	0	0	9	0	0	91	0	0	100,0	n.d.	n.d.	0	n.d.	n.d.
	Narcondum	beach	S4091	M.Limonta	32-355	none	area	205	23,3	86%	4%	10%	0	0	0	0	0	0	0	0	0	0	0	0	5	60	0	23	0	5	5	0	0	100,0	95	n.d.	0	n.d.	n.d.
	Interview	beach	S3222	M.Limonta	32-355	none	area	170	2,1	43%	54%	3%	4	2	1	0	0	0	6	11	1	0	0	0	8	2	2	24	0	39	0	1	0	100,0	31	n.d.	6	13	73
	Havelock	beach	S3223	M.Limonta	32-355	none	area	212	1,4	76%	16%	8%	0	0	0	0	0	0	17	2	0	0	0	0	4	13	0	23	0	29	6	5	0	100,0	85	n.d.	0	100	n.d.
	Smith	beach	S3221	M.Limonta	32-355	none	area	184	0,4	48%	36%	15%	2	1	1	1	0	2	29	15	1	0	1	0	0	1	1	3	0	0	0	43	0	100,0	n.d.	n.d.	4	96	90
	Ross	beach	S3218	M.Limonta	32-355	none	area	32	21,0	16%	26%	58%	28	16	0	3	3	0	0	13	16	0	0	3	9	0	0	6	0	0	0	3	0	100,0	n.d.	17	47	10	31
	N Rutland	beach placer	S4086	M.Limonta	bulk	none	area	20	98,6	2%	98%	0%	0	0	0	0	0	0	0	5	0	0	0	0	0	5	0	30	15	15	30	0	0	100,0	n.d.	n.d.	0	n.d.	100
	NW Rutland	beach	S4087	M.Limonta	32-355	none	area	202	33,2	39%	58%	3%	28	3	3	0	0	0	26	25	2	6	0	0	0	0	0	1	0	0	0	2	0	100,0	n.d.	28	35	7	48
GREAT NICOBAR																																								
	N Campbell Bay	beach	S4077	M.Limonta	32-355	none	area	118	2,2	20%	48%	32%	17	10	5	1	8	0	3	48	4	0	0	0	0	0	0	2	0	0	0	2	0	100,0	n.d.	n.d.	33	9	74
	Campbell Bay	beach	S4078	M.Limonta	32-355	none	area	207	2,4	53%	24%	22%	16	5	9	0	0	2	13	42	3	8	0	0	0	0	0	0	0	0	0	1	0	100,0	n.d.	25	30	6	72
	S Campbell Bay	beach	S4079	M.Limonta	32-355	none	area	221	21,1	56%	40%	5%	25	1	5	0	0	1	3	57	2	3	0	0	0	0	0	0	0	0	0	1	1	100,0	n.d.	20	31	5	70
	Jogindarnagar	beach	S4080	M.Limonta	32-355	none	area	206	7,7	53%	24%	23%	5	1	5	0	0	1	15	50	0	1	0	0	2	0	0	16	0	0	0	2	0	100,0	n.d.	n.d.	13	31	90
	Gandhinagar	beach	S4081	M.Limonta	32-355	none	area	106	0,4	58%	23%	19%	4	3	2	0	0	0	18	17	2	5	0	3	13	6	1	18	0	8	2	0	0	100,0	37	47	8	0	82
	Shastrinagar	beach	S4082	M.Limonta	32-355	none	area	202	2,7	63%	15%	22%	0	3	1	0	0	6	25	41	1	12	2	0	7	0	0	0	0	0	0	0	0	100,0	16	34	4	n.d.	100
	N Indira Point	beach	S4083	M.Limonta	32-355	none	area	29	0,1	43%	15%	43%	14	7	0	0	0	0	7	48	3	7	3	0	7	3	0	0	0	0	0	0	0	100,0	n.d.	n.d.	21	0	78
	S Indira Point	beach	S4084	M.Limonta	32-355	none	area	218	19,8	71%	21%	8%	1	2	2	0	1	1	16	64	0	6	2	0	4	0	0	0	0	0	0	0	0	100,0	n.d.	39	6	n.d.	98
Galathea	upper reaches	bar	S4085	M.Limonta	32-355	none	area	211	0,6	40%	14%	45%	7	13	4	0	0	2	48	7	9	0	0	0	5	1	1	1	0	0	0	0	0	100,0	36	2	24	7	52

Table A7. Bulk-petrography data for Cenozoic sandstones from the Bengal Basin, coastal Bangladesh, coastal Arakan and Andaman Islands

unit	age	sample	operator	n°points	Q	KF	P	Lvf	Lvm	Lmv	Lu	Lch	Lc	Lp	Lms	Lm	mica	HM		MI*	MI
SURMA BASIN (Bangladesh)																					
Dupi Tila	Pleistocene	BA03_6A	G.Vezzoli	400	51	6	6	4	0	6	0	0	0	0	5	5	2	15,6	100,0	227	178
Dupi Tila	Pleistocene	BA03-17A	G.Vezzoli	400	64	8	3	5	0	5	0	0	0	1	3	7	4	0,3	100,0	252	199
Tipam	Pliocene	BA03_3B	G.Vezzoli	400	46	10	2	2	0	1	0	0	0	1	5	3	26	3,9	100,0	203	156
Tipam	Pliocene	BA03_4A	G.Vezzoli	400	60	10	8	3	1	3	0	0	0	0	5	4	3	2,5	100,0	225	189
Tipam	Pliocene	BA05-6A	G.Vezzoli	400	57	9	8	2	0	2	0	1	0	1	4	6	7	4,3	100,0	247	223
Tipam	Pliocene	BA03 2B	G.Vezzoli	200	81	5	1	0	0	4	0	2	0	0	6	1	0	0,0	100,0	179	170
Surma	Miocene	BA03-18A	G.Vezzoli	400	71	4	2	1	0	1	0	0	3	0	3	1	15	0,0	100,0	183	174
Surma?	Miocene?	BA05-15A	G.Vezzoli	400	56	8	7	3	0	2	0	0	1	1	4	4	13	0,8	100,0	228	168
Barail?	Oligocene?	BA03-7A	G.Vezzoli	400	95	1	1	0	0	0	0	0	0	0	1	1	0	0,0	100,0	n.d.	n.d.
Upper Barail	Oligocene	BA03-13A	G.Vezzoli	400	67	6	1	1	0	5	0	0	0	0	4	11	5	0,0	100,0	235	226
Upper Barail	Oligocene	BA06-16A	G.Vezzoli	400	62	3	0	5	0	2	0	0	0	2	18	8	0	0,0	100,0	196	161
Upper Barail	Oligocene	BA05-9A	G.Vezzoli	400	70	6	1	2	0	1	0	1	0	0	10	8	1	0,6	100,0	215	199
Middle Barail	Oligocene	BA06-9A	G.Vezzoli	400	79	1	0	3	0	1	0	1	0	2	9	5	0	0,0	100,0	213	168
Middle Barail	Oligocene	BA06-8B	G.Vezzoli	400	81	0	1	1	0	0	0	1	0	2	7	6	0	0,3	100,0	240	195
Middle Barail	Oligocene	BA06-8A	G.Vezzoli	400	84	1	0	2	0	3	0	1	0	0	7	2	0	0,0	100,0	175	152
Middle Barail	Oligocene	BA06-10A	G.Vezzoli	400	84	0	0	3	0	0	0	0	0	0	9	4	0	0,0	100,0	209	174
Lower Barail	U.Eocene	BA03-10A	G.Vezzoli	400	78	1	1	1	0	3	0	0	0	1	14	1	0	0,0	100,0	155	142
Lower Barail	U.Eocene	BA05-15F	G.Vezzoli	400	71	4	2	4	1	3	0	0	0	1	11	2	0	0,5	100,0	161	117
Basal Barail	U.Eocene	BA06-6B	G.Vezzoli	400	90	2	1	2	0	1	0	0	0	1	2	2	1	0,0	100,0	206	132
Basal Barail	U.Eocene	BA06-6A	G.Vezzoli	400	94	2	1	1	0	0	0	0	0	0	2	0	0	0,3	100,0	n.d.	n.d.
Basal Barail	U.Eocene	BA06-6E	G.Vezzoli	400	90	0	0	1	0	0	0	0	0	1	6	1	0	0,3	100,0	152	103
Basal Barail	U.Eocene	BA06-4A	G.Vezzoli	400	95	0	0	2	0	0	0	0	0	1	1	1	0	0,0	100,0	n.d.	88
Basal Barail	U.Eocene	BA06-5A	G.Vezzoli	400	87	5	0	4	0	0	0	0	0	1	2	1	0	0,3	100,0	n.d.	92
Basal Barail	U.Eocene	BA05-14A	G.Vezzoli	300	83	2	3	1	0	0	0	0	0	0	4	3	3	0,7	100,0	217	192
Basal Barail	U.Eocene	BA06-21B	G.Vezzoli	400	70	3	0	1	0	1	0	0	0	3	15	4	2	0,6	100,0	181	149
Tura	Paleoc-Eoc.	BA05-19E	G.Vezzoli	400	93	5	0	0	0	0	0	0	0	0	0	0	1	0,0	100,0	n.d.	n.d.
Tura	Paleoc-Eoc.	BA05-19A	G.Vezzoli	400	98	1	0	1	0	0	0	0	0	0	0	0	0	0,0	100,0	n.d.	n.d.
HATIA TROUGH (Singra and Bogra Cores)																					
Surma	Miocene	900-903	G.Vezzoli	50	59	0	2	0	0	0	0	0	2	12	22	0	0	2,4	100,0	n.d.	n.d.
Surma	Miocene	1800-1804	G.Vezzoli	100	88	0	0	0	0	0	0	0	0	0	7	0	3	1,4	100,0	n.d.	n.d.
Barail	Oligocene	2000-2004	G.Vezzoli	100	94	0	0	0	0	0	0	0	0	0	3	0	0	3,8	100,0	n.d.	n.d.
Kopili	Eocene	1723-1732	G.Vezzoli	100	97	0	1	0	0	0	0	0	0	0	0	0	0	1,5	100,0	n.d.	n.d.
Cherra	Eocene	1990-1999	G.Vezzoli	400	96	0	0	0	0	0	0	0	0	3	0	0	0	0,0	100,0	n.d.	n.d.
HATIA TROUGH (SBZ and SIT Cores)																					
Tipam	Pliocene	1799-1800	G.Vezzoli	50	62	4	0	0	0	0	0	0	0	0	8	0	27	0,0	100,0	n.d.	n.d.
Tipam	Pliocene	2010-2011	G.Vezzoli	100	51	0	1	0	0	0	0	0	7	0	8	1	28	4,0	100,0	n.d.	n.d.
Surma	Miocene	3014-3015	G.Vezzoli	200	72	3	6	1	0	0	0	0	1	0	1	4	11	1,3	100,0	n.d.	n.d.
Surma	Miocene	3401-3402	G.Vezzoli	200	65	5	6	0	0	0	0	0	2	0	3	1	18	0,0	100,0	n.d.	n.d.
Barail	Oligocene	2648-2654	G.Vezzoli	100	72	4	1	1	1	0	0	0	0	1	5	1	10	3,8	100,0	n.d.	n.d.
Barail	Oligocene	2793-2799	G.Vezzoli	200	73	5	5	1	0	1	0	0	1	1	3	2	8	0,6	100,0	n.d.	n.d.
HATIA TROUGH (Sangu Core)																					
MS3	Pleistocene	150-160	G.Vezzoli	400	83	10	1	1	0	2	0	0	0	1	2	0	0	0,3	100,0	258	188
MS3	Pleistocene	220-230	G.Vezzoli	400	90	5	1	0	0	0	0	1	0	1	0	1	0	0,3	100,0	n.d.	52
MS3	Pleistocene	310-320	G.Vezzoli	400	83	5	3	0	0	0	0	1	0	2	1	2	1	1,4	100,0	n.d.	155
MS3	Pleistocene	360-370	G.Vezzoli	400	78	10	2	0	1	2	0	1	0	1	3	1	1	0,6	100,0	245	203
MS3	Pleistocene	440-450	G.Vezzoli	400	69	9	11	1	2	0	0	1	0	3	1	1	2	0,3	100,0	n.d.	60
MS3	Pleistocene	530-540	G.Vezzoli	400	65	9	5	2	1	0	0	1	0	3	1	4	7	1,0	100,0	350	179
MS3	Pleistocene	630-640	G.Vezzoli	400	30	1	1	2	1	0	0	1	25	33	0	2	3	0,7	100,0	n.d.	21
MS2	Pliocene	970-980	G.Vezzoli	400	9	1	1	0	0	0	0	1	19	65	0	0	4	0,0	100,0	n.d.	0
MS2	Pliocene	1050-1060	G.Vezzoli	400	62	10	12	1	1	0	0	1	1	8	1	1	2	0,3	100,0	n.d.	41
MS2	Pliocene	1070-1080	G.Vezzoli	400	71	12	8	1	2	2	0	0	0	0	3	0	1	0,0	100,0	239	181
MS2	Pliocene	1190-1200	G.Vezzoli	400	48	5	3	1	0	0	0	1	14	23	2	1	2	2,0	100,0	n.d.	18
MS2	Pliocene	1370-1380	G.Vezzoli	400	22	1	3	1	1	0	0	0	3	62	1	0	6	0,0	100,0	n.d.	3
MS2	Pliocene	1580-1590	G.Vezzoli	400	5	1	2	1	0	0	0	0	5	80	0	0	5	0,0	100,0	n.d.	0
MS2	Pliocene	1790-1800	G.Vezzoli	400	57	9	10	1	1	0	0	0	2	10	2	2	6	0,0	100,0	265	72
MS2	Pliocene	1890-1900	G.Vezzoli	400	70	7	10	1	0	0	0	1	1	2	2	1	4	0,3	100,0	282	135
MS2	Pliocene	2080-2090	G.Vezzoli	400	24	3	4	0	1	0	0	1	7	61	0	0	0	0,0	100,0	n.d.	7
MS2	Pliocene	2270-2280	G.Vezzoli	400	56	7	6	1	1	0	0	1	4	13	1	1	7	0,0	100,0	280	57
MS1	Miocene	2680-2690	G.Vezzoli	400	2	0	0	0	0	0	0	0	1	97	1	0	0	0,0	100,0	n.d.	1
MS1	Miocene	2880-2890	G.Vezzoli	400	4	0	1	0	0	0	0	0	4	91	0	0	0	0,0	100,0	n.d.	0
MS1	Miocene	3380-3390	G.Vezzoli	400	5	0	1	0	0	0	0	0	2	91	0	0	0	0,0	100,0	n.d.	0
CHITTAGONG HILLS (Coastal Bangladesh)																					
Dupi Tila	Pleistocene	BGL05-9A	G.Vezzoli	400	78	7	0	5	0	0	0	2	0	2	2	2	1	1,6	100,0	250	93
Dupi Tila	Pleistocene	BNG5-46	G.Vezzoli	400	80	7	2	2	0	1	0	0	0	1	2	1	3	1,0	100,0	n.d.	100
Tipam	Pliocene	BGL05-13A	G.Vezzoli	400	93	4	0	0	0	0	0	2	0	0	0	0	0	0,7	100,0	n.d.	n.d.
Tipam	Pliocene	BNG5-96	G.Vezzoli	400	78	3	0	4	0	1	0	1	0	1	4	1	1	4,5	100,0	196	109
Tipam	Pliocene	BNG5-26A	G.Vezzoli	300	62	2	0	1	0	0	0	0	0	4	9	4	18	0,0	100,0	197	140
Boka Bil	Miocene	BGL05-14A	G.Vezzoli	300	63	9	5	1	0	1	0	0	0	2	4	3	8	2,9	100,0	221	156
Boka Bil	Miocene	BNG5-40	G.Vezzoli	300	64	7	6	3	2	1	0	1	0	3	3	3	5	0,7	100,0	231	115
Bhuban	Miocene	BGL05-16A	G.Vezzoli	300	62	10	6	0	0	2	0	0	0	2	2	1	12	2,5	100,0	219	146
Bhuban	Miocene	BNG5-78	G.Vezzoli	300	71	10	7	1	1	0	0	0	0	3	1	3	3	0,7	100,0	261	152
Bhuban	Miocene	BNG5-83	G.Vezzoli	300	60	10	4	0	0	0	0	0	0	0	3	2	20	0,3	100,0	n.d.	n.d.
Bhuban	Miocene	BNG5-33	G.Vezzoli	300	66	6	3	1	1	1	0	0	0	1	4	3	14	0,4	100,0	224	174
Bhuban	Miocene	BNG5-34	G.Vezzoli	300	61	5	4	3	0	0	0	0	0	2	3	1	21	0,4	100,0	n.d.	100
Bhuban	Miocene	BNG5-123	G.Vezzoli	300	73	8	2	2	1	0	0	1	0	2	0	4	7	0,3	100,0	311	165
ARAKAN RANGE (Myanmar)																					
Sittwe	Miocene	MY052A	G.Vezzoli	400	50	19	5	3	1	2	0	0	0	0	4	2	15	0,0	100,0	200	142
Kyaktaw	Miocene	MY3D	G.Vezzoli	400	61	5	5	3	1	4	0	0	0	0	7	9	5	0,3	100,0	241	209
Lemro	Miocene	MY6B	G.Vezzoli	400	66	5	5	1	0	3	0	1	0	0	5	6	7	0,0	100,0	226	207
Lemro	Miocene	MY10B	G.Vezzoli	400	58	9	5	3	0	2	0	0	0	1	9	8	6	0,0	100,0	228	198
Sabadgi Mélange	Eocene	MY0514E	G.Vezzoli	400	12	2	24	8	45	4	0	1	0	1	1	1	1	0,5	100,0	167	17
ANDAMAN FLYSCH (South Andaman)																					
Corbyn's cove	Oligocene	FT1B	G.Vezzoli	400	50	13	5	3	1	4	0	0	0	1	15	6	1	0,6	100,0	202	175
Corbyn's cove	Oligocene	FT3	G.Vezzoli	400	48	17	11	2	1	4	0	0	0	2	6	6	2	0,6	100,0	217	160
Corbyn's cove	Oligocene	FT4	G.Vezzoli	400	47	10	9	5	0	3	0	1	0	3	14	6	1	0,0	100,0	201	150
NAMUNAGARH GRIT (Andaman Islands)																					
North Andaman	Paleoc-Eoc.	Kal2	G.Vezzoli	400	20	1	24	16	30	5	0	1	0	1	2	0	1	0,0	100,0	125	14
North Andaman	Paleoc-Eoc.	Kal5	G.Vezzoli	400	14	0	21	17	38	3	0	3	0	1	2	1	0	0,0	100,0	144	12
Namunagar Quarry	Paleoc-Eoc.	NAM 3D	G.Vezzoli	400	2	1	41	4	48	0	0	0	0	0	0	0	0	2,2	100,0	n.d.	2
Hopetown Quarry	Paleoc-Eoc.	NAM 25A	G.Vezzoli	400	21	2	27	13	27	1	0	2	0	2	3	1	0	1,3	100,0	156	15
Mungleton Quarry	Paleoc-Eoc.	NAM 26	G.Vezzoli	400	19	1	30	19	26	1	0	1	0	1	2	0	0	0,3	100,0	n.d.	11

Table A8. Heavy-mineral data for Cenozoic sandstones from the Bengal Basin, coastal Bangladesh, coastal Arakan and Andaman Islands

unit	age	sample	operator	class (microns)	acid treatment	counting method	HMC%w	% transparent	% opaque	% turbid	zircon	tourmaline	rutile	Ti oxide	apatite	titanite	epidote	garnet	chloritoid	staurolite	kyanite	sillimanite	b/g hornblende	g/b hornblende	& amphiboles	clinopyroxene	enstatite	hypersthene	olivine	spinel	others		HCl	MMI	ZTR	CZi	GZi
SURMA BASIN (Bangladesh)																																					
Dupi Tila	Pleistocene	BA03_6A	S.Andò	63-250	Na ditionite	area	8	85%	10%	5%	1	1	0	0	0	1	41	0	0	6	3	0	40	0	4	0	0	0	0	0	0	100,0	5	53	3	n.d.	n.d.
Dupi Tila	Pleistocene	BA03-17A	S.Andò	63-250	acetic	area	1,0	85%	7%	8%	1	1	2	1	0	0	42	1	4	3	7	0	26	3	8	0	0	0	0	0	0	100,0	14	34	6	n.d.	n.d.
Tipam	Pliocene	BA03_3B	S.Andò	63-250	Na ditionite	area	0,7	65%	5%	29%	0	8	3	7	5	3	44	13	6	0	2	0	6	0	0	0	0	0	0	0	0	100,0	3	15	19	n.d.	96
Tipam	Pliocene	BA03_4A	S.Andò	63-250	Na ditionite	area	2,1	78%	8%	14%	0	2	1	2	0	5	32	16	0	7	3	0	26	0	3	0	0	0	0	0	0	100,0	3	50	6	n.d.	100
Tipam	Pliocene	BA05-6A	S.Andò	63-250	Na ditionite	area	1,7	81%	10%	10%	0	6	0	3	0	1	42	5	0	6	3	0	27	1	6	0	0	0	0	0	0	100,0	6	47	10	n.d.	92
Tipam	Pliocene	BA03 2B	S.Andò	63-250	acetic	area	5	22%	7%	71%	2	4	2	0	0	0	49	1	3	11	11	2	11	1	4	0	0	0	0	0	0	100,0	17	48	8	n.d.	40
Bhuban	Miocene	BA05-3A	S.Andò	63-250	Na ditionite	area	0,1	57%	14%	29%	0	3	6	41	6	3	15	9	15	0	0	0	3	0	0	0	0	0	0	0	0	100,0	n.d.	0	50	n.d.	100
L. Bhuban	Miocene	BA05-10A	S.Andò	63-250	Na ditionite	area	0,1	46%	9%	45%	6	28	5	46	0	0	0	0	12	0	0	0	0	0	0	0	0	0	0	1	0	100,0	n.d.	2	86	14	0
Surma	Miocene	BA03-18A	S.Andò	63-250	acetic	area	0,1	52%	12%	36%	6	18	8	3	0	6	0	36	22	1	0	0	0	0	0	0	0	0	0	0	0	100,0	n.d.	2	34	0	87
Surma?	Miocene?	BA05-15A	S.Andò	63-250	Na ditionite	area	0,2	75%	2%	24%	1	5	4	8	7	13	26	21	10	1	2	0	0	0	0	0	0	0	0	0	0	100,0	n.d.	13	19	n.d.	93
Barail?	Oligocene?	BA03-7A	S.Andò	63-250	Na ditionite	area	0,6	28%	18%	54%	4	18	14	41	0	2	1	0	1	15	3	0	0	0	0	0	0	0	0	0	0	100,0	n.d.	46	77	11	0
Upper Barail	Oligocene	BA03-13A	S.Andò	63-250	Na ditionite	area	0,6	68%	2%	29%	13	29	12	22	0	2	0	0	8	12	0	0	0	0	0	0	0	0	0	1	0	100,0	n.d.	29	76	7	3
Upper Barail	Oligocene	BA06-16A	S.Andò	63-250	acetic	area	0,6	19%	1%	80%	2	11	6	60	0	0	0	0	16	4	0	0	0	0	0	0	0	0	0	0	0	100,0	n.d.	10	79	17	0
Upper Barail	Oligocene	BA05-9A	S.Andò	63-250	Na ditionite	area	2,4	3%	0%	97%	17	32	20	21	0	1	0	1	6	2	0	0	0	0	0	0	0	0	0	1	0	100,0	n.d.	14	89	4	4
Middle Barail	Oligocene	BA06-9A	S.Andò	63-250	acetic	area	0,8	39%	2%	60%	19	7	3	59	0	0	0	0	4	6	0	0	0	0	0	0	0	0	0	1	0	100,0	n.d.	30	89	0	0
Middle Barail	**Oligocene**	**BA06-8B**	**S.Andò**	**63-250**	**acetic**	**area**	**0,5**	**38%**	**1%**	**61%**	**3**	**8**	**1**	**43**	**0**	**0**	**0**	**0**	**32**	**11**	**0**	**0**	**0**	**0**	**0**	**0**	**0**	**0**	**0**	**1**	**0**	**100,0**	**n.d.**	**13**	**56**	**22**	**0**
Middle Barail	Oligocene	BA06-8A	S.Andò	63-250	acetic	area	0,5	32%	0%	68%	12	19	14	26	0	1	0	0	24	2	0	0	0	0	0	0	0	0	0	1	0	100,0	n.d.	4	72	7	0
Middle Barail	Oligocene	BA06-10A	S.Andò	63-250	acetic	area	0,5	38%	0%	62%	16	15	10	53	0	0	0	0	4	0	0	0	0	0	0	0	0	0	0	1	0	100,0	n.d.	5	94	0	0
Lower Barail	U.Eocene	BA03-10A	S.Andò	63-250	acetic	area	0,3	15%	1%	84%	19	38	28	13	0	0	0	0	0	0	0	0	0	0	0	0	0	0	0	0	0	100,0	n.d.	n.d.	99	0	0
Lower Barail	U.Eocene	BA05-15F	S.Andò	63-250	Na ditionite	area	0,2	33%	2%	65%	7	27	15	38	0	2	0	7	1	0	0	0	0	0	0	0	0	0	0	1	1	100,0	n.d.	n.d.	87	12	50
Basal Barail	U.Eocene	BA06-6B	S.Andò	63-250	acetic	area	0,3	35%	0%	65%	21	22	9	37	0	1	0	3	5	0	0	0	0	0	0	0	0	0	0	2	0	100,0	n.d.	0	89	0	12
Basal Barail	U.Eocene	BA06-6A	S.Andò	63-250	acetic	area	0,3	29%	1%	69%	17	32	12	36	0	1	1	0	1	0	0	0	0	0	0	0	0	0	0	2	0	100,0	n.d.	n.d.	96	0	0
Basal Barail	U.Eocene	BA06-6E	S.Andò	63-250	acetic	area	0,3	50%	1%	49%	9	31	8	50	0	0	0	0	0	0	0	0	0	0	0	0	0	0	0	0	0	100,0	n.d.	n.d.	99	0	0
Basal Barail	U.Eocene	BA06-4A	S.Andò	63-250	acetic	area	0,2	29%	3%	67%	9	51	14	27	0	1	0	0	0	0	0	0	0	0	0	0	0	0	0	0	0	100,0	n.d.	n.d.	100	0	0
Basal Barail	U.Eocene	BA06-5A	S.Andò	63-250	acetic	area	0,3	55%	1%	44%	20	28	21	30	0	0	0	0	0	0	0	0	0	0	0	0	0	0	0	1	0	100,0	n.d.	n.d.	99	0	0
Basal Barail	U.Eocene	BA05-14A	S.Andò	63-250	acetic	area	0,3	60%	0%	40%	8	13	7	67	0	0	1	0	1	0	0	0	0	0	0	0	0	0	0	0	0	100,0	n.d.	n.d.	96	0	0
Basal Barail	U.Eocene	BA06-21B	S.Andò	63-250	acetic	area	0,1	42%	0%	58%	13	12	4	69	0	0	0	0	0	0	0	0	0	0	0	0	0	0	0	0	0	100,0	n.d.	n.d.	98	4	4
Tura	Paleoc-Eoc.	BA05-19E	S.Andò	63-250	Na ditionite	area	1,6	6%	92%	2%	31	41	7	4	0	4	6	0	0	6	0	0	0	0	0	0	0	0	0	1	0	100,0	n.d.	n.d.	50	83	3	0
Tura	Paleoc-Eoc.	BA05-19A	S.Andò	63-250	Na ditionite	area	0,2	15%	0%	85%	80	2	7	0	0	0	0	0	0	0	0	0	0	0	0	0	0	0	0	4	5	100,0	n.d.	n.d.	90	5	0
HATIA TROUGH (Singra and Bogra Cores)																																					
Surma	Miocene	900-903	S.Andò	63-250	acetic	area	0,8	35%	46%	18%	4	29	5	2	0	1	10	36	1	2	1	0	3	0	0	1	0	0	0	0	1	100,0	n.d.	30	42	0	89
Surma	Miocene	1800-1804	S.Andò	63-250	acetic	area	0,04	61%	3%	36%	7	30	46	4	0	0	0	2	6	0	0	0	0	0	0	0	0	0	0	2	2	100,0	n.d.	5	88	21	25
Barail	Oligocene	2000-2004	S.Andò	63-250	acetic	area	0,03	77%	6%	17%	13	4	67	8	0	1	1	1	0	0	0	0	0	0	0	0	0	0	0	5	0	100,0	n.d.	n.d.	92	27	8
Kopili	Eocene	1723-1732	S.Andò	63-250	acetic	area	0,3	56%	22%	22%	20	35	28	5	0	2	0	1	0	0	0	0	0	0	0	0	0	0	0	6	0	100,0	n.d.	n.d.	89	23	7
Cherra	Eocene	1990-1999	S.Andò	63-250	acetic	area	0,2	60%	8%	32%	36	24	24	9	0	1	1	2	0	0	0	0	0	0	0	0	0	0	0	0	4	100,0	n.d.	n.d.	93	0	4
HATIA TROUGH (SBZ and SIT Cores)																																					
Tipam	Pliocene	1799-1800	S.Andò	63-250	acetic	area	0,2	53%	7%	40%	3	9	8	7	0	6	34	20	10	1	1	0	0	0	0	0	0	0	0	0	0	100,0	n.d.	8	27	0	88
Tipam	Pliocene	2010-2011	S.Andò	63-250	acetic	area	0,0	48%	5%	48%	3	17	9	8	7	8	2	26	15	3	1	0	0	0	0	0	0	0	0	1	0	100,0	n.d.	9	36	0	91
Surma	Miocene	3014-3015	S.Andò	63-250	acetic	area	1,0	85%	1%	15%	4	11	11	0	6	0	1	58	9	0	0	0	0	0	0	0	0	0	0	0	0	100,0	n.d.	0	27	0	93
Surma	Miocene	3401-3402	S.Andò	63-250	acetic	area	0,2	83%	0%	17%	4	19	10	5	3	1	1	43	14	0	0	0	0	0	0	0	0	0	0	0	0	100,0	n.d.	0	39	0	91
Barail	Oligocene	2648-2654	S.Andò	63-250	acetic	area	0,4	88%	0%	12%	5	11	7	1	11	0	0	55	7	0	0	0	0	0	0	0	0	0	0	2	0	100,0	n.d.	0	25	0	91
Barail	Oligocene	2793-2799	S.Andò	63-250	acetic	area	0,2	72%	1%	27%	5	23	8	4	10	0	0	33	13	0	0	0	0	0	0	0	0	0	0	2	1	100,0	n.d.	0	40	27	87
HATIA TROUGH (Sangu Core)																																					
MS3	Pleistocene	150-160	S.Andò	63-250	acetic	area	1,2	82%	6%	12%	0	4	1	1	0	1	22	4	1	9	7	8	32	2	3	0	0	0	0	0	0	100,0	9	62	7	n.d.	100
MS3	Pleistocene	220-230	M.Limonta	32-355	Na ditionite	area	1,2	78%	6%	15%	0	9	3	0	0	0	0	27	5	1	23	15	11	2	1	0	0	0	0	1	2	100,0	n.d.	58	12	n.d.	100
MS3	Pleistocene	310-320	M.Limonta	32-355	Na ditionite	area	1,0	93%	1%	6%	1	4	0	0	0	1	26	5	1	8	4	7	39	1	2	1	0	0	0	1	0	100,0	7	63	5	n.d.	89
MS3	Pleistocene	360-370	S.Andò	63-250	acetic	area	1,4	90%	3%	7%	0	2	1	0	0	0	25	3	1	3	2	6	44	2	6	0	0	0	0	0	1	100,0	7	65	4	n.d.	100
MS3	Pleistocene	440-450	M.Limonta	32-355	Na ditionite	area	2,1	94%	3%	4%	0	0	0	0	3	2	23	8	0	1	3	4	48	5	2	0	0	0	0	0	0	100,0	14	78	1	n.d.	95
MS3	Pleistocene	530-540	M.Limonta	32-355	Na ditionite	area	2,9	48%	13%	38%	1	0	0	0	2	1	14	9	1	3	11	13	40	4	0	1	0	0	0	0	1	100,0	12	78	1	n.d.	94
MS2 (mud)	Pliocene	860-870	M.Limonta	15-180	Na ditionite	area	9,5	74%	17%	9%	3	3	1	0	6	3	24	12	0	1	2	0	41	0	4	0	0	0	0	0	0	100,0	2	57	7	0	81
MS2	Pliocene	1050-1060	M.Limonta	32-355	Na ditionite	area	2,8	55%	26%	19%	6	1	0	0	2	3	19	15	0	1	2	1	47	2	1	0	0	0	0	0	1	100,0	8	67	7	0	69
MS2	Pliocene	1070-1080	S.Andò	63-250	acetic	area	4,5	81%	3%	16%	0	2	0	0	0	1	21	19	1	1	2	0	50	1	1	0	0	0	0	0	0	100,0	2	42	3	n.d.	98
MS2	Pliocene	1790-1800	M.Limonta	32-355	Na ditionite	area	0,6	44%	38%	18%	1	4	0	0	0	1	45	36	1	6	4	1	1	0	0	0	0	0	0	0	0	100,0	n.d.	47	5	n.d.	97
MS2	Pliocene	1890-1900	M.Limonta	32-355	Na ditionite	area	0,3	26%	47%	26%	3	5	3	0	0	0	34	42	0	3	0	5	4	1	0	0	0	0	0	0	0	100,0	n.d.	n.d.	11	0	94
MS2 (mud)	Pliocene	2000-2010	M.Limonta	15-180	Na ditionite	area	1,3	77%	11%	12%	3	5	2	0	16	11	22	22	3	0	11	0	0	0	0	0	0	0	0	0	0	100,0	n.d.	51	11	13	87
MS2	Pliocene	2470-2480	M.Limonta	32-355	Na ditionite	area	1,7	13%	80%	6%	16	2	2	0	24	2	8	44	0	2	0	0	0	0	0	0	0	0	0	0	0	100,0	n.d.	n.d.	20	0	73
MS1	Miocene	2880-2890	M.Limonta	32-355	Na ditionite	area	0,7	20%	14%	67%	16	16	11	0	21	0	0	26	11	0	0	0	0	0	0	0	0	0	0	0	0	100,0	n.d.	n.d.	42	0	63
CHITTAGONG HILLS (Coastal Bangladesh)																																					
Dupi Tila	Pleistocene	BGL05-9A	S.Andò	63-250	acetic	area	2,7	76%	11%	13%	1	11	3	6	0	0	25	0	2	26	19	3	0	0	2	0	0	0	0	0	1	100,0	n.d.	52	21	n.d.	n.d.
Dupi Tila	Pleistocene	BNG5-46	S.Andò	63-250	acetic	area	1,1	61%	25%	14%	8	6	8	13	0	0	34	1	3	11	7	3	0	0	5	0	0	0	0	0	0	100,0	n.d.	50	35	0	11
Tipam	**Pliocene**	**BGL05-13A**	**S.Andò**	**63-250**	**acetic**	**area**	**1,6**	**56%**	**32%**	**12%**	**7**	**5**	**7**	**15**	**0**	**0**	**11**	**0**	**1**	**18**	**29**	**7**	**0**	**0**	**1**	**0**	**0**	**0**	**0**	**0**	**1**	**100,0**	**n.d.**	**56**	**33**	**0**	**0**
Tipam	Pliocene	BNG5-96	S.Andò	63-250	acetic	area	0,6	43%	7%	50%	1	1	4	6	1	0	41	0	4	19	14	0	4	0	7	0	0	0	0	0	2	100,0	n.d.	47	12	n.d.	n.d.
Tipam	Pliocene	BNG5-26A	S.Andò	63-250	acetic	area	0,9	68%	5%	27%	0	5	2	4	0	3	40	1	7	2	1	0	27	0	8	0	0	0	0	0	0	100,0	4	16	11	n.d.	n.d.
Boka Bil	Miocene	BGL05-14A	S.Andò	63-250	acetic	area	3,2	80%	5%	15%	0	1	0	1	1	3	23	11	2	1	1	0	52	1	2	0	0	0	0	0	0	100,0	3	28	2	n.d.	100
Boka Bil	Miocene	BNG5-40	S.Andò	63-250	acetic	area	0,8	67%	19%	14%	4	13	3	5	14	7	2	38	6	6	0	0	0	0	0	0	0	0	0	1	0	100,0	n.d.	25	25	20	91
Bhuban	Miocene	BGL05-16A	S.Andò	63-250	acetic	area	1,0	72%	11%	17%	1	4	2	1	6	5	27	24	2	2	2	0	22	0	1	0	0	0	0	0	0	100,0	4	33	8	n.d.	96
Bhuban	Miocene	BNG5-78	S.Andò	63-250	acetic	area	0,3	60%	0%	40%	0	10	5	10	12	0	1	50	5	2	0	0	2	0	0	0	0	0	0	0	0	100,0	n.d.	14	26	n.d.	99
Bhuban	Miocene	BNG5-83	S.Andò	63-250	acetic	area	0,1	89%	3%	8%	3	6	6	23	11	0	0	40	9	0	0	0	0	0	0	0	0	0	0	1	0	100,0	n.d.	0	38	33	93
Bhuban	Miocene	BNG5-33	S.Andò	63-250	acetic	area	0,3	47%	22%	31%	8	27	12	21	3	0	3	4	18	2	0	0	0	0	0	0	0	0	0	0	0	100,0	n.d.	6	68	6	33
Bhuban	Miocene	BNG5-34	S.Andò	63-250	acetic	area	0,2	83%	4%	14%	2	23	4	11	19	0	1	24	16	0	0	0	0	0	0	0	0	0	0	0	0	100,0	n.d.	0	39	17	91
Bhuban	Miocene	BNG5-123	S.Andò	63-250	acetic	area	0,3	61%	3%	36%	10	21	6	36	0	0	0	4	11	9	0	0	0	0	0	0	0	0	0	1	0	100,0	n.d.	23	74	13	29
ARAKAN RANGE (Myanmar)																																					
Sittwe	Miocene	MY052A	S.Andò	63-250	Na ditionite	area	0,2	64%	13%	22%	3	6	4	21	20	1	4	32	5	0	0	0	0	0	1	0	0	0	0	0	0	100,0	n.d.	0	35	13	90
Kyaktaw	Miocene	MY3D	S.Andò	63-250	Na ditionite	area	0,5	66%	6%	27%	1	18	5	18	18	1	1	26	11	0	0	0	0	0	0	0	0	0	0	1	0	100,0	n.d.	0	42	40	95
Lemro	Miocene	MY6B	S.Andò	63-250	Na ditionite	area	0,3	58%	0%	42%	8	27	7	47	9	0	1	0	0	0	0	0	0	0	0	0	0	0	0	0	0	100,0	n.d.	n.d.	89	6	0
Lemro	Miocene	MY10B	S.Andò	63-250	Na ditionite	area	0,3	26%	1%	73%	14	16	12	50	6	1	1	0	0	0	0	0	0	0	0	0	0	0	0	0	0	100,0	n.d.	n.d.	91	3	0
Sabadgi Mélange	Eocene	MY0514E	S.Andò	63-250	Na ditionite	area	0,4	52%	7%	40%	4	3	0	67	8	0	0	0	0	0	0	0	0	0	0	0	0	0	0	17	0	100,0	n.d.	n.d.	75	81	0
ANDAMAN FLYSCH (South Andaman)																																					
Corbyn's cove	Oligocene	FT1B	S.Andò	63-250	Na ditionite	area	0,9	54%	9%	37%	3	8	5	24	10	3	18	14	12	0	0	0	0	0	0	0	0	0	0	2	0	100,0	n.d.	0	40	45	82
Corbyn's cove	Oligocene	FT3	S.Andò	63-250	Na ditionite	area	0,4	44%	7%	49%	4	9	5	32	17	2	2	13	12	0	0	0	0	0	0	0	0	0	0	3	1	100,0	n.d.	0	50	47	76
Corbyn's cove	Oligocene	FT4	S.Andò	63-250	Na ditionite	area	0,6	35%	8%	57%	4	9	7	25	11	0	0	15	25	1	0	0	0	0	0	0	0	0	0	2	0	100,0	n.d.	1	46	33	79
NAMUNAGARH GRIT (Andaman Islands)																																					
Namunagar Quarry	Paleoc-Eoc.	NAM 3D	S.Andò	63-250	Na ditionite	area	4,0	37%	38%	25%	0	0	0	0	3	1	11	0	0	0	0	0	13	10	0	62	0	0	0	0	0	100,0	61	n.d.	0	n.d.	n.d.
Hopetown Quarry	Paleoc-Eoc.	NAM 25A	S.Andò	63-250	Na ditionite	area	1,3	42%	16%	42%	1	0	1	3	1	15	45	0	0	0	0	0	0	0	0	18	0	0	0	16	0	100,0	n.d.	n.d.	5	91	n.d.
Mungleton Quarry	Paleoc-Eoc.	NAM 26	S.Andò	63-250	Na ditionite	area	1,0	53%	7%	40%	0	0	1	1	3	16	45	1	0	0	0	0	0	0	0	24	0	0	0	7	0	100,0	n.d.	n.d.	2	100	n.d.

Table A9. Bulk-petrography data from pebbles and granules of Cenozoic sandstones contained in modern sediments of the Arakan Range and Great Nicobar

unit	age	sample	operator	n°points	Q	KF	P	Lvf	Lvm	Lmv	Lu	Lch	Lc	Lp	Lms	Lm	mica	HM		MI*	MI
SANDSTONE PEBBLES IN ARAKAN RIVER GRAVEL																					
Lemro @ Atet Than Htaung		S3182-P1	A.Resentini	300	50	0	12	15	4	6	4	4	0	0	3	1	0	0	100,0	181	46
Lemro @ Atet Than Htaung		S3182-P2	A.Resentini	300	39	0	23	8	1	7	0	1	0	0	16	3	0	1	100,0	202	142
Lemro @ Atet Than Htaung		S3182-P3	A.Resentini	300	33	2	20	12	2	3	4	1	0	0	12	6	4	2	100,0	218	127
Lemro @ Atet Than Htaung		S3182-P4	A.Resentini	300	67	0	7	0	0	2	0	0	0	0	7	6	11	1	100,0	246	237
Lemro @ Atet Than Htaung		S3182-P5	A.Resentini	300	59	0	5	9	0	4	0	2	0	0	15	2	2	1	100,0	188	129
SANDSTONE GRANULES IN ARAKAN RIVER SANDS																					
Tanlwe @ Migyaunglu		S3193-A	A.Resentini	18	72	0	17	6	0	0	0	0	0	0	6	0	0	0	100,0	n.d.	n.d.
Tanlwe @ Migyaunglu		S3193-B	A.Resentini	21	67	0	24	0	0	0	0	0	0	0	10	0	0	0	100,0	n.d.	n.d.
Tanlwe @ Migyaunglu		S3193-C	A.Resentini	45	40	2	24	18	0	2	0	0	0	0	9	2	2	0	100,0	n.d.	n.d.
Tanlwe @ Migyaunglu		S3193-D	A.Resentini	29	45	0	7	24	21	0	0	0	0	0	3	0	0	0	100,0	n.d.	n.d.
Tanlwe @ Migyaunglu		S3193-E	A.Resentini	57	47	0	11	16	2	4	0	0	0	2	19	0	0	0	100,0	n.d.	73
Tanlwe @ Migyaunglu		S3193-F	A.Resentini	47	32	4	23	4	2	13	0	0	0	2	15	4	0	0	100,0	n.d.	n.d.
Tanlwe @ Migyaunglu		S3193-L	A.Resentini	88	57	0	11	9	1	6	0	0	0	6	10	0	0	0	100,0	n.d.	48
Tanlwe @ Migyaunglu		S3193-M	A.Resentini	58	34	2	28	9	2	5	0	0	0	7	12	2	0	0	100,0	n.d.	83
Thandwe @ Thandwe		S3197-A	A.Resentini	123	39	2	21	15	8	5	0	0	0	2	8	0	0	0	100,0	n.d.	59
Thandwe @ Thandwe		S3197-B	A.Resentini	80	36	4	14	9	32	0	0	0	0	0	3	3	0	0	100,0	n.d.	29
Thandwe @ Thandwe		S3197-C	A.Resentini	312	53	0	6	3	0	1	0	0	0	10	25	2	0	0	100,0	163	110
Thandwe @ Thandwe		S3197-D	A.Resentini	132	84	2	1	2	0	0	0	0	0	5	6	1	0	0	100,0	n.d.	111
Thandwe @ Thandwe		S3197-E	A.Resentini	124	41	0	18	14	8	2	0	0	0	2	15	1	0	0	100,0	135	55
Thandwe @ Thandwe		S3197-F	A.Resentini	107	35	2	29	7	1	5	0	0	0	3	17	2	0	0	100,0	195	122
Kyieintuli @ Kalabyin		S3188-A	A.Resentini	74	31	4	23	16	4	4	0	0	0	1	15	0	1	0	100,0	n.d.	87
Kyieintuli @ Kalabyin		S3188-B	A.Resentini	121	43	2	20	11	5	4	0	0	0	0	14	1	0	0	100,0	191	105
Kyieintuli @ Kalabyin		S3188-C	A.Resentini	63	86	0	0	5	0	0	0	0	0	2	6	2	0	0	100,0	n.d.	n.d.
Kyieintuli @ Kalabyin		S3188-D	A.Resentini	9	22	0	0	44	33	0	0	0	0	0	0	0	0	0	100,0	n.d.	n.d.
Kyieintuli @ Kalabyin		S3188-E	A.Resentini	46	43	4	11	30	4	0	0	0	0	0	7	0	0	0	100,0	n.d.	32
SANDSTONE GRANULES IN GREAT NICOBAR SANDS																					
N Campbell Bay beach		S4077-A	A.Resentini	44	66	5	9	2	0	2	0	0	0	0	14	0	2	0	100,0	n.d.	n.d.
N Campbell Bay beach		S4077-B	A.Resentini	38	45	0	11	8	5	0	0	0	3	0	26	3	0	0	100,0	n.d.	144
N Campbell Bay beach		S4077-C	A.Resentini	72	40	4	14	1	0	1	0	0	0	0	31	4	3	1	100,0	185	178
Galathea River		S4085-A	A.Resentini	50	75	2	0	6	0	0	0	0	0	0	14	0	4	0	100,0	n.d.	n.d.
Galathea River		S4085-B	A.Resentini	55	60	0	2	1	1	0	0	0	0	0	16	2	18	0	100,0	n.d.	n.d.